



Delft University of Technology

## The Nano-Aperture Ion Source

van Kouwen, Leon

### DOI

[10.4233/uuid:088f8e60-3e6f-4fcf-85af-be8555beb635](https://doi.org/10.4233/uuid:088f8e60-3e6f-4fcf-85af-be8555beb635)

### Publication date

2017

### Document Version

Final published version

### Citation (APA)

van Kouwen, L. (2017). *The Nano-Aperture Ion Source*. [Dissertation (TU Delft), Delft University of Technology]. <https://doi.org/10.4233/uuid:088f8e60-3e6f-4fcf-85af-be8555beb635>

### Important note

To cite this publication, please use the final published version (if applicable).  
Please check the document version above.

### Copyright

Other than for strictly personal use, it is not permitted to download, forward or distribute the text or part of it, without the consent of the author(s) and/or copyright holder(s), unless the work is under an open content license such as Creative Commons.

### Takedown policy

Please contact us and provide details if you believe this document breaches copyrights.  
We will remove access to the work immediately and investigate your claim.

# **The Nano-Aperture Ion Source**





This work is part of the Industrial Partnership Program (IPP) of the Stichting voor Fundamenteel Onderzoek der Materie (FOM), which is financially supported by the Nederlandse Organisatie voor Wetenschappelijk Onderzoek (NWO). The IPP programme is co-financed by FEI Company.

*Printed by:* Ridderprint BV, Ridderkerk, The Netherlands

*Front & Back:* Mart Veeke, Ink Strategy

Copyright © 2017 by Leon van Kouwen

ISBN 978-94-6186-791-9

An electronic version of this dissertation is available at  
<http://repository.tudelft.nl/>

# **The Nano-Aperture Ion Source**

## **Proefschrift**

ter verkrijging van de graad van doctor  
aan de Technische Universiteit Delft,  
op gezag van de Rector Magnificus prof.ir. K.C.A.M. Luyben;  
voorzitter van het College voor Promoties,  
in het openbaar te verdedigen op  
maandag 27 maart 2017 om 10:00 uur

door

**Leon VAN KOUWEN**

natuurkundig ingenieur  
Technische Universiteit Delft, Nederland  
geboren te Nijmegen, Nederland

This dissertation has been approved by the  
promotor: Prof. dr. ir. P. Kruit

Composition of the doctoral committee:

Rector Magnificus    chairman  
Prof. dr. ir. P. Kruit    Delft University of Technology

Independent members:

Prof.dr. R.F. Mudde	Delft University of Technology
Prof.dr. H.W. Zandbergen	Delft University of Technology
Prof.dr. K.K. Berggren	Massachusetts Institute of Technology
Dr.ir E.J.D Vredenburg	Eindhoven University of Technology
G. Schwind	Thermo Fisher Scientific (former FEI)

*"When you are studying any matter, or considering any philosophy, ask yourself only: what are the facts, and what is the truth that the facts bear out. Never let yourself be diverted, either by what you wish to believe, or what you think could have beneficent social effects if it were believed, but look only and surely at what are the facts."*

BERTRAND RUSSEL



# Contents

<b>Summary</b>	<b>3</b>
<b>Samenvatting</b>	<b>5</b>
<b>1 Introduction</b>	<b>7</b>
1.1 Why ion beams are fun. . . . .	8
1.2 A closer look at FIB systems . . . . .	14
1.3 The nano-aperture ion source. . . . .	20
1.4 Chip fabrication . . . . .	31
1.5 The mission. . . . .	35
References . . . . .	35
List of symbols . . . . .	39
<b>2 Nano-fluidic flow</b>	<b>41</b>
2.1 Introduction . . . . .	42
2.2 Flow model . . . . .	42
2.3 Flow experiments . . . . .	53
2.4 Conclusion . . . . .	58
References . . . . .	59
List of symbols . . . . .	60
<b>3 Optics of ion emission from a volume</b>	<b>61</b>
3.1 Introduction . . . . .	62
3.2 Source properties. . . . .	62
3.3 Emission in a uniform field . . . . .	67
3.4 Emission from a realistic geometry . . . . .	75
3.5 Brightness from phase space evolution. . . . .	86
3.6 Conclusion . . . . .	90
References . . . . .	91
List of symbols . . . . .	93
<b>4 A model for ion-neutral scattering</b>	<b>95</b>
4.1 Introduction . . . . .	96
4.2 Ion-neutral interaction. . . . .	96
4.3 Monte-Carlo implementation . . . . .	99
4.4 Model validation . . . . .	103
4.5 An effective mean free path . . . . .	106
4.6 Neutral particle-density distribution . . . . .	112
4.7 Monte-Carlo ray tracing . . . . .	114

4.8 Conclusion . . . . .	116
References . . . . .	117
List of symbols . . . . .	118
<b>5 Simulating ion emission</b>	<b>119</b>
5.1 Introduction . . . . .	120
5.2 Ion-induced surface charge . . . . .	120
5.3 Monte-Carlo ray tracing . . . . .	126
5.4 Ion-electron interactions . . . . .	138
5.5 Conclusion . . . . .	144
References . . . . .	145
List of symbols . . . . .	148
<b>6 Experimental source performance</b>	<b>149</b>
6.1 Introduction . . . . .	150
6.2 Experimental method . . . . .	150
6.3 Experimental Setup . . . . .	152
6.4 Brightness measurements . . . . .	161
6.5 Emission current measurements . . . . .	166
6.6 Conclusion . . . . .	170
References . . . . .	171
List of symbols . . . . .	172
<b>7 Other processes in the ionization volume</b>	<b>173</b>
7.1 Introduction . . . . .	174
7.2 Calculation method . . . . .	176
7.3 Estimates of the beam composition . . . . .	179
7.4 Conclusion . . . . .	181
References . . . . .	182
List of symbols . . . . .	183
<b>Acknowledgments</b>	<b>185</b>
<b>Curriculum Vitæ</b>	<b>187</b>

# Summary

The goal of this PhD research was to further develop the nano-aperture ion source (NAIS). Making brighter and more mono-chromatic ion beams is an obvious motivation for source development as this enables higher resolution. Even more driving is the desire for different ionic species. For efficient milling we like to use heavy ions, while for imaging, lighter elements minimize sample damage. Furthermore, preventing or employing chemical reactions can open up a variety of applications.

Ion production in the NAIS is based on electron impact gas ionization inside a sub-micron sized gas chamber. The gas chamber consists of two membranes of about 100 nm thick, which are separated by a distance of 100 nm to 1  $\mu\text{m}$ . A small aperture of 100 to 500 nm in the membranes allows the ions to escape and a focused electron beam to enter the ionization region while maintaining a high pressure inside the structure. The combination of a high current density electron beam and a highly confined ionization region makes excellent optical performance possible. The gas chamber can be filled with different gases such that a variety of ion species are available.

One crucial aspect of the concept is the delivery of a gas towards the double aperture structure. We found that naive fluidic channel design leads to unacceptable pressure drops across the channel. An analytical flow model was developed in order to estimate the fluidic properties of a variety of channel dimensions, separating proper designs from inadequate configurations. It is experimentally shown that measurements of the total flow rate in combination with the flow model can be an excellent tool for fluidic channel diagnostics.

An important part of this dissertation is devoted to understanding how the relevant physical processes determine the ion beam performance. The initial velocity and position distributions of the neutral gas particles, the ionization cross section, the electron current density, ion-neutral scattering, coulomb interactions, and the electric fields around the double membrane structure are fundamental aspects of operation. These matters are studied by analytical models, numerical calculation, and ray tracing.

If the particle density is kept sufficiently low, particle interactions are kept at a minimum and the optics are mainly determined by the electric fields. A first order lens effect and two types of aberrations are identified. One aberration is associated with the initial energy distribution of the ions and a second aberration is caused by the initial spatial spread in the direction of the optical axis. Simple equations are derived, which enable estimates of these optical effects. Best performance is in general achieved when the fields inside and outside the chip are equal and above 5 kV/mm.



When using a higher particle density we obtain more ion current, but at the same time ion-neutral scattering becomes important. An important notion is that the current and the brightness tend to keep increasing with increasing particle density, despite increasing ion-neutral scattering. Another result is that the spread in energies in the beam can be reduced as a consequence of more ion-neutral scattering.

Ion-to-ion coulomb repulsion is found to pose a limit to the achievable brightness. The effect is relevant inside the chip, but also in the region where the beam is accelerated up to high voltage. Besides the direct ion-to-ion force, the surface induced charges in the membrane are found to have a relevant effect on the ion beam as well. The background electrons traveling along the ion beam gives a negligible effect on the ion beam under nominal conditions.

The optical effects due to the electric fields, the ion-neutral scattering, and Coulomb interactions are studied simultaneously using Monte-Carlo ray tracing. In a realistic configuration the simulations predict a brightness of about  $3 \times 10^6$  A/m<sup>2</sup>srV in combination with an energy spread of 1 eV. Interestingly, the attainable brightness is not very sensitive to the geometry, nor was it very dependent on the noble gas species. To achieve the best performance, it is important that electric fields close to 10 kV/mm are used inside and outside of the gas chamber.

An ion focusing and scanning column in combination with a knife-edge ion transmission detector was built for the purpose of measuring brightness. The setup was used to experimentally demonstrate a brightness of  $B \approx 1 \times 10^5$  A/m<sup>2</sup>srV. A milestone result. This is already a competitive brightness, but there is clearly room for improvement. We identify poor electron beam performance, too weak ion acceleration field, and too low ion lens voltage as improvable aspects. The measured brightness matches reasonably well with the simulated values for this sub-optimal configuration.

A theoretical study on exotic species production inside the ionization region was conducted for argon. Besides single charged ions, multiple charged ions become constituents of the beam when using electron impact energies above the second ionization threshold. Rather surprisingly, a small amount of diatomic charged argon is predicted to become part of the beam. For a 1 keV electron beam we expect the beam to consist of about 88% single charged argon, 8% double charged argon, 2% triple charged argon, and 2% diatomic single charged argon.

# Samenvatting

Het doel van dit promotieonderzoek was het verder ontwikkelen van de *nano-aperture ion source* (NAIS). De helderheid verhogen en de bundel meer mono-energetisch krijgen is een voor de hand liggende motivatie voor dit onderzoek, want dit maakt hogere resolutie mogelijk. Echter, wellicht nog belangrijker is het verlangen naar ionen van alternatieve elementen. Wanneer we efficiënt willen graveren met de ionenbundel is het zaak om zware ionen te gebruiken, terwijl lichtere elementen juist zinnig zijn bij het maken van afbeeldingen omdat substraatschade dan beperkt blijft. Het voorkomen of juist bewust induceren van chemische reacties maakt een variëteit aan toepassingen mogelijk.

De productie van ionen in de NAIS is gebaseerd op elektroninslag ionisatie van een gas in een sub-micrometer gaskamer. Deze kamer bestaat uit twee membranen van ongeveer 100 nm dik, die tussen de 100 nm en 1  $\mu\text{m}$  van elkaar verwijderd zijn. Een kleine opening van 100 tot 500 nm in de membranen maakt het mogelijk voor de ionen de structuur te verlaten, en laat elektronen toe in de ionisatie regio, dit alles terwijl een hoge druk behouden kan blijven. De combinatie van een hoge elektronen stroomdichtheid en een zeer gelokaliseerd ionisatiegebied maakt excellente prestatie mogelijk. Aangezien de gaskamer kan worden gevuld met allerlei gassen, zijn er vele elementen beschikbaar om ionen van te maken.

Een cruciaal aspect van dit concept is de toevoer van een gas naar de gaskamer. We hebben ontdekt dat een naïef ontwerp van het aanvoerkanaal kan leiden tot een onacceptabele drukval. Een analytisch model voor de gasstroming is ontwikkeld zodat de eigenschappen van verschillende kanaalconfiguraties kunnen worden berekend, wat het mogelijk maakt te bepalen welke ontwerpen geschikt en welke ongeschikt zijn. Door middel van experimenten is aangetoond dat een totale gas-debietmeting in combinatie met het analytisch model uitstekend kan dienen voor aanvoerkanaal diagnostiek.

Een belangrijk deel van dit proefschrift is gewijd aan hoe de fysische processen de uiteindelijk ionenbundelkwaliteit bepalen. De initiële snelheidsdistributie en positiedistributie van het neutrale gas, de ionisatie efficiëntie, de elektronen-stroomdichtheid, ion-neutraal botsingen, Coulomb interacties, en de elektrische velden in en rondom de gaskamer zijn fundamentele aspecten van het systeem. Deze zaken zijn bestudeerd door middel van analytische modellen, numerieke berekeningen, en baansimulaties.

Wanneer de deeltjesdichtheid voldoende laag is, zijn deeltjesinteracties minimaal en wordt de optiek vooral bepaald door de elektrische velden. Een eerste orde lenswerking en twee type aberraties zijn vastgesteld. Een van de aberraties is geassocieerd met de initiële spreiding in energie, en de andere aberratie wordt

veroorzaakt door de spreiding in de positie van de ionen langs de optische as. Simpele vergelijkingen zijn afgeleid die het mogelijk maken de optische effecten af te schatten. Over het algemeen kan de beste prestatie bereikt worden wanneer de velden binnen en buiten de gaskamer gelijk zijn en tenminste 5 kV/mm.

Als een hogere deeltjesdichtheid gebruikt wordt, wordt er meer stroom gemaakt, maar tegelijkertijd vinden er meer ion-neutraal botsingen plaats. De stijging van stroom en helderheid neemt weliswaar af als gevolg van de ion-neutraal botsingen, maar de stijging wordt nooit compleet onderdrukt. Een ander resultaat is dat de energiespreiding van de bundel verlaagd kan worden als gevolg van meer ion-neutraal botsingen.

De Coulombkracht tussen de ionen levert een limiet voor de uiteindelijk haalbare helderheid. De gevolgen van de Coulomb interacties zijn relevant zowel binnen als buiten het ionisatiegebied. Ook de lading geïnduceerd in de membranen blijkt een relevante invloed te hebben op de uiteindelijke bundel. De elektronen die langs de ionen passeren leveren onder nominale omstandigheden geen problematische verstoring van de bundel.

De optische effecten als gevolg van de elektrische velden, ion-neutraal botsingen, en de Coulombkracht zijn tegelijkertijd bestudeerd door middel van stochastische baansimulaties. In een realistische configuratie voorspelt het model een helderheid van ongeveer  $3 \times 10^6 \text{ A/m}^2\text{srV}$  in combinatie met een energiespreiding van 1 eV. Interessant is dat de helderheid niet erg gevoelig is voor de precieze geometrie van de gaskamer. Ook het type edelgas dat wordt gebruikt maakt niet veel uit voor de haalbare helderheid. Om de beste prestaties te verkrijgen is het belangrijk om de elektrische velden dichtbij de 10 kV/mm te krijgen, zowel binnen als buiten de chip.

Een focuserende en rasterscannende kolom in combinatie met een mes-rand ionentransmissiedetector is gebouwd met de doelstelling om de helderheid te meten. De opstelling is gebruikt om experimenteel een helderheid van  $B \geq 1 \times 10^5 \text{ A/m}^2\text{srV}$  te meten. Een ware mijlpaal. Deze helderheid is al competitief, maar er is duidelijk ruimte voor verbetering. We kunnen een onderpresterende elektronenbundel, te zwak acceleratie veld, en een te lage energie in de ionenlens identificeren als verbeterbare aspecten. De gemeten waarden voor de helderheid zijn in redelijke overeenstemming met de gesimuleerde waarden voor deze sub-optimale configuratie.

Een theoretische studie naar de productie van exotische ionen in de ionisatie regio is uitgevoerd voor argon gas. Naast enkelvoudig geïoniseerd argon, kan meervoudig geïoniseerd argon een onderdeel uitmaken van de bundel wanneer de inslagenergie van de elektronen hoger is dan de dubbele ionisatie potentiaal. Verrassend is dat di-atomisch enkelvoudig geïoniseerd argon ook een kleine fractie van de bundel kan zijn. Voor een 1 keV elektronenbundel verwachten we dat de bundel voor ongeveer 88% bestaat uit enkelvoudig geïoniseerd argon, voor 8 % uit dubbel geïoniseerd argon, voor 2 % uit drievoudig geïoniseerd argon, en voor 2 % uit di-atomisch enkelvoudig geïoniseerd argon.

# 1

## Introduction

*"Change can be essential,  
but it should only be made with careful consideration and just cause."*

GARRY KASPAROV

*"We have friends in other fields – in biology, for instance. We physicists often look at them and say, 'You know the reason you fellows are making so little progress?' (Actually I don't know any field where they are making more rapid progress than they are in biology today.) 'You should use more mathematics, like we do.' They could answer us – but they're polite, so I'll answer for them: 'What you should do in order for us to make more rapid progress is to make the electron microscope 100 times better.'"*

RICHARD FEYNMAN

## 1.1. Why ion beams are fun

### 1.1.1. What is a focused ion beam system

A directed stream of ions traveling in a vacuum is what we call an ion beam. Excitement emerges from the precise control we can attain over such a beam by using electric and magnetic fields. It is common practice to focus an ion beam down to within a 10 nm diameter by using a high-end focused ion beam (FIB) system. Figure 1.1 shows what such a FIB system usually looks like and how it works in essence.

Sure enough such control of fields and particles is an achievement in itself, but it turns out to have very practical applications indeed. To understand what can be achieved we should look at the interaction ions have with a target material.

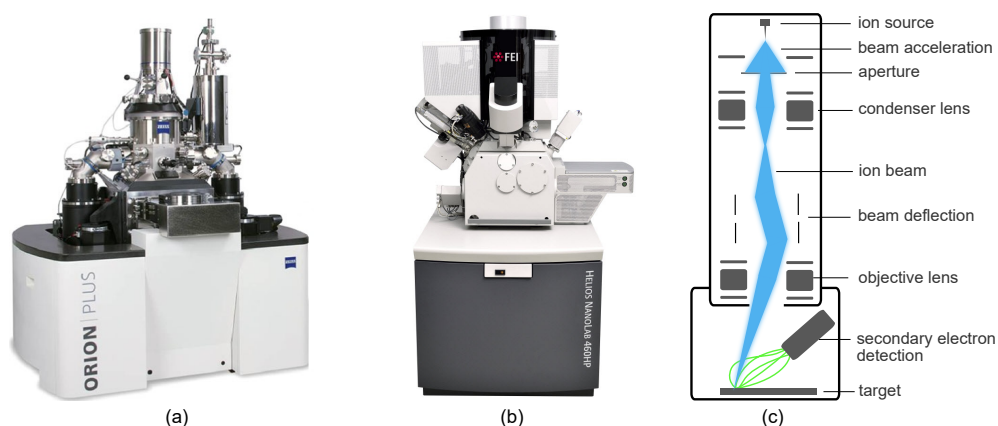


**Figure 1.1.** Focused ion beam systems consist of an optical column and the supporting elements such as vacuum pumps and electronics, together claiming one or two cubic meters of space. a) The Carl Zeiss Orion [1] is known for its unprecedented high resolution and for supplying helium ions. b) FEI's Helios dual beam system [2] is equipped with a gallium liquid metal ion source and an electron column, a very popular combination. c) The essence of any focused ion beam system is the optical system. The beam emerges from an ion source after which the ions are accelerated up to 1 to 40 kV. A series of lenses and apertures accommodate high resolution spot formation. Beam deflection electrodes steer the beam to achieve patterning and imaging by raster scanning while simultaneously collecting secondary electrons as signal input.

### 1.1.2. Ion-surface interactions

Besides a few exceptions, we like to accelerate the beam up to a high energy between 1 and 40 keV. This means a lot of energy is available to initiate various physical processes. The most important interactions are visualized in figure 1.2. The subject of ion-solid interaction is immensely broad and literature is abundant (see for example references [3, 4]). In this section the unfamiliar reader can get up to speed with some basics.

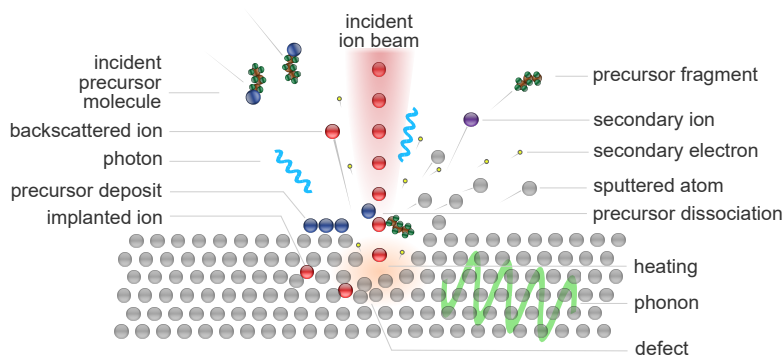


**Figure 1.2.** When a highly energetic ion beam hits a solid, a plurality of interactions occur. The most utilized interactions are the generation of secondary electrons, sputtering of the solid and deposition by dissociation of precursor molecules. The relative occurrence of the interactions depends strongly on the materials involved, the ionic species, and the beam characteristics.

Very comparable to electron beam impact, is the energy transfer to electrons bound in the material. Some of these can escape into the vacuum to become so-called secondary electrons (SE's). This can be relatively efficient, for example the SE yield of  $\text{Ga}^+$  30 kV on silicon is 3.3 electrons per incident ion [5] while for 30 keV electrons it is only 0.138 [6]. In general the SE yield is in the order of 0.5 to 15 depending on the ion species and the solid, and for a great deal on the angle of incidence [7].

Quite different from electron impact is the removal of material. Just like a cannonball removing bricks from a castle wall, an ion hitting a sample will knock out atoms. This is commonly referred to as sputtering and when performed in a controlled fashion, ion milling. Table 1.1 can be used to get acquainted with the typical rate and efficiency with which this phenomenon occurs. What we can see directly from the table is that efficiency of sputtering is greatly dependent on the impact material and the ionic species involved.

sputter yield (atoms/ion) // 30 kV					sputtering rate ( $\mu\text{m}^3/\text{s}$ ) // 30 kV // 1 nA				
	C	Al	Si	Au		C	Al	Si	Au
$\text{He}^+$	0.016	0.040	0.020	0.128	$\text{He}^+$	0.0006	0.0042	0.0025	0.0136
$\text{Ar}^+$	1.147	3.221	1.650	11.139	$\text{Ar}^+$	0.0407	0.3345	0.2058	1.1810
$\text{Ga}^+$	1.796	4.757	2.412	17.701	$\text{Ga}^+$	0.0637	0.4941	0.3008	1.8767
$\text{Au}^+$	2.529	6.747	3.379	28.225	$\text{Au}^+$	0.0896	0.7007	0.4215	2.9926

**Table 1.1.** The number of removed atoms per incident ion and the volumetric material removal rate for a typical ion beam (30 kV, 1 nA) is calculated using the empirical model by Yamamura and Tawara [8]. The material is assumed to be amorphous, the incidence of the beam is normal to the surface, and no redeposition effects are taken into account.

The energy required to remove an atom from the top surface (surface binding energy) is in the order of some eV's, for example 4.66 eV for silicon [9]. Comparing this energy to the beam energy of keV's, while considering the values for the sputtering yields from table 1.1, we conclude that only a fraction of the beam energy is transferred into sputtering.

Sputtering is not a simple process as many aspects such as re-deposition, angle of incidence dependent sputtering yield, and probe current-distributions with wide

beam tails make matters complex [10–12]. Furthermore, the presence of certain gases near the beam impact site can influence the sputtering rate and other aspects of sputtering to great extent [13].

The introduction of special gases called precursors gases allows a very useful type of ion-surface interaction. Namely, ion-beam-induced deposition (IBID). The gas molecules consist of a volatile part and a part that may attach to the surface. The bonds between the two parts can be broken using the ion beam and thereby a pattern can be deposited locally. Two examples of precursor gases are tungsten hexacarbonyl  $W(CO)_6$  for depositing tungsten and trimethyl platinum  $C_9H_{16}Pt$  for platinum deposits [14].

The interactions involved in IBID are rather complicated [15, 16]. Primary ions, secondary electrons, secondary atoms are all involved in IBID and it is not entirely clear what the most dominant mechanism is [17]. Inevitably during deposition, sputtering occurs, counter-acting the growth. The supply of precursor molecules is governed by molecules adsorbed to the surface and surface diffusion into the beam, which balances the depletion of the precursor molecules by the ion beam.

Most certainly we have not covered all surface interactions as we can induce plasmons [18], phonons, amorphization [19, 20], we may implant ions [21], have ions scatter back into the vacuum [12], create new ions (secondary ions) [22], and certainly there are more interactions possible, depending on the target material and the ion species. Interestingly, most energy is eventually transferred into heat, although this rarely leads to a temperature rise of more than a few degrees Kelvin. [23].

One important aspect of high energy ion impact on a solid is the many interactions a single ion experiences during the process of deceleration. Therefore, for certain calculations, ion impact has been described by a cascade model [24], meaning that the complete interaction is modeled as a series of binary events. This method has been used to study sputtering for example [25]. Figure 1.3 shows a simulation of ion trajectories combined with trajectories of energetic atoms that acquired energy from an ion-atom interaction. A comparison is made between different mass ions hitting silicon at 30 keV and we see the obvious trend that lighter ions penetrate more deeply. Such trajectories are also dependent on the primary ion beam energy, but in any case we can state that the penetration is far shallower than we see with electrons, which is in the order of microns.

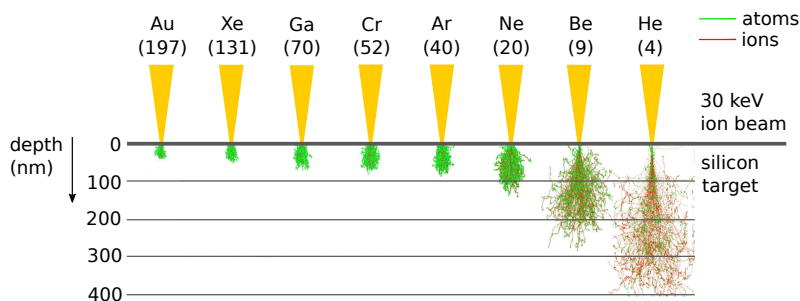


**Figure 1.3.** Simulations of ion and atom trajectories through silicon instantiated by a 30 keV primary ion beam hitting a flat surface. The trajectories show the strong dependence of the species on the interaction volume. The tendency is that heavy mass particles spread out more rapidly and penetrate less deeply compared to lighter elements. Despite the typical penetration depth being in the order of hundreds of nanometers, the lateral resolution is not limited by this measure. Only from the first few nanometers below the surface atoms and electrons can escape. The figure was adapted from ref. [26] with some esthetic modifications.

### 1.1.3. Applications of focused ion beams

Although the ion-surface interactions are quite complicated, they do open up a variety of possibilities. Figure 1.4 gives an impression of the most important applications.

A very basic, but important use of the FIB tool is making cross sections. By removing material one can see structures that are otherwise hidden. Opening up micro-machined devices to see if the structure is according to plan is common practice. It is also possible to investigate, for example, the internal structure of a cell-nucleus by milling away tissue at a very precisely defined location, something that can never be achieved by using macroscopic tools. This unprecedented cross sectioning capability has led to the development of the dual-beam machine, a device which comprises both a focused ion and a focused electron beam. The ion beam is used for milling while the electron beam provides well-known imaging possibilities. One can not imagine transmission electron microscopy without the aid of dual-beams. Properly preparing thin slices of the substrate, the so-called TEM-lamella, is essential for achieving good quality TEM images [27].

The removal of material can also be patterned in a more complicated fashion to achieve functional devices. In addition, we can deposit structures by using dissociation of precursor gases to grow material: ion beam induced deposition (IBID). This deposition technique is very comparable to the electron optical equivalent in terms of procedure and results, see ref. [28] for a comparison. The combination of milling and deposition makes the FIB tool a cut-and-paste device for the nano-scale. One example of combining milling and deposition is the direct fabrication of a hard mask for reactive-ion-etching [29]. While these techniques are mostly used for manipulating surfaces, sometimes the fabrication of three-dimensional structures is possible [30].



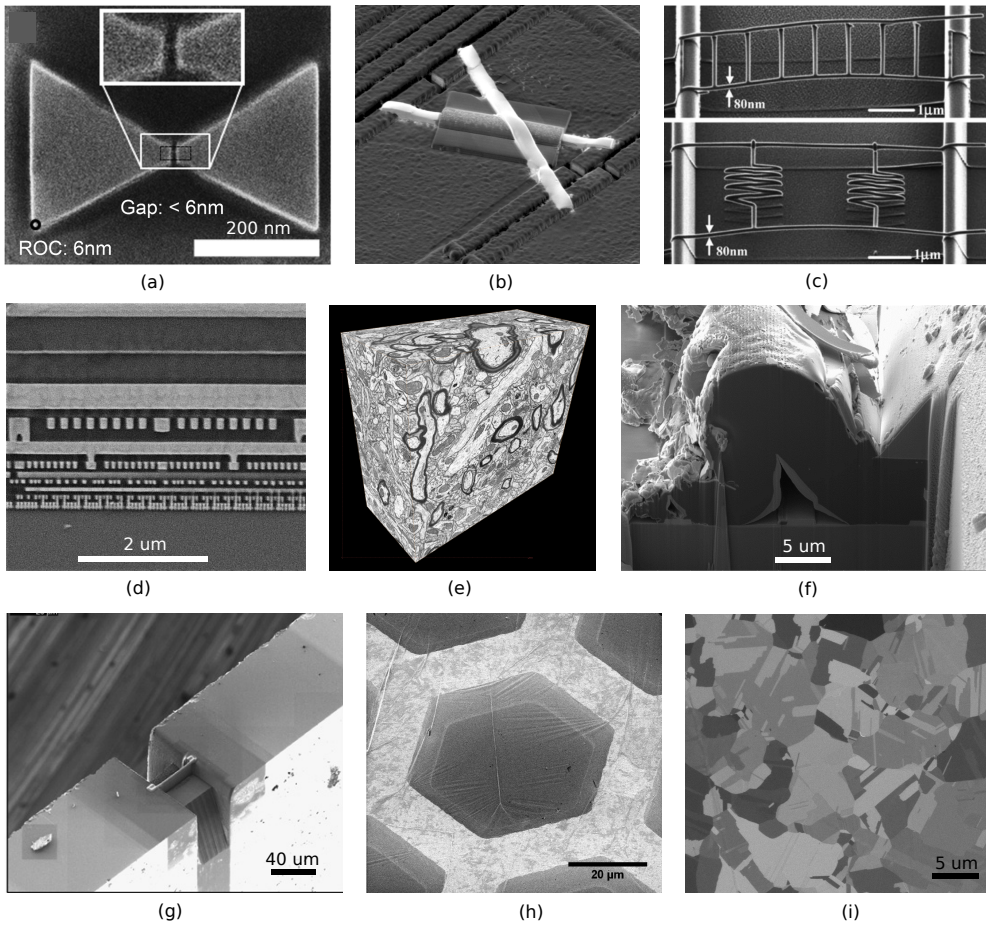


**Figure 1.4.** Focused ion beams are indispensable as shown by these examples. a) A gold nano-antenna is made by FIB milling (courtesy ref. [31]). b) For a quick development cycle, integrated circuits are often adjusted using focused ion beam milling and deposition. This procedure is known as circuit edit. In this image, re-routing of some wires is shown (courtesy ref. [32]). c) Free standing deposits can be grown from precursor molecules if the beam patterning speed is matched carefully with the deposition growth rate (courtesy ref. [33]). d) When fabricating on microscopic scales, inspection is paramount. Using FIB milling to cut open an integrated circuit yields a clean cross section ready for inspection (courtesy ref. [34]). e) By consecutively slicing away a layer of a tissue sample and imaging the layers, a three-dimensional map can be obtained (courtesy ref. [35]). f) Cutting open any kind of structure to perform failure analysis is considered routine in many labs. This example: a supposedly open gas channel turned out to be clogged with glue, which was found out after ion beam cross sectioning (courtesy ref. [36]), this failure analysis was part of the NAIS project). g) The popular transmission electron microscope relies on samples being thin enough for electrons to transmit through. The most common method to obtain such thin slices of material is by FIB milling (courtesy ref. [27]). h) Very thin membranes can be imaged relatively well with a focused ion beam due to the high surface sensitivity (courtesy ref. [37]). i) Different crystalline patches can be clearly distinguished on a poly-crystalline sample by employing channeling of ions through the atomic columns (courtesy ref. [38]).

The most important industrial branch that uses this cut-and-paste possibility is circuit edit. When micro-chips are designed and a prototype is developed, in practice there is always the need for some tweaking to get the right functionality. It is very impractical to develop a million dollar lithography mask for every tweak and FIB nano-surgery comes to the rescue.

Making functional devices with IBID can be challenging, as achieving high purity is not obvious. Most precursors result in carbon deposition as well, which causes poor resistivity or other unwanted properties. In fact, typically one finds only 30 to 40 % metallic content in a deposit [39]. This is still better than what is commonly achieved with electron-beam-induced deposition, though. The choice of precursor, the conditions of the sample, writing strategy and the beam characteristics all influence the purity. In industrial circuit edit systems,  $1$  to  $2 \times 10^{-6} \Omega \text{ m}$  is routinely achieved [40] from the precursor  $\text{W}(\text{CO})_6$ , which is about 25 times higher than pure tungsten. One example of an excellent result is the demonstration of 10 nm cobalt lines with  $0.5 \times 10^{-6} \Omega \text{ m}$  resistivity [41]. If the vacuum conditions and the cleanliness of the sample are poor though, or the precursor flux and the beam current are not carefully chosen, one easily ends up with many orders of magnitude poorer resistivity. Although the resistivity is commonly believed to be determined by the ratio of intended deposit versus the carbon fraction, some research suggest that it is the residual gallium content that determines the resistivity [42]. For very small platinum-based nano-wires, the deposit can transition from insulator-like to metal-like depending on the size of the structure [39].

Besides purity control, precise spatial control may be difficult as well due to the wide-tailed beam profile and proximity effects. Unwanted deposition up to 2  $\mu\text{m}$  away from the irradiated area may occur [43]. Despite the difficulties, ion beam induced deposition is often successfully employed, for example to fabricate superconducting nano-wires [44] or a nano-scale hall sensor [45].

Although focused ion beams are mainly fabrication tools, they are also used for imaging. Just like the well-known scanning electron microscope (SEM), we can raster scan the ion beam and measure at every position the response of the sample; most commonly one measures the electrons that are freed from the material. The two most noteworthy differences between scanning electron and ion microscopy is the difference in penetration depth, and the inevitable removal of material associated with ion beam impact. In practice often one prefers a SEM over a SIM for all-round imaging work, however, sometimes the specific advantages of ions are employed. Some examples of imaging techniques with helium ions are ionoluminescence [46], scanning reflection ion microscopy [47], employing channeling contrast [48, 49], and imaging ultra thin layers [37, 48].

One noteworthy aspect of scanning ion microscopy, and this is under-appreciated, is the relation between sputtering and resolution. More often than not the resolution is directly coupled to the spot size, but this neglects the act of sputtering while gathering enough statistics for an image. Simply put, a small structure may already be gone before enough signal is acquired to distinguish it properly from random signal fluctuations. One manifestation of this problem is the difficulty of imaging graphene with helium ions [50]. The interested reader is referred to the dissertation of Castaldo [51] for a full analysis of this matter. Ultimately, ions can never beat the resolution obtained in for example high energy scanning transmission electron microscopy.

An analytical technique that does not have an electron based analogue is secondary ion mass spectroscopy [22]. One acquires secondary ions that are generated by the impact of primary ions and determines their masses, by for instance time-of-flight spectroscopy. Often cesium or oxygen ions are preferred because of the high secondary ion yield; typically a factor 30 higher than gallium or argon. If the spatial resolution does not need to be very high, SIMS is unparalleled for its sensitivity, reaching parts per million even down to parts per billion as a detection limit [22].

## 1.2. A closer look at FIB systems

Bright and monochromatic charged particle sources have enabled high resolution scanning-probe microscopy and nano-fabrication. Poor sources have orders of magnitude less current in the final probe, leading to unworkable acquisition times at high resolution, hence bright and monochromatic sources are crucial. In this section it is explained how the source determines the final probe quality, what sources are available, and what we would like from a new source.

### 1.2.1. How to get high quality ion beams

Ultimately, the assessment for focused ion beam systems is the quality of the probe when it hits the sample, for that is what matters in applications. The final probe quality is influenced by many aspects of which the ion source and the optical column are the most obvious ones. Some more practical aspects are sample stage stability, magnetic shielding, electronic stability, vibration suppression, etc. Fortunately, these practical aspects can be addressed with mature technology, so it is usually a matter of money and adequate engineering to ensure the optics are living up to their potential.

From astronomy to electron optics, the most infamous limit in optical systems is diffraction. Next in line are the aberrations; the inability of lenses to form perfect images. We can estimate the spot blurring diameter diffraction contributions and the aberration contributions in terms of the final beam divergence angle as follows:

$$d_a = 0.54 \frac{\lambda}{\alpha}, \quad d_s = 0.18 C_s \alpha^3, \quad d_c = 0.6 C_c \frac{\Delta\Phi}{\Phi} \alpha, \quad d_g = M d_v. \quad (1.1)$$

We use  $d$  for the diameter of a particular contribution, the subscript a, s and c indicates diffraction, spherical aberration and chromatic aberration respectively. The subscript g indicates the source image or geometrical contribution and v the virtual source.  $\alpha$  represent the beam angle or half opening angle,  $M$  is the total magnification of the system,  $\lambda$  the de Broglie wavelength,  $C_s$  the spherical aberration coefficient, and  $C_c$  the chromatic aberration coefficient. If we use the full width 50 characteristic for the probe contributions, they can conveniently be added using the Barth and Krut power-sum law [52].

$$d^2 = \left( d_g^{1.3} + (d_A^4 + d_s^4)^{\frac{1.3}{4}} \right)^{\frac{2}{1.3}} + d_c^2 \quad (1.2)$$

Suppose we have a 1 keV hydrogen ion beam with a small beam angle of 1 mrad. The diffraction contribution to the spot size is about 1 nm. This example is for the lightest atom possible, a relatively low energy and a small aperture angle so that usually the diffraction contribution is much smaller. We can understand from this numerical example why focused ion beam opticians are usually not bothered too much with diffraction.

Far more relevant are the aberrations of the optical system. But since we can simply minimize them by using only a fraction of the beam and obtain a very small beam angle, it is no longer a question of what resolution we can achieve, but rather what resolution we can get at a certain beam current. The amount of current in a beam is conveniently calculated using the reduced brightness, a measure of intensity that is, under reasonable circumstances, constant throughout the optical system. This quantity will be discussed in more detail in the following chapters, but a quick definition for the reduced brightness  $B_r$  is: the total current in a probe, divided by the solid angle of the beam cone, divided by the area of illumination, divided by the beam voltage. Using the brightness, the current  $I$  of the final probe is given by

$$I = \frac{1}{4} \pi^2 B_r \Phi d^2 \alpha^2, \quad (1.3)$$

in which  $\Phi$  is the beam energy. The brightness  $B_r$  will be discussed in more detail and more formally in chapter 3.

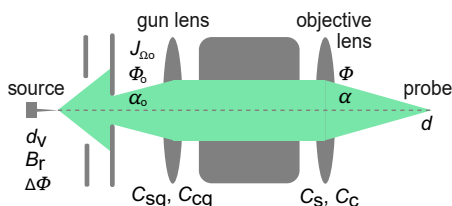


**Figure 1.5.** The basic parameters of a two-lens probe forming optical system are indicated. In an optimized system, the beam final beam angle  $\alpha$  and the total magnification  $M$  of the system are tuned to get the most current in the smallest final spot.

The equations 1.1, 1.2 and 1.3 are the essential ingredients needed for optimizing a FIB system, but they do not directly reveal the optimized situation. It is very convenient to use the probe-current relation of an optimized two-lens optical column. This means that the beam limiting aperture and the system's magnification are finely balanced to get the smallest spot size for a particular required beam current. The general optimization is not so easily expressed in one explicit equation nor would it be very enlightening. By looking at four limiting cases we can get a good grasp of the situation, though. The optimal current-probe size relations of a two-lens system are [53]:

$$I = 1.71 \frac{d^4 \Phi^3 B_r}{\Delta \Phi^2 C_c^2} \quad \text{objective lens chromatic} \quad (1.4)$$

$$I = 2.47 \frac{d^{\frac{8}{3}} \Phi B_r}{C_s^{\frac{2}{3}}} \quad \text{objective lens spherical} \quad (1.5)$$

$$I = 2.18 \frac{d^2 J_{\Omega o} \Phi_o^{\frac{1}{2}} \Phi^{\frac{3}{2}}}{\Delta \Phi^2 C_{cg} C_c} \quad \text{gun lens + objective lens chromatic} \quad (1.6)$$

$$I = 6.86 \frac{d^{\frac{2}{3}} J_{\Omega o} \Phi^{\frac{1}{4}}}{C_{sg}^{\frac{1}{2}} C_s^{\frac{1}{6}} \Phi_o^{\frac{1}{4}}} \quad \text{gun lens + objective lens spherical} \quad (1.7)$$

In these equations we have  $I$  the current in the final beam,  $d$  the diameter of the final spot,  $\Phi$  the landing electrostatic energy,  $\Delta\Phi$  the electrostatic energy spread,  $B_r$  the reduced brightness,  $C_s$  the spherical aberration of the objective lens,  $C_c$  the chromatic aberration of the objective lens  $C_{sg}$  the spherical aberration of the gun lens,  $C_{cg}$  the chromatic aberration of the gun lens,  $\Phi_o$  the electrostatic energy at the object side, and  $J_{\Omega o}$  the angular current density at the object side. See figure 1.5 for the system schematic. The pre-factors relate to the probe size diameter and the energy spread both measured in the full width 50 characteristic.

These equations give excellent insight in how to optimize a focused ion beam system. In all equations we see that the objective lens aberrations should be as low as possible. Unfortunately there is even with the best lens design a theoretical limit to minimizing the aberrations of a lens [54]. Only aberration correctors can offer solace, but these are still very inconvenient and expensive. Secondly, we see that simply increasing the landing energy is always beneficial, although this consideration should go hand in hand with the ion-surface interactions one desires, and in addition, very high voltages become technically more challenging.

Besides an indication of what a good optical column can do, one can see from these equations that a good ion source is a very effective way of achieving high performance from a FIB-system. Equations 1.4 and 1.5 describe the low current regime (alternatively: the high resolution regime, or source de-magnifying regime), where we may be limited by spherical or chromatic aberration of the objective lens. We see from the equations that the current in the beam is proportional to the brightness. The brightness of ion sources can vary orders of magnitude so the source can make a huge impact on the final performance. The same accounts for the energy spread in the chromatic limit. For the highest resolution, the chromatic aberration dominates and high brightness low energy spread sources can outperform lesser sources greatly as the current in a given probe size scales with  $\frac{B_r}{\Delta\Phi^2}$ .

In the higher current regime described by equations 1.6 and 1.7, loosely speaking when the source needs to be magnified, the gun lens aberrations become important. This can be understood by inevitably magnifying the gun lens aberration along with magnifying the source image. Again the energy spread squared comes into play and a low energy spread can be highly advantageous. We see that not the brightness, but the angular current density becomes the figure of merit for source intensity. This is a somewhat tricky situation, for it seems that increasing the brightness is futile. However, when increasing the brightness without changing the virtual source size, effectively the angular current density is increased and thereby this does lead to enhanced performance. So, interpretation of these equations requires some care,

but in any case it should be evident that the better source can make the final beam perform better.

It is interesting to look also at the power of  $d$  in the spherically limited case for the higher current regimes. We can see that we need to make the probe diameter quite a bit bigger for some increase in current, when compared to the other regimes. This regime is sometimes avoided all together by using a different source for high current applications [55].

One aspect that is not apparent from these equation is the importance of the virtual source size. It is always possible, in principle, to design an optical system with the magnification needed to arrive at the optimum so the virtual source size may seem relatively unimportant. However, if the virtual source size is very large, say microns, one needs huge demagnification to arrive at nanometer probe size. This is no easy task for optical system designers. On the other hand, if the virtual source size is very small, one will very quickly arrive at the source magnifying regime, making such a source only useful for the very low current regime.

It should be clear that the source quality to great extent determines the quality of the final probe in terms of current and size. This explains the abundance of research on better sources and it motivates this research as well.

### 1.2.2. State-of-the-art FIB systems

For many years, the gallium liquid metal ion source (LMIS) has been the industrial standard. It is bright, reliable, cheap, and provides a relatively high current; a sensible all-round choice. See figure 1.6 for a cartoon of the principle mechanism. The source employs electrospray to generate ions. A sharp tungsten needle is provided with a flow of liquid metal towards its tip and a strong electric field is applied in the direction of the needle. The sharpness of the tip causes field enhancement. In addition, the liquid metal is deformed by opposing forces of the surface tension and the electric field into an even sharper shape called a Taylor cone [56]. The field at the tip becomes about  $1 \times 10^{10} \text{ V m}^{-1}$  and the radius as small as 1.5 nm [57]. One would expect an amazing brightness from such a small emitter, however, the virtual source size is not determined by this small radius, but by the ion-ion coulomb forces the ions endure right after emission [53], yielding an effective source diameter of 50 nm or so. One obtains a brightness up to  $1 \times 10^6 \text{ A/m}^2\text{srV}$ , which is still fairly good.

Using gallium is not a strict necessity for a LMIS to operate and other metals, mostly alloys, can be used as well. Gallium is usually preferred for its low melting point and low vapor pressure. Furthermore, alloy sources are considered more difficult to operate and require a mass filter [58]. Nevertheless, liquid metal ion sources of other species have been developed and found applications [58, 59]. Some examples of species available are B, Be, Si, Sn, Au, Fe, Ni, Cr; all positively charged and sometimes multi-ionized. When comparing brightness, energy spread and total current, as well as lifetime and stability, the gallium LMIS is superior. Lighter species such as beryllium can show performance that comes close to gallium though [60].

One intrinsic aspect of liquid metal ion sources is that they deliver metals. This may or may not be desirable, but the restriction is certainly a demerit. For



example, when repairing UV nano-imprint masks using gallium ions, the gallium contamination can decrease the transparency of the mask down to unacceptable levels [61]. For mesoscopic thin-films, even the slightest gallium dose can destroy the functionality [62]. Gallium ions being the industrial standard is mostly the result of excellent source performance, not because gallium is always the preferred ion species.

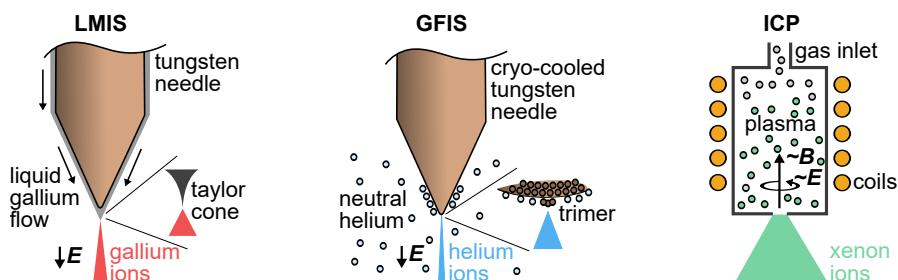


**Figure 1.6.** Cartoons of three industrially available methods for generating ions indicating their main concept and differences. LMIS and GFIS technology are similar as they both use a tungsten needle to get initial field enhancement. Furthermore they both employ additional sharpening of the final tip to get even more field enhancement. For the LMIS, the additional field enhancement is automatically achieved by the formation of a Taylor cone in the liquid metal. The supply of liquid metal runs along the tungsten needle. For the GFIS, the additional field enhancement is achieved by creating a 3-atom supertip (trimer) at the end of the tungsten needle. The supply of helium is governed by supplying the needle-surrounding vacuum by a trace amount of helium gas. The neutral atoms are polarized by the strong electric field and will be drawn towards the needle. The ICP does not comprise a tip, but relies on a plasma volume maintained by an alternating magnetic and consequentially an electric field.

The helium ion microscope [63] received a warm welcome when it got introduced to the focused ion beam community. Many scientific endeavors are associated with the tool, which can be attributed to the wide variety of applications it enabled [64]. In concept it is comparable to the liquid metal ion source in that it uses a sharp tip and field ionization. However, the neutral helium atoms awaiting promotion to ions are not supplied across the needle but are inserted into the vacuum around the needle. When a helium atom reaches the tip, it may become ionized due to the strong field at the tip surface. The key trick to make the performance exceptional is the manipulation of the end form of the tip until it assumes the shape of a three sided pyramid. This concentrates the electric field at the apex of the pyramid, hence the field ionization takes place predominantly at only a few atoms. A very small virtual source size is the result. Employing the high brightness and low energy spread with good optical column design gives a small probe size of 0.4 nm at a beam current of 0.25 pA and 35 keV landing energy [65].

The GFIS providing helium ions may, in some cases, prevent the defunctionalization that is seen with gallium due to the inert nature of helium. However, the low sputtering yield (see table 1.1) and the low total current makes the technology somewhat limited in application. Note that the low sputtering yield for a great deal counter-acts the very high brightness. It should also be noted that sub-surface bubble formation is an issue one has to deal with [66, 67].

On the other end of the spectrum in terms of brightness and total current, are the plasma based ion sources. Different techniques exist to acquire and maintain the plasma, but they all use an (alternating) electric field in an enclosed volume to generate charged species. Typically these sources have a low brightness making them not the obvious choice for high resolution applications. They can deliver staggering mA's of currents though and are often versatile in the delivered species.

One well-known plasma source is the duoplasmatron, which is used for a variety of applications, notably particle colliders and spacecraft propulsion. This source may be operated with a brightness of  $1 \times 10^3 \text{ A/m}^2\text{srV}$  [68], but this is an absolute maximum for argon. Commercially available sources usually operate at 250–500  $\text{A/m}^2\text{srV}$  and for  $\text{O}^-$  it can be as low as 25–50  $\text{A/m}^2\text{srV}$ . Energy spreads are typically 5 to 15 eV.

Another example is the multi-cusp plasma source, which can deliver, with some effort,  $2 \times 10^3 \text{ A/m}^2\text{srV}$  [69]. In pulsed mode one may reach a peak brightness of  $1 \times 10^5 \text{ A/m}^2\text{srV}$  [70], but with a duty time of 1 ms at 12 Hz repetition rate the brightness is on average almost two orders of magnitude lower.

More recently, effort has been put in the development of a bright inductively-coupled plasma source (ICP) in order to enable reasonably high resolution while maintaining the merit of high current [71]. It delivers xenon ions, which are heavy and inert. The achieved brightness is about  $1 \times 10^4 \text{ A/m}^2\text{srV}$ . At around 20–50 nA it becomes favorable to use such an ICP source rather than a gallium LMIS in terms of current versus probe size [55]. Decent performance has also been shown for argon ions [72] and other gaseous ionic species are in principle possible too.

Table 1.2 makes a comparison of three ion sources for high resolution applications currently available on the market.

	LMIS	GFIS	ICP	
brightness	$6 \times 10^5$	$1.0 \times 10^9$	$9.1 \times 10^3$	$\text{A/m}^2\text{srV}$
energy spread fwhm	5	$\leq 1$	6.7	eV
virtual source size	38	$\leq 0.25$	$7.2 \times 10^3$	nm
max. beam current	30	0.1	250	nA
main ion species	Ga	He	Xe	
compatible species	B, Be, Si, Sn, Au, ...	Ne	H, He, Ne, Ar, O <sub>2</sub> ,...	

**Table 1.2.** Comparison of established ion sources by listing nominal specifications. The maximum beam current may differ from the total emission current because the outermost part of the beam can be difficult to focus into a small spot. **LMIS:** Liquid metal ion source, data from ref. [53, 73]. The source properties are in general worse for other species than gallium. **GFIS:** gas field ionization source, data from ref. [63, 74]. The denoted measure of the energy spread is claimed as an upper bound. Values of 0.25–0.5 eV were measured by Ernst [75] in a field ionization setup, but not directly in a helium ion microscope in its present form. **ICP:** inductively-coupled plasma source, data from ref. [71]. The source properties are in general worse for other species than Xenon.

### 1.2.3. Future FIB sources

Developing new ion sources is an ongoing quest. Making ion sources even brighter and more mono-chromatic, is an obvious motivation for source development. Acquiring more total current with a decent resolution is also desirable for certain



applications. Note that considerations of lifetime, stability, reliability and costs can not be excluded when trying to improve upon commercial devices. Perhaps even most driving, is the desire for different ionic species. For example, for efficient milling we like to use heavy ions, while for imaging, preventing sputtering as much as possible is beneficial. Preventing or employing chemical reactions determine the desired ion species as well.

By using table 1.2 we can make the goals for new source development more concrete. The GFIS offers incredible brightness and low energy spread but delivers only light elements and offers a low total current. While the ICP can deliver heavy noble gas ions, it reaches a brightness that is two orders of magnitude lower than the LMIS. We begin to see that one may like to have all three sources at the same time, or at least a source that scores reasonable on all fronts. A source offering a brightness of, say,  $1 \times 10^6$  A/m<sup>2</sup>srV, an energy spread of 1 eV or smaller, at least 1 nA of current, and of course a variety of available species, is likely to become very popular.

A natural follow-up of the GFIS technology is the extension to heavier species than helium, as is often desired [76]. In fact, a system delivering neon ions next to helium is now on the market [74]. However, the GFIS technology is not easily extended to higher mass noble gases [77]. Furthermore, this technology seems not to be extendable to beam currents above 100 pA, thus GFIS will likely continue to find its main purpose in the highest resolution applications. Note furthermore that using a relatively high current of 100 pA from such a small emitter usually leads to the problem of large gun lens aberrations, as explained earlier in this section.

Making bright, mono energetic ion beams using laser cooling was proposed by Freinkman et al. [78]. The ultra-cold ion source (UCIS) [79] and the magneto-optical trap ion source (MOTIS) [80, 81] are two manifestations of using laser cooling in combination with three dimensional magneto-optical trapping and laser ionization. The anticipated high brightness was never achieved due to the slow diffusion rate in the trap, limiting the supply of atoms to be ionized. One way to overcome this problem seems to be using an atomic beam rather than relying on diffusion. Calculations of this approach look promising [82–84].

More ideas have been proposed, for instance an ion source based on ionic liquids [85]. However, none of the novel ideas for making high performance ion beams has been rigorously demonstrated experimentally. Even if high performance would be shown, no single source will be able to offer the complete set of desired ion species. We are therefore driven to develop a high-end ion source that may very well open a variety of applications for a wide audience.

### ***1.3. The nano-aperture ion source***

We propose an ion source based on electron impact gas ionization inside a sub-micron sized gas chamber [86–88]. The gas chamber consists of two very thin membranes of about 100 nm thick, which are separated by a small distance of 100 nm to 1  $\mu$ m, as shown in figure 1.7. A small aperture of 100 to 500 nm in the

membranes allows the ions to escape and a focused electron beam to enter the ionization region while maintaining a high pressure inside the structure. An electric field between the membranes directs the ions towards the exit aperture to ensure fast emission. Outside the membrane structure an electric field further accelerates the beam up to the desired high energy. The combination of a high current density electron beam and a highly confined ionization region is believed to give excellent optical performance.

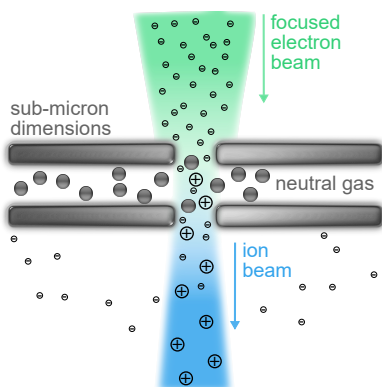


**Figure 1.7.** The nano-aperture ion source: forming high brightness beams of various species by ionizing a gas confined in a sub-micron volume using electron beam impact ionization. An electric field across the membranes extract the ions out of the double-membrane structure.

Figure 1.8 shows the concept with more technical details than figure 1.7. A key aspect of the concept is using a complete electron column on top of an ion column. This enables a well focused and well positioned electron beam into the electron-entrance aperture. The required voltages on the optical elements of the complete system can become somewhat tricky as indicated by the example in the figure for creating 30 keV ions at the sample from a 1 keV electron impact energy. The double membrane structure is so small, that fabrication of the device relies on micro-machining methods. This nano-fluidic and electrical device is referred to as the chip. The use of a differential vacuum is needed to maintain a good enough vacuum for the Schottky electron source, while leaking out gas from the chip. The chip needs to mediate between the sub-micron scale of the source and the macroscopic scale of wires and tubes.

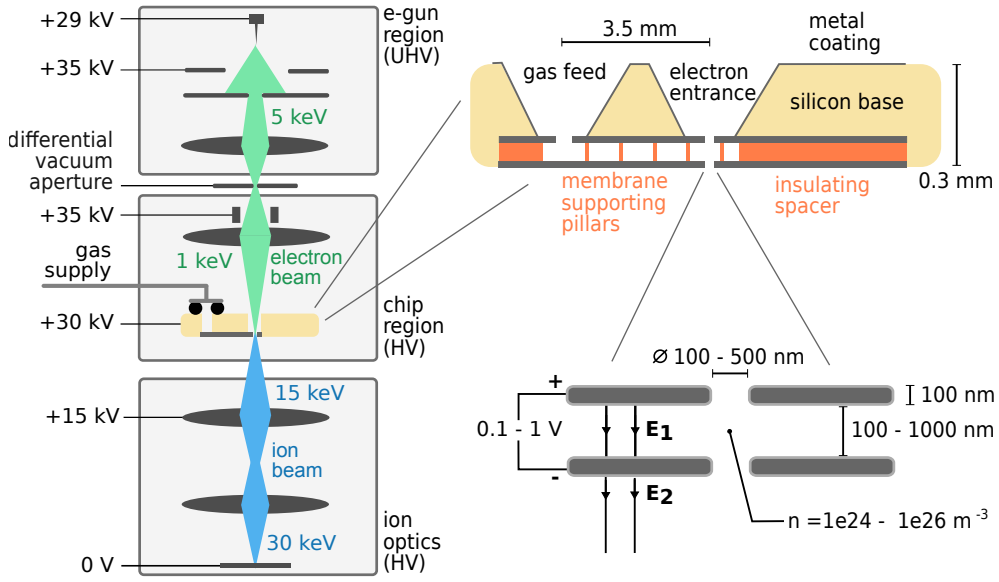


**Figure 1.8.** A more detailed implementation of the concept shown in figure 1.7. A fully capable SEM is used to focus and steer a high intensity electron beam into the double membrane structure. Below the chip an ion optical column is needed to control the ion beam for practical use. As an example, the applied high voltages for creating 30 keV ions from a gas that is hit by 1 keV electrons are indicated. It illustrates that one needs to operate the electron gun, including beam scanning, at high voltage, even though the final electron beam energy is only 1 keV. We intend to apply a bias voltage across the chip membranes so the membrane spacer needs to be of insulating material.

Many aspects of the NAIS are motivated by obtaining a high brightness, so we begin by elaborating the estimation of the brightness. Langmuir [89] derived an equation for the emission of electrons from a flat cathode, from which we can deduce the following expression for the reduced brightness:

$$B_r = \frac{eJ}{\pi kT} \quad (1.8)$$

We may try to use this equation for our configuration, as is seen throughout the literature for various configurations. Since the brightness is determined by the thermal transverse energy spread in both cases, this isn't an unreasonable attempt. We consider very small membrane spacing such that we can assume emission from a plane rather than from a volume. We note that a crucial aspect of the equation is the assumption that the initial transverse momenta are thermally distributed. This may be clear when the particles are still neutral and in thermal equilibrium, but when ionized and extracted, this is not necessarily the case. What we need to do in order to get a meaningful estimate using this equation is determine the current density we can reasonably expect under the condition that the transverse momenta are still thermally distributed. The next two sections are working towards that goal.

### 1.3.1. Electron impact ionization and ion-neutral scattering

Essential for the concept is the efficiency at which we can generate ions from the impinging electrons on the neutral gas. Electron impact ionization is thoroughly

studied and cross sections describing the ionization probability ( $\sigma_+$ ) are widely available. As first candidates for ion species in the NAIS we consider noble gases as they show little chemical activity and are available in a nicely spaced variety of masses. In figure 1.9 a set of noble gas single ionization cross sections are plotted. We observe that heavier gases are easier to ionize and secondly we see that the maxima for the single ionization are in the range 50 to 100 eV. The double ionization cross sections are one to two orders of magnitude lower.

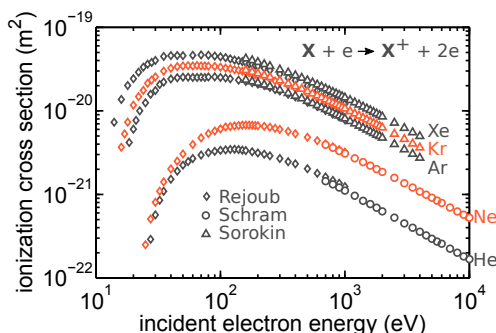


**Figure 1.9.** Single charged ionization cross sections for electrons hitting a noble gas. Data from Rejoub et al. [90], Schram et al. [91], and Sorokin et al. [92]

A second important cross section is associated with ion-neutral scattering ( $\sigma_{i-n}$ ). Once an ion is created somewhere in the gaseous volume, it is accelerated towards the exit aperture and in its path may encounter one or several neutrals. Previously, a molecular diameter has been used to describe this [86], however this does not take into account the polarization of the neutral and thereby not the energy dependence of the cross section, nor does it consider the possibility of exchanging charge. A better alternative is introduced in chapter 4, but for introductory purposes we will use the molecular diameter anyhow.

Ion neutral scattering events will greatly affect the transverse momentum distribution as energy acquired in the extraction field can be transferred to transverse energy. The acquired kinetic energy from the field in the downstream direction is in the order of 0.5 eV, a typical voltage that is needed for good extraction. The transverse energy spread is in the order of  $kT$ . Comparing the energy scales of  $kT = 0.025$  eV at room temperature to the 0.5 eV of the membrane voltage, we conclude that scattering events will indeed greatly affect the transverse thermal momenta distributions. Hence, the brightness acquired will be much lower than predicted by equation 1.8 if a large fraction of the generation ions have experienced scattering.

We may try to use a sufficiently rarefied configuration such that the ion-neutral scattering effects are not dominating. We can estimate the conditions for such a situation by a simple balance equation of ion generation. We assume a top-hat distribution of the gas of length  $l$  in the  $z$ -direction while stretching to infinity in  $x$  and  $y$ . The electron irradiation follows a radial top-hat distribution and is directed parallel along the  $z$ -axis. See figure 1.10 for a sketch of this model. We assume that once an ion scatters on a neutral it is no longer contributing to the brightness, so

we consider it removed. Under these conditions we can write

$$dJ = dJ_{\text{gen}} - dJ_{\text{scat}} = (J_e \sigma_+ - J \sigma_{i-n}) n dz. \quad (1.9)$$

We use  $J$  for the unscattered ion current density,  $J_{\text{gen}}$  and  $J_{\text{scat}}$  for the generated and scattered ion current density,  $n$  for the particle density,  $J_e$  the electron current density. There is some ambiguity regarding the electron current density as a function of  $z$ . If an electron engages in an ionization process, it returns two electrons, although their energies and directions are different. We will ignore this for now and assume the electron current density to be constant in  $z$ . The solution to equation 1.9 is then  $J(z) = J_e \frac{\sigma_+}{\sigma_{i-n}} (1 - e^{-n\sigma_{i-n}z})$  and the total generated current is simply  $J_{\text{gen}}(z) = J_e n \sigma_+ z$ .

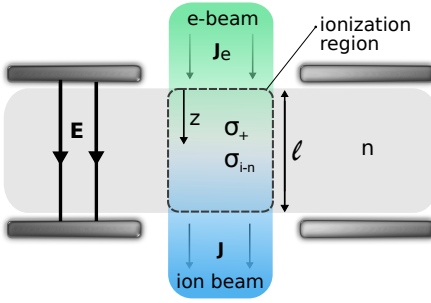


**Figure 1.10.** We model our system by assuming a cylindrical ionization region at uniform particle density. Inside this region all ionization and ion-neutral scattering occurs.

Intuitively, we may tune the particle density of the gaseous region such that the mean free path of the ions equals the length of the gas region, after all, we were aiming for unscattered ions. So, we set  $z = \lambda = (n\sigma_{i-n})^{-1}$  to give for the total generated current  $J_{\text{gen}}(z) = J_e \frac{\sigma_+}{\sigma_{i-n}}$ . Because  $\sigma_+ \ll \sigma_{i-n}$ , we conclude that most of the electrons will never engage in ionization at all and the assumption of constant electron current density is quite reasonable; most electrons fly through the gaseous region unaffected. The total unscattered ion current is slightly lower due to some scattering and is given by  $J = J_e \frac{\sigma_+}{\sigma_{i-n}} (1 - \frac{1}{e})$ .

We may ask the question if it is useful to further increase the particle density. If we find the optimum mathematically from  $\frac{dJ}{dz} = 0$ , we find for the total unscattered ion current  $J = J_e \frac{\sigma_+}{\sigma_{i-n}}$ . A value that is only slightly different from the intuitive optimum. The particle density increase required to reach this value goes to infinity. Surely, now the assumption that the current density is constant is violated.

We can try a slightly different version of the model. If we assume that the electrons that have ionized an atom can no longer contribute to any other ionization process, the electron current density follows a simple exponential decay:  $J_e = J_{e,0} e^{-\sigma_+ n z}$ . Physically this means that after ionization the two electrons scatter away from the region from which ionized particles can be extracted or don't have enough energy for ionization. This is rather simplified as well, but prevents the unphysical situation of the optimum occurring for an infinite particle density. Note that this is quite a conservative approach because both electrons that ionize and ions that gas-scatter are removed in the model, while in reality they may still contribute a little. Under this assumption the solution to equation 1.9 is  $J(z) =$

$J_{e,0} \frac{\sigma_+}{\sigma_{i-n} - \sigma_+} (e^{-n\sigma_+ z} - e^{-n\sigma_{i-n} z})$ . If we compute the optimum from  $\frac{dJ}{dz} = 0$  we obtain an optimum when  $nl = (\sigma_{i-n} - \sigma_+)^{-1} \ln \frac{\sigma_{i-n}}{\sigma_+}$ . This optimum gives for the unscattered ion current density  $J = J_{e,0} \frac{\sigma_+}{\sigma_{i-n}} \frac{\sigma_{i-n}}{\sigma_{i-n} - \sigma_+}$ . Again, we use  $\sigma_{i-n} \gg \sigma_+$ , to simplify and we get  $J \approx J_{e,0} \frac{\sigma_+}{\sigma_{i-n}}$ .

From the analysis presented here we conclude that a reasonable estimate for the best attainable unscattered ion current density is simply  $J_e \frac{\sigma_+}{\sigma_{i-n}}$ . Even though the models used do not consider the details of the system, they capture the essence of balancing ionization and ion-neutral scattering. That is to say, the product of pressure and gaseous length can be increased to yield more ionization, but if the ion mean free path becomes in the order of the gaseous length or smaller, a further increase is hardly beneficial for extracting more unscattered ions. Note that the total generated current will in fact continue to rise because the scattered ions can still be extracted; they are simply not expected to contribute much to a high brightness.

### 1.3.2. An electron beam for a NAIS system

There may be little remedy for ion-neutral scattering, however, we can optimize the ion current density by optimizing the electron beam. Since the ion current density is proportional to the electron current density, we seek an electron optical configuration that yields the highest current density. This is different from electron microscopes, where usually you would like a certain resolution and then try to get the highest current in that particular probe size. In this case, a small probe size is not directly what we are after. The ion current density is also proportional to the ionization cross section, which is dependent on the impact energy. Therefore, the most ions are generated when the product of the electron current density and the ionization cross section is highest.

We can use the equations 1.4-1.7 to investigate what this means for an optical system if we substitute for the current density  $J = \frac{4I}{\pi d^2}$ . In the objective lens chromatically and spherically limited cases the current scales with  $d^4$  and  $d^{8/3}$  respectively, so in both cases the current density is increased by increasing the probe size. This means that this is never an optimized regime as increasing the probe is beneficial. The current in the regimes where the chromatic aberration of the gun lens becomes important scales with  $d^2$ , so in that case the current density is constant. The gun lens spherical aberration limited situation scales with  $d^{2/3}$  so increasing the probe size starts to decrease the current density. Considering these scaling effects there must be some optimum where the high and low current regimes intersect.

We can see from the equations 1.4-1.7 that in order to achieve the best performance, we need low aberrations for the objective lens as well as for the gun lens. Furthermore, high brightness, low energy spread and high angular current density all improve the current density. A natural choice for an electron source becomes the Schottky electron gun. Besides its excellent optical properties, it is also highly stable and durable. We also consider a LaB<sub>6</sub> source and a cold field emitter.

column		
$C_{sg}$	10	mm
$C_{cg}$	10	mm
$C_{s,e}^*$	2	mm
$C_{c,e}^*$	2	mm
$C_{s,m}^*$	1	mm
$C_{c,m}^*$	1	mm
$V^*$	1	kV

**Table 1.3.** The characteristics of an hypothetical electron optical column as used in the optimization of highest current density. These values are considered realistic for high-end lenses and are comparable to what is used elsewhere [93].

electron sources			
source	$B_r$ A/m <sup>2</sup> srV	$\Delta\epsilon$ eV	$d_v$ nm
Schottky	$7.5 \times 10^7$	0.6	30
LaB <sub>6</sub>	$5.0 \times 10^5$	1.0	$10^4$
cold field emitter	$5.0 \times 10^8$	0.3	5

**Table 1.4.** The most important characteristics of three electron sources that may be considered in a current density optimized electron column. The values are taken from reference [94] and [95].

In order to get an estimate for the current density we may expect, we will optimize a hypothetical column based on realistic optical characteristics. The equations 1.4-1.7 give certain limiting conditions but in order to do a full optimization we use the equations 1.1, 1.2, 1.3 and balance the opening angle and magnification for achieving the smallest spot size for a particular current. This method is well described in the literature [93]. The chosen values for the characterizing the column are listed in table 1.3. The properties of the considered electron sources are shown in table 1.4.

Since we haven't decided on the electron beam impact energy, we need to bring the energy dependence of the objective lens aberrations to attention. Suppose we scale down a particular lens configuration, effectively we scale down all trajectories proportionally and so the aberrations scale down accordingly too. It is well-known that for obtaining minimal aberrations, the smallest lenses are best. However, for electrostatic lenses, a maximum field that can be maintained before break-down occurs should be respected, often 10 kV/mm is used as a rule of thumb. This means that there is a limit to how far we can downscale. We can only downscale beyond this limit if we scale the beam energy and the lens potential accordingly. If we consider only good lenses that are operated at the field strength limit, we can expect the aberration coefficients to scale proportionally to the landing energy. For magnetic lenses there is a similar limit, namely that the metal can maintain a certain magnetic field before saturation effects occur. This leads to the aberration coefficients scaling proportionally to the square root of the landing energy, as explained by Hawkes [96]. So, we have for the scaling of the aberrations:

$$C_{s,m} = C_{s,m}^* \sqrt{\frac{V}{V^*}}, \quad C_{c,m} = C_{c,m}^* \sqrt{\frac{V}{V^*}} \quad (\text{magnetic lenses}) \quad (1.10)$$

$$C_{s,e} = C_{s,e}^* \frac{V}{V^*}, \quad C_{c,e} = C_{c,e}^* \frac{V}{V^*} \quad (\text{electrostatic lenses}) \quad (1.11)$$

in which the starred aberration coefficients are known reference values of a lens that is operated at a beam voltage  $V^*$ .

The results of the electron column optimization assuming a magnetic objective lens are shown in figure 1.11. Clearly a maximum at the point where both gun and objective lens aberrations become important is visible, as was explained earlier. For the Schottky gun we find the maximum somewhere between 40 and 100 nm full width 50 probe size. This sets the typical dimension of the inlet aperture in the double membrane structure. For 1 keV electrons, the maximum current density is  $6.5 \times 10^7 \text{ A m}^{-2}$ , the probe size is 40 nm, and the total current of the beam is 167 nA. Interestingly, if we would use a SEM under normal operation conditions and focus down to a few nanometer, we easily loose an order of magnitude or more in current density compared to this optimum. In addition, this would also mean a much lower total current. A NAIS devoted e-beam is quite different from a high resolution SEM.

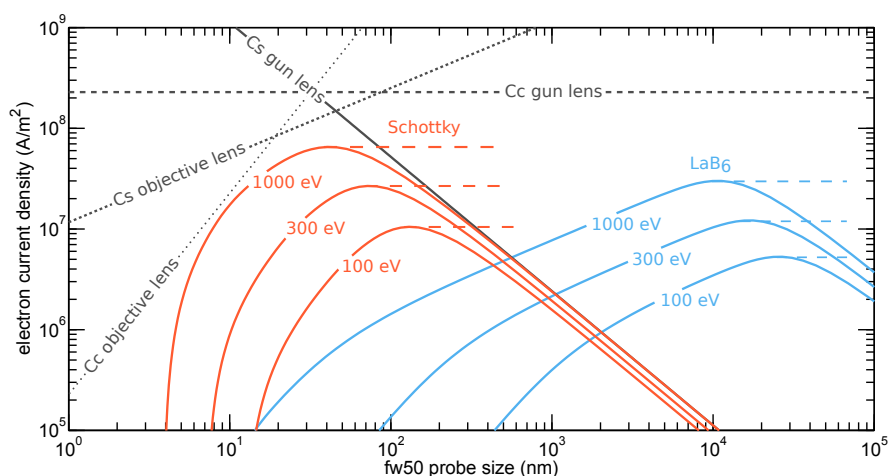


**Figure 1.11.** Optimization curves of a two-lens electron column with a magnetic objective lens. The electron current density is shown, for that is the figure of merit of a NAIS devoted electron column. For 1 keV electrons from a Schottky source the curves of limiting regimes as calculated by the equations 1.1 are shown. The dashed red and blue lines indicate that the current density in the center of the probe can always be made at least as high as the maximum for probe sizes larger than where the maximum occurs even though the average current density of the probe will decrease.

We have chosen to use a Schottky electron gun as the e-gun for the NAIS, even though the a LaB<sub>6</sub> gives comparable current density. The problem with LaB<sub>6</sub> is that the optimum occurs at a very high probe size, which leads to several complications. For high resolution applications we would need a huge demagnification. In contrast, the spot size of the Schottky optimum is very close to the virtual source size of LMIS emitters, enabling the use of already existing optical columns. The big spot size of the Lab6 also leads to the need of a very large aperture, which gives a big amount of gas leaking into the vacuum. Furthermore, a 10  $\mu\text{m}$  virtual source size is inconvenient for high resolution applications.

A cold field emitter can give a very high current density of  $8.7 \times 10^7 \text{ A m}^{-2}$ , but with only a 10 nA of total current. These specs are interesting for certain applica-



tions, but a cold field emitter is rather sensitive and unreliable so it is disregarded anyhow. See ref. [87] for a detailed analysis of using a cold field emitter for the NAIS.

We should make the remark that in the calculations so far we have looked at the average current density in the probe. If we, however, would look at the current density in the center of the probe, the curves would look different. Suppose from some particular optical configuration we would increase the beam angle, then, the current density in the center of the probe can only stay the same or increase. It is impossible to lower a current density by adding more current. However, the total probe size full width 50 increases more rapidly than the current, so the average current density does decrease. In practical terms this means we could use a very large opening angle and use a small electron-entrance aperture in the top membrane to select the high current density region of the focused probe. In figure 1.11 this notion is indicated by dashed lines continuing from the optima. Using such a configuration would mean a very high current hitting the membrane continuously, which may cause deformation by heating, or give rise to charging effects. While it may be possible, we have chosen to not pursue this direction as it seems a little risky.

From this optimization we could conclude that we want to use the highest possible energy. This, however, would neglect the energy dependence of the ionization cross section. By looking at the product of the ionization cross section and the electron current density we get the best figure of merit. Figure 1.12 shows the results of multiplying the optima as obtained in figure 1.11 for the Schottky electron gun with the ionization cross section.

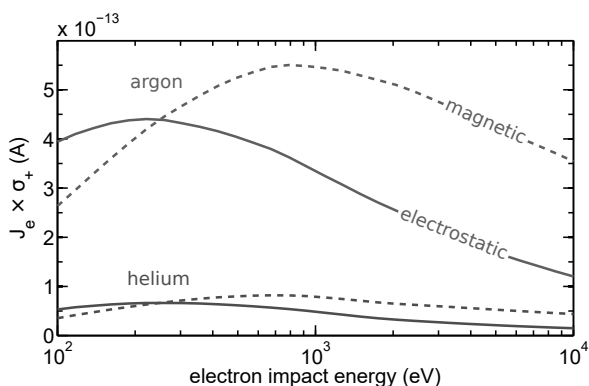


**Figure 1.12.** Optimizing the electron beam for the NAIS by finding the highest combination electron current density and ionization cross section. A magnetic or electrostatic objective lens performs differently because the aberrations scale differently with the impact energy. The best impact energy seems to be in the sub-1 keV regime, but the optimum is not very steep. We show two example gases to indicate that the difference in ionization cross section makes the performance species dependent. The position of the optima is quite comparable though, so a particular e-gun optimization is good for different gases. The ionization cross sections used for this calculation are shown in figure 1.9

We see in figure 1.12 that the optimum is rather shallow, meaning that a very specific energy is not required. What impact energy would be best depends a little on the choice of a magnetic or electrostatic objective lens, but roughly speaking we find the optimal energy at a few hundred eV. We are, however, inclined to choose 1

keV. While 1 keV seems sufficiently low to obtain a good ionization efficiency, it is high enough to comfortably work with. Low energy beams are preferably avoided as they are more prone to magnetic disturbances, are easier affected by parasitic charging, and are more troubled by statistical coulomb interactions.

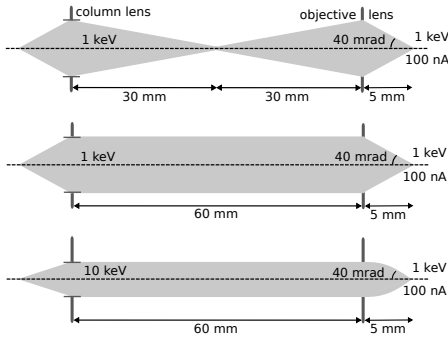
Speaking of coulomb interactions, the values of this optimization should make every charged particle optician a little worried. We are suggesting to operate an electron beam at 1 keV with about 100 nA of current; that is a very high current at a relatively low energy. It becomes necessary to at least estimate the coulomb interactions. We use the slice method [97] to estimate the probe deterioration due to coulomb interactions (see chapter 5 appendix A)

Figure 1.13 shows two manifestations one may encounter in a typical column design; a single cross over and a parallel beam. We denote the pre-final lens as the column lens, this may be the gun lens or an intermediate lens. In the most simple configuration the beam energy in the region after the column lens, through the objective lens, up to the sample, is equal to the landing energy.

We consider a relatively short, but feasible length of 60 mm between the column lens and the objective lens. This is usually the region where we find a deflection system, a stigmator, the objective lens coils, a valve, detectors, etc. A 5 mm distance from the objective lens center to the sample is quite typical. We assume that any coulomb interactions prior to the column lens are negligible. In a conventional SEM, a so-called coulomb tube achieves this; a region at which the electrons are maintained at very high voltage. Alternatively one simply designs a very short electron column where the gun is placed right in front of the column lens. In the gun region we usually do have coulomb interactions but these are already accounted for in source characterizing parameters of brightness, energy spread, and virtual source size.

For the beam properties we use values close to what was found in the optimization demonstrated in figure 1.11, namely  $I = 100$  nA,  $V = 1$  kV,  $\alpha = 40$  mrad,  $d_{\text{probe}} = 40$  nm. We calculate the contribution of the trajectory displacement at the probe forming location. We find in the single cross over configuration a trajectory displacement of 199 nm and a Boersch effect contribution to the energy spread of 144 meV. In the parallel beam configuration we find 168 nm and 18 meV. The Boersch effect contribution is quite acceptable, but the trajectory displacement becomes the probe size limiting factor when comparing to our 40 nm target value. Interestingly it doesn't matter a great deal if one prevents a cross over or not for the trajectory displacement [98, 99]. This indicates that we can not solve the issue by simply reconfiguring the optics a bit.

When running a parallel beam at 10 keV with deceleration at the last moment we obtain a total trajectory displacement fw50 disk of 29.6 nm. This is comprised by 7.2 nm in the deceleration region and 22.4 nm in the beam line. This is quite alright, but getting it below 20 nm would make it insignificant. Further increasing the intermediate energy and shortening the beam line are means that help to this end.



**Figure 1.13.** Three different beam segments are considered for a statistical coulomb interaction calculation of a NAIS electron gun. All configurations have the same final probe characteristics: 40 mrad opening angle, 1 keV landing energy, 100 nA of total current, and 40 nm fw50 probe size, if no coulomb interactions would be present. Two configurations are maintained at 1 keV, while the bottom configuration runs the electrons at 10 keV until the beam is decelerated in the last 5 mm.

One may argue that these few calculations are not representative for all possible optical configurations, and this is true. The point is mainly to create awareness of coulomb interactions of NAIS optimized electron columns. More specifically, we see that beam segments of tens of millimeters at 1 keV are just not going to cut it.

### 1.3.3. Expected performance

From the previous section we found that we may get an electron beam with 100 nA of current in a 50 nm fw50 spot at 1 keV. This still requires skillful optical design, but is certainly feasible. We have assumed that the coulomb interactions are sufficiently reduced to not be dominating. We also learned that a decent guess for the ionization efficiency of brightness contributing ions is  $\frac{\sigma_+}{\sigma_{i-n}}$ . This gives typically around 1 nA of total current. Using equation 1.8 we get for the brightness

$$B_r = \frac{\sigma_+}{\sigma_{i-n}} \frac{eJ_e}{\pi kT}. \quad (1.12)$$

We find for all noble gases a brightness higher than  $1 \times 10^6 \text{ A/m}^2 \text{ srV}$ . In table 1.5 the estimated brightnesses are listed more concisely. As a first approximation, we can assume that the virtual ion source is an image of the e-beam spot profile, giving 50 nm for the fw50 virtual source size.

We note that on one hand, the brightness given here is quite conservative. We have taken aberration coefficients as often encountered in a SEM. However, a dedicated electron beam column could have lower aberrations, as we could decelerate at the last moment, or put the chip much closer to the objective lens than a sample in a SEM. We may also improve the gun lens aberrations. Furthermore we have neglected the brightness contribution of scattered particles, which may contribute anyway.

On the other hand, we haven't looked in detail at ion neutral interactions, the curved electric fields inside the chip, and the coulomb interactions of the ions. It is perhaps good to start of a little conservative.

	$\sigma_{i-n}$ m <sup>2</sup>	$\sigma_+$ m <sup>2</sup>	$\eta_I^+$ %	estimated $B_r$ A/m <sup>2</sup> srV
Helium	$2.46 \times 10^{-19}$	$1.24 \times 10^{-21}$	0.50	$1.9 \times 10^6$
Neon	$2.98 \times 10^{-19}$	$3.21 \times 10^{-21}$	1.08	$3.2 \times 10^6$
Argon	$4.44 \times 10^{-19}$	$7.83 \times 10^{-21}$	1.76	$5.5 \times 10^6$
Krypton	$5.13 \times 10^{-19}$	$9.84 \times 10^{-21}$	1.92	$6.2 \times 10^6$
Xenon	$5.86 \times 10^{-19}$	$1.21 \times 10^{-20}$	2.06	$6.7 \times 10^6$

**Table 1.5.** Estimated ionization efficiency and brightness of noble gas ions by using a 1 keV, 50 nm, 100 nA electron beam. The ion-neutral cross sections are based on van der Waals diameters [100]. Ionization cross sections are taken from Rejoub et al. [90]

The energy spread is directly related to the voltage across the membranes. Because the ions are generated at different locations and thus at different equipotential planes, an energy spread is created. The purpose of the bias voltage is two-fold. Firstly, it helps extracting the ions by steering them towards the exit aperture. Secondly, the membrane bias is extracting the ions quickly before they can repel each other. If we equate the average chip residential time to the average time between the generation of two ions and if we assume Poissonian statistics for ion generation, we can make the following statement : 58% of the time an ion is present in the chip, it is the only one. We consider this to be a situation where we expect limited influence of coulomb interactions in the chip. An estimate for the bias voltage required to achieve  $\langle t_{\text{res}} \rangle = \langle t_{\text{gen}} \rangle$  is  $V_b = \frac{8}{9} \frac{m}{q^3} m l^2 I^2$ . If  $l = 200$  nm and  $I = 1$  nA we find that we need 0.58 V for argon. The effective fw50 energy spread will in general be lower than the bias voltage, so the prospect of getting a low energy spread is quite good.

## 1.4. Chip fabrication

Crucial for a nano-aperture ion source is the sub-micron-scaled gas chamber. While nano-fluidics is a broad field of research, no readily available devices or fabrication schemes adhere to all our requirements. Electrons need to enter from the top and ions need to come out below, so one requirement is a free standing region of the double membrane structure. The membranes need to be conducting as to prevent charging, but also to enable an electric field across the ionization region. The latter requires electrical insulation between the two conducting membranes. The spacing between the membranes needs to be below 1  $\mu\text{m}$  and the membrane thickness is preferably below 100 nm. Such thin and free standing membranes might become fragile, but actually need to hold pressures of 1 bar and above. We are aiming to connect the devices with tiny o-rings, so the associated clamping force needs to be applicable to the chip as well. Obviously the membranes need to be leak tight.

Figure 1.14 helps to get familiar with some, so far, general attributes of any NAIS chip; a free standing membrane, a FIB milled aperture, and a FIB milled gas entrance.

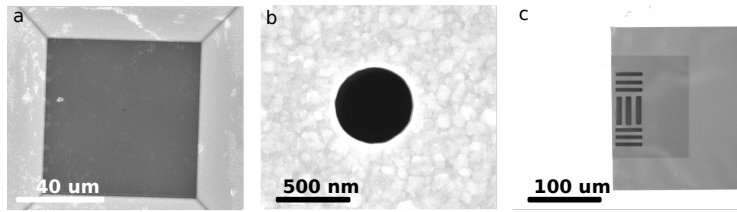


**Figure 1.14.** Three essential aspect of a NAIS chip. a) SEM image of the free standing double membrane structure as viewed down the KOH etched recess) b) A typical aperture produced by FIB milling c) Gas entrance membrane opening produced by FIB milling.

#### 1.4.1. Adhesively bonded chips

The concept of attaching two wafers on top of each other as a means of fabrication NAIS gas chambers was first investigated by Tondare [87]. A layer of resist was used to bond the chips together. A similar technique was used by Jun et al. [88, 101], although a self-curing adhesive was used rather than resist. The conceptual structure of such a device is shown in figure 1.15.

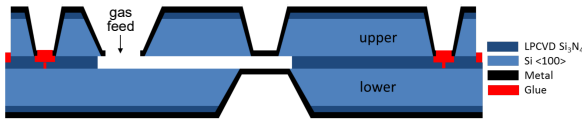


**Figure 1.15.** Adhesive bonding as a means of fabricating NAIS gas chambers. (courtesy ref. [88])

Jun et al. managed to produce chips with spacings of 1.0 to 2.5  $\mu\text{m}$ . The target spacing was 200 nm, but glue seepage seemed to be causing much larger spacings. Another problems was the difficulty of acquiring high quality, large, free-standing metal membranes. However, a particular sandwich of different metals did seem to work quite well. Bowing of the membranes due to the applied gas pressure is another issue. If the free standing area can be reduced to  $10\mu\text{m} \times 10\mu\text{m}$ , the deflection can be brought well below 100 nm, but such small membranes are difficult to align and produce. We should also mention that this is a one-chip-at-the-time procedure and thereby quite time consuming. Nevertheless, devices produced by this method were successfully used to make ion beams [86].

#### 1.4.2. Fully micro-machined chips

A more advanced method of chip fabrication is based on micro-machining methods, using a single wafer [88]. Comparable work was done by Creemer et al. [102]. Figure 1.16 gives an impression of this method. No adhesives are used, so glue seepage and the tedious one-at-the-time-production disadvantages are circumvented. After a sandwich of  $\text{Si}_3\text{N}_4$ -TEOS- $\text{Si}_3\text{N}_4$  is deposited, holes are etched in the top  $\text{Si}_3\text{N}_4$  layer. This allows buffered HF to etch away the sacrificial TEOS layer, while the silicon nitride membranes remain. By diligently tuning the etching time, not all TEOS is removed such that pillars remain. These minimize membrane bowing and increases the integrity of the membranes.

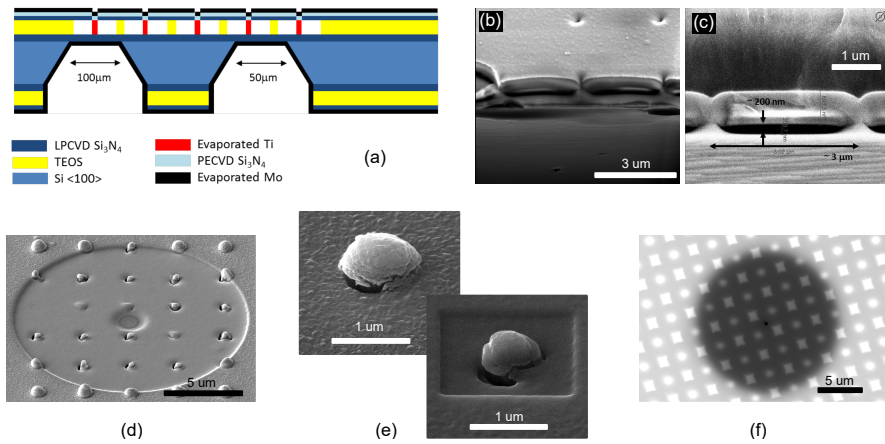


**Figure 1.16.** NAIS chips produced by micro-machining procedures on one side of the wafer. a) The crucial aspects of this design are the single sided KOH-etch hole, membrane supporting pillars, and plugged membrane etch holes. b-c) FIB cross sectioning indicates a 200 nm spaced hollow channel (courtesy ref. [88]). d) Locally thinning the membrane in two steps. Note the apparent leakage around the plugs. e) A possible leak along an etch hole plug. When FIB milling around the pillar it became clear this defect runs down all the way to the channel. f) By using a 25 keV electron beam, we can look through the membrane and see pillars and hole plugs. The dark circle indicates the locally thinned membrane with in the center a nano-aperture.

One of the most difficult tasks was plugging the etch holes. A layer of about  $1\text{ }\mu\text{m}$  was needed to get a leak tight membrane. To obtain a thin membrane anyway, FIB milling is used for thinning the membrane locally around the nano-aperture. Even with a thick etch hole plugging layer, membrane closure was not always successful. Figure 1.16d and 1.16e shows a chip where almost all membrane plugs were leaking. A similar recipe was followed as a batch that did produce proper plugging, so apparently the success is in the details of the procedure.

In general this method comprises tens of micro-machining steps, making it a challenging production method. The efforts pay off in small membrane spacing and good membrane integrity. In addition, the ion side of the chip is flat, which is an advantage for applying a high electric field. The necessity of this will become clear in the following chapters.

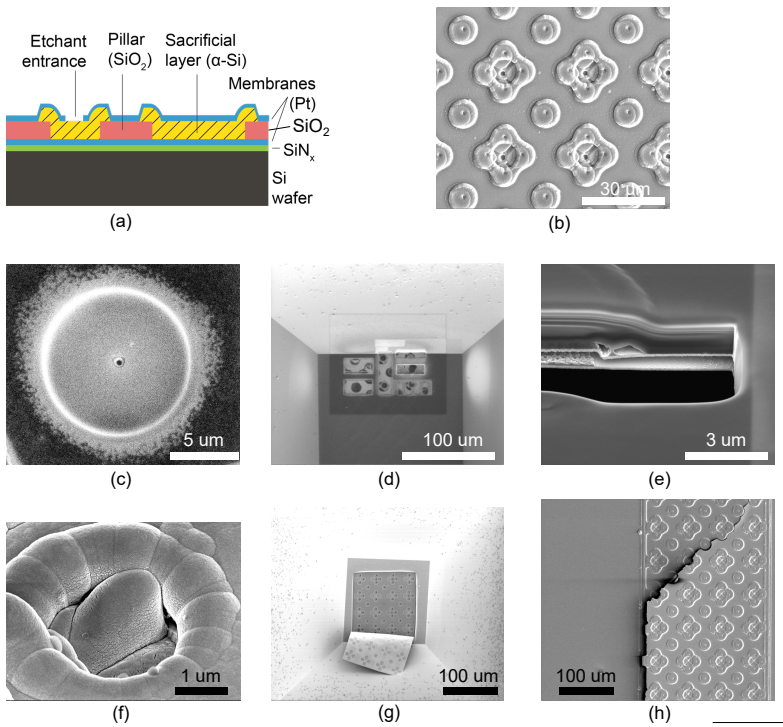


**Figure 1.17.** Full metal membrane chips fabricated by micro-machining methods on a single wafer. a) A sacrificial amorphous silicon layer is removed by an isotropic  $\text{SF}_6$  plasma etch, leaving platinum membranes. b) An ion-side SEM image of a successful channel. c) Locally thinned membrane with an aperture in the center. d) FIB-milled gas channel entrance, revealing the pillar and etch hole plugging structure. e) Hollow channel separated by two 100 nm thick platinum membranes. On top of the platinum membrane an additional layer of silicon nitride ensures solid membrane step coverage. f) Proper etch hole plugging is a challenge, as can be seen from the black slits due to bad deposition uniformity. g) A detached membrane caused by bad step coverage of the edge of the channel at the electron side. h) A damaged membrane due to bad step coverage of the ion side membrane.

An improvement of this concept with the goal of making full metal membranes was developed mostly by Rademaker and Heerkens. Details are discussed in ref. [103]. The requirement of metal membranes makes the selection of sacrificial layer and membrane material difficult. Nevertheless, an amorphous silicon sacrificial layer and platinum membranes in combination with an isotropic  $\text{SF}_6$  plasma etch was found to be a good combination. Figure 1.17 shows the concept and some results of this approach. We found again that plugging the etch holes is a challenge (see figure 1.17f), so a thick top layer was needed. This plugging layer is patterned around the etch holes such that the overall membrane could remain thin. A second problem was the difficulty of getting good step coverage for the membranes. Ultimately, a thick top layer was needed on the entire ion side anyway, which near the aperture needs to be thinned by FIB milling.

We also bring attention to some problems with membrane integrity as shown in 1.17g and 1.17h. These are some examples of failed attempts in trying to successfully go through the entire procedure. The great number of delicate steps make chip fabrication an enormous challenge.



## 1.5. The mission

While the physics and technology involved in building the nano-aperture ion source are great fun, the project can be marked as industrial in nature. Not the act of making a high-quality ion beam is in itself useful, the potential applications is what grants this research existence.

At the charged particle optics group for many years effort has been put in the realization of a commercially viable nano-aperture ion source [87, 88]. Great steps forward have been made already, notably the first production of ions [86], emission simulations [88], progress on chip fabrication [88, 101], and measurements of the energy spectrum [88].

Still lacking is true proof for the NAIS being a good candidate as a competitor in the ion source market. Therefore, it is pivotal to demonstrate a high brightness. Different aspects of commercial viability are for example source lifetime, stability, and costs. While these aspects should certainly not be overlooked, the main focus of this research has been on demonstrating a high brightness as it is the most important and most uncertain aspect at present. The problem of measuring brightness is that everything needs to be perfect, both the source as well as the measurement system. A true challenge. This is the reason that it hasn't been measured already. What we desire is a brightness better or comparable to that of the gallium LMIS. So, the goal is to show a brightness of  $1 \times 10^6 \text{ A m}^{-2} \text{ sr}^{-1} \text{ V}^{-1}$ .

What is lacking as well, is good understanding of the relevant physics, specifically the source optics. Scattering of ions on neutrals has been described by a molecular diameter, which is normally only used for non-ionic interaction. Coulomb interactions have mostly been ignored and also the optical effects of emission from a volume in which an electric field is present hasn't been studied very deeply. Surely it was reasonable to start off as simple as possible, but this research aims at improving the modeling done so far. A better theoretical basis gives better guidance for the experimental direction and further optimization of the system.

## References

1. Carl Zeiss. "Orion Plus". [www.zeiss.com/microscopy](http://www.zeiss.com/microscopy). (The latest successor is known as the Orion NanoFab) (2016).
2. FEI Company. "Helios NanoLab Dual-Beam". [www.fei.com/products/dualbeam/helios-nanolab](http://www.fei.com/products/dualbeam/helios-nanolab) (2016).
3. C. J. P. Alvin W. Czanderna, Theodore E. Madey. *Beam Effects, Surface Topography, and Depth Profiling in Surface Analysis* (Kluwer academic publishers - New York, Boston, Dordrecht, London, Moscow, 2002). See chapter 3, authors: L.S. Dake, D.E. King, J.R. Pitts, and A.W. Czanderna.
4. L. Giannuzzi and F. Stevie. *Introduction to Focused Ion Beams: Instrumentation, Theory, Techniques, and Practice* (Springer Science+Business Media, Inc., 2005).
5. S. Lipp, L. Frey, C. Lehrer, E. Demm, S. Pauthner, and H. Rysse. "A comparison of focused ion beam and electron beam induced deposition processes". *Microelectron. Reliab.* **36** (11–12), pp. 1779–1782 (1996).
6. L. Reimer and C. Tollkamp. "Measuring the backscattering coefficient and secondary electron yield inside a scanning electron microscope". *Scanning* **3** (1), pp. 35–39 (1980).
7. V. Castaldo, J. Withagen, C. Hagen, P. Kruit, and E. van Veldhoven. "Angular Dependence of the Ion-Induced Secondary Electron Emission for He+ and Ga+ Beams". *Microsc. Microanal.* **17**, pp. 624–636 (2011).
8. Y. Yamamura and H. Tawara. "Energy dependence of ion-induced sputtering yields from monatomic solids at normal incidence". *At. Data Nucl. Data Tables* **62** (2), pp. 149–253



- (1996).
9. Y. Kudriavtsev, A. Villegas, A. Godines, and R. Asomoza. "Calculation of the surface binding energy for ion sputtered particles". *Appl. Surf. Sci.* **239** (3–4), pp. 273–278 (2005).
  10. C. Lehrer, L. Frey, S. Petersen, and H. Ryssel. "Limitations of focused ion beam nanomachining". *J. Vac. Sci. Technol. B* **19** (6), pp. 2533–2538 (2001).
  11. L. Frey, C. Lehrer, and H. Ryssel. "Nanoscale effects in focused ion beam processing". *Appl. Phys. A* **76** (7) (2003).
  12. S. Lindsey and G. Hobler. "The significance of redeposition and backscattering in nanostructure formation by focused ion beams". *Nucl. Instrum. Meth. B* **282**, pp. 12–16 (2012).
  13. I. Utke, P. Hoffmann, and J. Melngailis. "Gas-assisted focused electron beam and ion beam processing and fabrication". *J. Vac. Sci. Technol. B* **26** (4), pp. 1197–1276 (2008).
  14. B. Schmidt and K. Wetzig. *Ion Beams in Materials Processing and Analysis* (Springer Vienna, 2012). P. 272.
  15. P. Chen, P. F. A. Alkemade, and H. W. M. Salemink. "The Complex Mechanisms of Ion-Beam-Induced Deposition". *Jpn. J. Appl. Phys.* **47** (6S) (2008).
  16. P. F. A. Alkemade and H. Miro. "Focused helium-ion-beam-induced deposition". *Appl. Phys. A* **117** (4) (2014).
  17. P. Chen, H. W. M. Salemink, and P. F. A. Alkemade. "Roles of secondary electrons and sputtered atoms in ion-beam-induced deposition". *J. Vac. Sci. Technol. B* **27** (6), pp. 2718–2721 (2009).
  18. R. Baragiola, S. Ritzau, R. Monreal, C. Dukes, and P. Riccardi. "Mechanisms for ion-induced plasmon excitation in metals". *Nucl. Instrum. Methods. Phys. Res. B* **157**, pp. 110–115 (1999).
  19. T. Henkel, V. Heera, R. Kögler, W. Skorupa, and M. Seibt. "Kinetics of ion-beam-induced interfacial amorphization in silicon". *J. of Appl. Phys.* **82** (11), pp. 5360–5373 (1997).
  20. Y. Huh, K. J. Hong, and K. S. Shin. "Amorphization Induced by Focused Ion Beam Milling in Metallic and Electronic Materials". *Microsc. Microanal.* **19**, pp. 33–37 (2013).
  21. A. Joshi-Imre and S. Bauerdick. "Review article: Direct-Write Ion Beam Lithography". *Journal of Nanotechnology* **2014**, p. 170415 (2014).
  22. See ref. [4], Chapter: Focused Ion Beam Secondary Ion Mass Spectrometry (FIB-SIMS), p. 269–280, author: Stevie, F. A.
  23. See ref. [4], p. 47.
  24. P. Sigmund. "Theory of Sputtering. I. Sputtering Yield of Amorphous and Polycrystalline Targets". *Phys. Rev.* **187**, pp. 768–768 (1969).
  25. H. Hofsass, K. Zhang, and A. Mutzke. "Simulation of ion beam sputtering with SDTrimSP, TRIDYN and SRIM". *Appl. Surf. Sci.* **310**, pp. 134 – 141 (2014).
  26. S. Tan, R. Livengood, D. Shima, J. Notte, and McVey. "Gas field ion source and liquid metal ion source charged particle material interaction study for semiconductor nanomachining applications". *J. Vac. Sci. Technol. B* **28**, p. C6F15 (2010).
  27. J. Mayer, L. A. Giannuzzi, T. Kamino, and J. Michael. "TEM Sample Preparation and FIB-Induced Damage". *MRS Bulletin* **32** (2007).
  28. G. Rius. "Technology basis and perspectives on focused electron beam induced deposition and focused ion beam induced deposition". *Nucl. Instrum. Methods Phys. Res., Sect. B* **341**, pp. 37–43 (2014).
  29. S. Waid, H. D. Wanzenboeck, M. Muehlberger, M. Gavagnin, and E. Bertagnolli. "Focused ion beam direct patterning of hardmask layers". *J. Vac. Sci. Technol., B* **32** (4), 041602 (2014).
  30. W. Li, C. Gu, A. Cui, J. Fenton, Q. Jiang, P. Warburton, and T. Shen. "Three-dimensional nanostructures by focused ion beam techniques: Fabrication and characterization." *J. Mater. Res.* **28** (22) (2013).
  31. H. Kollmann, X. Piao, M. Esmann, S. F. Becker, D. Hou, C. Huynh, L.-O. Kautschor, G. Bösker, H. Vieker, A. Beyer, A. Göhlhäuser, N. Park, R. Vogelgesang, M. Silies, and C. Lienau. "Toward Plasmonics with Nanometer Precision: Nonlinear Optics of Helium-Ion Milled Gold Nanoantennas". *Nano Lett.* **14**, pp. 4778–4784 (2014).
  32. NanoScope Services Ltd, Bristol. [www.nanoscopeservices.co.uk/fib-circuit-edit/](http://www.nanoscopeservices.co.uk/fib-circuit-edit/) (2016).
  33. S. Matsui, chapter: B. Bhushan. *Encyclopedia of Nanotechnology* (Springer Netherlands, Dordrecht, 2012). Chapter: Focused-Ion-Beam Chemical-Vapor-Deposition (FIB-CVD), p. 872.
  34. Teshima - LatticeGear, Jamil J. Clarke - Hitachi High Technologies America Inc. "Cross section of an integrated circuit". [goo.gl/KPl2rM](http://goo.gl/KPl2rM) (2014).
  35. FEI Company. "FIB-SEM tomography of tissue". [www.fei.com/products/dualbeam/helios-nanolab](http://www.fei.com/products/dualbeam/helios-nanolab) (2016).
  36. A. Botman - FEI Company. "Failure analysis of an adhesively bonded chip". private communication (2015).

37. A. Beyer, H. Vieker, R. Klett, H. M. zu Theenhausen, P. Angelova, and A. Götzhäuser. "Imaging of carbon nanomembranes with helium ion microscopy". *Beilstein J. Nanotechnol.* **6** (2015).
38. Institut für Angewandte Materialien. "Channeling-Kontrast bei Kupfer (FIB-Aufnahme)". [www.iam.kit.edu/wbm/324.php](http://www.iam.kit.edu/wbm/324.php) (2016).
39. A. Fernández-Pacheco, J. M. De Teresa, R. Córdoba, and M. R. Ibarra. "Metal-insulator transition in Pt-C nanowires grown by focused-ion-beam-induced deposition". *Phys. Rev. B* **79**, p. 174204 (2009).
40. J. Remes, J. Vahakangas, and A. Uusimäki. "Improving the Yield and Turn-Around Time of Focused Ion Beam Microsurgery of Integrated Circuits by LCVD Method". *Adv. Packag. IEEE Trans.* **32** (2) (2009).
41. H. Wu, L. A. Stern, D. Xia, D. Ferranti, B. Thompson, K. L. Klein, C. M. Gonzalez, and P. D. Rack. "Focused helium ion beam deposited low resistivity cobalt metal lines with 10 nm resolution: implication for advanced circuit editing". *J. Mater. Sci. Mater. Electron.* **25** (2) (2014).
42. P. Bandaru. "Electrical contacts to nanomaterials". *J. Nanosci. Nanotechnol.* **15** (12) (2015).
43. Y. Lan, W. Chang, Y. Chang, C. Chang, and C. Chen. "Effect of focused ion beam deposition induced contamination on the transport properties of nano devices." *Nanotechnology* **26** (5) (2015).
44. P. Dhakal, G. McMahon, S. Shepard, T. Kirkpatrick, J. I. Oh, and M. J. Naughton. "Direct-write, focused ion beam-deposited, 7 K superconducting C-Ga-O nanowire". *Appl. Phys. Lett.* **96** (26) (2010).
45. M. Gabureac, L. Bernau, I. Utke, and G. Boero. "Granular Co-C nano-Hall sensors by focused-beam-induced deposition". *Nanotechnology* **21** (11) (2010).
46. S. A. Boden, T. M. Franklin, L. Scipioni, D. M. Bagnall, and H. N. Rutt. "Ionoluminescence in the Helium Ion Microscope". *Microsc. Microanal.* **18**, pp. 1253–1262 (2012).
47. Y. V. Petrov and O. F. Vyvenko. "Scanning reflection ion microscopy in a helium ion microscope". *Beilstein J. Nanotechnol.* **6**, p. 1125–1137 (2015).
48. G. Hlawacek, V. Veligura, S. Lorbek, T. F. Mocking, A. George, R. van Gastel, H. J. W. Zandvliet, and B. Poelsema. "Imaging ultra thin layers with helium ion microscopy: Utilizing the channeling contrast mechanism". *Beilstein J. Nanotechnol.* **3**, p. 507–512 (2012).
49. V. Veligura, G. Hlawacek, R. van Gastel, H. J. W. Zandvliet, and B. Poelsema. "Channeling in helium ion microscopy: Mapping of crystal orientation". *Beilstein J. Nanotechnol.* **3** (2012).
50. D. Y. B. Zhou, A. O'Neill, S. Kumar, J. J. Wang, J. N. Coleman, G. S. Duesberg, J. F. Donegan, and H. Z. Zhang. "Helium ion microscopy of graphene: beam damage, image quality and edge contrast". *Nanotechnology* **24** (33) (2013).
51. V. Castaldo. *High Resolution Scanning Ion Microscopy*. Ph.D. thesis, Delft University of Technology (2011).
52. J. Barth and P. Kruit. "Addition of different contributions to the charged particle probe size". *Optik* **101** (3), p. 101 (1996).
53. C. W. Hagen, E. Fokkema, and P. Kruit. "Brightness measurements of a gallium liquid metal ion source". *J. Vac. Sci. Technol. B* **26** (6), p. 2091 (2008).
54. O. Scherzer. "Über einige Fehler von Elektronenlinsen". *Zeitschrift für Physik* **101** (9) (1936).
55. S. Kellogg, R. Schampers, S. Zhang, A. Graupera, T. Miller, W. Laur, and A. Dirriwacher. "High Throughput Sample Preparation and Analysis Using an Inductively Coupled Plasma (ICP) Focused Ion Beam Source". *Microsc. Microanal.* **16**, pp. 222–223 (2010).
56. G. Taylor. "Disintegration of Water Drops in an Electric Field". *Proc. R. Soc. A* **280** (1382), pp. 383–397 (1964).
57. See ref. [95], Chapter 3: G.L.R. Mair, Liquid metal ions sources.
58. L. Bischoff. "Alloy liquid metal ion sources and their application in mass separated focused ion beams". *Ultramicroscopy* **103** (1), pp. 59–66 (2005).
59. L. Bischoff. "Application of mass-separated focused ion beams in nano-technology". *Nucl. Instrum. Meth. B* **266** (8), pp. 1846–1851 (2008).
60. G. A. Schwind and L. W. Swanson. "Emission characteristics of Au<sub>60</sub>Be<sub>40</sub> and Au<sub>62</sub>Si<sub>23</sub>Be<sub>15</sub> liquid metal ion sources". *J. Vac. Sci. Technol. B* **25**, p. 2586 (2007).
61. S. Waid, H. D. Wanzenböck, M. Gavagnin, R. Langeegger, M. Muehlberger, and E. Bertagnolli. "Focused ion beam induced Ga-contamination—An obstacle for UV-nanoimprint stamp repair?" *J. Vac. Sci. Technol. B* **31** (4) (2013).
62. J. Barzola-Quiquea, S. Dusari, G. Bridoux, F. Bern, A. Molle, and P. Esquinazi. "The influence of Ga<sup>+</sup> irradiation on the transport properties of mesoscopic conducting thin

- films". *Nanotechnology* **21** (2010).
63. Ward. "Helium ion microscope: A new tool for nanoscale microscopy". *J. Vac. Sci. Technol. B* **24** (6) (2006).
  64. G. Hlawacek, V. Veligura, R. van Gastel, and B. Poelsema. "Helium ion microscopy". *J. Vac. Sci. Technol. B* **32** (2) (2014).
  65. R. Hill and F. F. Rahman. "Advances in helium ion microscopy". *Nucl. Instrum. Meth. A* **645** (1), pp. 96–101 (2011).
  66. R. Siegele, G. C. Weatherly, H. K. Haugen, D. J. Lockwood, and L. M. Howe. "Helium bubbles in silicon: Structure and optical properties". *Appl. Phys. Lett.* **66** (11), pp. 1319–1321 (1995).
  67. C. C. F. Daniel Fox, Yanhui Chen and H. Zhang. "Nano-structuring, surface and bulk modification with a focused helium ion beam". *Beilstein J. Nanotechnol.* **3**, p. 579–585 (2012).
  68. N. Smith, P. Tesch, N. Martin, and D. Kinion. "A high brightness source for nano-probe secondary ion mass spectrometry". *Appl. Surf. Sci.* **255** (4), pp. 1606–1609 (2008).
  69. Q. Ji, X. Jiang, T.-J. King, K.-N. Leung, K. Standiford, and S. B. Wilde. "Improvement in brightness of multicusp-plasma ion source". *J. Vac. Sci. Technol. B* **20** (6), pp. 2717–2720 (2002).
  70. S. Guharay, S. Douglass, and J. Orloff. "High-resolution primary ion beam probe for SIMS". *Appl. Surf. Sci.* **231–232**, pp. 926–929 (2004).
  71. N. S. Smith, W. P. Skoczylas, S. M. Kellogg, D. E. Kinion, P. P. Tesch, O. Sutherland, A. Aanesland, and R. W. Boswell. "High brightness inductively coupled plasma source for high current focused ion beam applications". *J. Vac. Sci. Technol. B* **24** (6), pp. 2902–2906 (2006).
  72. P. Nabhiraj, R. Menon, G. M. Rao, S. Mohan, and R. Bhandari. "Characterization of compact ICP ion source for focused ion beam applications". *Nucl. Instrum. Meth. A* **621** (1–3), pp. 57–61 (2010).
  73. R. Forbest. "Understanding how the liquid-metal ion source works". *Vacuum* **48** (1), pp. 85–97 (1997).
  74. Carl Zeiss. "Orion NanoFab". [www.zeiss.com/microscopy/en\\_us/products/multiple-ion-beam.html](http://www.zeiss.com/microscopy/en_us/products/multiple-ion-beam.html) (2016).
  75. N. Ernst, G. Bozdech, H. Schmidt, W. Schmidt, and G. L. Larkins. "On the full-width-at-half-maximum of field ion energy distributions". *Appl. Surf. Sci.* **67** (1–4), pp. 111–117 (1993).
  76. S. Tan, R. Livengood, P. Hack, R. Hallstein, D. Shima, J. Notte, and S. McVey. "Nanoma-  
chining with a focused neon beam: A preliminary investigation for semiconductor circuit editing and failure analysis". *J. Vac. Sci. Technol. B* **29** (6), p. 06F604 (2011).
  77. F. H. M. Rahman, S. McVey, L. Farkas, J. A. Notte, S. Tan, and R. H. Livengood. "The Prospects of a Subnanometer Focused Neon Ion Beam". *Scanning* **34** (2), pp. 129–134 (2012).
  78. B. Freinkman, A. Eletskii, and S. Zaitsev. "A proposed laser source of ions for nanotechnology". *Microelectron. Eng.* **73–74** (New J. Phys.), pp. 139–143 (2004).
  79. S. B. van der Geer, M. P. Reijnders, M. J. de Loos, E. J. D. Vredendregt, P. H. A. Mutsaers, and O. J. Luiten. "Simulated performance of an ultracold ion source". *J. Appl. Phys.* **102** (11), p. 094312 (2007).
  80. J. L. Hanssen, J. J. McClelland, E. A. Dakin, and M. Jacka. "Laser-cooled atoms as a focused ion-beam source". *Phys. Rev. A* **74** (063416) (2006).
  81. B. Knuffman, A. V. Steele, J. Orloff, and J. J. McClelland. "Nanoscale focused ion beam from laser-cooled lithium atoms". *New J. Phys.* **13** (10) (2011).
  82. S. H. W. Wouters, G. ten Haaf, R. P. M. J. W. Notermans, N. Debernardi, P. H. A. Mutsaers, O. J. Luiten, and E. J. D. Vredendregt. "Performance predictions for a laser-intensified thermal beam for use in high-resolution focused-ion-beam instruments". *Phys. Rev. A* **90**, p. 063817 (2014).
  83. G. ten Haaf, S. H. W. Wouters, S. B. van der Geer, E. J. D. Vredendregt, and P. H. A. Mutsaers. "Performance predictions of a focused ion beam from a laser cooled and compressed atomic beam". *J. Appl. Phys.* **116** (24), 244301 (2014).
  84. B. Knuffman, A. V. Steele, and J. J. McClelland. "Cold atomic beam ion source for focused ion beam applications". *J. Appl. Phys.* **114** (4) (2013).
  85. A. N. Zorzos and P. C. Lozano. "The use of ionic liquid ion sources in focused ion beam applications". *J. Vac. Sci. Technol. B* **26** (6), pp. 2097–2102 (2008).
  86. D. S. Jun, V. G. Kutchoukov, and P. Kruit. "Ion beams in SEM: An experiment towards a high brightness low energy spread electron impact gas ion source". *J. Vac. Sci. Technol. B* **29** (6), p. 06F603 (2011).
  87. V. Tondare. Towards a High Brightness, Monochromatic Electron Impact Gas Ion Source. Ph.D. thesis, Delft University of Technology. [repository.tudelft.nl](http://repository.tudelft.nl) (2006).
  88. D. Jun. Development of the nano-aperture ion source (NAIS). Ph.D. thesis, Delft Uni-

- versity of Technology. repository.tudelft.nl (2014).
89. D. Langmuir. "Theoretical limitations of cathode-ray tubes". *Proc. Inst. Radio Eng.* **2** (8), pp. 977–991 (1937).
  90. R. Rejoub, B. G. Lindsay, and R. F. Stebbings. "Determination of the absolute partial and total cross sections for electron-impact ionization of the rare gases". *Phys. Rev. A* **65**, p. 042713 (2002).
  91. B. Schram, F. de Heer, M. van der Wiel, and J. Kistemaker. "Ionization cross sections for electrons (0.6 - 20 keV) in noble and diatomic gases". *Physica* **31**, pp. 94–112 (1965).
  92. A. A. Sorokin, L. A. Shmaenok, S. V. Bobashev, B. Mobus, M. Richter, and G. Ulm. "Measurements of electron-impact ionization cross sections of argon, krypton, and xenon by comparison with photoionization". *Phys. Rev. A* **61**, p. 022723 (2000).
  93. P. Kruit, M. Bezuijzen, and J. E. Barth. "Source brightness and useful beam current of carbon nanotubes and other very small emitters". *J. Appl. Phys.* **99**, p. 024315 (2006).
  94. A. Bogner, P.-H. Jouneau, G. Thollet, D. Basset, and C. Gauthier. "A history of scanning electron microscopy developments: Towards wet-STEM imaging". *Micron* **38** (4), pp. 390–401 (2007).
  95. J. Orloff. *Handbook of Charged Particle Optics* (CRC Press, 1997).
  96. P. Hawkes. *Magnetic Electron Lenses* (Springer-Verlag Berlin Heidelberg, 1982). Chapter: Practical Lens Design, Author: W. D. Riecke, p. 178.
  97. J. Orloff. *Handbook of Charged Particle Optics*, Second Edition (CRC Press, 2009). Chapter: Space Charge and Statistical Coulomb effects, authors: P. Kruit and G.H. Jansen.
  98. G.H. Jansen. *Coulomb interactions in particle beams*. Ph.D. thesis, Delft University of technology (1988).
  99. X. Jiang and P. Kruit. "Comparison between different imaging modes in focussed ion beam instruments". *Microelectronic Engineering* **30** (1–4), pp. 249–252 (1996).
  100. A. Bondi. "van der Waals Volumes and Radii". *J. Phys. Chem.* **68** (3), pp. 441–451 (1964).
  101. D. Jun, V. Kutchoukov, C. Heerkens, and P. Kruit. "Design and fabrication of a miniaturized gas ionization chamber for production of high quality ion beams". *Microelectron. Eng.* **97**, pp. 134–137 (2012).
  102. J. Creemer, F. Santagata, B. Morana, L. Mele, T. Alan, E. Iervolino, G. Pandraud, and P. Sarro. An all-in-one nanoreactor for high-resolution microscopy on nanomaterials at high pressures, pp. 1103–1106 (2011).
  103. G. Rademaker. *Fabrication and analysis of a freestanding nanofluidic channel*. Master's thesis, Delft University of Technology - Charged Particle Optics group (2014).

## List of symbols

$d$	probe size	m	$C_{sg}$	gun lens spher. aberr. coeff.	m
$d_g$	geometrical probe contribution	m	$C_{cg}$	gun lens chrom. aberr. coeff.	m
$d_a$	diffraction probe contr.	m	$C_{s,m}$	magnetic lens spher. aberr. coeff.	m
$d_s$	spherical aberr. probe contr.	m	$C_{s,e}$	electrost. lens spher. aberr. coeff.	m
$d_c$	chromatic aberr probe contr.	m	$C_{c,m}$	magnetic lens chrom. aberr. coeff.	m
$d_v$	virtual source size	m	$C_{c,e}$	electrost. lens chrom. aberr. coeff.	m
$\lambda$	wavelength	m	$n$	neutral particle density	$m^{-3}$
$\alpha$	half beam angle	rad	$J$	ion current density	$Am^{-2}$
$\Delta\Phi$	energy spread	V	$J_{scat}$	scattered ion current density	$Am^{-2}$
$\Delta\epsilon$	energy spread	eV	$J_{gen}$	generated ion current density	$Am^{-2}$
$\Phi$	ion landing energy	V	$J_e$	electron current density	$Am^{-2}$
$M$	magnification		$\sigma_+$	ionization cross section	$m^2$
$I$	ion beam current	A	$\sigma_{i-n}$	ion-neutral cross section	$m^2$
$B_r$	reduced brightness	$A/m^2srV$	$\eta_I^+$	unscattered ionization efficiency	%
$J_{\Omega 0}$	angular current dens. gun lens	$Asr^{-1}$	$V$	lens voltage	V
$\Phi_0$	beam voltage gun lens	V	$V^*$	lens voltage reference	V
$C_s$	spherical aberration coeff.	m			
$C_c$	chromatic aberration coeff.	m			



# 2

## Nano-fluidic flow

*"No one trusts a model except the man who wrote it;  
everyone trusts an observation, except the man who made it."*

HARLOW SHAPLEY

## 2.1. Introduction

Essential to the nano-aperture ion source concept is the delivery of gas to the electron beam irradiated area. The local particle density at the ion-producing region is critical for the performance of the NAIS. At the same time, this is not a directly controllable nor easily measurable quantity. Therefore, adequate analysis of the nano-fluidic flow properties is needed.

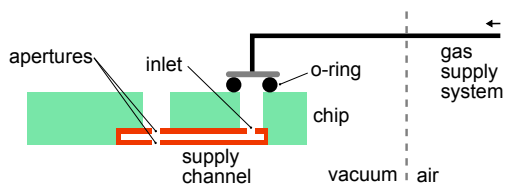


**Figure 2.1.** A possible implementation of the fluidic supply chain for the nano-aperture ion source using an o-ring. The required transition from macroscopic tubing to the sub-micron double aperture configuration makes a nano-fluidic channel seem inevitable.

With the present ideas on chip design, it is required to have a relatively long supply channel (mm's) to connect between the macroscopic tubing and the nano-scale aperture membrane construction. This has practical, mostly geometrical reasons, such as an o-ring not blocking the ebeam and tubing that shouldn't interfere with the extraction field. Even though alternatives such as gluing in stead of an O-ring are possible, a relatively long supply channel seems a part of many solutions. Figure 2.1 shows a general overview of the system. Despite the difficulty of controlling the local particle density near the aperture directly, we can accurately set the inlet pressure of this supply channel with ease. The main question addressed in this chapter is the following: when a certain pressure at the channel inlet is applied, how does that translate to the local pressure?

A very concrete motivation for this fluidic endeavor was a surprising experimental result. In the setup described in chapter 6, a set of measurements of the emission current came out rather low. A membrane spacing of 200 nm and aperture diameters between 100 and 500 nm, supplied with 1 bar of inlet pressure, led to measured currents below 15 pA. We expected at the very least more than 100 pA. One hypothesis was that the local pressure near the apertures was much lower than the pressure at the inlet. The methods in this chapter aim at confirming or disproving the hypothesis that a significant pressure drop across the channel can occur.

Some secondary objectives relating to flow properties can be identified as well. The flow rate into the vacuum is important for designing the vacuum system. Pump-down speed indicates how quickly one can exchange gas and what purity can be reached. Furthermore, the required inlet pressure and required mass flow rate enables proper design of the macroscopic part of the gas supply system.

## 2.2. Flow model

Three aspects of flow can be identified in our system. The first is the outflow through the double aperture structure. It is characterized by a rapid decrease in density, typically from atmospheric pressures into vacuum across a length of only 100 to 500

nm. Secondly, we identify the region near the apertures inside the channel, where we have rotationally symmetric flow. Thirdly, the flow through the supply channel is identified, characterized by a relatively weak density gradient in one direction over a long distance. By mass conservation, the flow through the channel is constant and determined by the outflow through the apertures. Figure 2.2 shows the geometry of the studied flow system.

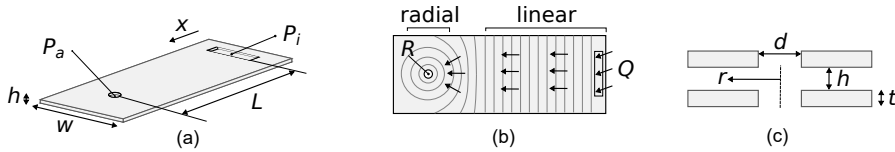


**Figure 2.2.** The nano-fluidic channel for the NAIS in its most obvious form is a narrow and long double membrane structure with a double aperture. a) 3D view of the channel. b) Top view of the channel with an indication of isobaric lines. A radially symmetric and a linear regime are identified. c) Cross sectional view of the double aperture structure.

From an optical perspective, the membranes need only to be narrowly spaced close to the double apertures, but for ease of fabrication it is most obvious to maintain this dimension throughout the channel. Therefore, a constant channel height is assumed in the presented model.

This section develops an analytical model in which only the peak pressure near the apertures and the mass flow rate are ultimately considered. We do not investigate the particle density distribution of the complete system in detail. A more comprehensive approach could be based on direct simulation Monte Carlo (DSMC). For long channels [1] and apertures [2, 3] such simulations can be found in the literature, however the combination in one simulation might be difficult due to the large difference in scale. In addition, DSMC simulations are notoriously time consuming, so a fast and wide parameter exploration is not easy.

Specifically for the NAIS, Jun [4] looked at the neutral particle density distribution around the double aperture structure based on the molecular flow assumption. Rademaker, confirmed that for at least one common geometry the molecular flow simplification is applicable [5]. In section 4.6 the local neutral particle distribution is discussed in more depth.

### 2.2.1. Dimensionless numbers and flow conductance

Before discussing the transport equations for the configuration in question, we introduce some essential concepts in fluid dynamics and use them to determine the appropriate flow regime.

Dimensionless numbers are often used to characterize a fluidic system. The three most relevant numbers for the NAIS are the Knudsen, Reynolds and Mach number:

$$\text{Kn} = \frac{\lambda}{l}, \quad \text{Re} = \frac{\rho v l}{\mu}, \quad \text{Ma} = \frac{v}{v_s} \quad (2.1)$$



The Knudsen number indicates the ratio of particle-wall to particle-particle interaction, the Reynolds is a measure for the amount of turbulence and the Mach number is an average flow velocity normalization. Figure 2.3 indicates the flow type corresponding to the values of these numbers.

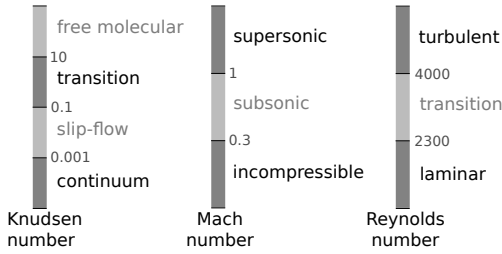


**Figure 2.3.** Three dimensionless numbers that are relevant for indicating the type of flow. For Knudsen [6] and Mach the scales are rather universal, for Reynolds the scale is more geometry dependent and this scale relates to flow through a pipe [7]. Incompressible refers to very small gradients along the flow direction rather than static compressibility.

A slight problem with the Knudsen number is that the mean free path is not a directly measurable quantity. We follow Sharipov [8] in writing the mean free path in terms of the viscosity, molecular mass, pressure, and temperature. Furthermore we express the speed of sound in terms of the molecular properties [9] and obtain:

$$\lambda = \frac{\sqrt{\pi}\mu}{2P} \sqrt{\frac{2kT}{m}}, \quad v_s = \sqrt{\gamma \frac{kT}{m}}. \quad (2.2)$$

For single atom gasses, the specific heat ratio  $\gamma = \frac{5}{3}$ . A convenient relation between Knudsen, Mach and Reynolds [6] is

$$\text{Kn} = \sqrt{\frac{\pi\gamma}{2}} \frac{\text{Ma}}{\text{Re}}. \quad (2.3)$$

We intend to operate the NAIS such that the mean free path of the ions is close to or a little shorter than the membrane spacing, as explained in the introductory chapter. The mean free path of ions is slightly shorter than for neutrals (see chapter 4 for an extensive analysis), so we may roughly say that the operation regime of the NAIS is characterized by  $\text{Kn} \approx 1$ . This is only a rough indication and in addition we would like to be able to tune the pressure, so we state that the Knudsen range for the NAIS is 0.1 to 10. In figure 2.3 we can see that this range is called the transition regime. This means that molecular and continuum effects are both relevant and flow analysis is not trivial.

The Mach number is best first examined at the outflow through the apertures. Consider the aperture to be an orifice, i.e. a zero thickness membrane. Continuum outflow into vacuum is said to be choked [10, 11], meaning that a maximum flow speed is attained and (small) changes in the downstream pressure are irrelevant. In fact, for constant cross section tubes the maximum Mach number is simply one [10]. In the case of free molecular flow into vacuum, the Mach number is close to or smaller than one. Since the channel cross section will always be orders of magnitude larger than the aperture cross section, and the Mach number through

the aperture is in any case close to one, we can state that the Mach number in the channel is close to zero and incompressible flow conditions apply.

We can use equation 2.3 to estimate the maximum Reynolds number occurring in our system. If we set  $Ma = 1$  and  $Kn = 0.1$  for a worst case estimate, we obtain  $Re \leq 17$ . This is in fact an overestimate because at the position where  $Ma = 1$ , the local Knudsen number is higher due to a density decrease. We conclude that turbulence effects do not play a role in our system. Surely this was to be expected for such small dimensions. In the linear region of the channel  $Re \ll 1$ .

In the high Knudsen regime ( $Kn > 10$ ), it is customary to work with the flow conductance  $C$  and a gas flow rate  $Q$ , or a mass flow rate  $\dot{M}$ . The transport equations are

$$\frac{d(PV)}{dt} = Q = -C\Delta P, \quad \dot{M} = -\frac{m}{kT}C\Delta P, \quad (2.4)$$

These expressions can easily be derived from Fick's law if the gas is assumed to be ideal. An expression for the conductance of an arbitrarily shaped open area  $A$  in an infinitely thin membrane is [12]

$$C_0 = \frac{1}{4}A\langle v \rangle, \quad \langle v \rangle = \sqrt{\frac{8kT}{\pi m}}. \quad (2.5)$$

To account for the non-zero length of a channel, the concept of a transmission probability  $\alpha$  is introduced [13, 14]. The flow conductance of the entrance (equation 2.5) is multiplied by the probability of a molecule that enters the channel making it out to the other side of the channel:

$$C = \alpha C_0 \quad (2.6)$$

It can be convenient to relate a transmission probability or a flow conductance to a diffusion coefficient as follows:

$$D = C \frac{L}{A} = \frac{1}{4}\alpha L\langle v \rangle. \quad (2.7)$$

Note that this simple expression is only valid in the case of constant cross section channels because the diffusion coefficient is a local property while the flow conductance is an average quantity for the full channel.

### 2.2.2. Flow conductance of apertures

The simplest and most familiar aspect of the flow system is the outflow through the apertures. In the case of short ducts, Dushman [15] proposed a simple expression that is often found in vacuum technology handbooks [12]. It gives a maximum error of 11 % [16]. A slightly more advanced expression suggested by Henning [16] gives errors less than 0.6 % on the domain  $t/d = (0.01, 19)$ . We choose Henning's expression as its applicable range and accuracy is excellent, while being fairly simple. Further discussion on the various alternatives can be found elsewhere

[13, 17]. We get for the free molecular flow conductance  $C_{\text{fm}}$  of a short duct

$$C_{\text{fm}} = \alpha C_0, \quad \alpha = \frac{1}{0.996 + 0.94 \left(\frac{L}{d}\right)^{0.94}}. \quad (2.8)$$

2

An often encountered expression for continuum flow through an orifice derived from the Euler equation is [9, 11]

$$C_{\text{is}} = \sqrt{\gamma} \left( \frac{2}{\gamma + 1} \right)^{\frac{\gamma+1}{2(\gamma-1)}} \sqrt{2\pi} C_0. \quad (2.9)$$

Since for single atom gasses  $\gamma = \frac{5}{3}$ , and we can simplify to  $C_v = 1.82C_0$ . Interestingly, it differs from free molecular flow only by a numerical factor. This expression is based on isentropic flow, requiring  $\text{Re} \gg 1$  [9], which is not quite met in our case and the results may be doubtful. Furthermore, it does not incorporate the non-zero membrane thickness.

Equation 2.8 and 2.9 give values for the limiting cases of free molecular flow and continuum flow. However, we would like to have a more generally valid expression. An alternative suiting our needs very well was proposed by Fujimoto and Usami [18]. They devised an interpolation equation that works over a wide range of Knudsen values (see also refs. [9, 19, 20]). In addition, it interpolates over duct aspect ratio. If  $\text{Kn} > 0.00025$  and  $\text{Re} < 2800$  their empirical formula for the flow conductance of short ducts  $C_F$  ('F' denotes Fujimoto) is

$$\frac{C_F}{C_0} = \left( \alpha + \frac{0.4733 + 0.907z^{0.5}}{1 + 10.4z + 16.1z^2} \right), \quad (2.10)$$

with

$$z = \text{Kn} \cdot \left( \alpha + 0.125 \exp[-0.5(12\alpha - 11.2)^2] + 0.18 \exp[-14.7\alpha] - 0.08 \right)^{-1}. \quad (2.11)$$

Although it may not be very elegant, it is highly practical. The tested domain of tube length over tube diameter is 0.00025 up to 12.7, quite broad indeed. The precision of this interpolation is more than required and surely a more simple interpolation scheme could be used. We may even get a false sense of accuracy because this model assumes flow out of a large vessel, while we start from a restricted channel and double aperture configuration. Next to that, it will be very difficult to precisely know the critical dimensions. With this in mind, it is the closest model that is readily available; not correcting for tube length and viscous flow effects would give an even worse inaccuracy.

$d$ nm	$t$ nm	$C_0$ $\text{m}^3 \text{s}^{-1}$	$C_{\text{fm}}/C_0$	$C_{\text{is}}/C_0$	$C_F/C_0$		
					Kn = 0.1	Kn = 1	Kn = 10
100	0	$2.45 \times 10^{-12}$	1.00	1.82	1.35	1.06	1.01
100	100	$2.45 \times 10^{-12}$	0.52	1.82	0.73	0.53	0.52
300	100	$2.20 \times 10^{-11}$	0.75	1.82	1.04	0.78	0.75
1000	100	$2.45 \times 10^{-10}$	0.91	1.82	1.24	0.95	0.91

**Table 2.1.** The flow conductance for a short tube as predicted by different models for a few typical geometries.  $C_0$  denotes the free molecular conductance of zero-thickness orifices (equation 2.5),  $C_{\text{fm}}$  is the free molecular conductance of a short tube (equation 2.8) and  $C_{\text{is}}$  is the isentropic flow conductance (equation 2.9). The empirical formula by Fujimoto and Usami's  $C_F$  (equation 2.10) has negligible error compared to their experimental values for  $\text{Kn} > 0.1$  [18]. For  $\text{Kn} < 0.1$  the error may be up to 5 % [9] compared to experimental data on mono-atomic gases by Jitschin [21]. All calculations assume a single aperture in combination with a large vessel.

Some examples of calculated flow conductances are given in table 2.1. Interestingly, the values acquired from the empirical formula of Fujimoto are never more than a factor two different from  $C_0$ . This means that despite operating in the transition regime, decent estimates can be made by just using the free molecular flow conductance. This strokes with findings by Sharipov [19], who concluded that for orifices, the flow conductance is at most 1.5 times the molecular flow conductance.

We are working towards a model for the full flow characteristics of the NAIS, however we can already analyze the aspect of vacuum load due to aperture outflow. If for example  $d = 100 \text{ nm}$ ,  $t = 100 \text{ nm}$ , and  $\text{Kn} = 1$ , equation 2.10 gives:  $C = 1.3 \times 10^{-12} \text{ m}^3 \text{s}^{-1}$  yielding a total vacuum load of  $Q = 2.5 \times 10^{-7} \text{ Pa m}^3 \text{s}^{-1}$ . Suppose we would like to acquire a Schottky-emitter-friendly vacuum of  $1 \times 10^{-7} \text{ Pa}$ , then we need a pumping speed of  $2.5 \text{ m}^3 \text{s}^{-1}$  to cope with the outflow load. This is a near-impossible requirement. A typically used small ion-getter pump delivers a mere  $0.025 \text{ m}^3 \text{s}^{-1}$ , not even considering the low efficiency for noble gases. Even a high end turbo-molecular-pump can only reach  $1.0 \text{ m}^3 \text{s}^{-1}$ . Additionally, this example considers just one, quite small, aperture. We conclude that in the chip region we should settle for a more modest pressure of say  $1 \times 10^{-4} \text{ Pa}$ , hence a Schottky electron gun can never reside in the same vacuum.

### 2.2.3. Flow through shallow channels

The flow through a long rectangular channel is considered in this section. One may suspect that a relatively wide channel of say,  $100 \text{ }\mu\text{m}$  in width, will have negligible flow restriction compared to a  $100 \text{ nm}$  sized aperture. If we assume free molecular flow for the moment, we can use the transmission probability of a long narrow slit to estimate this. Weissler [22] gives  $\alpha = \left(1 + \frac{3}{8} \frac{(w+h)L}{wh}\right)^{-1}$ . With the requirement  $L \gg w \gg h$ , it is easy to show that  $\alpha \approx \frac{8}{3} \frac{h}{L}$ . We find for a typical channel of  $L \times w \times h = 3000 \times 100 \times 0.1 \text{ }\mu\text{m}$  from equation 2.5 that  $C = 8.2 \times 10^{-13} \text{ m}^3 \text{s}^{-1}$ . We compare this to the flow conductance  $C = 2.5 \times 10^{-12} \text{ m}^3 \text{s}^{-1}$  of a  $100 \text{ nm}$  aperture using equation 2.10. The channel flow conductance is more than 10 times lower, which directly leads to pressure drops of more than a factor 10.

It may even be worse. At  $\text{Kn} \approx 1$ , molecular collisions lower the flow conductance compared to free molecular flow. Furthermore, if a large pressure drop is acquired, the Knudsen number at the inlet is low and diffusion is restricted even further. On the other hand, we are neglecting any advective transport, which may not be appropriate to do. It seems worthwhile to investigate channel flow in more detail.

Colloquially, the term convective transport is often used for advective transport. Formally, convective transport includes diffusion and bulk movement of a fluid, while advective transport refers to bulk movement only. In this analysis the distinction plays an important role and we will use the formal nomenclature.

Literature on the subject of micro channel flow is quite abundant [23] and several models are available, notably one proposed by Livesey [10, 24]. This particular model is quite broad in application as it can account for turbulence and channel entrance effects. For our purpose, this seems to unnecessarily complicate matters. We have also considered a model by Dongari et. al. [25–28], developed specifically for flow in rectangular micro-channels. They introduce a mass diffusivity term in the Navier-Stokes (NS) equation to extend the validity of NS to higher Knudsen numbers. The model is fairly simple in use, but we could not reproduce the claimed excellent agreement when comparing predictions of the model to experimental data by Maurer [29] or Ewart [30].

The method we use is based on adding an advective and a diffusive contribution to acquire the total flow rate. This is equivalent to a method outlined by Thomson and Owens [31]. The advective component needs to be valid up to high Knudsen numbers for which we use a second order slip flow model [29]. We follow Browne and John [32] in multiplying the first order slip flow term in the advective transport equation by  $(1 + \text{Kn})^{-1}$ . This removes the unphysical contribution of viscous flow in the free molecular flow regime. Along the same line of reasoning we multiply the second order term by  $(1 + \text{Kn})^{-2}$ . The diffusive flow contribution needs to interpolate between bulk and free molecular diffusion. The proposed advective and diffusive flow rate contributions are:

$$Q_A = -\frac{wh^3}{12\mu} \left( 1 + 6A_1 \frac{\text{Kn}}{1 + \text{Kn}} + 12A_2 \left( \frac{\text{Kn}}{1 + \text{Kn}} \right)^2 \right) P \frac{dP}{dx} = -f_A(P) \frac{dP}{dx} \quad (2.12)$$

$$Q_D = -wh \left( \frac{D_b D_{\text{fm}}}{D_b + D_{\text{fm}}} \right) \frac{dP}{dx} = -f_D(P) \frac{dP}{dx} \quad (2.13)$$

Note that the Knudsen number as function of the pressure is obtained by using equation 2.2. The constants of the slip-flow model are  $A_1 = 1.2$ ,  $A_2 = 0.23$  for helium [29]. These coefficients depend on the channel wall and gas species, but typically do not vary more than 10%.

The diffusive term is based on a inverse addition of the bulk diffusion coefficient  $D_b$  and the free molecular diffusion coefficient  $D_{\text{fm}}$ . In the limit of high Knudsen numbers, the diffusive contribution converges to a molecular flow expression while for low Knudsen numbers bulk diffusion is obtained. For intermediate Knudsen values the term is an interpolation between bulk and free molecular diffusion. The

bulk diffusion coefficient from kinetic gas theory is  $\frac{1}{3} \langle v \rangle \lambda$ , which in terms of the Knudsen number reads

$$D_b = \frac{1}{3} \langle v \rangle \text{Kn} h. \quad (2.14)$$

For free molecular flow, an expression for the flow conductance of rectangular channels is used [14, 31], which is based on theory by Smoluchowski [33]. By employing equation 2.7 we obtain

$$D_{\text{fm}} = \frac{1}{4} \langle v \rangle \left( h \cdot \ln \left( \frac{w}{h} + \sqrt{1 + \frac{w^2}{h^2}} \right) + w \cdot \ln \left( \frac{h}{w} + \sqrt{1 + \frac{h^2}{w^2}} \right) - \frac{(h^2 + w^2)^{3/2}}{3hw} + \frac{h^3 + w^3}{3hw} \right). \quad (2.15)$$

When using the abbreviating functions  $f_A$  and  $f_D$  in equations 2.12 and 2.13, the transport equation becomes

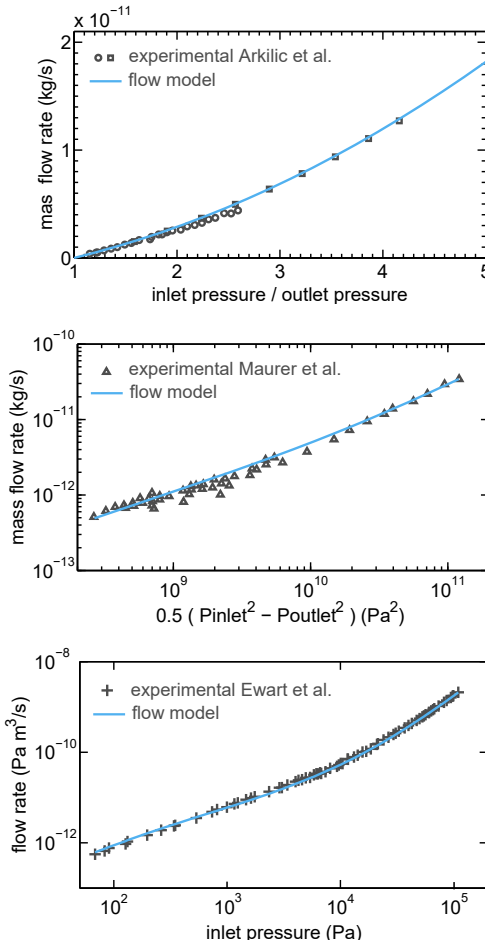
$$Q = - (f_A(P) + f_D(P)) \frac{dP}{dx}. \quad (2.16)$$

For calculating the flow rate we can employ that equation 2.16 is separable and obtain

$$Q = - \frac{1}{L} \int_{P(0)}^{P(L)} (f_A(P) + f_D(P)) dP. \quad (2.17)$$

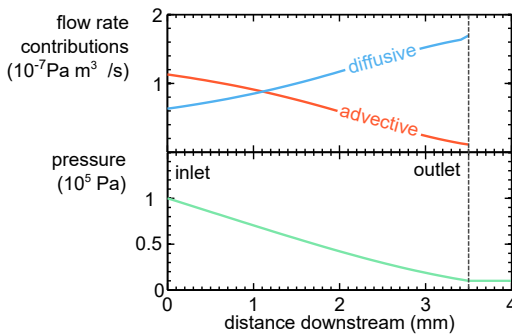
If  $Q$  is known, we can solve equation 2.16 to obtain the pressure profile along the channel for a given upstream or downstream pressure. It is important to realize that the used Knudsen number is a local property in the channel. This means that the relative contributions of advective and diffusive transport can vary along the channel. Very large pressure differences in a channel are therefore acceptable in calculations.

Figure 2.4 shows flow calculations using equation 2.17, compared to experimental data by Maurer, [29], Ewart [30] and Arkilic [34, 35]. These three data sets are acquired in different ways of varying the inlet and the outlet pressure, so the sets offer good diversity for testing the model. The resulting correspondence is about as good as the experimental variation. This is fortunate, given the relative simplicity of the model, notably the somewhat bold interpolation scheme for bulk and free molecular diffusion. Since our model is simple and reproduces experimental data well, it is a good choice for calculating channel flow.



**Figure 2.4.** Comparison of the proposed model using equation 2.17 and experimental data shows excellent agreement. All measurements are performed using helium gas. No free parameter was adjusted to fit the data; the theoretical curves are obtained by directly using the reported channel dimensions and pressure settings. The channel dimensions of data by Arkilic et al. [34, 35] are  $L \times w \times h = 7500 \times 52.25 \times 1.33 \mu\text{m}$ . The outlet pressure was fixed at  $P_{\text{outlet}} = 1 \times 10^5 \text{ Pa}$ . The data by Maurer et al. [29] is obtained from a channel of  $L \times w \times h = 10000 \times 200 \times 1.14 \mu\text{m}$ . The inlet and outlet pressure were varied together linearly in the range  $P_{\text{inlet}} = 0.26 \times 10^5 - 5 \times 10^5 \text{ Pa}$  and  $P_{\text{outlet}} = 0.12 \times 10^5 - 1 \times 10^5 \text{ Pa}$ . Ewart et al. [30] used a channel of  $L \times w \times h = 9390 \times 492 \times 9.38 \mu\text{m}$ . A fixed inlet to outlet pressure ratio of 5 was maintained.

Figure 2.5 shows the calculated flow contributions and the pressure profile of an example channel. In this example, both advective as well as diffusive transport plays a role and their relative importance changes across the channel.



**Figure 2.5.** Flow calculation for a rectangular channel of  $h \times w \times L = 500 \text{ nm} \times 100 \mu\text{m} \times 3.5 \text{ mm}$ , supplied with an inlet pressure  $P = 1 \times 10^5 \text{ Pa}$  and  $P = 1 \times 10^4 \text{ Pa}$  at the outlet. Notice how the diffusive and advective contribution vary along the channel.

Figure 2.6 shows the flow conductance for a variety of inlet pressures, as characterized by the local Knudsen number at the inlet. Since the effects of free molecular flow, molecular diffusion and advective flow are competing as a function of the

Knudsen number, a minimum known as the Knudsen minimum or Knudsen paradox is obtained.

The reasonably shallow region around  $Kn = 1$  results in the free molecular flow assumption yielding a fair order of magnitude estimate, even down to  $Kn \approx 0.1$ . The underlying transport mechanism is not free molecular flow though. For low Knudsen values ( $Kn < 0.1$ ), the advective contribution becomes very large and a free molecular approximation leads to underestimates of the flow conductance. In general, the shape of this curve depends on the pressures and geometry involved, so it is best to rely on equation 2.17 for accurate results.

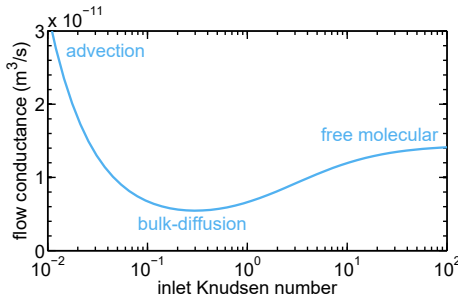


**Figure 2.6.** Flow calculations for a rectangular channel of  $h \times w \times L = 500 \text{ nm} \times 100 \mu\text{m} \times 3.5 \text{ mm}$ , supplied with different pressures at the inlet, and vacuum at the outlet. The Knudsen number varies along the channel and the given number is calculated at the channel entrance. The flow conductance is defined as the flow rate divided by the inlet pressure. The dominant flow mechanisms are indicated in the different regimes.

#### 2.2.4. Radial distribution around the apertures

In the close proximity of the double aperture structure we expect a radially symmetric pressure drop. The range of this radial symmetry is at most the width of the channel, typically some tens of micro meters. This distance is relatively short compared to the channel length of some mm's, however, the channel size decreases when approaching the double apertures, so an appreciable flow resistance may be obtained anyway.

The channel flow model from the previous section can be recycled when appropriately transformed to cylindrical symmetry. Since the model does not consider the sidewall effects, the sidewalls can be considered connected. The substitutions  $w = 2\pi r$  and  $x = r$  in equation 2.12 and 2.13 lead to radial symmetry. The bulk diffusivity is not a geometrical property, so it can be used as is. The molecular flow diffusivity, however, was derived for the rectangular geometry and may not describe the radial symmetry very well. We follow Browne and John [32] and use

$$D_{\text{fm}} = \frac{2}{3} \langle v \rangle h. \quad (2.18)$$

Strictly speaking, this expression is theoretically not completely sound. It is based on Knudsen's method, which is known to be only fully correct for tubes [31]. No improved expression seems to be available and Browne and John [32] showed good correspondence to experimental data.

When using the substitutions  $w = 2\pi r$  and  $x = r$ ,  $f_A$  and  $f_D$  become functions of  $r$ . Equation 2.16 is no longer separable, but can still be solved numerically with relative ease. Figure 2.7 shows the result of the radial pressure drop calculation for a few geometrical configurations. The pressure drop is defined as the pressure at



$r = R = 40 \text{ } \mu\text{m}$ , divided by the pressure at the aperture position. The flow rate is calculated by equation 2.10, and the result has been used to solve equation 2.16 in combination with the aforementioned substitution.

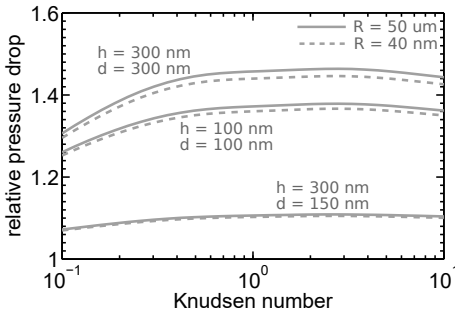


**Figure 2.7.** Calculations in the radial regime show a small relative pressure drop and a weak dependence on the Knudsen number. The relative pressure drop is defined as the pressure 50  $\mu\text{m}$  away from the apertures divided by the pressure between the two apertures. The Knudsen number is defined at the aperture location. The curves for  $R = 40 \text{ } \mu\text{m}$  shows that the result is insensitive to the choice of  $R$ .

From figure 2.7 we conclude that the effect of a radial pressure drop is not negligible. On the other hand, it is not so severe that it poses a fundamental problem. Secondly, we note that the dependence on the Knudsen number is fairly weak.

The dashed lines in the graphs show a different choice for the end of the radial regime of 40  $\mu\text{m}$ . The lines are very close to the 50  $\mu\text{m}$  line, showing that the result is very insensitive to the choice of  $R$ . This is not surprising, far away from the center the channel is relatively large and the contribution to the flow resistance is only minor. This justifies the somewhat arbitrary choice of  $R$ . In all calculations  $\text{Ma} < 0.2$ .

### 2.2.5. Full system analysis

We have discussed the flow along the channel, the radial flow towards the aperture, and the outflow through the aperture. The combination of these gives us the behavior of the full system. The pressure between the apertures  $P_a$  is the independent variable, as it is the pressure we need to tune for NAIS operation. The dependent variable is the inlet pressure, as it is the pressure we will need to apply in an experiment.

For a given geometry and required aperture pressure, we can calculate the mass flow through the entire system using equation 2.4 and 2.10. The aperture pressure is the boundary condition for equation 2.16 in the radial regime. The resulting pressure at  $R$  serves as the boundary condition for the calculation of equation 2.16 in the linear regime. It was shown in figure 2.7 that the end of the radial regime is not very important and we choose for  $R$  half the width of the channel ( $R = 50 \text{ } \mu\text{m}$ ). The channel length is specified as the distance between the inlet and the aperture center.

Figure 2.8 shows the calculation result for the typical NAIS nano-fluidic channel. It is not obvious from an ion optical point of view what the ideal channel height and aperture diameter should be, so a variety of configurations is shown in one plot. We consider a fixed Knudsen number of  $\text{Kn}=1$ . It is not possible to simply scale these curves, so for other values of the Knudsen number a new calculation is required.

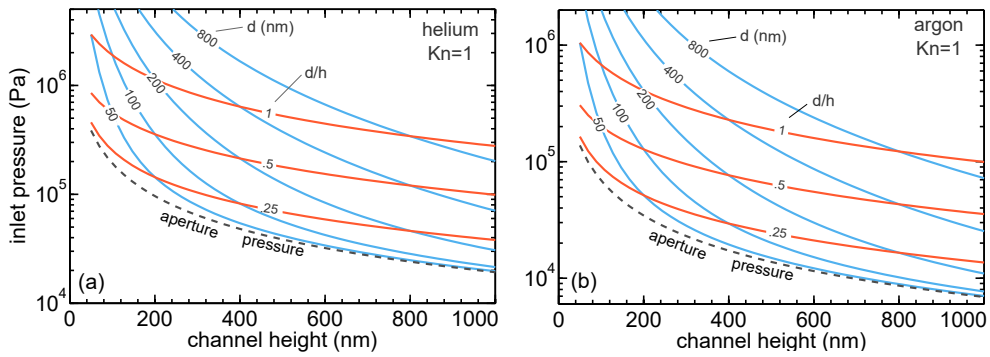


**Figure 2.8.** Calculated required inlet pressure for achieving an aperture pressure such that  $Kn = 1$  at the aperture location. The calculation incorporates the outflow through two apertures, the drop in the radial regime, and the drop in the linear regime. The dashed line indicates the aperture pressure determined by the height and  $Kn = 1$ . The fixed channel dimensions used are  $L = 3.5$  mm and  $w = 100$   $\mu$ m.

Perhaps most striking in figure 2.8 is the large pressure drop for various configurations. Without the proper remedies or a least awareness of the pressure loss, we can expect poor performance. More specifically, consider a channel of 100 nm high and 100 nm aperture. This configuration requires more than ten bar of pressure at the inlet. This is undesirable as it poses high requirements on the channel integrity.

The largest factor of this big pressure drop is the linear regime of the channel. Widening the channel is one way to improve and does not influence the ion optical properties, but we may need a very wide channel to achieve sufficiently low inlet pressures. A disadvantage of wide channels is the large membrane surface, which makes the chips more prone to membrane failure. Decreasing the channel length is always advantageous, but may not be possible due to practical limitations. A very effective way of lowering the pressure drop is increasing the channel height, but the ion optical consequences need to be considered.

### 2.3. Flow experiments

A set of flow experiments are performed with the intention of testing the applicability of the models to the NAIS situation. It is out of the scope of these experiments to seek for an accurate confirmation of the presented flow models. The aperture flow conductance model by Fujimoto and Usami [18] is compared to various experimental results already. A comparison of the linear channel flow model to experimental data from other researchers is given in section 2.2.3.

Some differences between the ideal channels used for the calculations and the channels we encounter in the experiment can be identified beforehand. The channels we use comprise membrane supporting pillars, can have bowing of the membrane, and may suffer from an irregular surface. The apertures we use are not always perfectly round and are very small compared to the sizes commonly encountered in conductance experiments. We intend to identify if the deviation from the modeled situation leads to appreciable differences in estimated properties.

We use a rather simple setup, involving a standard leak testing device. More accurate setups are certainly possible, but this is so simple, that it allows rapid set-up of an experiment. Quickly testing the flow properties of a potential chip becomes possible. It has been proven very useful to simply check whether a certain channel gives any flow at all, and if it does, if the value is in right ballpark. One may quickly find out if a channel is clogged, or perhaps much larger than specified due to fabrication errors. So, besides trying to test modeling, the experiments described here are also intended to show how one can quickly debug NAIS chips by looking at the flow characteristics.

### 2.3.1. Experimental setup

A setup for measuring a helium flow rate through the nano-fluidic system is shown in figure 2.9. We use a leak detector (Adixen ASM graph D) to measure the helium flow rate. The nano-fluidic device is encapsulated in an o-ring sealed housing such that the nano-fluidic channel is the only connection between the helium supply and the leak detector.

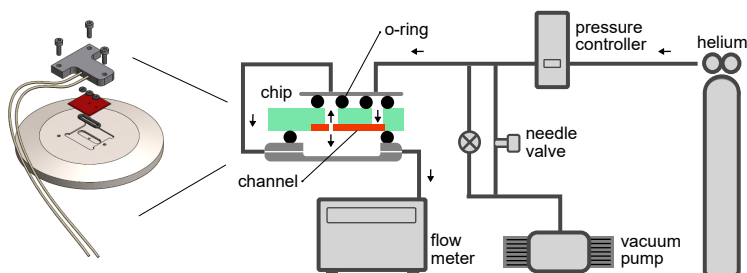


**Figure 2.9.** A nano-fluidic NAIS chip is encapsulated such that all supplied helium that is transported through the channel is detected by a flow rate leak tester.

We have performed two types of measurements. One experiment considered only flow through a channel. Both the entrance and the exit of the channel have large openings such that the channel is the only flow restriction element. One large channel is fabricated by gluing two wafers together. The length, width and height of this channel are: 3.3 mm x 200  $\mu$ m x 7.4  $\mu$ m. Two other channels are fabricated by micro-fabrication techniques as described by Rademaker [5]. The target dimensions are 3.3 mm x 116  $\mu$ m x 300 nm and 3.3 mm x 116  $\mu$ m x 100 nm.

A second experiment considers only aperture outflow. For this purpose, a set of a 50 nm thick  $\text{Si}_3\text{N}_4$  membranes were suspended on top of a relatively large channel (mm scale). In this configuration, only the aperture is restricting the flow. The target diameters were 100, 100, 150, 300 and 1000 nm.

A standard rotary pump could pre-evacuate the system down to 50 Pa at the inlet. A few cycles of helium flushing ensured only helium to be responsible for the flow. For adjusting and measuring the pressure during the channel flow experiments, we used a flow controller (Bronkhorst EL-PRESS IP-40), which yields pressure accuracies better than 100 Pa. When performing the aperture outflow experiments, an equally accurate capacitive pressure gauge was used. At pressures

above 1 bar, we were forced to rely on the manometer of the helium cylinder though. These are highly inaccurate, so to improve on this, a calibration using the capacitive gauge at  $1 \times 10^5$  Pa was employed. Still we estimate the error to be about 10%.

### 2.3.2. Channel flow

The results for channel flow measurement are shown in figure 2.10, together with the theoretical model discussed earlier in this chapter. The measured data of the medium sized chip with a target channel height of 300 nm was more accurately described by the model when using a 230 nm in the calculation. The shape of the curve could not accurately be modeled. The differences may be attributed to model-deviating geometry from pillars, irregular membrane surface, and possible membrane bowing.

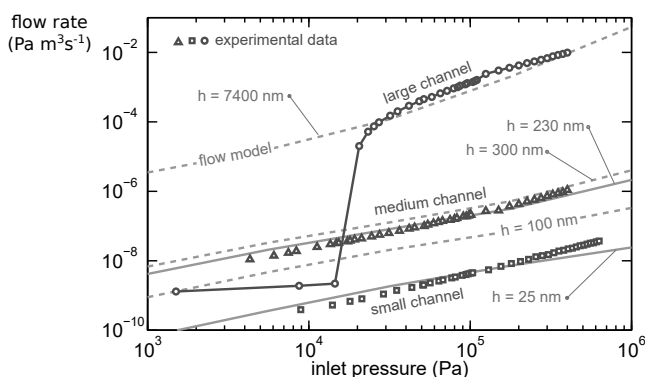


**Figure 2.10.** Measured flow through nano-fluidic channels. The theoretical flow model is plotted along for a few channel heights.

The small chip with specified height 100 nm fitted very poorly, and using 25 nm for the height gave a more reasonable correspondence. It was decided to investigate the geometry of this channel in more detail. Figure 2.11 shows some SEM images of cross sections of such a channel. A height measurement yielded,  $88 \pm 5$  nm, which is slightly smaller than 100 nm indeed, but doesn't explain the big discrepancy between the model and the experimental data. In figure 2.11c we see a region of the membrane that was sagged. Clearly this would restrict flow severely. In addition, we are not sure if the etching process was completely successful in delivering smooth membrane surfaces. In fact, residual material between the membranes is a known issue in the fabrication of these chips. It is not known what fraction of the channel was affected by sagging or other irregularities and we can only conclude that the flow is diminished to some extent. In any case the difference between 25 nm and 100 nm was enough to raise suspicion and closer inspection did indeed show evidence for geometrical flow restrictions.

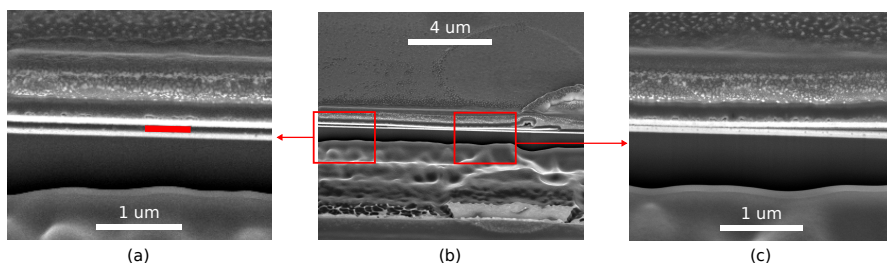


**Figure 2.11.** SEM images (52° tilt angle) of focused ion beam cross sections of a nano-fluidic channel. The imaged chip stems from the same wafer from which the smallest channel measurement are made with. The specified height was 100 nm but the measured value is  $88 \pm 5$  nm. a) Zoom of a region where the height is measured, the red rectangle indicates what is considered the channel height. b) Overview image, showing on the right hand side part of a membrane supporting pillar. c) Zoom of a region where the membrane is sagged.

The measurement of the largest channel is very peculiar. For pressures above  $2 \times 10^4$  Pa the model is inaccurate in following the exact trend of the data, but does give the right order of magnitude. For lower pressures, the flow drops to values even below the medium sized channel. No flow mechanism of a fixed geometry can be identified for such an effect. It looks like pressure induced bulging of the channel. This channel did indeed have no pillars and bulging is known to be a relevant effect [36] for free standing membranes. This chip was, however, missing the free standing membrane and only consisted of a channel produced by gluing two wafer-thick chips together. Peculiar as well, is the rather discrete manifestation of the flow increase. This hints at some geometrical confinement that under a certain pressure suddenly gets resolved. The effect was reproducible when increasing and decreasing the pressure back and forth. A definitive explanation remains absent.

### 2.3.3. Channel evacuation time scale

We have learned from the model and the experiments that a narrow channel can act as a considerable flow restriction. This may leave the suspicion that pumping down and refilling the channel is a challenge. This is fortunately not the case. We use the smallest channel to demonstrate this. After setting the inlet pressure at  $2 \times 10^5$  Pa, we suddenly open a valve such that the supply of helium is removed in less than 0.5 s. This leaves the situation of helium filled channel that is open to evacuated regions on the two ends of the channel. Figure 2.12 shows the flow rate as a function of time for this measurement.

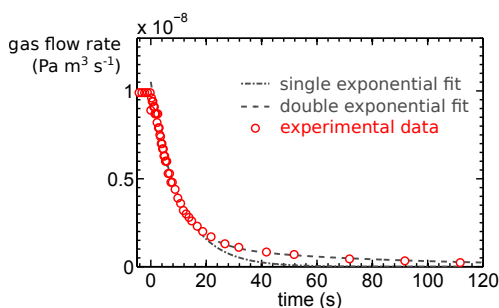


**Figure 2.12.** Starting from a steady-state flow situation with  $2 \times 10^5$  Pa inlet pressure, a valve is opened such that the supply side is rapidly evacuated. The channel target dimensions are: 3.3 mm x 117 μm x 100 nm and the acquired time constant is  $\tau = 8.2 \pm 1.0$  s.

A single exponential did not seem to fit very well, while a double exponential did. Apparently, two decaying processes are relevant. The slowest ( $\tau \approx 68$  s) and weakest process, is considered an artifact; possibly degassing of the vacuum wall. The faster process with time constant  $\tau = 8.2 \pm 1.0$  s, is associated with pumping down the channel. We can already conclude that pumping down the channel and supplying it with another gas with say a 0.1% purity is a matter of minutes for this very narrow channel. Note that most channels are higher, so we can expect a complete gas switch cycle of under a minute.

### 2.3.4. Aperture flow

Experimental results for helium flow out of nano-scale apertures are shown in figure 2.13. The model of equation 2.10 has been fitted using the known membrane thickness  $t = 50 \times 10^{-9}$  nm and room temperature  $T = 293$  K. From these fits, aperture diameters are obtained as listed in table 2.2. A free molecular flow model is plotted as well, which uses the acquired diameters as input. The fit quality can be considered decent, although aperture d in particular clearly has some non-linearity in the curve that is not explained by the model.

aperture	SEM inspection	flow model fit	
a	$1141 \pm 10$	$1516 \pm 15$	nm
b	$301 \pm 5$	$351 \pm 1$	nm
c	$110 \pm 5$	$108 \pm 1$	nm
d	$85 \pm 5$	$90 \pm 1$	nm

**Table 2.2.** Comparison of the obtained aperture diameters. The SEM images are fitted with a circle and the error is based on the inaccuracy of determining the aperture edge in the image. The flow data is fitted with equation 2.10.

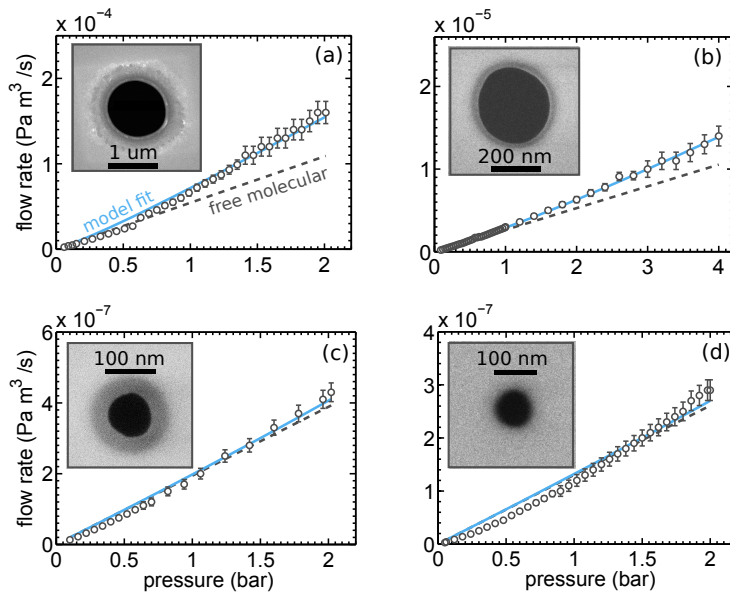


**Figure 2.13.** Experimental results of nano-aperture outflow combined with model fits by equation 2.10 and SEM images of the apertures. The figure labels correspond to the labels in table 2.2

More problematic is the discrepancy between the SEM inspection diameters and the model fit results. While the smaller aperture diameter results correspond

rather well, for the largest aperture a 50% discrepancy is obtained. Any leak can cause a too high flow measurement, but this should be more present in the smaller flow configurations, exactly opposite to what is found. This argument holds for any consistent absolute error. Any effect that is associated with the apertures being of nano-scale would also be more pronounced for the smallest apertures. One possible explanation is an inaccuracy in the flow measurement. A calibration procedure was run with a built-in calibrated leak at  $Q = 1 \times 10^{-8} \text{ Pa m}^3 \text{ s}^{-1}$ . This value is relatively close to the typical flows measured with the smaller apertures. The larger apertures are orders of magnitude away from this calibration and maybe the flow measurement becomes inaccurate. We have not pursued any further examination of the observed discrepancy. Despite the inaccuracy, the flow measurements do offer a quick indication of the aperture diameter.

## 2.4. Conclusion

A relatively simple model of gas flow for the NAIS nano-fluidic configuration was established. Good correspondence to experimental data of other researchers validates the presented method for calculating flow through a rectangular nano-channel. The flow is governed by an advective and a diffusive component and the relative contributions depends strongly on the Knudsen number.

Employing the model, we found a significant pressure drop between the inlet of the channel and near the double aperture structure for the typical dimensions and pressures we are aiming to operate the NAIS with. The main cause is the poor flow conductance of the relatively long nano-fluidic channel. The pressure drop locally around the aperture is also significant but less severe.

For ion-optical reasons a particular aperture size is chosen and preferably the channel is designed in accordance with this aperture. Simply choosing a large height is very effective in reducing the pressure drop, but if the height is constant across the entire device this influences the ion-optical properties as well. Widening or shortening the channel reduces the pressure drop too, though less effectively than increasing the channel height and has other practical disadvantages. An alternative channel design is a deep channel of say tens of microns, that is only confined very close to the aperture, if fabrication permits.

Figure 2.8 shows the required inlet pressure for achieving  $\text{Kn}=1$  at the aperture. The figure reveals how serious the pressure drop can be in many configurations. An illustrative example is a 100 nm channel in combination with a 100 nm aperture diameter for argon. In this situation the pressure at the aperture needs to be  $1.9 \times 10^5 \text{ Pa}$ . In order to achieve that, a  $1.9 \times 10^6 \text{ Pa}$  inlet pressure is required. A 300 nm channel height in combination with a 100 nm aperture only requires  $1.4 \times 10^5 \text{ Pa}$  at the inlet. If the aperture to channel height ratio needs to be fixed and larger than 0.5, a pressure drop of at least 3 times is unavoidable.

Simple flow experiments with a few different channels and nano-apertures were conducted. The experiments did only roughly agree to the computations. We should therefore acknowledge that the correspondence is not good enough



to deliver accurate predictions of the pressure drop ratio for a given geometry. On the other hand, the agreement is sufficient to have demonstrated that such measurements can serve as a manner of testing NAIS chips. If the flow conductance is very different from the calculation, one may have leaks or a clogged channel. It may serve as an initial chip quality control method, or aid as a diagnostic tool for further chip development.

## References

1. S. Varoutis, S. Naris, V. Hauer, C. Day, and D. Valougeorgis. "Computational and experimental study of gas flows through long channels of various cross sections in the whole range of the Knudsen number". *J. Vac. Sci. Technol. A* **27** (1), pp. 89–100 (2009).
2. S. Varoutis, D. Valougeorgis, O. Sazhin, and F. Sharipov. "Rarefied gas flow through short tubes into vacuum". *J. Vac. Sci. Technol. A* **26** (2), pp. 228–238 (2008).
3. S. Varoutis, D. Valougeorgis, and F. Sharipov. "Simulation of gas flow through tubes of finite length over the whole range of rarefaction for various pressure drop ratios". *J. Vac. Sci. Technol. A* **27** (6), pp. 1377–1391 (2009).
4. D. Jun. Development of the nano-aperture ion source (NAIS). Ph.D. thesis, Delft University of Technology. repository.tudelft.nl (2014).
5. G. Rademaker. Fabrication and analysis of a freestanding nanofluidic channel. Master's thesis, Delft University of Technology - Charged Particle Optics group (2014).
6. S. Colin. "Rarefaction and compressibility effects on steady and transient gas flows in microchannels". *Microfluid. Nanofluid.* **1**, p. 268–279 (2005).
7. J. P. Holman. *Heat Transfer* (McGraw-Hill, 2002). Page 207.
8. F. Sharipov and V. Seleznev. "Data on internal rarefied gas flows". *J. Phys. Chem. Ref. Data* **27**, p. 657 (1998).
9. F. Sharipov. "Numerical simulation of rarefied gas flow through a thin orifice". *J. Fluid Mech.* **518**, pp. 35–60 (2004).
10. R. Livesey. "Solution methods for gas flow in ducts through the whole pressure regime". *Vacuum* **76** (1), pp. 101–107 (2004).
11. T. Gronych, L. Peksa, D. Prazak, M. Vicar, P. Repa, Z. Krajicek, F. Stanek, and J. Tesar. "Changes in the {NPL} orifice conductance on a transition from molecular gas flow to transitional flow". *Vacuum* **84** (1), pp. 280–282 (2010).
12. G. Weston. *Ultrahigh Vacuum Practice* (Butterworth and Co., 1985).
13. D. van Essen and W. C. Heerens. "On the transmission probability for molecular gas flow through a tube". *J. Vac. Sci. Technol.* **13** (6), pp. 1183–1187 (1976).
14. J. M. Lafferty. *Foundations of Vacuum Science and Technology* (John Wiley & Sons Inc., 1998). Material used: chapter 2, author R.G. Livesey.
15. S. Dushman. *Production and Measurement of High Vacuum* (General electric review, 1922).
16. H. Henning. "The approximate calculation of transmission probabilities for the conductance of tubulations in the molecular flow regime". *Vacuum* **28** (3), pp. 151–152 (1978).
17. D. Santeler. "New concepts in molecular gas flow". *J. Vac. Sci. Technol. A* **4**, p. 338 (1986).
18. T. Fujimoto and M. Usami. "Rarefied Gas Flow Through a Circular Orifice and Short Tubes". *J. Fluids Eng.* **106**, pp. 367–373 (1984).
19. F. Sharipov. "Rarefied Gas Flow into Vacuum Through Thin Orifice: Influence of Boundary Conditions". *AIAA J.* **40**, pp. 2006–2008 (1986).
20. F. Sharipov and D. V. Kozak. "Rarefied gas flow through a thin slit into vacuum simulated by the Monte Carlo method over the whole range of the Knudsen number". *J. Vac. Sci. Technol. A* **27** (3) (2009).
21. Jitschin, R. M. W., and S. Khodabakhshi. "Gas flow measurement by means of orifices and venturi tubes." *Vacuum* **53**, pp. 181–185 (1999).
22. G. Weissler and R. Carlson. *Vacuum Physics and Technology* (Academic press inc. (London), 1979). P. 16.
23. A. Agrawal. "A comprehensive review on gas flow in microchannels". *Int. J. Micronano Scale Transp.* **2** (1), pp. 1–40 (2011).
24. R. G. Livesey. "Method for calculation of gas flow in the whole pressure regime through ducts of any length". *J. Vac. Sci. Technol. A* **19** (4), pp. 1674–1678 (2001).
25. N. Dongari, A. Sharma, and F. Durst. "Pressure-driven diffusive gas flows in microchannels: from the Knudsen to the continuum regimes". *Microfluid. and Nanofluid.* **6** (5) (2009).



26. N. Dongari, R. Sambasivam, and F. Durst. "Extended Navier-Stokes Equations and Treatments of Micro-Channel Gas Flows". *J. of Fluid Sci. and Technol.* **4**, pp. 454–467 (2009).
27. F. Durst, J. Gomes, and R. Sambasivam. "Thermofluidynamics: Do we solve the right kind of equations?" *Proceedings of the international symposium on turbulence - Dubrovnik, Croatia* pp. 3–18 (Sept. 25 - 29, 2006).
28. N. Dongari, S. K. Dadzie, Y. Zhang, and J. M. Reese. "Isothermal micro-channel gas flow using a hydrodynamic model with dissipative mass flux". *AIP Conference Proceedings* **1333** (1), pp. 718–723 (2011).
29. J. Maurer, P. Tabeling, P. Joseph, and H. Willaime. "Second-order slip laws in microchannels for helium and nitrogen". *Phys. Fluids* **15** (9), pp. 2613–2621 (2003).
30. T. Ewart, P. Perrier, I. A. Graur, and J. G. Méolans. "Mass flow rate measurements in a microchannel, from hydrodynamic to near free molecular regimes". *J. Fluid Mech.* **584**, pp. 337–356 (2007).
31. S. L. Thompson and W. R. Owens. "A survey of flow at low pressures". *Vacuum* **25** (4), pp. 151 – 156 (1975).
32. V. d'A Browne and J. E. John. "Vacuum radial flow from the viscous through the free molecule regime". *Vacuum* **20** (12), pp. 525–533 (1970).
33. M. Smoluchowski. *Ann Physik* **33**, p. 1559 (1910).
34. E. B. Arkilic, M. A. Schmidt, and K. S. Breuer. "Slip Flow in Microchannels". *Proceedings: Rarefied Gas Dynamics symposium 19, Oxford* July 1994 (1995).
35. E. B. Arkilic, M. A. Schmidt, and K. S. Breuer. "Gaseous Slip Flow in Long Microchannels". *J. Microelectromech. Syst.* **6** (2) (1997).
36. D. Jun, V. Kutchoukov, C. Heerkens, and P. Kruit. "Design and fabrication of a miniaturized gas ionization chamber for production of high quality ion beams". *Microelectron. Eng.* **97**, pp. 134–137 (2012).

## List of symbols

$C_0$	orifice flow conductance	$\text{m}^3\text{s}^{-1}$	$L$	channel length	m
$C_{is}$	isentropic flow cond.	$\text{m}^3\text{s}^{-1}$	$w$	channel width	m
$C_{fm}$	mol. flow cond. aperture	$\text{m}^3\text{s}^{-1}$	$h$	channel height	m
$C_F$	interpolated flow cond.	$\text{m}^3\text{s}^{-1}$	$x$	coordinate in flow direction	m
$Q$	gas flow rate	$\text{Pam}^3\text{s}^{-1}$	$t$	membrane thickness	m
$Q_A$	advective flow rate	$\text{Pam}^3\text{s}^{-1}$	$r$	radial position from aperture	m
$Q_D$	diffusive flow rate	$\text{Pam}^3\text{s}^{-1}$	$R$	end radial symmetric region	m
$D_b$	bulk diffusivity	$\text{m}^2\text{s}^{-1}$	$m$	molecular mass	kg
$D_{fm}$	free mol. diffusivity	$\text{m}^2\text{s}^{-1}$	$\rho$	mass density	$\text{kgm}^{-3}$
$\alpha$	transmission probability		$\mu$	(dynamic) viscosity	Pas
Kn	Knudsen number		$\gamma$	ratio of heat capacities	
Re	Reynolds number		$\lambda$	molecular mean free path	m
Ma	Mach number		$v_s$	speed of sound	$\text{ms}^{-1}$
$l$	typical dimension	m	$\langle v \rangle$	average molecular velocity	$\text{ms}^{-1}$
$P_i$	inlet pressure	Pa	$v$	flow velocity	$\text{ms}^{-1}$
$P_o$	outlet pressure	Pa	$T$	temperature	K

# 3

## Optics of ion emission from a volume

*"Complexity is your enemy. Any fool can make something complicated.  
It is hard to keep things simple."*

RICHARD BRANSON

*"Physics is like sex: sure, it may give some practical results, but that's not why we do  
it."*

RICHARD FEYNMAN

### 3.1. Introduction

A good ion source is crucial for high resolution ion optical systems, but such a system also needs a well designed optical column. Optimization of an optical column does not require knowing all the details of the charged particle source. More useful is the description of a particle source in terms of its characteristic quantities, notably brightness, energy spread, and virtual source size (see for example ref. [1] for such an optimization).

The source properties of familiar sources such as the Schottky electron source [2] and the liquid metal ion source [3] have been studied quite well. For the nano-aperture ion source, the theory isn't as well established.

Studies on the source properties so far promised good performance; a brightness above  $1 \times 10^6 \text{ A/m}^2 \text{ srV}$  and sub 1 eV energy spread [4]. Some interesting trends regarding the voltage across the membrane and the aperture diameter were found. The modeling does not yet provide an understanding of how the gas and the electric fields in and around the chip relate to the optical properties. It furthermore doesn't include an analysis of the brightness dependence on the selected current, aberrations in the emission region, and an adequate analysis on the virtual source size and position.

In this chapter we are interested in how the initial emission volume, the properties of the gas and the electric fields establish the source properties. This enables appropriate optical column design and gives more insight in optimizing the source itself. Furthermore, experimental proof of the concept is easier when having a good idea what to expect under what conditions.

### 3.2. Source properties

The complicated emission region is usually replaced by a virtual source; an imaginary particle emitting object in a field-free region, instantaneously emitting at an energy equal to the acceleration voltage. This concept is visualized in figure 3.1. The resulting situation is optically equivalent to the real situation. This means that the column designer doesn't need to know about all the details at the real source region, the virtual source properties are sufficient.

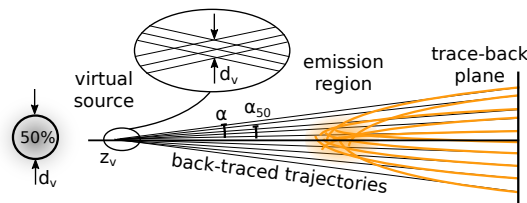


**Figure 3.1.** Particles are emitted from a source and the trajectories are determined by their initial conditions and the electrostatic fields. After acceleration up to a high voltage the trajectory tangent lines can be traced back to obtain the virtual properties.

### 3.2.1. Virtual source size

The transverse size of the virtual source is important in probe forming systems because it determines the required magnification of the total system. The optical image of this object on the final target is called the geometrical contribution to the probe size. This contribution should always be as large as possible, without dominating the total probe size in order to get the most current in the probe. Said differently, any optimized system which is not limited by diffraction will have a significant geometrical contribution to its probe. For ions, the diffraction contribution is practically always negligible.

Most sources require a demagnification of a few times, but very large sources require very high demagnification, which may require several lenses and high alignment accuracy. On the other hand, very small sources such as carbon nanotubes require magnification in order to get sufficient current in the probe [5]. This inherently means that the gun lens aberrations are magnified, which can cause challenging lens design. It is clear that the virtual source size is a crucial property of a particle source.

dim	fw50	25-75%	fwhm	$\sigma$
1D	1	1	0.573	1.349
2D	1	1.761	1	2.355

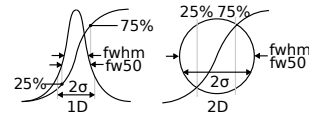


**Table 3.1.** Conversion table for different measures of distribution functions (rotationally symmetric in 2D case):  $\text{fw50} = cX$  with  $c$  the value in table and  $X$  the measure. The "fw50" is the diameter containing 50% of the intensity. The "fwhm" is the full width at half maximum. "25-75%" refers to a knife-edge rise distance; for 1D distributions this is also called the inter-quartile range. The conversion between fw50 and 25-75% in 2D is valid for a wide range of distributions as shown by Barth [6], while the conversion between a fw50 and a fwhm or standard deviation is only exact for Gaussian distributions.

It is important to use a clear and appropriate measure to quantify the virtual source size. We use the full width 50% (fw50), which is the disk in the virtual object plane containing 50% of the total current. Barth and Kruit recommend the fw50 as it is fairly insensitive to the type of distribution and allows for easy addition of aberrations [6]. Furthermore, it behaves well with respect to noise or outliers. Alternatives such as the RMS, full width half maximum or beam waist all score lower on robustness and applicability. Judging from the literature, not everyone is convinced of the fw50 superiority. In order to relate a fw50 to a perhaps more familiar measure table 3.1 can be used.

The virtual source position is defined as the virtual plane at which we obtain the smallest fw50 disk and is essentially the object position.

### 3.2.2. Brightness

One of the most important characteristics of a charged particle source is the brightness. In essence it is a measure of the beam intensity. The brightness comes in a few flavors and figure 3.2 indicates the three most important ones.

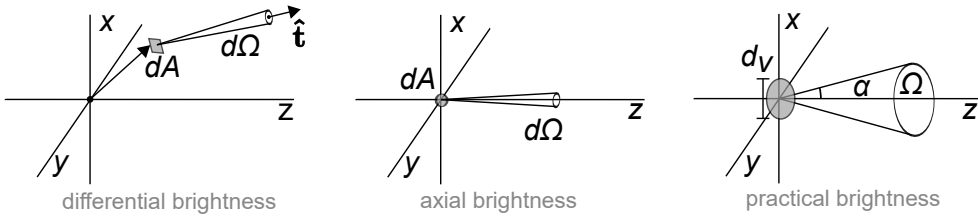


**Figure 3.2.** Three different flavors of the brightness. The differential brightness is the most general, where the position in space and the direction of the emitting cone are free variables. The axial brightness is the differential brightness at the origin and in the direction of the optical axis (z-axis). The practical brightness avoids using infinitesimal quantities and is the most useful brightness for column optimization and performance estimates. It is also typically the quantity acquired from measurements.

The definition of the differential brightness is

$$B_r(\mathbf{r}, \hat{\mathbf{t}}) = \frac{d^2 I}{d\Omega dA \Phi}. \quad (3.1)$$

It describes the amount of current that is confined in an infinitesimal solid angle  $d\Omega$ , originating from the infinitesimal area  $dA$ , aimed at direction  $\hat{\mathbf{t}}$ . The subscript "r" denotes reduced by the beam accelerating voltage  $\Phi$  at position  $\mathbf{r}$ . No lenses, apertures nor acceleration or deceleration can change the brightness [7] as a consequence of Liouville's theorem on the conservation of phase space density [8]. Related is the Helmholtz-Lagrange invariant [9], which can be used to show the invariance of brightness as well. We should note that the invariance relies on the assumption of no internal interaction. This is often the situation, but when statistical coulomb interactions become significant this assumption fails and the brightness can deteriorate.

The differential brightness is very difficult to determine for every  $\mathbf{r}$  and  $\hat{\mathbf{t}}$  and one may question the purpose of such detailed information. For optical systems, the axial brightness is often more sensible to consider; brightness in the direction of the optical axis, originating from the optical axis. The definition is

$$B_{\text{axial}} = B_r(z, \hat{\mathbf{z}}). \quad (3.2)$$

Bronsgeest [2] explained that an even more useful version of the brightness is the practical brightness:

$$B_{\text{pract}} = \frac{I}{\frac{1}{4} \pi d_v^2 \pi \alpha^2 \Phi} \quad (3.3)$$

with  $d_v$  the fw50 of the virtual source size and  $\alpha$  the half beam angle. It can conveniently be used to calculate the relation between current and spot size in an optical system. The axial and practical brightness are often closely related, for instance by a factor  $\ln(2)$  for Schottky and thermionic sources. We can make the axial brightness also a bit more practical by using  $J = 4I/\pi d_v^2$  in stead of  $dI/dA$ .

The full beam current is rarely used in charged particle optical columns and more commonly a beam fraction is selected by an aperture. The most relevant brightness in such a configuration is the average practical brightness of the selected beam fraction. This quantity is found from

$$B(\Omega) = \frac{J}{\Omega\Phi} \int_0^\Omega \rho_\Omega d\Omega \quad (3.4)$$

If we use  $J = 4I/\pi d_v^2$  we make it a practical brightness as well. Quite often we work with the beam divergence angle  $\alpha$ , which is related to the solid angle by  $\Omega = 2\pi(1 - \cos \alpha) \approx \pi\alpha^2$ .

### 3.2.3. Energy spread

Any charged particle source has an energy distribution associated with it. The range of energies in the distribution is much smaller than the final beam energy; typically 1 eV compared to 30 keV. Nevertheless, this small a-chromaticity can cause significant resolution loss due to the inability of electromagnetic lenses to focus the different energies at the same spot. The details of the distribution are usually summarized by a single number: the energy spread. For the same arguments as for the virtual source size, the use of a full width 50 is advocated.

Standard optical systems, so excluding time-dependent fields and energy filters, leave the energy distribution unaffected. This means that the energy spread is another constant source parameter. The energy spread is not truly invariant as the statistical coulomb interaction can make the spread larger, which is known as the Boersch effect [10]. Most often this occurs right after emission and it is common to consider the Boersch effect as an inherent property of the source.

### 3.2.4. Source aberrations

Source aberration is blurring of the virtual source as a consequence of non-ideal imaging. Usually it is preferred to keep the virtual source properties and properties of the optical column, such as aberrations, separated. However, the optical effects of the initial acceleration stage and the virtual source formation are intimately related and cannot be considered individually.

We study the aberrations of the virtual source as attained during acceleration by looking at effects that cause a spread in the virtual source position. The size of the aberration disk can be estimated from  $d_v \sim \Delta z_v \cdot \alpha$ , with  $\Delta z_v$  a measure for the spread of the virtual source position. Analyzing a particular aberration boils down to finding an appropriate expression for  $\Delta z_v$ . The fw50 value of the aberration disk is given by

$$d_{50} = c_{50} \Delta z_v \alpha_{50}, \quad (3.5)$$

in which  $c_{50}$  is a dimensionless constant in the order of one.  $\alpha_{50}$  is the angle that defines a cone that contains 50% of the current as selected by an aperture angle  $\alpha$ .

$\alpha_{50}$  can be found from

$$\int_0^{\Omega_{50}} \rho_{\Omega} d\Omega = 0.5 \int_0^{\Omega} \rho_{\Omega} d\Omega, \quad (3.6)$$

in combination with  $\Omega_{50} = \pi\alpha_{50}^2$ . The simplest approximation to  $\alpha_{50}$  is assuming isotropic intensity, which is equivalent to a constant solid-angular probability density. It yields  $\alpha_{50} = \frac{1}{\sqrt{2}}\alpha$ .

### 3

#### 3.2.5. Virtual source properties from ray tracing

Ray tracing is used extensively throughout this dissertation. We acquire the results as a set of position and velocities at a plane sufficiently far away from the chip such that all emission effects are included and the beam energy is much larger than any energy associated with the emission. This typically means acceleration up to 10 kV in 1 to 10 mm.

For determining the virtual source properties from our ray trace results we use a post-processing algorithm in MATLAB. We trace  $N$  particles, but may only select a fraction of the beam for the analysis, effectively placing an aperture. We choose  $N_{\text{sub}} \leq N$  and sort according to  $\sin \alpha_i = v_{r,i} / v_{z,i}$ . We relabel the set such that  $\dots < \sin \alpha_{i-1} < \sin \alpha_i < \sin \alpha_{i+1} < \dots$  and select all particles for which  $i \leq N_{\text{sub}}$ .

We define trace-back position functions as:

$$x_i(z) = \frac{v_{x,i}}{v_{z,i}}(z - z_0) + x_{0,i}, \quad y_i(z) = \frac{v_{y,i}}{v_{z,i}}(z - z_0) + y_{0,i}. \quad (3.7)$$

These functions are the black lines in figure 3.1 of the  $i^{\text{th}}$  particle. The subscript 0 relates to the trace-back plane, also indicated in the figure. We define  $r_i^2 = x_i^2 + y_i^2$  and for any requested value of  $z$  we relabel the set of  $r$ 's by  $j$  such that  $\dots < r_{j-1} < r_j < r_{j+1} < \dots$ . We have  $j_{50} = N_{\text{sub}}/2$ , such that  $j_{50}$  is the index of the particle that defines a radius including 50% of the intensity. We use an optimizer to look for the value of  $z$  that yields the smallest  $r_{j_{50}}$ . The obtained value for  $z$  is the virtual source position  $z_{\text{virt}}$  and the virtual source full width 50 diameter is

$$d_v = 2r_{j_{50}}(z_{\text{virt}}). \quad (3.8)$$

The obtained virtual source size can be used as input for the computation of the practical brightness as defined by equation 3.4. Note that we do not actually need to solve the integral as the angular distribution is represented in particle counting. The integral is simply the number of particles within the subset divided by the total number of particles:  $N_{\text{sub}}/N$ . The appropriate  $\Omega$  is found from the beam angle of the particle  $N_{\text{sub}}$ .

This method may be somewhat complex, but is as close as one can get to what will be measured in a real optical system. A perhaps more common alternative is first computing the (RMS) emittance and henceforth relating it to a brightness. This can be problematic though when incorporating the angular dependence of the

brightness and is less resilient towards outliers. We note that the method used by van der Geer [11] using a 4D hyperellipsoid that just encompasses the sub-selected beam fraction before computing the emittance should give a comparable results as our method.

The electric fields for complex geometries are computed with the FEM-based Electron Optical Design program [12]. Due to the very large scale difference of 100 nm typical dimension to 1 mm, we stitch the FEM-computed field with an analytical expression for a uniform field at a position where the computed field is considered sufficiently uniform. This is typically after 1  $\mu\text{m}$ . Ray tracing is performed with the General Particle Tracer code [13], using 10 to 100 k particles and high accuracy.

### 3.3. *Emission in a uniform field*

In essence the NAIS configuration consists of two membranes for confining the gas and two apertures to allow for electron entrance and ion emission. A bias voltage is applied across the membranes to extract the ions and an accelerating field right behind the exit membranes brings the beam to high energy, say 10 keV. The simplest manifestation of this is having infinitely thin membranes and equal electric fields between and outside of the membranes. The convenience of this configuration is that the electric field is uniform from the start of the emission region up to the end of the accelerating field. This allows for a fairly simple description of the optics. Such a simplification is not unrealistic; membranes of only tens of nanometers are not uncommon with modern day micro-machining techniques.

Since the ions are generated from within a gas, scattering of ions on neutral particles is inevitable. One aspect of the NAIS is operating it such that ion-neutral scattering does not deteriorate the performance. Previous work assumed that we can have about 1% of the electrons engaging in ionization in a gas with the gas still sufficiently dilute for neglecting ion neutral scattering [14].

In this chapter we focus on the rarefied limit as well, with the notion that higher particle density requires a more comprehensive approach, but may give a better performance. Ion-neutral scattering is the subject of the next chapter. We will use a slightly conservative ionization efficiency of  $\eta < 0.5\%$ . An electron column optimized for the NAIS may deliver 100 nA in a 50 nm (fw50) spot [4, 15] so we expect about 500 pA of generated ion current in the rarefied limit.

#### 3.3.1. Initial particle distributions

For setting up an emission model, we will need to know the distributions for the initial conditions of the generated ions. We use these distributions to predict how the ions move after generation and use this to predict the optical properties of the source.

Upon ionization, there may be some momentum transfer from the impinging electron to the ion. Intuitively we can expect this to be negligible due to the large mass difference of the atom and the electron, as for example argued by Nanbu [16]. We can try to back up this claim quantitatively. It is a textbook exercise to show



that the maximum energy transfer ratio in a binary collision of an electron with mass  $m_e$  and an atom with mass  $m$  is  $\frac{m_e}{m} \left(1 + \frac{m_e}{m}\right)^{-2}$ . For a 1 keV electron hitting a helium atom this gives 0.5 eV of energy transferred to the atom, which is much more than  $kT$ . This is of course a huge simplification and should be interpreted as an upper bound, but it does show that simply stating the mass-difference is insufficient argumentation for neglecting the ion recoil momentum.

Authors that have studied the kinematics of the outgoing electrons (electron-impact coincidence experiments, referred to as "(e,2e)"), argue that the recoil ion momentum can be significant in ionizing collisions. See for example references [17–21] for mostly helium results, or [22, 23] for some results on molecules. In the terminology of (e,2e) experiments, a so-called recoil peak is identified in the differential cross section of the scattered electron. It is associated with a large momentum transfer to the ion, while a second peak called the binary peak corresponds to a clean knock-out of the electron. Without going into the details, the explanation of the recoil peak is that after ionization, the electrons, mostly the slowest one, interact with the potential of the newly generated ion [24].

It is difficult to use the work on (e,2e) experiments for deciding upon the importance of ion recoil momentum in modeling the NAIS system. Typically only a specific configuration rather than the full cross section is computed or measured, for example the angular distribution of the resulting electrons for only a particular value of the ejected electron energy. For the NAIS we will inevitably have to deal with all possibilities and it is a matter of statistics whether or not the effect is important.

It may be possible to use the results for some representative particular configurations to estimate the average ion momentum, but fortunately something better is available. Jagutzki [25] measured the ion recoil momentum in all three spatial dimensions of helium at 500 eV and 2000 eV initial electron energy. The most important result from their work for our purpose is that most collisions are associated with an ion momentum transfer in the order of 1 atomic unit of momentum. This corresponds to an energy of 1.8 meV for helium. Comparing this to a thermal energy of 25 meV we conclude that the ion recoil can at most cause a small deviation from the results based on purely thermal properties. For heavier gases, the effect will be even less important.

We will neglect the small momentum transfer of the impinging electron and assume a Maxwell-Boltzmann distribution of the gas. This also ignores the variations due to the confined geometry and the effect of temperature change caused by the expansion of the gas into a vacuum.

Some additional explanation is in place here as expanding gases are often associated with a big temperature decrease. An ideal gas will show no temperature change when it is freely expanding because it is not doing any work. When the van der Waals forces are important, the increase in inter-atomic distances requires work and the gas cools. A second mechanism is: when inter-atomic distances increase, fewer collisions occur, which means that on average the atoms spend less time high up in the repulsive part of the inter-atomic potential. This causes a temperature increase upon expansion.

The two competing effects are combined in the Joule-Thompson coefficient. For helium at room temperature and at 1 atm the coefficient is  $-0.0616 \text{ K atm}^{-1}$  [26]. So the temperature deviation caused by the expansion (increase in the case of helium) will typically be around 0.1 K. For argon and xenon the coefficients are 0.438 K/atm [27] and 1.87 K/atm [28] respectively, so we acquire a typical temperature decrease in the order of 1 K; not very exciting either. We can safely neglect the Joule-Thompson effect for further purposes.

Under the aforementioned assumptions the probability density of a particular momentum vector is proportional to the Boltzmann factor:  $\rho(\mathbf{p}) \sim e^{-p^2/2mkT}$ . If we define  $p_r^2 = p_x^2 + p_y^2$  with  $dp_x dp_y = p_r dp_\phi dp_r$ , and  $I$  is the current generated in some control volume, we obtain the radial momentum distribution

$$\rho_r(p_r) = \frac{1}{I} \frac{dI}{dp_r} = \frac{p_r}{mkT} e^{-p_r^2/2mkT}. \quad (3.9)$$

We can relate this to the more particle optical relevant angular probability density using  $|\rho_r(p_r) dp_r| = |\rho_\Omega(\Omega) d\Omega|$ , with  $2me\Phi\Omega \approx \pi p_r^2$  and introducing the abbreviation  $\gamma = e\Phi/\pi kT$ , with  $e\Phi$  being the final beam energy. Note that  $2me\Phi \gg p_r^2$  was used.  $d\Omega$  is the z-axis centered, annular shaped, differential solid angle. We obtain

$$\rho_\Omega(\Omega) = \frac{e\Phi}{\pi kT} e^{-e\Phi\Omega/\pi kT} = \gamma e^{-\gamma\Omega}. \quad (3.10)$$

We are often interested in the fraction of current in the selected beam cone. If we introduce  $\eta$  and integrate equation 3.10 up to  $\Omega$  we obtain

$$\eta = \frac{I(\Omega)}{I_{\text{tot}}} = \int_0^\Omega \rho_\Omega d\Omega = 1 - e^{-\gamma\Omega}. \quad (3.11)$$

With the angular distribution known we can find the 50 % beam angle as a function of the accepted aperture angle as described by equation 3.6. Or, alternatively in terms of the selected current by using equation 3.11. By using equation 3.10 and equation 3.6 we get

$$\alpha_{50} = \sqrt{\frac{1}{\pi\gamma} \ln \frac{2}{e^{-\pi\gamma\alpha^2} + 1}} = \sqrt{\frac{1}{\pi\gamma} \ln \frac{2}{2-\eta}}. \quad (3.12)$$

Furthermore, we would like to know the initial energy distribution. We will give the radial energy distribution  $\rho_{\epsilon_r}$  and the normal energy distribution  $\rho_{\epsilon_z}$ . Using conservation of differential probability:  $|\rho_{\epsilon_r}(\epsilon_r) d\epsilon_r| = |\rho_r(p_r) dp_r|$  and by definition  $2m\epsilon_r = p_r^2$ , we find

$$\rho_{\epsilon_r}(\epsilon_r) = \frac{1}{kT} e^{-\epsilon_r/kT}. \quad (3.13)$$

Likewise we find the normal energy distribution,

$$\rho_{\epsilon_z}(\epsilon_z) = \frac{1}{\sqrt{\pi k T}} \frac{1}{\sqrt{\epsilon_z}} e^{-\epsilon_z/kT}. \quad (3.14)$$

### 3.3.2. Test-ray analysis

The emission region is a volume and in order to cope with this we divide the volume into thin slices, see figure 3.3. We study how one particular slice is virtually mapped and we study how the different slices are combined in the virtual plane. To do so, we use test ray analysis. The test ray starts on the axis at a distance  $s$  in front of  $z = 0$  and travels across the acceleration length  $L$ . Note that  $s$  is in the order of the gas region length (or membrane spacing), that is a few hundred nm, while  $L$  is typically some mm's; so  $s \ll L$ .

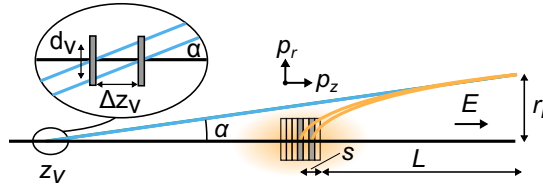


**Figure 3.3.** The concept of dividing the volumetric emission into slices and using test rays to obtain the virtual source properties and interpreting aberrations as a de-focus in the virtual plane. Volumetric aberration occurs because not all slices are imaged on to the same virtual source position. Normal energy aberration is a single emission slice not being mapped to the same virtual source position as a result of the initial energy variation. The rays start with radial momentum  $p_r$  and axial momentum  $p_z$ .  $L$  is length over which the particles are accelerated up to high voltage  $\Phi$ .

The test ray starts with initial momentum  $\mathbf{p}_0 = p_r \hat{\mathbf{r}} + p_z \hat{\mathbf{z}}$  and we derive the virtual source position  $z_v$  from  $z_v = L - r_L / \tan \alpha \approx L - r_L / \alpha$ , with  $r_L$  the axial distance of the ray after an acceleration of length  $L$ . In appendix A, a brief derivation of  $r_L$  is shown and the result is

$$r_L = 2(L + s) \frac{p_r}{p_{L,s}} (1 - Z), \quad 1 - Z = \left( \sqrt{1 + \left( \frac{p_z}{p_{L,s}} \right)^2} - \frac{p_z}{p_{L,s}} \right) \quad (3.15)$$

with  $p_{L,s}^2 = 2meE(L + s)$  by definition. Note that the abbreviating term  $Z \ll 1$  since the accelerating energy is in nearly any practical case much larger than the initial energy ( $p_{L,s} \gg p_z$ ). The uniform field has no radial force so the final beam angle is simply  $\alpha \approx \frac{p_r}{\sqrt{p_{L,s}^2 + p_z^2}} \approx \frac{p_r}{p_{L,s}}$ . We find for the axial intersection of the virtual ray

$$z_v = -L - 2s + 2(L + s) \cdot Z. \quad (3.16)$$

Interestingly, the virtual axis intersection only depends on the initial momentum in the axial direction and not on the radially directed momentum, which in turn solely governs the final beam angle.

### 3.3.3. First order properties

As a first step we look at a single emission slice. We set this plane in the origin so  $s = 0$  and since the acceleration voltage is almost always much larger than the initial energy we can use  $Z \approx 0$ . So, to first approximation we observe from equation 3.16 that all the particles emitted from the origin appear to come from a single virtual point located at  $z_v = -L$ . Due to symmetry, non-axial rays have the same property only shifted in  $x$  and  $y$ . This means that at  $-L$  a real image of the emission plane is made with magnification  $M = 1$ .

Almost inevitably, an accelerating electrode is apertured to allow the beam to pass through. This leads to an additional optical effect after uniform acceleration, which is well-known [29]. It will reposition the virtual source to  $z_v = -L/3$  and the magnification becomes  $M = 2/3$ . For the rest of the presented analysis, this lens effect is deliberately excluded for simplicity, as it can always be added later. Of course, when an optical system is designed for a NAIS-based system, this lens effect should be incorporated.

What is described here shows similarity to a thermionic electron gun in the diode configuration [29], however, very often the emission region is orders of magnitude larger. A real image is no longer the smallest possible back-traced image, but determined by the first lens. In that case it is easy to show that the virtual source is located at  $-3L$  and an estimate for the virtual source size is  $d_v \approx 4L\sqrt{\frac{kT}{e\Phi}}$ . This typically yields a virtual source size of at least several microns and is not applicable to the NAIS sub-micron sized emission region.

### 3.3.4. Chromatic aberration

Again, we consider a single slice in the gas emission region, but now we consider the distribution of initial momenta by looking at the small, but non-zero value of  $Z$ . From equation 3.16 we note that  $z_v$  is only dependent on  $p_z$ , so only a variation in the normal direction needs to be considered. The average normal momentum is simply zero, hence a ray with  $p_z = 0$  can serve to define the Gaussian image plane. For the characteristic ray representing the distribution in  $p_z$  we use the momentum variation  $\Delta p_z$ . Following the idea explained in section 3.2.4 of describing the aberration by a variation in the virtual source position and using equation 3.16 we obtain

$$\begin{aligned}\Delta z_v &= 2L \cdot (Z(\Delta p) - Z(0)) \\ &= 2L \left( \frac{\Delta p_z}{p_L} - \sqrt{1 + \left( \frac{\Delta p_z}{p_L} \right)^2} + 1 \right) \approx 2L \left( \frac{\Delta p_z}{p_L} - \frac{1}{2} \left( \frac{\Delta p_z}{p_L} \right)^2 + \dots \right)\end{aligned}\quad (3.17)$$

This aberration can be interpreted as a chromatic effect and it is more customary to express it in terms of an energy spread. In this case we can simply use  $\Delta p_z^2 = 2me\Delta\epsilon_z$  because the variation is defined with respect to zero energy. For this particular energy distribution (equation 3.14) the most sensible definition of  $\Delta\epsilon_z$  is the 50%

point, such that 50% of intensity lies between zero and  $\Delta\epsilon_z$ . Integration of equation 3.14 up to 50% intensity gives  $e\Delta\epsilon_z = 0.2275kT$ .

We estimate the aberration disk in the virtual plane from equation 3.5, and by keeping only the first order term in equation 3.17 to obtain

$$d_n = 2c_{50}L\sqrt{\frac{\Delta\epsilon_z}{\Phi}}\alpha_{50}. \quad (3.18)$$

For  $\alpha_{50}$  we use the isotropic approximation  $\alpha_{50} = \frac{1}{\sqrt{2}}\alpha$  to obtain a simple expression. From ray tracing we find  $c_{50} = 1.75$  (see figure 3.4) and we get

$$d_n = 2.47\frac{\sqrt{\Delta\epsilon_z}}{E}\sqrt{\Phi}\alpha \quad (3.19)$$

This is a very practical form for the normal energy aberration disk. It is easily evaluated and we can see that the normal energy aberration can be minimized by using a high electric field. Note that keeping the field constant while changing the acceleration length has no influence as  $\sqrt{\Phi}\alpha$  will remain constant.

Figure 3.4 shows the result of a ray tracing simulation intended to get acquainted with the typical magnitude of this aberration and to compare to the theory. The particles start from a 293 K Maxwell-Boltzmann distribution, starting from the origin and being accelerated up to 10 keV of energy for a few different acceleration lengths (figure 3.4). A master curve is formed by dividing the obtained virtual source sizes by the acceleration length, showing indeed its proportionality. Also equation 3.19 is depicted.

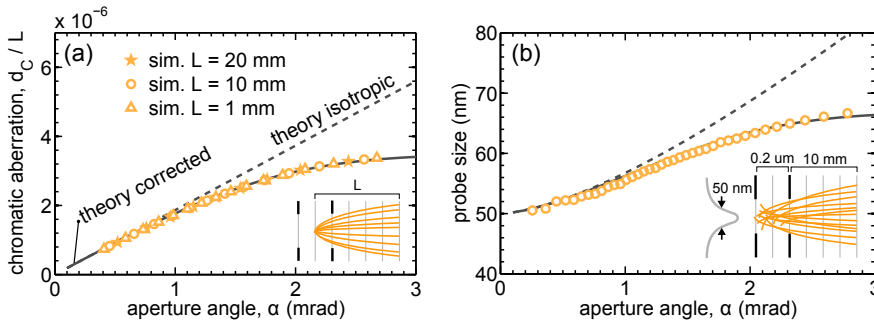


**Figure 3.4.** Ray tracing of 20k particles through a uniform field up to a final energy of 10 keV. Initial momenta are Maxwell-Boltzmann distributed. The dashed corrected theoretical curves uses equation 3.12 in stead of an isotropic angular distribution. a) All particles originate from the origin so the final  $fw50$ 's represent a point spread function. The chromatic aberration is indeed inversely proportional to the acceleration field hence the reduction by the extractor length for constant final beam energy aligns the different simulation results on one curve. b) Ray tracing particles originating from a realistic emission volume shows the combination of the geometrical contribution and the aberration disk.

An acceleration voltage of 1 kV/mm over 10 mm seems reasonable for a system that does not rely on field ionization. From figure 3.4a we can obtain that under these conditions the aberration disk nearly reaches 40 nm. This is considerable compared to a typically expected geometrical size of 50 nm. Nevertheless, when

using an often employed engineering limit of 10 kV/mm of maximum field strength the aberration can be minimized to only a few nanometer.

The curves in figure 3.4 are not entirely linear. This can be explained by the decreasing angular density with increasing angle. We can account for this by using equation 3.12 in stead of  $\alpha_{50} = \frac{1}{\sqrt{2}}\alpha$  and henceforth the well-matching solid curve in figure 3.4a is obtained.

A second ray tracing simulation uses ions starting between  $z = -100$  and  $100$  nm around the origin and a Gaussian radial intensity with a  $50$  nm  $\text{fw50}$  to account for the expected electron beam profile. The acceleration length was  $10$  mm and the final energy  $10$  keV. The resulting virtual source size is shown in figure 3.4b.

In the figure we see that for angles approaching zero we find a  $50$  nm  $\text{fw50}$ , as expected since the magnification between emission and virtual plane is one. At higher aperture angles the normal energy aberration start to contribute. We find that a decent addition rule between the normal energy aberration and the geometrical spot size is

$$d_{50} = \left( d_g^{1.55} + d_n^{1.55} \right)^{1/1.55}. \quad (3.20)$$

### 3.3.5. Relation to low energy electron microscopy

The chromatic aberration discussed here shows resemblance to the aberrations encountered in low energy electron microscopy (LEEM), so it is interesting to compare the results. Aberrations in LEEM systems were first studied by Bauer [30], but later also by others [31–34]. Both the NAIS as well as the LEEM system suffers from aberrations of a uniform field, yet, some essential differences can be identified.

For the NAIS, the initial energy and energy spread is in the order of  $kT$  and the normal and tangential energies are independent. Low energy electron microscopy deals with energies of typically a few to a few hundred eV with sub-eV energy spread and the tangential and normal energy distributions are not independent. Another, rather obvious, difference is for the NAIS the possibility of particles having an initial velocity vector in the negative  $z$ -direction, while in LEEM only forward emitted particles are possible.

Despite the differences we can try to relate the formalism of LEEM aberration to the formalism shown here. First we assume only forward emitted particles. Backward emitted particles have a considerably lower probability of escaping the gas confining membrane structure and so ignoring them all together is somewhat bold but not unreasonable. We describe the problem in terms of energy and realize that if no particles go backwards, the Gaussian image plane is defined by the average forward energy rather than zero energy. We use equation 3.16 to obtain

$$\begin{aligned} \Delta z_v &= 2L \cdot (Z_2(\epsilon_z + \Delta\epsilon_z) - Z_2(\epsilon_z)) \\ &= 2L \left( \sqrt{\frac{\epsilon_z + \Delta\epsilon_z}{\Phi}} - \sqrt{1 + \frac{\epsilon_z + \Delta\epsilon_z}{\Phi}} - \sqrt{\frac{\epsilon_z}{\Phi}} + \sqrt{1 + \frac{\epsilon_z}{\Phi}} \right) \end{aligned} \quad (3.21)$$

$$(3.22)$$

If we keep only the smallest terms we can fill in equation 3.5 to obtain the aberration disk as

$$d_n = 2Lc_{50} \left( \sqrt{\frac{\epsilon_z + \Delta\epsilon_z}{e\Phi}} - \sqrt{\frac{\epsilon_z}{e\Phi}} \right) \alpha_{50}. \quad (3.23)$$

This result, although slightly differently derived and formulated, was reported by Rempfer [32]. We can rewrite it in a more familiar form by expanding equation 3.21 over  $\frac{\Delta\epsilon_z}{\epsilon_z}$ :

$$d_n \sim L \sqrt{\frac{\epsilon_z}{\Phi}} \left( \frac{\Delta\epsilon_z}{\epsilon_z} \pm \frac{1}{4} \left( \frac{\Delta\epsilon_z}{\epsilon_z} \right)^2 + \dots \right) \alpha. \quad (3.24)$$

If we only keep the lowest order term we get

$$d_n \sim C_c \frac{\Delta\epsilon_z}{\Phi} \alpha, \quad C_c = L \sqrt{\frac{\Phi}{\epsilon_z}} \quad (3.25)$$

where  $C_c$  is the chromatic aberration coefficient. We have now obtained the more familiar expression that is linear with the relative energy spread and uses an aberration coefficient. This expression is very similar to what is found in low energy electron microscopy [31–34]. We should note that the expansion over  $\frac{\Delta\epsilon_z}{\epsilon_z}$  is not always appropriate because the condition  $\Delta\epsilon_z \ll \epsilon_z$  is not always met. In fact, for a MB-distribution  $\Delta\epsilon_z > \epsilon_z$ . Equation 3.19 does not rely on this condition and is therefore the preferred expression.

### 3.3.6. Volumetric emission aberration

The effect of volumetric emission compared to emission from a plane can be interpreted as an aberration because first order optical systems can only form sharp images of planes. We model this aberration by looking at the variation in the virtual source position of different slices.

We use two rays starting on the axis but separated by  $\Delta s$ , representing two characteristic slices. We ignore any chromatic effect because the two effects can be approached independently, just like conventional spherical and chromatic aberration for example. We can use equation 3.16 to obtain the difference in virtual position between the two rays and get  $\Delta z_v = 2\Delta s$ . As a first approximation we assume isotropic angular density and use equation 3.5 to get  $d_v = \sqrt{2}c_{50}s\alpha$ . With  $c_{50} = 0.81$  found from ray tracing we obtain

$$d_v = 0.57\Delta s\alpha. \quad (3.26)$$

To get a feeling for the magnitude we suppose that the aperture angle is such that it selects a decent fraction of the beam. Then,  $\alpha \approx \sqrt{\frac{kT}{e\Phi}} = 1.6$  mrad. The typical membrane spacing is a few hundred of nm's, say 500 nm, so for a 10 keV acceleration voltage we find  $d_v < 1$  nm. This is much smaller than the typical virtual source size

of around 50 nm. We conclude from this estimate that emitting from a volume in a uniform field does not cause a significant aberration contribution.

### 3.3.7. Brightness

For the situation of particles emitted from a Maxwell-Boltzmann distributed gas we can use equation 3.4 and equation 3.10 to find

$$B(\Omega) = \frac{J}{\Omega\Phi} (1 - e^{-\gamma\Omega}) \approx \frac{eJ}{\pi kT} (1 - \frac{1}{2}\gamma\Omega + \dots) \quad (3.27)$$

The axial brightness is obtained when selecting a vanishingly small cone of the beam ( $\Omega \rightarrow 0$ ) and by doing so we obtain the familiar Langmuir [35] equation  $B = \frac{eJ}{\pi kT}$ .

An angular brightness dependence can be deceiving as simply changing the beam energy already changes the solid angle corresponding to an equal beam current. We can rewrite equation 3.27 in terms of the beam fraction  $\eta$  using equation 3.11 and obtain

$$B(\eta) = \frac{\eta}{\ln \frac{1}{1-\eta}} \cdot \frac{eJ}{\pi kT}. \quad (3.28)$$

This expression is the same everywhere in the optical system as long as the conditions for phase space conservation are met.

Figure 3.5 shows a ray tracing simulation for comparison to equation 3.28. A high electric field of 10 kV/mm was applied to ensure negligible aberrations. We see that when nearly the full beam current is required, one will obtain a quite low brightness. For example 95% of the beam current relates to 32% of the axial brightness. A better figure of merit is the brightness of half the beam current, this gives 72% of the axial brightness.

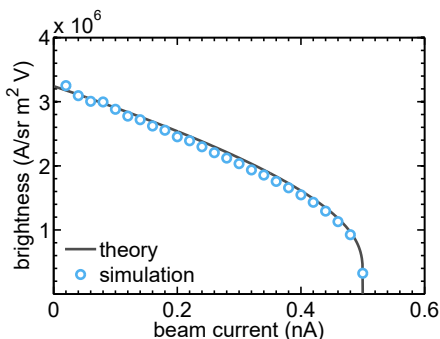


**Figure 3.5.** Ray tracing of particles starting uniformly from within a 200 nm distance in  $z$  and a Gaussian initial radial distribution with a 50 nm  $fw_{50}$ . The gas temperature was 293 K and the initial velocities are Maxwell-Boltzmann distributed. The electric field strength was 10 kV/mm.

## 3.4. Emission from a realistic geometry

The uniform field case is a good start for basic understanding, and may even be approachable. However, in practice this configuration is not so easily achieved. Restrictions to the applicable field across the membranes vary between chip designs, so it is important to study the influence of different field strengths in and outside the



chip. It may even be desirable to have a different field in and outside. Furthermore, the finite membrane thickness and the blockage of ions by the membrane can be important. This section is concerned with the implications of a realistic geometry compared to the uniform case.

### 3.4.1. Chip exit aperture lens

We will try to extend our simple uniform model by the inclusion of a lens effect at the exit aperture. Again we use a test ray and determine its virtual z-position from which we derive the optical properties. In figure 3.6 the test ray and the symbols used are shown. The test ray starts at distance  $s$  from the chip exit, has initial momentum  $p_x, p_z$ , and is accelerated over a length  $L$  up to a high voltage  $\Phi$ . Variations in  $s$  and the initial momenta are related to the gaseous volume and its properties.

For the sake of obtaining a model that is simple enough to be useful we assume the lens to be thin, consider only the first order focusing effect, and neglect the lens effect from the back of the chip. It is known from earlier work that the lens effect from the back can influence the escape probability [4], so a complete model should include this as well. However, only a small fraction of the generated particles feel it so it can never be a dominant effect.

So, in the presented model the ions travel through a uniform field up to the membrane, feel a thin lens focusing effect, and again encounter a uniform electric field up to some high voltage. We use the fact that the thermal initial energy is much smaller than the energy acquired from the field in the chip, which is in turn much smaller than the final beam acceleration voltage ( $kT \ll E_1 s \ll E_2 L$ ). We do take into account, and this is crucial, the difference in energy by which the particles pass through the lens. This is what makes the chip lens so extraordinary; the energy difference between particles is as big as the average energy.

Surely this model is not expected to describe all the involved optical effects in detail, however, it should encompass the most dominant effects. Further analytical modeling might become so complicated that its use can be questioned.

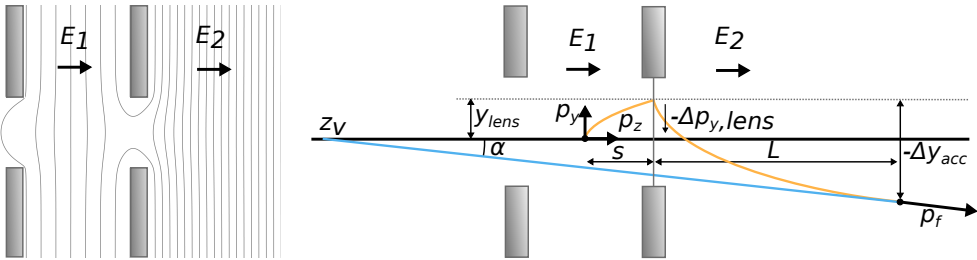


**Figure 3.6.** a) Example field map in and around a NAIS chip ( $E_2 = 2E_1$ ). b) symbol definitions for the presented theory.

The focal distance of a lens created by a field difference separated by a thin electrode is [29]

$$f = \frac{2V_a}{E_2 - E_1} = \frac{2E_1 s}{E_2 - E_1} = \frac{2ks}{1 - k}, \quad k = \frac{E_1}{E_2} \quad (3.29)$$

in which we have introduced the field ratio  $k$ . The momentum kick associated with this lens effect is

$$\Delta p_{y,\text{lens}} = \frac{e(E_1 - E_2)}{2v_{z,\text{lens}}} y_{\text{lens}}. \quad (3.30)$$

The radial distance at the lens location is governed by the travel through the uniform field in the chip. For this purpose convenient equations are derived in appendix A and the result is

$$y_{\text{lens}} = 2s \frac{p_y}{p_s} (1 - Z_1), \quad 1 - Z_1 = \left( \sqrt{1 + \left( \frac{p_z}{p_s} \right)^2} - \frac{p_z}{p_s} \right). \quad (3.31)$$

with  $p_s = \sqrt{2meE_1s}$ . Since  $v_{z,\text{lens}} = \frac{p_z}{m}$  for  $p_z \ll p_s$ , which we have assumed, we now have the ingredients to derive the final beam angle. A little algebra gives

$$\sin \alpha = \frac{p_y + \Delta p_{y,\text{lens}}}{p_f} = \frac{p_y}{p_f} \left( \frac{3}{2} - \frac{E_2}{2E_1} - Z_1 \left( \frac{1}{2} - \frac{E_2}{2E_1} \right) \right). \quad (3.32)$$

We can derive the magnification from the Helmholtz invariant:  $p_i^2 d_i^2 \sin^2 \alpha_i = p_f^2 d_f^2 \sin^2 \alpha$  with  $i$  for initial and  $f$  for final. The initial angle is  $\sin \alpha_i = \frac{p_y}{p_i}$ , so

$$M = \frac{d_f}{d_i} = \frac{\sin \alpha_i}{\sin \alpha} \frac{p_i}{p_f} = \frac{p_y}{p_i} \frac{1}{\sin \alpha} \frac{p_i}{p_f} = \left( \frac{3}{2} - \frac{E_2}{2E_1} - Z_1 \left( \frac{1}{2} - \frac{E_2}{2E_1} \right) \right)^{-1}. \quad (3.33)$$

Now we can also see that  $\sin \alpha = \frac{p_y}{p_f} M^{-1}$ .

We find the virtual source position from

$$z_v = L - \frac{y_{\text{lens}} + \Delta y_{\text{acc}}}{\tan \alpha} \quad (3.34)$$

We use the result from appendix A again to obtain

$$\Delta y_{\text{acc}} = 2L \frac{p_y + \Delta p_{y,\text{lens}}}{p_L} (1 - Z_2), \quad 1 - Z_2 = \left( \sqrt{1 + \left( \frac{p_s}{p_L} \right)^2} - \frac{p_s}{p_L} \right). \quad (3.35)$$

with  $p_L = \sqrt{2meE_2L}$ . Since  $p_y + \Delta p_{y,\text{lens}} = p_f \sin \alpha = p_y M^{-1}$  we obtain

$$\Delta y_{\text{acc}} = 2L \frac{p_y}{p_L} M^{-1} (1 - Z_2) \quad (3.36)$$

We use  $\tan \alpha \approx \alpha \approx \sin \alpha = M^{-1} \frac{p_y}{p_f}$ ,  $p_f = \sqrt{2me(E_1s + E_2L)}$ . After some tedious algebra of filling in equation 3.34 we get






$$z_v = L - 2L(1 - Z_2) \sqrt{1 + \frac{sk}{L}} - 2s(1 - Z_1) M \sqrt{1 + \frac{L}{sk}}. \quad (3.37)$$

### 3.4.2. First order properties

If we set  $Z_1 = 0$  in equation 3.33 we obtain

$$M = \left( \frac{3}{2} - \frac{1}{2k} \right)^{-1} = \frac{2k}{3k-1}. \quad (3.38)$$

Since a small variation in the magnification does not give rise to aberrations the small non-zero value of  $Z_1$  is irrelevant. Note that the magnification is independent of  $s$ , meaning that the magnification is uniform with respect to the starting slice position. Table 3.2 summarizes the different operation regimes possible due to the chip exit aperture lens.

fields		f	M	
$E_1 > E_2$	$k > 1$	-	+	
$E_1 = E_2$	$k = 1$		1	
$E_2 < 3E_1 < 3E_2$	$\frac{1}{3} < k < 1$	+	+	
$3E_1 = E_2$	$k = \frac{1}{3}$	+	$\infty$	
$3E_1 < E_2$	$k < \frac{1}{3}$	+	-	

**Table 3.2.** Different regimes for the chip exit lens are identified, depending on the relative field strengths inside and outside of the chip. The focal distance for equal field strengths is undefined as no lens effect is present.

Firstly, if we look at the uniform field case ( $k = 1$ ) we obtain  $M = 1$ . This result corresponds to what was found in the previous section; a good sanity check. Furthermore we obtain  $z_v = -L - 2s$  from equation 3.37, also the result we obtained in the uniform field analysis.

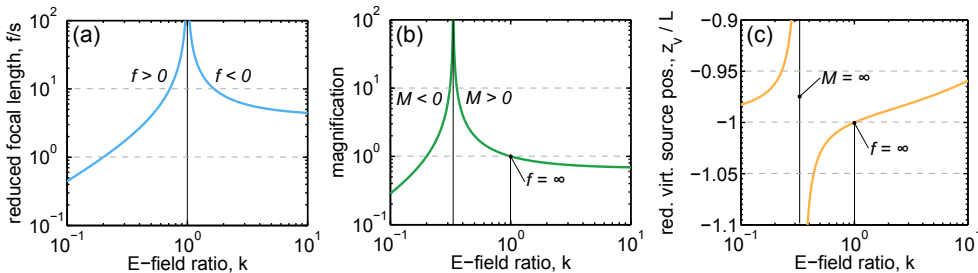


**Figure 3.7.** Theoretical predictions for the first order optical properties resulting from modeling the exit aperture as a thin lens and the fields before and after as uniform. a) The focal distance  $f$  divided by the object to lens distance  $s$  is a general measure of the exit membrane lens effect potency. The lens is strongest for the lowest  $k$ -value. b) The magnification can vary by an order of magnitude and shows asymptotic behavior at  $k = 1/3$ . c) The reduced virtual source position is in general close to 1, but is weakly depending on  $s$  and  $L$ . In this example  $L = 10$  mm and  $s = 500$  nm.

The first order optical properties of the presented theory are shown in figure 3.7. We can see from equation 3.29 that  $\frac{f}{s} = \frac{2k}{1-k}$ . The quantity  $f/s$  is a quite general measure for the exit aperture lens strength. Note that this does not include the influence of the uniform field before and after the exit aperture. In contrast, the magnification and the virtual source position are quantities of the full imaging system. If  $k = 1$  we see in all the graphs that the uniform properties are obtained.

We note that the magnification shows asymptotic behavior for  $3E_1 = E_2$ . Besides this remarkable asymptotic behavior, the magnification varies roughly between 0.3 and 3 for  $k = 0.1$  to 10. Clearly the exit aperture lens effect is important.

In figure 3.8 we compare the prediction of the virtual source position to a realistic ray trace example of two different chip geometries. We compare to a situation with realistic starting conditions due to the neutral particle distribution, as well as the blockage of the membranes. (The method of finding the neutral particle density distribution is discussed in section 4.6). We assume the radial emission profile to follow the ebeam intensity profile, which we assume to be Gaussian. A more simplified comparison is run too, in order to avoid any aberration as to study the first order properties. This is done by letting all particles start at the middle of chip, with a radial  $\text{fw}_{50}$  of 5 nm and a gas temperature of 5 K. We see in the figure that indeed the virtual source position is close to  $-L$ . The variations around  $-L$  are reasonably well described by the theory, especially when  $k > 0.4$ . One aspect of the difference is the penetration of the  $E_2$  field into the chip. The fact that the discrepancy is larger for the larger apertured chip supports this claim.

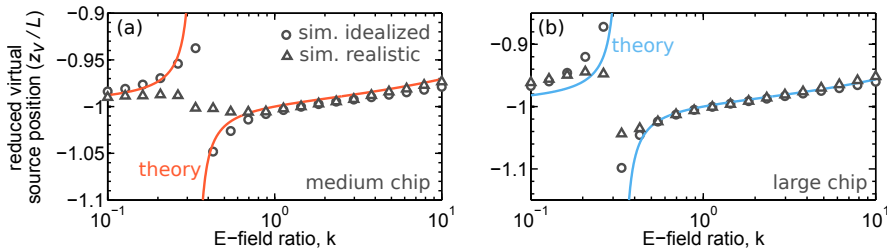


**Figure 3.8.** Theory compared to ray tracing using realistic ion starting conditions. The theory shows fair agreement, although the asymptote is not as explicit in ray tracing as it is theoretically. The idealized situation is a gas at  $T = 5$  with particles starting from the plane in the center of the chip. a) spacing  $\times$  thickness  $\times$  aperture = 300-100-150 nm b) spacing  $\times$  thickness  $\times$  aperture = 1000  $\times$  100  $\times$  500 nm

We do not see the predicted asymptotic behavior, but merely a tamed tendency of such. We note that the asymptotic behavior depends on a very precise balance of quantities, but in a realistic situation this balance is easily destroyed by small non-uniformities of the fields or the non-zero lens thickness. Furthermore, in the presented analysis it is assumed that the smallest back-traced image is a real image of the emission distribution. This is reasonable and was already shown to be valid in the uniform case. However, if the magnification becomes very large, the exit aperture becomes source size defining.

The virtual source size of the same ray trace simulation is shown in figure 3.10, but is better discussed in conjunction with the aberrations.

### 3.4.3. Aberrations

We can study the aberrations by looking at the variations in the virtual source positions according to equation 3.37. The normal energy aberration is found by

looking at the variation in the initial normal momentum while keeping  $s$  fixed:

$$\Delta z_v = z_v(\Delta p_z) - z_v(0) = 2sM\sqrt{1 + \frac{L}{sk}}(Z_1(\Delta p_z) - Z_1(0)) \quad (3.39)$$

$$\approx 2M\frac{\sqrt{E_1s + \Phi}}{E_1}\frac{\Delta p_z}{\sqrt{2m}} \approx 2M\frac{\sqrt{\Phi}}{E_1}\frac{\Delta p_z}{\sqrt{2m}} \quad (3.40)$$

$$(3.41)$$

3

Note that we have used  $\Phi = E_2L$  and  $E_1s \ll \Phi$ , and expanded  $Z_1$  up to first order. We would like to transform the aberration into terms of energy spread. Because  $\Delta p$  is defined with respect to zero we have  $\Delta p_z^2 = 2me\Delta\epsilon$ . The equation for the normal energy aberration disk with  $d_n = c_{50}\Delta z_v\alpha$  becomes

$$d_n = 2c_{50}M\frac{\sqrt{\Delta\epsilon_z}}{E_1}\sqrt{\Phi}\alpha. \quad (3.42)$$

We see great resemblance to the uniform case (equation 3.19). Since this more general case converges to the uniform case we can use  $c_{50} = 1.75$ , as found earlier. The relevant electric field is shown to be the in-chip field, so the normal energy aberration is effectively all generated right in the beginning of the trajectory.

Secondly we look at volumetric emission effects caused by the variations in  $s$ . It is easier to first look at the virtual source position for a particular  $s$  and taking the lowest order in the chromatic effects, so  $Z_1 = 0$ . From equation 3.37 we get

$$z_v = -L + 2L\sqrt{1 + \frac{ks}{L}}\left(\sqrt{1 + \frac{ks}{L}} - \sqrt{\frac{ks}{L}}\right) - 2s\sqrt{1 + \frac{L}{sk}}M \quad (3.43)$$

We have used  $p_s/p_L = \sqrt{\frac{E_1s}{E_2L}}$  to write  $Z_2$  in terms of  $k$ ,  $s$  and  $L$ . We can simplify by expanding over  $s/L$ , which is small, resulting after convenient rearrangement into

$$z_v = -L + 3\sqrt{L}\left(k^{\frac{1}{2}} - k^{-\frac{1}{2}}\right)M\sqrt{s} - 2ks. \quad (3.44)$$

We have kept the higher order term  $-2ks$  just to show that if  $k = 1$  the virtual source position is  $z_v = -L - 2s$ , exactly what was found in the uniform case. If  $k$  is only slightly non-zero, we find that this term is negligible compared to the others and is omitted for further use. The variation in the virtual source position is found from the variation in  $s$  and gives  $\Delta z_v = 3\sqrt{L}\left(k^{\frac{1}{2}} - k^{-\frac{1}{2}}\right)M(\sqrt{s_+} - \sqrt{s_-})$  where  $s_{\pm} = s_0 \pm 0.5\Delta s$ , such that  $s_0$  is the center of the chip and the region in  $z$  determined by  $\Delta s$  should contain half the ion generation intensity. The full width 50 disk of the volumetric aberration becomes

$$d_V = 3c_{50}M\left(k^{\frac{1}{2}} - k^{-\frac{1}{2}}\right)E_2^{-\frac{1}{2}}(\sqrt{s_+} - \sqrt{s_-})\sqrt{\Phi}\alpha. \quad (3.45)$$

with  $c_{50} = 0.57$ . We observe that we can minimize the aberration by making the fields as equal as possible, and by making  $E_2$  as high as possible.

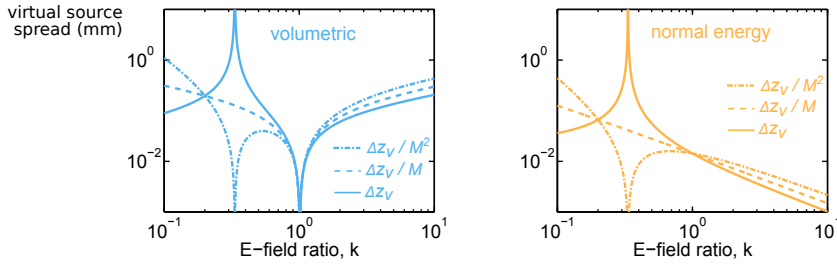


**Figure 3.9.** The spread in  $z_v$  is measure for the aberrations, however, because also a magnification is present in the system it is unclear what is the right figure of merit for the influence of these aberrations. Three different candidates are shown here. In this example:  $E_2 = 1$  kV/mm,  $T = 293$ K,  $s_+ = 750$  nm, and  $s_- = 250$  nm.

In figure 3.9 we have visualized the normal energy and the volumetric aberrations by showing the spread in the virtual source position. It is important to compare the contribution of the aberrations to the geometrical probe size. If we simply look at  $\Delta z_v$  we neglect that a magnification can make the aberration more or less important. A better figure of merit would be  $\Delta z_v / M$ . What is then still neglected is that the beam angle for a particular current scales with  $1/M$ . So, purely theoretically, the influence on the virtual source size when selecting a particular current is measured by  $\Delta z_v / M^2$ . From this point of view, we see that two sweet spots exist for the volumetric aberration, namely  $k = 1/3$  and  $k = 1$ . Since at  $k = 1/3$  the normal energy aberration is also least influential, this analysis suggest that operating at  $k = 1/3$  is most favorable for minimizing aberrations.

We compare the theory to ray tracing in figure 3.10. First we look at the ray trace curve with the circular marks. This curve is found from a cold gas (5K) for which all ions are generated at the center of the chip. This configuration is in practice not achievable, but a good setup for comparing to the theory because aberrations are negligible. We compare to the theoretical magnification and see good correspondence down to  $k = 0.4$ . For the lowest  $k$ -values we see that the theory describes the trend, but lacks accuracy. This can be attributed to the field penetration making the particle's energy at the lens higher than is incorporated in the theory.

When looking at the more realistic simulation (triangular markers), we see that the combination of source magnification and aberrations can reasonably well explain the behavior of the virtual source size. At the lowest  $k$ -values, the aberrations seem to be an overestimate though, particularly for the medium sized chip. That is partially attributed to field penetration, but also because not all ions get extracted. The solid theoretical lines are based on the assumption that all current is emitted, while the dashed theoretical lines use the simulated emitted current to convert to an effective 50% beam angle according to equation 3.6. This correction seems to explain why the aberrations in the medium sized chip are not as large as predicted by the simplest theory for these low  $E_1$  values.

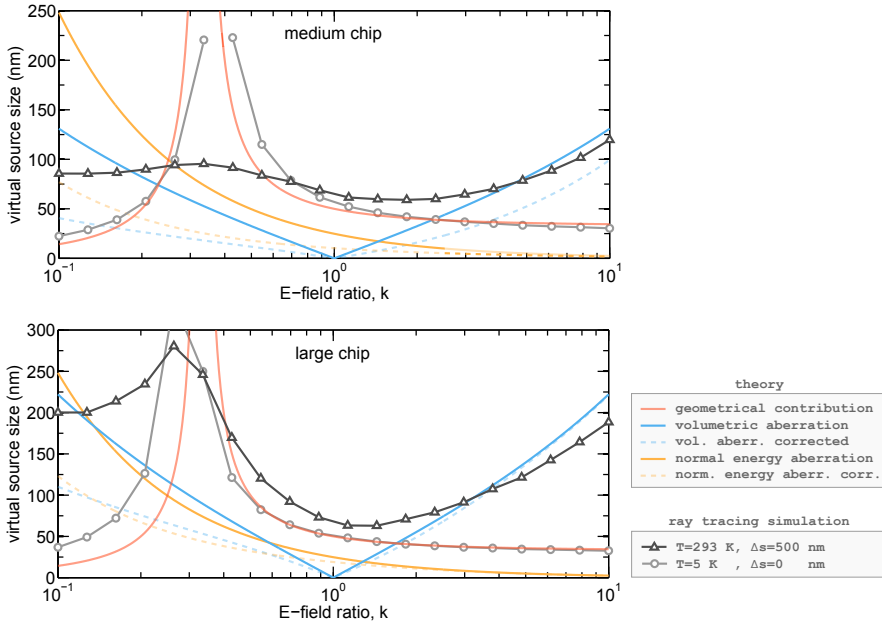


**Figure 3.10.** Virtual source size ray tracing results a medium sized chip (spacing×thickness×aperture = 300×100×150 nm) and a larger chip (spacing×thickness×aperture = 1000×100×500 nm) compared to theoretical predictions for different contributions. For further comparison an ideal situation at low temperature, with all particles originating from the center of the chip is included. The theory seems to predict the general trends well, although for  $k < 0.3$  deviation occurs. The corrected theoretical curves take into account the limitation of the current as blocked by the exit aperture

An important difference between the two simulated chip geometries is the severity of the asymptotic behavior, which for the larger chip is much more pronounced. The theory does not take into account that the exit aperture can become the source size determining factor. The smaller chip runs quicker into this transition. This makes us doubt the idea that  $\Delta z_v / M^2$  is the best figure of merit for the aberration for it assumes a fully developed asymptote. More practical is to use  $\Delta z_v / M$  as a measure for the aberration influence.

In equation 3.42 and 3.45 we see that both aberration disks are proportional to the magnification. The aforementioned analysis tells us then, that the influence of the aberrations is not very much affected by the first order properties of the exit aperture lens. The normal energy is minimized by the highest  $E_1$ . The volumetric aberration is lowest when  $E_2$  is highest and when the fields are most equal. In general  $k \approx 1$  is a good choice. The normal energy aberration is not necessarily lowest then, but we find it to be negligible for a wide range of configurations as long as  $E_1$  is reasonably high, say  $> 3$  kV/mm.

#### 3.4.4. Brightness

We study the brightness by ray tracing using realistic starting conditions in two different chip geometries. The result is shown in figure 3.11a, the brightness shown here is formed by 50% of the beam cone. Immediately we notice the maximum at

$k = 1$ . The reduction of the brightness with respect to its maximum is caused by the blurring, mostly due to volumetric emission aberration.

Interestingly, there is no clear notion of the asymptotic behavior at  $k = 1/3$ . This is maybe not surprising because the asymptotic behavior only causes first order effects, which are inherently not affecting the brightness. It also shows that  $\Delta z_v/M$  is indeed a good figure of merit for the aberration, for would it be  $\Delta z_v$  or  $\Delta z_v/M^2$ , we would see a peak or valley respectively in the brightness at  $k = 1/3$ .

Figure 3.11b shows the escape probability due to the varying field  $E_1$ , by which we vary  $k$ . Obviously the larger apertured chip has a higher escape probability and for any chip a higher in-chip field minimizes membrane blockage. More subtle is the notion that a lower escape probability means that the 50% beam cone will have a smaller beam defining angle and so the aberrations are smaller then. This explains why the brightness reduction for  $k < 1$  is less severe than for  $k > 1$ .

Note that the reduced escape probability is not directly related to brightness loss. The aperture mostly blocks particles with a high initial transverse energy and this group of particles ends up in the outer beam cone. Loosing them does lower the current, but also the 50% beam angle and the brightness is not very much affected.

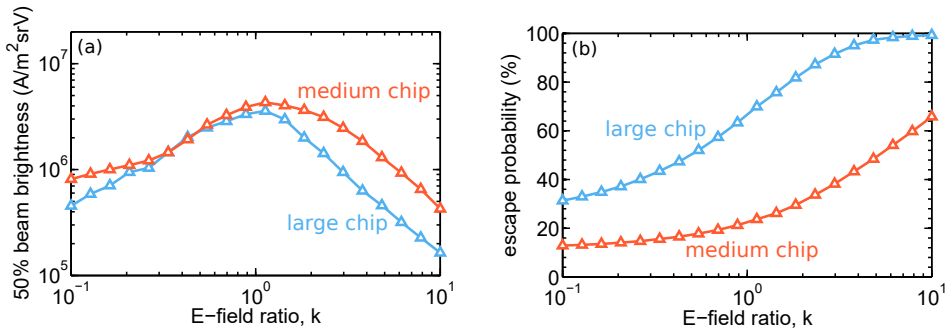


**Figure 3.11.** Ray trace results for a medium sized chip (spacing $\times$ thickness $\times$ aperture = 300 $\times$ 100 $\times$ 150 nm) and a larger chip (spacing $\times$ thickness $\times$ aperture = 1000 $\times$ 100 $\times$ 500 nm) with fixed  $E_2 = 1 \times 10^6$  V/m. The total generated current was fixed at 500 pA. a) The brightness is computed by using a back-traced fw50 probe size made out of the inner 50% current of the total beam cone. Clearly  $k = 1$  is the optimum, where the volumetric aberration is lowest. b) The escape probability is defined as the total emitted current to generated current ratio. In this case,  $k$  is varied by varying the in-chip field  $E_1$ , hence the large difference in escape probabilities.

Perhaps a clearer, or more fair way of looking at the brightness is by comparing the same currents. Figure 3.12 does so by plotting the average of a particular selected current. The theoretical prediction assuming a uniform field and no chip blockage is plotted as well (equation 3.28). The theoretical curve is never matched, except for the lowest currents where the ray trace results tend to converge towards the theory for all but the lowest  $k$ -values. For such small currents, the beam angle is vanishingly small such that the axial aberrations vanish as well. The fact that for the lowest  $k$ -values the curves do not converge towards the theoretical curve is rather unexpected. Since it cannot be an axial aberration, and current directed towards the aperture can not be blocked the effect is not obvious.



If  $k = 0.1$  the total energy acquired in the field is for the medium and large chip respectively 30 meV and 100 meV in the case of  $E_2 = 1$  kV/mm. The typical thermal energy is 25 meV and we conclude that a reasonable amount of particles can exit the chip from the back. This can explain up to a factor of two because only half of the particles start in the backward direction. Looking quantitatively at the discrepancy, this can't be the full explanation. Throughout the theoretical analysis it was assumed that  $eE_1 s \gg kT$ , however this assumption breaks down at these low  $k$  values. This gives rise to an additional variation in the lens strength and hence a variation in magnification. Furthermore, we may have off-axis effects, notably a distortion of the initial ion distribution profile when mapped on to the virtual source plane. The last two effects can both cause brightness decrease. A quantitative analysis of these plausible influences is omitted as it is tricky as well as of limited use. We remember that when  $eE_1 s$  approaches  $kT$ , bad performance and bad understanding occurs.

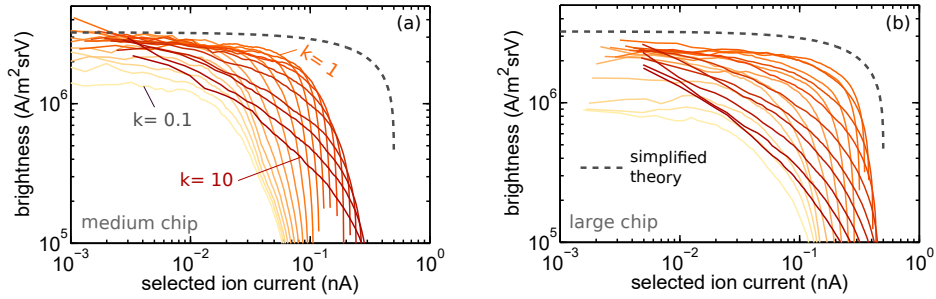


**Figure 3.12.** The computed average brightness of a selected beam current (equation 3.4) from a realistic ray tracing setup. The theoretical curve is given by equation 3.28. Note how the theoretical curve serves as an upper-bound and the largest deviation occurs for the highest current. For very low currents, all but the lowest  $k$ -value configurations converge towards the theoretical prediction. a) spacing $\times$ thickness $\times$ aperture = 300 $\times$ 100 $\times$ 150 nm b) spacing $\times$ thickness $\times$ aperture = 1000 $\times$ 100 $\times$ 500 nm

### 3.4.5. Energy spread

The ion-energy distributions of the NAIS have been studied in quite some detail by Jun [4]. Here we briefly discuss the most important results. Since we apply a bias voltage across the membranes, the ions are generated at different potential planes. The result is an energy spread in the beam in the order of the applied bias voltage. Figure 3.13 shows simulated energy distributions and it can be seen that the width of the distributions indeed resemble the applied bias voltage. Note that the thermal energy is only 25 meV, typically much smaller than the applied bias voltage. The field penetration of the acceleration field outside of the chip adds extra spread. This is mostly noticeable when the applied bias voltage is low, and when the aperture is large, see figures 3.13a and e. The ions generated in front of the chip are responsible for a low energy tail.

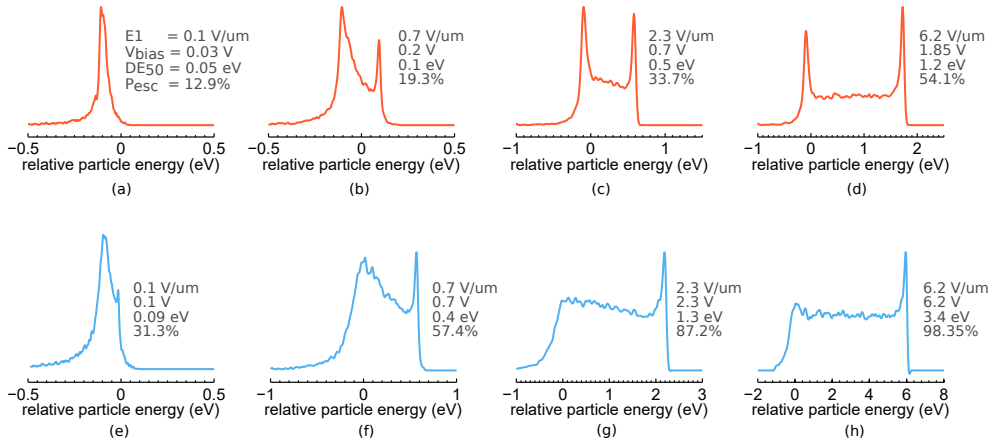


**Figure 3.13.** The energy distributions of scatter-free, coulomb interaction free, ray tracing simulations. The indicated energy is relative to an acceleration energy of 10 keV. (a-d) Medium sized chip, spacing $\times$ thickness $\times$ aperture = 300 $\times$ 100 $\times$ 150 nm. (e-h) A larger chip, spacing $\times$ thickness $\times$ aperture = 1000 $\times$ 100 $\times$ 500 nm.

One of the key insights resulting from Jun's work [4] is that the geometry and the field strengths determine the shape of the distributions. The field strength inside the chip determines which ions make it out of the double membrane structure. For example, a very weak field does not direct many ions from the back-side towards the exit aperture. This can be observed in the energy spectrum because not many high energy particles become part of the beam. Notice how in figure 3.13a to d or e to h, the high-energy part of the spectrum becomes more dominant when increasing the field strength.

Jun also explains that a bi-modal distribution is obtained when the field strength is rather high. This is as a consequence of a lensing effect at the back, causing the back-side ions to have a higher probability of being emitted than some ions halfway. While we do not dispute this insight, it is not the complete story. Even if this lens effects was completely absent, the bi-modality is obtained. This is because the field strength near and within the membranes is weaker, which results in a larger region at similar energies, hence an increased region in the energy spectrum. Furthermore, when increasing the field strength, ions make it out easier, simply because their trajectories are more parallel to the direction of the field, which is in the direction of the optical axis towards the exit aperture. The resulting distribution is a combination of these effects and the balance of the effects depends on the geometry and the field strengths. Notice how the low energy peak can be wider and less high compared to the high energy peak. This can be explained by the field penetration, increasing the local field strength and thereby causing the local spread to be wider than at the back.

### 3.5. Brightness from phase space evolution

For most sources, the theoretical brightness is derived by starting from the phase space density function,

$$f(\mathbf{r}, \mathbf{p}) = \text{phase-space density.} \quad (3.46)$$

It represents the number of particles in an infinitesimal 6D volume in real and momentum space combined. Alternatively, it is the particle density at position  $\mathbf{r}$  for particles having momentum  $\mathbf{p}$ . We have already derived an equation for the brightness starting from the energy distributions in the gas. It is good to check if this different approach leads to the same conclusion, but it also gives some new insight. It may also be a better basis for further study, such as the inclusion of gas scattering.

We will assume a simplified configuration and later comment on the relaxation of the assumptions. The configuration is a top hat gas distribution with length  $L$  and uniform neutral particle density  $n$  with a constant electric field  $E$  applied in the positive  $z$  direction. Very much like the thin-membrane equal-field configuration discussed earlier in this chapter.

#### 3.5.1. From phase space to brightness

We begin the derivation by giving the differential current from a phase space element in direction  $\hat{\mathbf{t}}$ . To acquire the current from an ion particle density  $n_i$  we use  $dI = en_i v dA$ , with  $v$  the ion velocity. In this case, we also need to take the momentum space volume element into account. We obtain

$$d^2 I = e f(\mathbf{r}, p\hat{\mathbf{t}}) v dV_p dA. \quad (3.47)$$

The term  $dV_p$  represent the volume in momentum space and in terms of the solid angle it is  $dV_p = p^2 d\Omega dp$ . We aim to relate this differential current to the brightness as defined by equation 3.1. We can establish this by taking the derivative of the brightness with respect to the momentum in the  $\hat{\mathbf{t}}$  direction to obtain

$$\frac{dB(\mathbf{r}, \hat{\mathbf{t}})}{dp} = \frac{d^3 I}{\Phi d\Omega dA dp} \quad (3.48)$$

If we plug equation 3.47 into equation 3.48 we find that the differential brightness can be found from the phase space density as

$$dB(\mathbf{r}, \hat{\mathbf{t}}) = \frac{e}{m\Phi} f(\mathbf{r}, p\hat{\mathbf{t}}) p^3 dp. \quad (3.49)$$

An integral form of this relation between phase space density and brightness, with integration over energies rather than momentum is found in the books of Hawkes and Kasper [7]. The derivation is different, but the result can be shown to be equivalent to equation 3.49

### 3.5.2. Evolution of phase space

In order to calculate the brightness from the phase space density, we first need to have an expression for the phase space density. The evolution of phase space density in the case of non-interacting particles is described by the kinetic Boltzmann equation,

$$\frac{\partial f}{\partial t} = -\mathbf{v} \cdot \nabla f(\mathbf{r}, \mathbf{p}) - \mathbf{F} \cdot \nabla_p f(\mathbf{r}, \mathbf{p}) + S(\mathbf{r}, \mathbf{p}). \quad (3.50)$$

The term  $S(\mathbf{r}, \mathbf{p})$  is the source term, representing the production of ions at position  $\mathbf{r}$  having momentum  $\mathbf{p}$ .  $\mathbf{F}$  is the local external force and  $\mathbf{v}$  the particle velocity.  $\nabla_p$  is the gradient with respect to momentum space.

Equation 3.50 is a non-trivial partial differential equation and simplifications are required to solve it. We are looking for steady state solutions so  $\frac{\partial f}{\partial t} = 0$ . Furthermore, we will try to calculate the axial brightness so only the axial phase space needs to be found. The axial phase space density  $f(0, 0, z, 0, 0, p)$  is formed only by particles starting on the axis, in the direction of the axis. So, we can simplify the 6D problem to a 2D problem because we only need to solve 3.50 on the optical axis.

The force term appearing in the kinetic Boltzmann equation is in this system simply a constant electric field  $E$  directed in the positive  $z$ -direction. The source term needs to be related to the electron beam that generates the current. We can write  $eS(\mathbf{r}, \mathbf{p}) = \frac{dI}{dV} \rho(\mathbf{p})$ , in which  $\rho(\mathbf{p})$  is the momentum probability density function of a generated particle. The differential ion current as generated by the ebeam is  $dI = I_e n \sigma_+ dz = J_e n \sigma_+ dV$ , so we obtain  $eS(z, p) = J_e n \sigma_+ \rho(p)$ .

We assume the particles to obey Boltzmann statistics, so every micro state (a particular momentum vector in this case) has a probability  $\sim e^{-\epsilon/kT}$ , thus  $\rho = a_n e^{-p^2/2mkT}$ . The constant  $a_n$  is found by integration over 3D momentum space and gives  $a_n = 2(2\pi mkT)^{-3/2}$  (the factor 2 here is not obvious, which will be explained hereafter). The source term becomes:

$$eS(z, p) = J_e \sigma_+ n a_n e^{-\frac{p^2}{2mkT}}. \quad (3.51)$$

and the kinetic Boltzmann equation then reads

$$\frac{p}{meE} \frac{\partial f(z, p)}{\partial z} + \frac{\partial f(z, p)}{\partial p} = A e^{-\beta p^2}, \quad (3.52)$$

with the abbreviations  $A = \sigma_+ n J_e a_n / e^2 E$  and  $\beta = \frac{1}{2} mkT$ . Note that independence of the momentum probability density on  $z$  and independence of the particle generation rate on  $p$  is implicitly assumed. This essentially corresponds to uniform properties of the gas, and no influence of the neutral particle's momentum on the ionization probability.

This PDE can be solved by the method of characteristics [36]. The first step is defining the appropriate boundary conditions. It is easiest to consider only particles traveling in the positive  $z$ -direction. We can incorporate particles traveling in the

opposite direction by realizing that they will be reflected forward. By energy conservation they act as if initially directed forward. Since ion production is isotropic we can simply use double the forward-directed ion production rate to account for backward propagating particles. This explains the factor 2 in  $a_n$ . Note that this only holds if no particles escape from the backside, which is typically negligible indeed.

In the case of only forward propagating particles we need to solve the equation in the positive  $z$  and positive  $p$  quadrant. The boundary condition at  $z = 0$  is rather trivial. No ions are produced for  $z < 0$  so we obtain  $f(0, p) = 0$ . This condition is not sufficient as it still allows negative momentum, i.e. ions propagating in the negative  $z$ -direction. This is not allowed because we specified our system in the positive  $zp$ -quadrant. Note that an alternative description could allow negative momentum, but this will make the math more difficult. One problem is then, that we need to solve the PDE between  $z$  is minus infinity and zero as well, otherwise particles can escape from the solution domain. Then, to name something, the source term becomes a non-continuous function and things become pretty hairy pretty quickly.

What we need besides  $f(0, p) = 0$  is the condition  $f(z, 0) = 0$ . It is perhaps counter intuitive as  $\rho(0) \neq 0$  and so one might expect  $f(z, 0) \neq 0$ . However, the phase space density at any particular position  $z_{\text{par}}$  is a summation of all the infinitesimal contributions of ion production coming from  $z < z_{\text{par}}$ . For  $p = 0$ , only ions originating from that particular position can contribute, as particles from other positions must have higher energies when arriving at  $z$  due to the electric field. This means that only an infinitesimal amount of ions contribute to  $f(z, 0)$ , hence  $f(z, 0) = 0$ .

We can use the method of characteristics to solve the PDE (see for example [36] for an introduction to the method). We start from

$$\frac{df}{dp} = \frac{\partial f}{\partial p} + \frac{\partial f}{\partial z} \frac{\partial z}{\partial p} \quad (3.53)$$

and conclude that if  $\frac{\partial z}{\partial p} = \frac{p}{emE}$ , looking at 3.52, we have

$$\frac{df}{dp} = Ae^{-\beta p^2} \quad (3.54)$$

Straightforward integration yields

$$f(z, p) = \sqrt{\frac{\pi}{4\beta}} A \operatorname{erf}(\sqrt{\beta} p) + C, \quad (3.55)$$

with  $C$  a unknown integration constant. Note that the solution is only valid on the characteristic curves defined by  $\frac{\partial z}{\partial p} = \frac{p}{meE}$ . Explicitly the curves are

$$z = \frac{p^2}{2meE} + z_0 = \frac{p^2 - p_0^2}{2meE}, \quad (3.56)$$

where  $z = z_0$  if  $p = 0$  and  $p = p_0$  if  $z = 0$ . In the case of  $z_0 > 0$ , which is equivalent to  $eEz > \frac{p^2}{2m}$ , the characteristic curve is space-like and we need to use the boundary  $f(0, z_0) = 0$  to obtain

$$f(0, z_0) = \sqrt{\frac{\pi}{4\beta}} A \operatorname{erf}(\sqrt{\beta} \cdot 0) + C = 0, \quad (3.57)$$

so  $C = 0$ . If  $z_0 < 0$ , so  $eEz < \frac{p^2}{2m}$ , we need to use the momentum-like boundary condition  $f(p_0, 0) = 0$  and obtain

$$C + \sqrt{\frac{\pi}{4\beta}} A \operatorname{erf}(\sqrt{\beta} p_0) = 0. \quad (3.58)$$

We relate  $p_0$  to  $z$  and  $p$  using equation 3.56 and get

$$C = -\sqrt{\frac{\pi}{4\beta}} A \operatorname{erf}(\sqrt{\beta} \sqrt{p^2 - 2meEz}). \quad (3.59)$$

Combining the results for the two different regimes yields the full solution as

$$f(p, z) = \begin{cases} \sqrt{\frac{\pi}{4\beta}} A \operatorname{erf}(\sqrt{\beta} p), & \text{if } eEz < \frac{p^2}{2m} \\ \sqrt{\frac{\pi}{4\beta}} A \left( \operatorname{erf}(\sqrt{\beta} p) - \operatorname{erf}(\sqrt{\beta} \sqrt{p^2 - 2meEz}) \right), & \text{if } eEz > \frac{p^2}{2m} \end{cases}$$

Note that  $z \in (0, s)$  and  $p \in (0, \infty)$  with  $s$  the length of the gaseous region.

### 3.5.3. Computing the brightness

We now know  $f$  right after the ionization volume so we could calculate the brightness using equation 3.49. However, the brightness of a non-accelerated beam is not as meaningful and we prefer the brightness of an accelerated beam, up to a potential  $\Phi$ , typically several kV. If we indicate the variables after acceleration by primes, we have from equation 3.49  $dB = \frac{e}{m\Phi} f'(z', p') p'^3 dp'$ . After the gaseous region there are no phase space sources so that by Liouville's theorem  $f'(z', p') = f(s, p)$ . From energy conservation we get  $p^2 + 2me\Phi = p'^2$ , and thereby  $p dp = p' dp'$  to finally obtain

$$B_{\text{axial}} = B(L, \hat{\mathbf{z}}) = \frac{e}{m\Phi} \int_0^\infty (p^2 + 2me\Phi) f(s, p) p dp. \quad (3.60)$$

The integral needs to be split for  $p > \sqrt{2meEs}$  and  $p < \sqrt{2meEs}$  because the phase space density function is different for these two intervals. The integral is tricky, but it turns out to be analytically solvable and the result is

$$B_{\text{axial}} = \frac{eJ_e \sigma + ns}{\pi kT} \left( 1 + \frac{Es}{2\Phi} + \frac{kT}{2e\Phi} \right). \quad (3.61)$$

If we look at  $\Phi \gg Es$ ,  $e\Phi \gg kT$ , we obtain the familiar  $B = \frac{eJ_e\sigma_{+ns}}{\pi kT} = \frac{eJ}{\pi kT}$ . We conclude that with the phase space method we get the same result as working directly with energy distributions.

We have calculated the on-axis brightness, but since the E-field was assumed uniform, the analysis actually does not rely on being on-axis, so the result is valid for a practical brightness of vanishingly small acceptance angle. If the field is not uniform, it is still a very close estimate for the axial brightness because on the axis only a field in the z-direction is possible. Furthermore, on-axis current will never be blocked by a membrane.

Since it is rare that the axial and the practical brightness are very different (only a very spiky intensity distribution can do that), we expect that the small-angle practical brightness is quite independent of chip design. This is also what is observed when studying the chip lens effects. Only when the field ratio  $k$  is very low ( $k < 0.3$ ) we see that the small-angle practical brightness is different from the brightness predicted here.

If the gaseous region was not a top hat but a more realistic smooth distribution, the math would be more complicated, but the final result won't change as long as  $e\Phi \gg eEs$ . The result here is only valid in the rarefied limit, where gas scattering is insignificant. In principle scattering can be included in the kinetic Boltzmann equation, however the tricky math already encountered in this simplified situation demonstrates that this is not a very promising direction. For a more comprehensive model we will need to rely on Monte-Carlo simulations, as is the subject of chapter 4 and 5.

### 3.6. Conclusion

The optics of ion emission from a chip were studied in the limit of a rarefied gas, i.e. particle-particle interactions are negligible. It was found that the exit aperture of the chip can cause a significant lens effect, depending on the ratio of the electric fields inside and outside of the chip. The most direct effect of this lensing is a magnification from the ion emission area to the virtual source area. The virtual source position is always close to one extractor length before the chip, excluding the extractor aperture lens.

Two aberrations were identified, namely chromatic and volumetric emission aberration. The chromatic aberration is caused by the intrinsic thermal energy spread of the ions in the direction of the optical axis. This spread leads to a variation in the virtual source position, hence can be interpreted as an aberration. The volumetric aberration originates from the ions being emitted from different positions along the optical axis, rather than from a plane. This aberration is affected strongly by the chip exit aperture lens. Poor choice of source configuration can cause these aberrations to lead to reduced performance. A good rule of thumb is that the electric fields inside and around the chip need to be approximately equal and above 3 kV/mm in order to suppress these aberrations sufficiently.



We note that the rarefied limit is not necessarily the best choice, as a higher gas density is expected to give better performance. However, the optical effects described here will be reminiscent in more complex situations and should be understood first. Furthermore, the analysis here can be very helpful for exploring alternative optimizations, such as ultra low energy spread, high current, low-end model (larger chip), or different e-beam properties.

## References

1. C. Hagen and P. Kruit. "Optimization of focused ion beam performance". *J. Vac. Sci. Technol. B* **27** (6), p. 2654 (2009).
2. M. S. Bronsgeest, J. E. Barth, L. W. Swanson, and P. Kruit. "Probe current, probe size, and the practical brightness for probe forming systems". *J. Vac. Sci. Technol. B* **26** (3), p. 949 (2008).
3. L. Swanson. "Liquid metal ion sources: mechanism and applications". *Nucl. Instr. Meth. Phys. Res.* **218** (1-3), p. 347–353 (1983).
4. D. Jun. Development of the nano-aperture ion source (NAIS). Ph.D. thesis, Delft University of Technology. repository.tudelft.nl (2014).
5. P. Kruit, M. Bezuijen, and J. E. Barth. "Source brightness and useful beam current of carbon nanotubes and other very small emitters". *J. Appl. Phys.* **99**, p. 024315 (2006).
6. J. Barth and P. Kruit. "Addition of different contributions to the charged particle probe size". *Optik* **101** (3), p. 101 (1996).
7. P. Hawkes and E. Kasper. *Principles of Electron Optics*, Volume 2 (Academic press, 1989). Page 971, 973.
8. M. Kardar. *Statistical physics of particles* (Cambridge university press, 2007).
9. M. Szilagy. *Electron and Ion Optics* (Plenum Press - New York and London, 1988).
10. J. Orloff. *Handbook of Charged Particle Optics* (CRC Press, 1997).
11. S. B. van der Geer, M. P. Reijnders, M. J. de Loos, E. J. D. Vredenbregt, P. H. A. Mutsaers, and O. J. Luiten. "Simulated performance of an ultracold ion source". *J. Appl. Phys.* **102** (11), p. 094312 (2007).
12. SPOC. "Electron Optical Design, version 3.072". [www.lencova.com](http://www.lencova.com).
13. PulsarPhysics. "General Particle Tracer, version 3.10". [www.pulsar.nl/gpt](http://www.pulsar.nl/gpt) (2011).
14. D. S. Jun, V. G. Kutchoukov, and P. Kruit. "Ion beams in SEM: An experiment towards a high brightness low energy spread electron impact gas ion source". *J. Vac. Sci. Technol. B* **29** (6), p. 06F603 (2011).
15. V. Tondare. Towards a High Brightness, Monochromatic Electron Impact Gas Ion Source. Ph.D. thesis, Delft University of Technology. repository.tudelft.nl (2006).
16. K. Nanbu. "Probability Theory of Electron-Molecule, Ion-Molecule, Molecule-Molecule, and Coulomb Collisions for Particle Modeling of Materials Processing Plasmas and Gases". *IEEE Trans. Plasma Sci.* **28**, p. 3 (2000).
17. M. Durr, C. Dimopoulou, A. Dorn, B. Najjari, I. Bray, D. V. Fursa, Z. Chen, D. H. Madison, K. Bartschat, and J. Ullrich. "Single ionization of helium by 102 eV electron impact: three-dimensional images for electron emission". *J. Phys. B: At. Mol. Opt. Phys.* **39** (20), p. 4097–4111 (2006).
18. E. H. M. Fischer, and K. Jung. "Triple Differential Cross Section Measurements for the Electron Impact Ionization of Helium: Comparison with a Second Born Approximation". *Z. Phys. A - Atoms and Nuclei* **304** (2), pp. 119–124 (1982).
19. F. Catoire, E. M. Staicu-Casagrande, M. Nekkab, C. D. Cappello, K. Bartschat, and A. Lahmam-Bennani. "Investigation of the (e, 2e) single ionization of He and Ar at large energy loss close to minimum momentum transfer". *J. Phys. B: At. Mol. Opt. Phys.* **39** (12), p. 2827 (2006).
20. A. S. Kheifets, A. Naja, E. M. S. Casagrande, and A. Lahmam-Bennani. "DWBA-G calculations of electron impact ionization of noble gas atoms". *J. Phys. B: At. Mol. Opt. Phys.* **41** (14), p. 145201 (2008).
21. A. S. Kheifets, A. Naja, E. M. S. Casagrande, and A. Lahmam-Bennani. "An energetic (e, 2e) reaction away from the Bethe ridge: recoil versus binary". *J. Phys. B: At. Mol. Opt. Phys.* **42** (16), p. 165204 (2009).
22. A. Lahmam-Bennani, E. M. S. Casagrande, and A. Naja. "Experimental investigation of the triple differential cross section for electron impact ionization of N 2 and CO 2 molecules at intermediate impact energy and large ion recoil momentum". *J. Phys. B: At. Mol. Opt. Phys.* **42** (23) (2009).
23. A. Naja, E. M. Staicu-Casagrande, A. Lahmam-Bennani, M. Nekkab, F. Mezdari, B. Joulakian,



- O. Chuluunbaatar, and D. H. M. 5. “Triply differential (e,2e) cross sections for ionization of the nitrogen molecule at large energy transfer”. *J. Phys. B: At. Mol. Opt. Phys.* **40** (18), p. 3775–3783 (2007).
24. L. Vriens. “Angular correlation of scattered and ejected electrons in ionizing collisions”. *Physica* **45** (3), pp. 400 – 406 (1969).
  25. O. Jagutzki, L. Spielberger, R. Dorner, V. M. S. Nuttgens, H. Schmidt-Bocking, J. Ullrich, R. Olson, and U. Buck. “Recoil-ion momentum distribution for He(e,2e) He<sup>+</sup> - and He(e,e3) He<sup>++</sup> - reactions”. *Z. Phys. D* **36**, pp. 5–10 (1996).
  26. R. McCarty. “Thermodynamic properties of helium 4 from 2 to 1500 K at pressures up to 1e8 Pa”. *J. Phys. Chem. Ref. Data.* **2** (4), p. 923 (1973).
  27. A. Michels, J. Levelt, and G. Wolkers. “Thermodynamic properties of Argon at temperatures between 0 C and 140C and at densities up to 640 Amagat (pressures up to 1050 atm.)”. *Physica* **14**, pp. 769–794 (1958).
  28. A. Michels, T. Wassenaar, G. Wolkers, and J. Dawson. “Thermodynamic properties of xenon as a function of density up to 520 Amagat and as a function of pressure up to 2800 atmospheres at temperatures between 0 C and 150 C”. *Physica* **12**, pp. 17–21 (1956).
  29. H. Liebl. *Applied charged particle optics* (Springer, 2008).
  30. E. Bauer. “The Resolution of the Low Energy Electron Reflection Microscope”. *Ultramicroscopy* **17**, pp. 51–56 (1984).
  31. R. Tromp, W. Wan, and S. Schramm. “Aberrations of the cathode objective lens up to fifth order”. *Ultramicroscopy* **119**, pp. 33–39 (2012).
  32. G. Rempfer and O. Griffith. “The resolution of photoelectron microscopes with uv, x-ray, and synchrotron excitation sources”. *Ultramicroscopy* **27**, pp. 273–300 (1989).
  33. M. Scheinfein, W. Qian, and J. Spence. “Aberrations of emission cathodes: Nanometer diameter field-emission electron sources”. *J. Appl. Phys.* **37** (5) (1993).
  34. Z. Shao and A. Crewe. “On the resolution of the low-energy electron reflection microscope based on wave electron optics”. *Ultramicroscopy* **31**, pp. 199–204 (1989).
  35. D. Langmuir. “Theoretical limitations of cathode-ray tubes”. *Proc. Inst. Radio Eng.* **2** (8), pp. 977–991 (1937).
  36. R. Haberman. *Applied Partial Differential Equations - Fourth Edition* (Pearson Prentice Hall, 2004).

## Appendix A

Deriving relations of charged particles in a uniform field is a textbook exercise [29], but it is shown here briefly anyhow to introduce the specific formalism. We start from a particle in the origin at  $t = 0$ , having initial momentum  $\mathbf{p}_0 = p_r \hat{\mathbf{r}} + p_z \hat{\mathbf{z}}$ . From Newton's second law and a uniform field pointing to the z-direction we obtain

$$\mathbf{r}(t) = \left( \frac{1}{2} \frac{eE}{m} t^2 + \frac{p_z}{m} t \right) \hat{\mathbf{z}} + \left( \frac{p_r}{m} t \right) \hat{\mathbf{r}}. \quad (3.62)$$

Suppose the particle is accelerated across length  $u$  and has final coordinates  $\mathbf{r}(t_u) = u \hat{\mathbf{z}} + r_u \hat{\mathbf{r}}$ . We eliminate  $t$  and obtain

$$r_u^2 + 4u \frac{p_r p_z}{2emEu} r_u - 4u^2 \frac{p_r^2}{2emEu} = 0. \quad (3.63)$$

and solve for  $r_u$  to finally get

$$r_u = 2u \frac{p_r}{p_u} \left( \sqrt{1 + \left( \frac{p_z}{p_u} \right)^2} - \frac{p_z}{p_u} \right), \text{ with: } p_u = \sqrt{2meEu} \quad (3.64)$$

$$= 2u \frac{p_r}{p_u} (1 - Z_u) \approx 2u \frac{p_r}{p_u} \left( 1 - \frac{p_z}{p_u} + \dots \right) \quad (3.65)$$

Most often the energy obtained in the accelerating field is much larger than the initial energy, making  $Z_u \ll 1$ .

## List of symbols

$B, B_r$	reduced brightness	$A/m^2srV$	$k$	Boltzmann constant or $E_1/E_2$	
$B_{axial}$	axial brightness	$A/m^2srV$	$s$	distance to chip exit	m
$B_{pract}$	practical brightness	$A/m^2srV$	$\Delta s$	ion emission spread	m
$B(\Omega)$	angular dep. brightness	$A/m^2srV$	$s+, s-$	$s_0 \pm \frac{1}{2}\Delta s$	m
$\Omega$	solid angle	sr	$d_{50}$	aberration disk fw50	m
$\alpha$	beam angle	rad	$c_{50}$	constant for the fw50	
$d_v$	virtual source size	m	$\alpha_{50}$	50% beam angle	rad
$\Phi$	ion acceleration voltage	V	$d_n$	normal energy aberration	m
$I$	ion current	A	$d_v$	volumetric emission aberr.	m
$J$	ion current density	$A m^{-2}$	$d_i, d_f$	initial, final object size	kgm/s
$L$	acceleration length	m	$p_i, p_f$	initial, final momentum	kgm/s
$\rho$	probability density function		$p_s, p_L$	$\sqrt{2meE_1s}, \sqrt{2meE_2L}$	kgm/s
$\epsilon_z, \epsilon_r$	normal energy, radial energy	eV	$Z, Z_1, Z_2$	abbreviation of expansion	
$\Delta\epsilon_z$	normal energy spread fw50	eV	$M$	magnification	
$z_{virt}$	virtual source position	m	$f$	phase-space density	m,
$\Delta z_v$	virt. source pos. variation	m	$f$	focal distance	m,
$E$	electric field strength	$V m^{-1}$	$J_e$	electron current density	$A m^{-2}$
$E_1$	inside chip field	$V m^{-1}$	$\sigma_+$	ionization cross section	m
$E_1$	inside chip field	$V m^{-1}$	$\sigma_+$	ionization cross section	m
$E_2$	outside chip field	$V m^{-1}$	$V_p$	momentum-space volume	$kg^3m^3/s^3$
$\gamma$	$e\Phi/\pi kT$		$\beta$	$\frac{1}{2}mkT$	
$\eta$	beam fraction		$A$	$\sigma_+ n J_e a_n / e^2 E$	
$\Delta p_z$	normal momentum spread	kgm/s	$p_{L,s}$	$\sqrt{2meE(L+s)}$	kgm/s
$a_n$	normalization constant		$z_0$	boundary position	m
$S$	phase space source		$m$	ion mass	kg
$r_L$	radial distance at $z = L$	m	$m_e$	electron mass	kg
$n_i$	ion particle density	$m^{-3}$	$\mathbf{F}$	external force	N
$p_0$	boundary momentum	kgm/s	$\mathbf{v}$	ion velocity	m/s



# 4

## A model for ion-neutral scattering

*"Every atom in your body came from a star that exploded. And, the atoms in your left hand probably came from a different star than your right hand. It really is the most poetic thing I know about physics: you are all stardust."*

LAWRENCE M. KRAUSS

*"I don't trust most numerical calculations. I tend to think of them as being like a sausage, they are just fine until you find out what went into them."*

CARL M. BENDER

## 4.1. Introduction

When ions are generated inside a NAIS chip, they are inevitably surrounded by neutral gas particles. On the way out of the ionization volume, an ion may interact with one or more of these particles. In this chapter, a model is presented that is used to investigate ion-neutral interaction in the nano-aperture ion source. Partially this chapter is a stepping stone, since the Monte-Carlo implementation of the model discussed here is primarily used for the simulations described in chapter 5.

Atomic modeling is found in a wide variety of complexity; one may, for example, consider the full electronic structure, or simply model atoms as billiard balls. We intend to quantitatively show that the NAIS is a promising idea, but also use the model for understanding and optimization. Furthermore, we try to lay a solid foundation for future computations on the NAIS. Therefore, we need reasonable quantitative accuracy. On the other hand, full insight in the underlying quantum mechanics would be out of the scope of this research.

Previously, a hard-sphere molecular diameter was used to estimate a pressure such that the mean free path of the ions equals the membrane spacing [1, 2]. Ion-neutral scattering is then assumed to be almost negligible. One problem is that the molecular diameter is a rather ambiguous concept, but moreover this approach is problematic for the following two reasons. Firstly, although a molecular diameter model may have been successful in describing neutral-neutral scattering, it is inappropriate for ion-neutral interaction. Secondly, one may find better performance in a regime where ion-neutral scattering is more abundant. In fact, it is evident that gas scattering is a significant phenomenon any optimized NAIS system. If the particle density is sufficiently low to have negligible gas scattering, an optimum is not reached as the brightness can be increased by simply increasing the particle density.

## 4.2. Ion-neutral interaction

### 4.2.1. Momentum transfer and charge exchange

Qualitatively we can describe ion-neutral interaction as follows. Upon encounter, the ion polarizes the neutral atom, creating a strong interaction potential, when compared to neutral-neutral interaction. Hence, scattering with large momentum transfer is more likely for ions than for neutrals. The interaction potential acts over a long range such that a high probability of weak scattering is present as well. We furthermore recognize hitting the rigid core of the interaction potential, which resembles a hard-sphere collision.

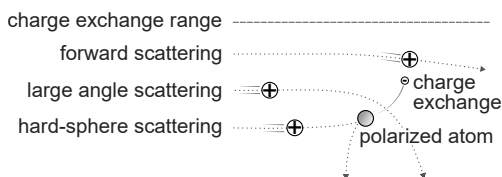


**Figure 4.1.** Ion-neutral encounter. The ion trajectory may be hardly affected, follow a curved path closely passing the neutral, or scatter on the rigid core of the atom. In addition one electron may be exchanged.

In addition to momentum transfer, the ion and the neutral can exchange an electron fairly easily because of the symmetry in the electron energy level. Rapp and Francis [3] showed that the probability of exchanging charge is a rapidly oscillating function of the impact parameter up until a particular length, whereafter it attenuates quickly. Most often, the detailed oscillating behavior is neglected and an average probability of 0.5 is used for ions passing a neutral within a particular distance. For energetic ions ( $\epsilon > 1$  eV), the inter-atomic distance over which charge exchange can occur is much larger than the distances over which significant momentum transfer occurs. In that case, the identity of the ion and the neutral essentially change without any deflection. When the impact parameter is small though, charge exchange still occurs with probability of about 0.5, but an identity switch is no longer a sufficient description of the collision.

#### 4.2.2. Cross sections for ion-neutral scattering

A hard-sphere model for ion-atom scattering using double the molecular cross section for neutral particles in combination with an identity switch of probability 0.5 has been used [4]. This gave reasonable results for the drift velocity under certain conditions, but gives considerable errors in for example the transverse diffusion of ions in a neutral gas.

A very accurate approach to ion-neutral interaction would be using an energy dependent differential cross section. Such an approach can take into account momentum transfer as well as charge exchange, when combined with energy and momentum conservation. In the end, it is just an atom and an ion going in and the same going out. Whether the outgoing ion was originally an atom or an ion doesn't matter for the post-collision momentum vector calculation. The disadvantage of a differential cross section approach is the scarcity of data and the computational complexity. It also diminishes intuitive understanding to some extent.

Phelps [5] argues that the differential cross section in the center-of-mass frame can be separated, artificially, into an isotropic part, a forward scattering peak, and a back-scatter peak. One can recognize the isotropic part as a variable hard sphere collision with or without charge exchange. For isotropic scatter events, charge containment and charge exchange are indistinguishable. It can be shown that the back-scatter peak in the center-of-mass frame is identical to an ion-neutral identity switch in the lab-frame. This also called idealized charge exchange, meaning that charge is exchanged without any exchange of momentum. The velocity distributions of isotropic and charge exchange collisions are sketched in figure 4.2. The forward scatter peak corresponds to ions being affected very weakly by the polarizing potential. This peak is neglected because it doesn't influence the kinematics very much.

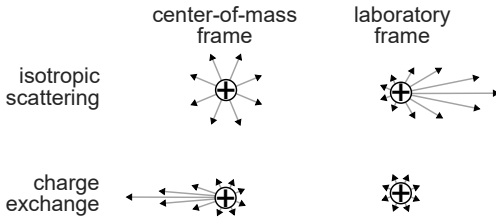


**Figure 4.2.** A sketch of the post-collision ion velocity distribution. In this example the initial ion velocity is much larger than the thermal neutral. The term isotropic collision is claimed due to the isotropy in the center-of-mass frame, but in the laboratory frame the distribution is forward-skewed due to the conservation of the ion momentum.

A word of caution is in place here. In the literature one can find total charge exchange cross sections, see for example Pullins [6]. However, using such cross sections and assume the charge exchange to be ideal, leads to an underestimate of the momentum exchange for low energies. In the Phelps model, the portion of charge exchange events with considerable momentum transfer is included in the isotropic cross section and excluded from the idealized charge exchange cross section. This improves the accuracy for describing the anisotropy at low energies.

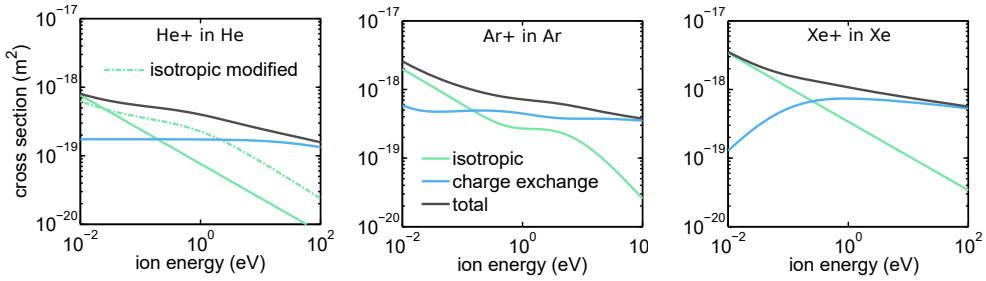


**Figure 4.3.** Ion-neutral scattering cross sections of argon [5], helium, and xenon [7] ions in their parent gas proposed by Phelps on an energy domain relevant for the NAIS

It should be mentioned that yet a different model was proposed by Nanbu [8], but this is more computationally demanding and quite frankly a bit non-transparent. A simplified version of this model is also proposed by Nanbu [9] and it shows fair agreement with experimental data, but not as good as the Phelps model.

Phelps described his model for argon [5] initially and gave fits for the cross sections. The cross sections are given as a function of the relative energy between the ion and the neutral  $\epsilon = \frac{1}{2}m|\mathbf{u}_i - \mathbf{u}_n|^2$  in units of electron volt with the cross section in  $\text{m}^2$ . The fit for the isotropic part of the cross section is

$$\sigma_{\text{iso,Ar}}(\epsilon) = \frac{2 \times 10^{-19}}{\epsilon^{0.5}(1 + \epsilon)} + \frac{3 \times 10^{-19}\epsilon}{(1 + \epsilon/3)^2}. \quad (4.1)$$

The idealized charge exchange cross section is found indirectly through the use of a total momentum transfer cross section. This cross section is associated with the average momentum transferred in a collision. The total momentum transfer cross section is found to follow the fit

$$\sigma_{\text{m,Ar}}(\epsilon) = \frac{1.15 \times 10^{-18}(1 + 0.015/\epsilon)^{0.6}}{\epsilon^{0.1}}. \quad (4.2)$$

Phelps explains that back-scatter events on average transfer double the momentum compared to isotropic collisions. So, a total cross section describing the net momentum transfer is  $\sigma_m = \sigma_{\text{iso}} + 2\sigma_{\text{cx}}$ . Hence, the idealized charge exchange cross section is given by

$$\sigma_{\text{ctr,Ar}}(\epsilon) = \frac{1}{2}(\sigma_{m,\text{Ar}} - \sigma_{\text{iso,Ar}}). \quad (4.3)$$

Note that the total cross section describing the probability of any event happening, is simply  $\sigma_{\text{tot}} = \sigma_{\text{iso}} + \sigma_{\text{cx}}$ .

Elsewhere, fits for other noble gases are reported by Phelps [7], but these are never officially published and not as thoroughly verified as the ones for argon. For xenon the cross sections are

$$\sigma_{\text{iso,Xe}}(\epsilon) = \frac{33.9 \times 10^{-20}}{\epsilon^{0.5}} \quad (4.4)$$

$$\sigma_{\text{cx,Xe}}(\epsilon) = \frac{36 \times 10^{-20} (1 + 100\epsilon^2)^{0.2}}{\epsilon^{0.42} (1 + 0.09/\epsilon)^{1.3} (1 + 0.001\epsilon)^{0.25}} \quad (4.5)$$

The isotropic cross section is essentially the Langevin spiraling cross section [10] (see for example reference [11] for more on this relation).

For helium we found it necessary to make changes to the cross sections from the fits proposed by Phelps. We will state the result here and motivate the changes in section 4.4.

$$\sigma_{\text{iso,He}}(\epsilon) = \frac{4.5 \times 10^{-20} (1 + 8\epsilon^{0.65})}{\epsilon^{0.5} (1 + 1.3\epsilon)^{0.7}} \quad (4.6)$$

$$\sigma_{\text{cx,He}}(\epsilon) = \frac{1 \times 10^{-19}}{(0.001\epsilon)^{0.15} (1 + 5/\epsilon)^{0.15} (1 + 0.001\epsilon)^{0.25}} \quad (4.7)$$

Surely there is a lot more complexity to ion-neutral interaction than this model encompasses [12], but these details are not relevant for estimating the properties of the NAIS. The limitation of the Phelps model is found mainly in the accuracy of approximating the differential cross section by an isotropic and a back-scatter part. The model has been used by various others for example Jovanovic et. al. [13], Robertson and Sternovsky [14] and more recently by Ristivojevic and Petrovic [15]. All authors concluded good agreement with the experimental data.

### 4.3. Monte-Carlo implementation

We intend to use the interaction model discussed in the previous section in a Monte-Carlo ray tracing scheme. The details of the Monte-Carlo implementation are elaborated in this section. The method is similar, though not identical to what is used elsewhere [4, 13–15].



#### 4.3.1. Collision kinematics

When ray tracing, we are interested in the change in the velocity vector of the ion in the case of a scatter event. It is a textbook exercise to calculate the post collision velocities of isotropically scattering equal-mass particles. The result [4] is

$$\mathbf{u}'_i = \frac{1}{2}(\mathbf{u}_i + \mathbf{u}_n) + \frac{1}{2}|\mathbf{u}_i - \mathbf{u}_n|\hat{\mathbf{R}} \quad (4.8)$$

$$\mathbf{u}'_n = \frac{1}{2}(\mathbf{u}_i + \mathbf{u}_n) - \frac{1}{2}|\mathbf{u}_i - \mathbf{u}_n|\hat{\mathbf{R}} \quad (4.9)$$

A primed vector indicates post-collision and  $\hat{\mathbf{R}}$  is a randomly oriented unit vector. The pre- and post-collision velocity vectors here are given in the lab-frame and can be used right away in a simulation. We use i for ion, n for neutral atom and  $\mathbf{u}$  for velocity.

Idealized charge exchange is essentially an identity switch and the post collision velocities are given by:

$$\mathbf{u}'_i = \mathbf{u}_n \quad (4.10)$$

$$\mathbf{u}'_n = \mathbf{u}_i. \quad (4.11)$$

#### 4.3.2. The scattering frequency

In the Monte-Carlo ray-tracing scheme we need to determine every time step which ions should change their velocity due to a scatter event. Therefore, we define a scattering frequency as the number of scatter events per unit of time:

$$\nu(\mathbf{u}_i) = \text{scattering frequency}. \quad (4.12)$$

The use of this quantity is finding the probability of an event in one time step. In the simple case that the medium is stationary, we can find it from  $\nu = n\sigma(u_i)u_i$ . If, however, the medium is not static, the contribution to the collision frequency should be integrated over all possible velocity vectors of the neutral atoms. The generalized scatter frequency becomes

$$\nu(\mathbf{u}_i) = n \iiint \sigma(\mathbf{u}_i - \mathbf{u}_n) |\mathbf{u}_i - \mathbf{u}_n| f(\mathbf{u}_n) d\mathbf{u}_n \quad (4.13)$$

with  $f(\mathbf{u}_n)$  the probability density function for the velocity of neutral particles.

We simplify the system by assuming the neutrals to be in thermal equilibrium. This means that the neutral velocities are Maxwell-Boltzmann distributed:

$$f(\mathbf{u}_n) = \left( \frac{m}{2\pi kT} \right)^{3/2} e^{-\frac{m|\mathbf{u}_n|^2}{2kT}}. \quad (4.14)$$

For neutrals that are expanding into the vacuum this assumption becomes shaky. However, in section 4.6 it is explained that the density outside the chip is very low, so inaccurate modeling at these locations is not problematic.

Equation 4.13 is quite problematic from a practical point of view. Suppose using it as-is, then, every time step one would need to calculate the full 3D integral for

every ion. This would be unacceptably slow. We could generate a 3D look-up table prior to the simulation, but luckily we have a better trick.

In equation 4.13, the ion velocity vector can be chosen in any direction due to the rotational symmetry of the neutral velocity distribution  $f(\mathbf{u}_n)$ . Essentially, we employ the observation that  $v(\mathbf{u}_i) = v(|\mathbf{u}_i|\hat{\mathbf{x}})$ , for rotationally symmetric  $f$ . The advantage of using this symmetry is that the collision frequency becomes a function of the ion velocity magnitude only. All of a sudden, we can suffice with a 1D look-up table, which is quite convenient indeed.

The look-up table we pre-calculate is not exactly equation 4.13. Since the scattering frequency is proportional to the particle density we can tabulate  $v(u_i)/n$  and at run-time multiply by the local particle density.

### 4.3.3. Event probability and time step control

For deciding if an event occurs in a time step, we need to transfer the scattering frequency to a scattering probability. The scattering frequency is time-independent so the number of collisions in a time interval  $\Delta t$  is described by a Poisson distribution:  $P_k = (k!)^{-1} \mu^k e^{-\mu}$  with  $\mu = v\Delta t$ .

Our simulation is incapable of handling more than one collision per time-step so a Poisson distribution only makes sense if the criterion  $P_{k>1} \ll P_1$  is met. This simply states that the probability of multiple scatter events needs to be negligible and this is equivalent to  $v\Delta t \ll 1$ .

An alternative to the Poisson distribution is

$$P_0 = 1 - v\Delta t \quad (4.15)$$

$$P_1 = v\Delta t \quad (4.16)$$

$$P_{k>1} = 0 \quad (4.17)$$

The advantage is that now we only require  $v\Delta t < 1$  as  $P_{k>1} \ll P_1$  is automatically met. The number of events over a long time  $T$  is clearly just  $vT$ , indeed what it should be, even if  $v\Delta t$  is close to 1. A second advantage is that this distribution is computationally less costly.

The only error made here is the unjustified spatial separation of events. This boils down to an inaccuracy in the location of the scatter events. The criterion for a time step size thus becomes  $\Delta t < \Delta x u_i$ , with  $\Delta x$  the maximum allowed positional inaccuracy. The required time step depends on the specific simulation, but for example for 1 eV argon ions and a required positional accuracy of 2 nm, we require time-steps of about 1 ps.

More generally we try to relate the positional accuracy to the mean free path. Suppose we have an estimate for the mean free path  $\lambda$  in a particular configuration (see section 4.5), then, we can estimate the maximum ion velocity from

$$u_i = \sqrt{\frac{2eE\lambda}{m}} + u_t, \quad (4.18)$$

with  $E$  the electric field strength. Note that the addition of the thermal velocity  $u_t$  is needed to ensure a small enough time step in the case of a weak field or a dense gas. The maximum allowed time step is given by

$$\Delta t < \frac{\Delta x}{\lambda} \left( \sqrt{\frac{2eE}{m\lambda}} + \frac{u_t}{\lambda} \right)^{-1} \quad (4.19)$$

Setting  $\frac{\Delta x}{\lambda} = 0.1$  was tested to be sufficient for most NAIS simulations.

The scatter probability depends on the ion velocity, the neutral particle density, and the time step and should therefore be calculated every time step for every particle. This is costly so an improvement here is effective. The null collision method, as explained for instance by Vahedi [16] introduces a constant probability that is larger than any possible real scattering probability. The null collision probability is  $P_{\text{null}} = \max(nv_n \Delta t)$ . Only in case that a random number between 0 and 1 is smaller than this maximum probability do we calculate the real scattering probabilities.

#### 4.3.4. Sampling a neutral atom

In the case of a scatter event, we need to sample a neutral atom such that we can calculate the kinematics of the ion. As pointed out by Robertson and Sternovsky [14] and by Ristivojevic and Petrovic [15], sampling a neutral atom should not be done using a Maxwell-Boltzmann distribution, even though the neutral gas is assumed to be Maxwell-Boltzmann distributed. The probability of sampling a particular neutral velocity vector should be proportional to the amount it contributes to the collision frequency. This is simply the integrand of equation 4.13. So the probability density function for sampling a neutral atom  $g(\mathbf{u}_i, \mathbf{u}_n)$ , is given by

$$g(\mathbf{u}_i, \mathbf{u}_n) = \frac{\sigma(\mathbf{u}_i - \mathbf{u}_n) |\mathbf{u}_i - \mathbf{u}_n| f(\mathbf{u}_n)}{v(\mathbf{u}_i)/n}. \quad (4.20)$$

When sampling from a distribution function, inverse transform sampling is often used. This requires the inverse of the cumulative probability density function, which is not attainable in this case. An alternative is the acceptance-rejection method. One generates uniformly distributed random variables over a pre-defined domain and any sample under the curve of the probability distribution is usable. This method requires the peak value of the probability density function. We can use the symmetry of the Maxwell-Boltzmann function again, as  $\max g(\mathbf{u}_i, \mathbf{u}_n) = \max g(|\mathbf{u}_i| \hat{\mathbf{x}}, \mathbf{u}_n)$  and a numerical optimization routine in MATLAB is used to find the maximum for a broad range of ion velocities. It turns out, a look-up table is not needed because the peak value of the distribution is fairly constant, so we can use a single number. For helium, argon and xenon we find that the values  $1.4 \times 10^{-10} \text{ s}^3 \text{ m}^{-3}$ ,  $4.2 \times 10^{-9} \text{ s}^3 \text{ m}^{-3}$ , and  $2.6 \times 10^{-8} \text{ s}^3 \text{ m}^{-3}$  are at least  $\max g(\mathbf{u}_i, \mathbf{u}_n)$ . The values work for both isotropic as well as charge exchange collisions.

If  $u_i \gg u_n$  then  $g(\mathbf{u}_i, \mathbf{u}_n) \approx f(\mathbf{u}_n)$ , so in many cases sampling from a MB-distribution will give only a limited inaccuracy. Using the distribution described

here, however, ensures proper sampling in any case. In particular this could be important in weakly accelerating situations with ion energies not much larger than the thermal energy.

#### 4.3.5. Software

A useful model of the NAIS does, besides ion-neutral scattering, include the electrostatic field inside the chip, the acceleration field outside the chip, and the coulomb interactions between the ions. Therefore, it is chosen to implement the ion neutral scattering model into the general particle tracer software from Pulsar Physics [17]. This software takes care of the ray tracing including coulomb interactions. In this way, all relevant physics can be simulated simultaneously. We calculate the electric fields using the Electron Optical Design software [18].

### 4.4. Model validation

#### 4.4.1. Method of validation

To check if the simulation implementation is sound, a simple configuration was set up and tested. Ions starting in the origin are traced through a region of constant particle density  $n = 3.535 \times 10^{22} \text{ m}^{-3}$ , constant temperature of 293 K. Figure 4.4 shows an example of some traced trajectories. After traveling for several thousands of mean free path-lengths, two quantities often encountered in plasma physics are computed and compared to literature values: the drift velocity and the reduced transverse diffusion coefficient. This approach is similar to what is done by Robertson and Sternovsky [14]. The computed quantities are

$$u_{\text{drift}} = \frac{\langle z \rangle}{t_{\text{sim}}}, \quad D_t = \frac{1}{4} \frac{\langle r^2 \rangle}{t_{\text{sim}}}, \quad \mu = \frac{u_{\text{drift}}}{E}. \quad (4.21)$$

Particularly the reduced transverse diffusion coefficient ( $D_t/\mu$ ) is infamous for its sensitivity to errors in the model or inaccurate handling of the anisotropy in the cross sections [13].

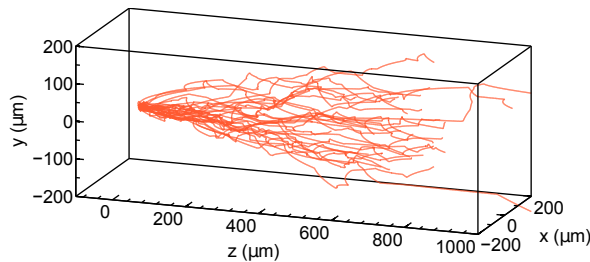


**Figure 4.4.** Example of tracing  $\text{Ar}^+$  ions through argon gas with particle density  $3.535 \times 10^{22} \text{ m}^{-3}$  and a temperature of 293 K. An electric field of 10 V/mm was applied in the positive  $z$ -direction. Such tracing is used to determine the drift velocity and the transverse diffusion coefficient for testing the simulation. Shown here is a set of 30 particles each having around 25 scattering events, but in a typical model validation simulation 3000 particles are traced each undergoing around 5000 scattering events.

The maximum simulation time step was determined by equation 4.19 using a very accurate setting:  $\Delta x / \lambda_{\text{eff}} = 1/200$  with mean free path estimates are taken from section 4.5. The simulation time  $t_{\text{sim}}$  is adjusted accordingly to run for about 5000 mean free paths lengths. A total of 3000 particles are used.

#### 4.4.2. Argon

Figure 4.5 shows the ray tracing result for argon. The correspondence with experimental drift velocities is nearly perfect and the match for the transverse diffusion coefficient is also quite good. This result indicates that there are no problems with the implemented code, but also that the cross sections suggested by Phelps are describing the ion-neutral interaction quite well.

For the sake of comparison, a fixed-size hard-sphere simulation was run, with twice the molecular cross section of neutral-neutral interaction, as suggested by Nanbu [4]. The molecular diameter used was 369 pm [19]. We see that for both quantities the values are quite far off and one can not expect accurate results from this, perhaps a little too simple, model.

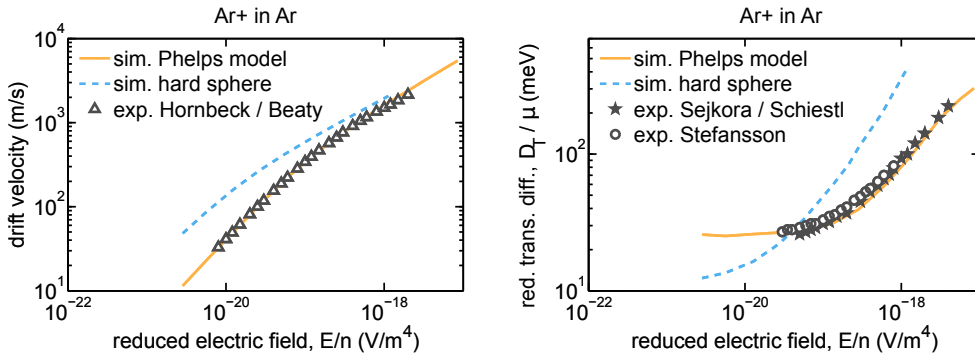


**Figure 4.5.** Comparison of the simulation implementation used in this work to experimental data. Settings:  $n = 3.535 \times 10^{22} \text{ m}^{-3}$  and  $T = 293 \text{ K}$ , the electric field was varied. The experimental values for the drift velocity are taken from tabular data composed by Ellis [20], which is based on measurements performed by Hornbeck [21] and by Beatty [22]. The transverse diffusion coefficient data is taken from measurements by Stefansson [23] and also from tabulated values composed by Viehland [24], which is based on measurements from Sejkora [25] and Schiestl [26].

#### 4.4.3. Helium

The cross sections proposed for helium [7] were tested, but didn't show such a great accordance with measured transverse diffusion data as can be seen by dashed curve in figure 4.6. An adjustment to the cross sections was made, notably at energies around 1 eV the isotropic cross section is made a little larger than the Langevin cross section [10]. The same type of adjustment can be seen in the isotropic cross section for argon. The result of the adjustment is an excellent match between the simulation and the experimental data. Equation 4.6 give the adjusted cross sections.

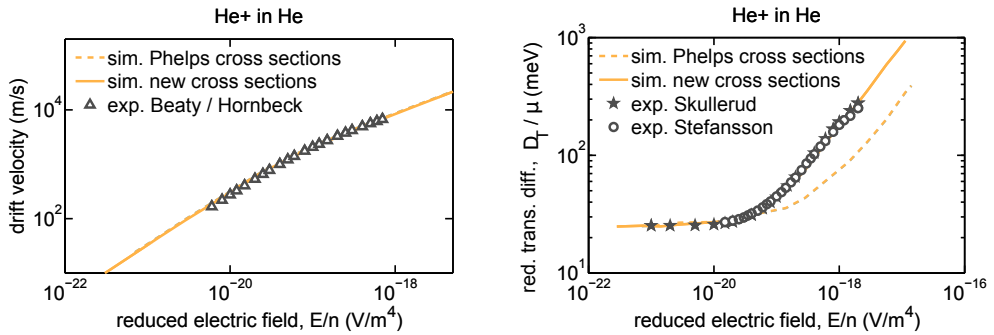


**Figure 4.6.** Comparison of the simulation implementation used in this work to experimental data. Settings:  $n = 3.535 \times 10^{22} \text{ m}^{-3}$  and  $T = 293 \text{ K}$ , the electric field was varied. The experimental values for the drift velocity are taken from tabular data composed by Ellis [20], which is based on measurements performed by Hornbeck [21] and by Beaty [22]. The transverse diffusion coefficient data is taken from measurements by Skullerud [27] and by Stefansson [28]

#### 4.4.4. Xenon

Cross sections for xenon [7] were also tested. In the literature [29] we find for the drift velocity a distinction between the ionic ground state  $P_{3/2}$  and the metastable state  $P_{1/2}$ . The energy difference between these state is 1.31 eV and the lifetime of the metastable state is 48 ms [30]. Phelps does not elaborate on different excitations of the ionized states for his cross sections and we can only assume the cross sections to represent a combination of unknown proportion. The proportion of both states depends mainly on the means and details of ionization and will differ from experiment to experiment. Despite this ignorance, we can boldly state that knowing the exact proportion is not so relevant as it gives nearly the same scattering properties. We can see in figure 4.7 that the experimental data of drift velocity for the different excitations is hardly distinguishable. Note that this applies to argon as well [12].

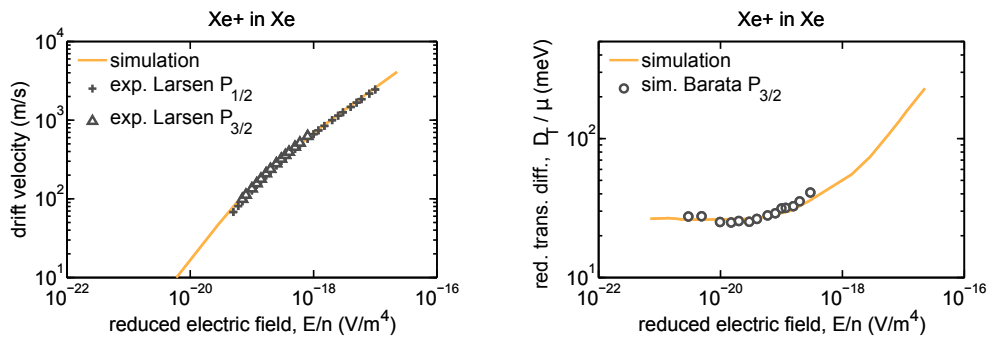


**Figure 4.7.** Comparison of the simulation implementation used in this work to experimental data. Settings:  $n = 3.535 \times 10^{22} \text{ m}^{-3}$  and  $T = 293 \text{ K}$  while the electric field was varied. The drift velocity measurements are taken from Larsen [29] and the distinction between the ground state  $P_{1/2}$  and the excited metastable state  $P_{3/2}$  is made. No experimental data for the transverse diffusion coefficient was available and a comparison was made to a simulation performed by Barata [30].

We could not find experimental data for the reduced transverse diffusion coefficient for xenon, so the next best thing was a comparison to other calculations

executed by Barata [30]. These calculations were based on ion-atom interaction potential models by Tang and Toennies [31] and have no direct relation to the cross sections proposed by Phelps. We find a good correspondence between the work by Barata and this work, at least in the range for which calculations were performed.

## 4.5. An effective mean free path

### 4.5.1. MFP for constant velocity

A useful and intuitive way of describing scattering is via a mean free path (MFP). For a constant cross section, a MFP is fairly simply given by  $\lambda_{\text{eff}} = (\sigma n)^{-1}$ . However, when the cross section is energy dependent, and the medium is non-stationary as well, the calculation is more tricky. We can calculate the MFP as the inverse of the collision density (number of collisions per unit length) and get

4

$$\lambda^{-1} = \frac{v(u_i)}{u_i} = \frac{n}{u_i} \iiint \sigma(|\mathbf{u}_i - \mathbf{u}_n|) |\mathbf{u}_i - \mathbf{u}_n| f(\mathbf{u}_n) d\mathbf{u}_n. \quad (4.22)$$

It is interesting to relate the cross sections discussed in the previous section to a mean free path using this equation. Numerical evaluation is performed for a 1 bar pressure and the result is shown in figure 4.8a. Note that the MFP is inversely proportional to the particle density (or pressure) so the presented curve can be scaled accordingly.

### 4.5.2. MFP in an electric field

The mean free path calculation of the previous section gives some insight, however does not quite cut it for the purpose of the NAIS. It is rather unclear what energy appropriately describes the NAIS. In fact, the ions are accelerated through the gas, starting with thermal energy, up to say 1eV, hence there is not really one particular energy assignable. Nevertheless, what is unambiguous, is the electric field strength. Furthermore, in a NAIS system we are interested in unscattered particles, as these are responsible for the high beam quality. Therefore, we define a mean free path as follows: the average unscattered travel distance for ions being accelerated in an electric field. To be clear, this MFP relates to the first scatter event after generation

A mean free path is normally non-directional, but for the purpose of the NAIS, we are more interested in how far the particle travels towards the end of the gas region. Therefore we define the mean free path as the average traveled z-distance; not as the average length of the trajectory. Note that the particle starts with an initial thermal energy in the x and y directions. A most comprehensive analysis integrates over the initial thermal velocity vectors, but this leads to a numerical challenge, so this is avoided. In stead, we pick a typical initial ion, having  $kT$  of energy in the transverse direction. We assign no initial energy to the z-direction because the particle can travel forward or backward, and setting the initial velocity to zero approximately balances this out.

The mean free path as described above can be calculated from

$$\lambda_{\text{eff}} = \int_0^{\infty} z(t) \rho(t) dt, \quad (4.23)$$

with  $\rho(t)$  the probability density function of an ion scattering between  $t$  and  $t + dt$ . The calculation is performed in the time domain to keep the equations and the numerical computation later-on a bit neater. We find  $\rho$  from an intensity attenuation analysis. If  $I$  is the current of an initial ion beam, then the loss in current by scattering is described by

$$dI = -Iv dt \rightarrow I = I_0 e^{-\int_0^t v dt'}. \quad (4.24)$$

This is similar to a Lambert-Beer law, but the integral in the solution can not be expressed explicitly because the collision frequency is not an analytical function; it is the result of the volume integral of equation 4.13. We can relate the current to a probability density according to

$$\rho(t) dt = -\frac{dI}{I_0} = -d(e^{-\int_0^t v dt'}) = v e^{-\int_0^t v dt'} dt. \quad (4.25)$$

We also need the ion position and velocity as a function of time, while being accelerated in an electric field:

$$z(t) = \frac{eE}{2m} t^2, \quad |\mathbf{v}(t)| = \sqrt{\frac{2kT}{m} + \left(\frac{eE}{m} t\right)^2}. \quad (4.26)$$

Combining equations 4.23, 4.25, and 4.26, the effective mean free path to a first scatter event in an electric field is given by

$$\lambda_{\text{eff}} = \frac{eE}{2m} \int_0^{\infty} t^2 v(t) e^{-\int_0^t v(t') dt'} dt. \quad (4.27)$$

The numerical evaluation of this integral for atmospheric pressure as a function of the electric field is shown in figure 4.8b. Note that, in contrast to the energy dependent MFP, this MFP does not scale simply with the particle density.

To get a feeling for the relative influence of the isotropic and charge exchange events to the MFP, we compute an effective MFP for both type of events according to

$$\lambda_{\text{iso}}^{-1} = \lambda_{\text{eff}}^{-1} \int_0^{\infty} v_{\text{iso}}(t) e^{-\int_0^t v(t') dt'} dt \quad (4.28)$$

$$\lambda_{\text{cx}}^{-1} = \lambda_{\text{eff}}^{-1} \int_0^{\infty} v_{\text{cx}}(t) e^{-\int_0^t v(t') dt'} dt. \quad (4.29)$$

Note that the non-sub-scripted  $v$  represents the total collision frequency. These MFP's interpolate to the total MFP by inverse addition; exactly what is common



for mean free paths. The integrals in these equations essentially represent the contributing fraction of the particular event-type to the full MFP calculation.

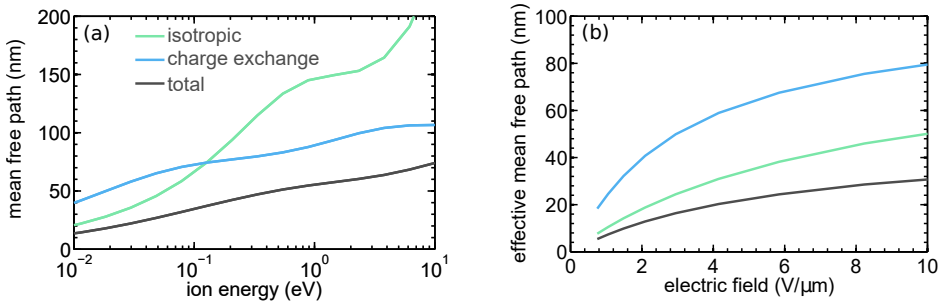


**Figure 4.8.** Ionic mean free path calculations at atmospheric pressure of argon ions through argon gas, based on the cross sections discussed in section 4.2.2 at  $T=293\text{K}$ . a) The argon ions travel through their parent gas at constant velocity. b) Ions are accelerated in an electric field and the effective mean free path is calculated according to equation 4.27.

Figure 4.8b is the result of evaluating equation 4.27 for argon at atmospheric pressure. For a field of 4 kV/mm, the mean free path is about 20 nm. Rather small, compared to 70 nm derived from a molecular diameter model. The graph shows that at this particle density, isotropic collisions are more important than charge exchange events. Charge exchange events are not negligible though. Since the kinematics of the two event types are not the same, a molecular diameter model will have an additional error in describing the collisions, besides being of the wrong magnitude. The mean free path can be tuned between 10 to 30 nm by changing the electric field. The quick explanation is: a higher field brings the ions up to higher energy quicker, which makes the polarization potential less influential.

The calculations shown in figure 4.8 are only valid for atmospheric pressure. We would like to have a more general result, but the difficulty is that the mean free path does not simply scale with the particle density due to the energy dependence of the cross sections. However, if the particle density and the electric field are scaled simultaneously, all possible ions trajectories are scaled proportionally in terms of energy at the moment of a collision. This means that we can write  $\lambda_{\text{eff}} = f\left(\frac{E}{n}\right) \frac{1}{n}$ , with  $f$  some unknown function.  $E/n$  is the reduced electric field and the quantity  $n\lambda_{\text{eff}}$  is a function of this variable only; a more general result indeed. Reasonable fits for  $f\left(\frac{E}{n}\right)$  were found, allowing us to summarize a lot of information:

$$n\lambda_{\text{eff}} = f\left(\frac{E}{n}\right) \approx a \cdot \ln\left(b \frac{E}{n}\right) \quad \text{or} \quad \left(a \frac{E}{n}\right)^b \quad (4.30)$$

We can use this equation to estimate the MFP for a particular combination of  $E$  and  $n$ . This circumvents the need for the complicated evaluation of equation 4.27 (the evaluation of 4.27 was of course needed to acquire the fits in the first place). The fitting results are given in table 4.1. Note that sometimes a power law was more appropriate than the natural log to describe the curve.

	fit	$a$	$b$	fit domain $E/n$ $\text{Vm}^2$	mean err. %	max err. %
<b>Helium</b>						
Total	ln	$6.93 \times 10^{17}$	$5.39 \times 10^{19}$	$3.7 \times 10^{-20} - 5.0 \times 10^{-18}$	4.0	13.0
Isotropic	p	$4.84 \times 10^{56}$	0.484		3.9	8.9
Char. Exch.	ln	$6.46 \times 10^{17}$	$4.59 \times 10^{21}$		3.7	13.2
<b>Argon</b>						
Total	ln	$2.50 \times 10^{17}$	$5.56 \times 10^{19}$	$2.3 \times 10^{-19} - 2.0 \times 10^{-17}$	1.2	5.0
Isotropic	ln	$5.58 \times 10^{17}$	$2.24 \times 10^{19}$		2.6	4.8
Char. Exch.	ln	$3.97 \times 10^{17}$	$4.35 \times 10^{20}$		3.0	8.6
<b>Xenon</b>						
Total	ln	$2.22 \times 10^{17}$	$2.32 \times 10^{19}$	$3.1 \times 10^{-19} - 2.4 \times 10^{-17}$	0.2	0.3
Isotropic	p	$6.24 \times 10^{48}$	0.591		2.0	10.0
Char. Exch.	ln	$1.02 \times 10^{17}$	$3.04 \times 10^{23}$		0.9	1.7

**Table 4.1.** Fit parameters for equation 4.30. Outside the specified domain the quality of the fits is not assessed. 'ln' indicates the natural logarithm fit and 'p' denotes power law. The units in the fit functions are meter and Volt.

### 4.5.3. Unscattered ionization efficiency

The fit functions (equation 4.30) for  $n\lambda_{\text{eff}}$  are very useful for calculations, but  $n\lambda_{\text{eff}}$  is somewhat of an indirect quantity in itself. More instructive is the efficiency of electron to ion current. For the moment, we simplify the gas density by a top-hat distribution of length  $l$  and particle density  $n$ . The ion current  $J_I$  as generated by electron impact ionization is then given by  $J_I = J_e n \sigma_I l$ , with  $J_e$  the electron current density.

Suppose the length  $l$  is at least a few MFP's long. The generated ions from the back won't make it out unscattered, but the ones generated within one or two MFP's from the exit aperture are quite likely to make it out. A reasonable simplification is to say that all ions within one MFP from the end make it out unscattered, and no other. This gives as an estimate for the ionization efficiency of unscattered particles:

$$\eta_{\text{unscat}} \approx n \sigma_I \lambda_{\text{eff}} \quad (4.31)$$

We could plot the ionization efficiency versus  $E/n$  however  $E/n$  doesn't tell a whole lot either. We introduce a quantity with units of energy as

$$\epsilon_E = eE\lambda_{\text{eff}} = \text{mean free energy.} \quad (4.32)$$

This quantity represents the average energy an ion gains before it scatters. Since we can write it as  $\epsilon_E = n\lambda_{\text{eff}} \frac{E}{n} = f\left(\frac{E}{n}\right) \frac{E}{n}$ , we can combine it with equation 4.30 and obtain  $n\lambda_{\text{eff}}$  as a function of  $\epsilon_E$  only. So,  $\epsilon_E$  is an alternative independent variable to  $E/n$ .

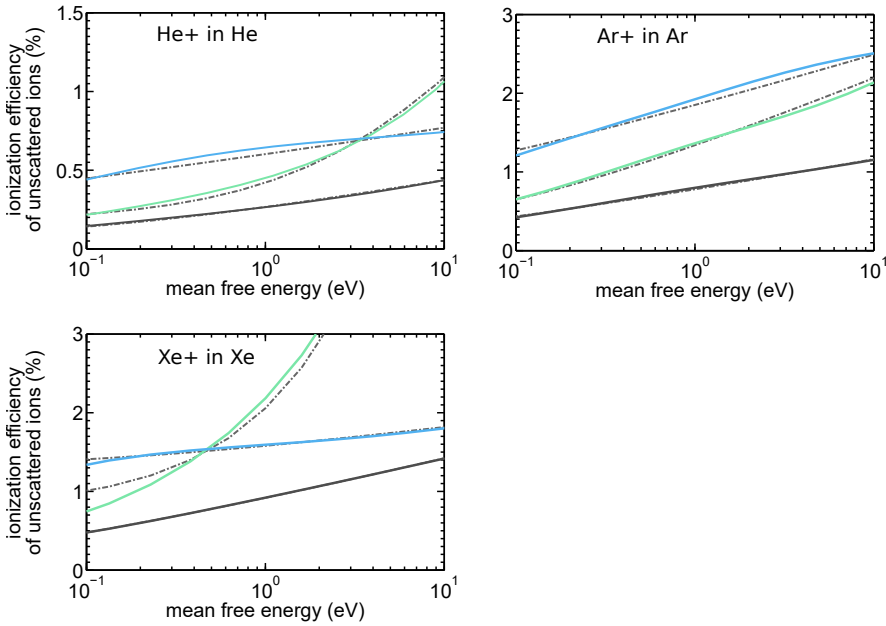


**Figure 4.9.** Calculated conversion ratio of electron current to unscattered ion current for a 1 keV electron beam. The ions are accelerated in a gas with uniform particle density and uniform electric field. Cross section data from Rejoub [32]. The dashed gray lines are calculated from the fit functions given by equation 4.30.

Figure 4.9 shows the result of the unscattered ionization efficiency as a function the mean free energy  $\epsilon_E$ . In this example we have used the ionization cross section of a 1 keV electron beam. Perhaps the most important message here is that we can expect in the order of 1% of unscattered ionization efficiency for typical NAIS configurations. The unscattered ionization efficiency may be somewhat tunable, but this requires orders of magnitude difference in the acquired energy. A high mean free energy translates to a high energy spread. We may get a higher total ionization efficiency, but the excess generated current will scatter on neutral particles and does not contribute as much to the brightness as unscattered ions do.

#### 4.5.4. The ionic Knudsen number

So far in this section we have tried to develop an intuitive assessment of the NAIS emission region. We have introduced an effective mean free path and in the previous subsection we have simplified the particle density distribution by a top-hat distribution of length  $l$ . Both the mean free path and the gaseous length only have meaning relative to each other, and here we introduce a more general concept for characterizing the operation condition of a particular geometry. In the case of neutral particles, characterizing confined geometries is often done by the Knudsen number. We can extend that idea by introducing the ionic Knudsen number. It is the effective MFP, divided by an appropriate length measure for the gaseous region:

$$\text{iKn} = \text{ionic Knudsen number} = \frac{\text{ion mean free path}}{\text{length of gas region}}. \quad (4.33)$$

Arguably, Knudsen defined his number inconveniently. It is actually better to work with the inverse ionic Knudsen, as will become apparent. To avoid confusion, however, we keep the definition in line with the original Knudsen number.

The inverse ionic Knudsen number,  $iKn^{-1}$ , indicates the average number of scatter events for particles starting from the back of the confined gas region. If  $iKn^{-1} > 1$ , this is strictly speaking not entirely correct because the MFP used was calculated for single scatter events and not for multiple scatter events. In practice  $iKn^{-1}$  is a good indicator of the expected number of scatter events anyhow.

An inverse ionic Knudsen number  $iKn^{-1} = 10$  means that most generated ions will scatter several times while a value of 0.2 is practically a scatter free situation.  $iKn^{-1} = 1$  essentially marks the transition from scatter free to scatter rich systems.

The ionic Knudsen number can be found from the fit function of equation 4.30 as

$$iKn = \frac{1}{nl} f\left(\frac{E}{n}\right) \quad (4.34)$$

The total and the unscattered ionization efficiencies are related by

$$\eta_{\text{unscat}} \approx iKn \cdot \eta_{\text{tot}}. \quad (4.35)$$

The mean free energy can be calculated from

$$\epsilon_E = iKn \cdot eEl = \frac{E}{n} f\left(\frac{eE}{n}\right) \quad (4.36)$$

We give two examples of how to use the ionionic Knudsen number. We begin by setting  $iKn^{-1}$  to 3. Thus, the ions from the back will scatter about three times on average. Furthermore we choose  $E = 3 \times 10^6 \text{ V}\mu\text{m}^{-1}$  and  $l = 600 \text{ nm}$ , so the bias voltage accross the membranes will be 1.8V.

We calculate the mean free energy from equation 4.36 and get  $\epsilon_E = 0.6 \text{ eV}$ . Because  $\epsilon_E$  is smaller than the membrane bias, some energy redistribution will be present. From  $l = 600 \text{ nm}$  and  $iKn^{-1} = 3$  we have directly  $\lambda_{\text{eff}} = 200 \text{ nm}$ . The required particle density can be obtained from equation 4.30 and gives  $n = 4.5 \times 10^{24} \text{ m}^{-3}$ , or 180 mbar. We calculate the total generated current efficiency and obtain 2.1%. The total unscattered efficiency is estimated to be 0.70 %, so for a 100nA ebeam we get 700pA of high quality current. If the spatial fw50 of the ebeam is 100 nm, the brightness by equation 3.28 becomes about  $2 \times 10^6 \text{ A/m}^2\text{srV}$ .

Suppose we would like to generate a large current, say 25% of the e-beam engaging in ionization. Furthermore, we want to keep the pressure below 1 bar ( $n = 2.5 \times 10^{25} \text{ m}^{-3}$  at room temperature). This leads to  $l > 1 \mu\text{m}$ . If we choose a field of  $3 \times 10^6 \text{ V}\mu\text{m}^{-1}$  again, the mean free path is only 19 nm and  $iKn^{-1} = 68$  for  $l = 1.3 \mu\text{m}$ , so heavy scattering will be present.

Inevitably, part of the generated current is blocked by the membranes. The escape probability is typically 50%, but the value depends strongly on the geometry

and field strengths. In the simplified analysis here we can not take this into account quantitatively.

## **4.6. Neutral particle-density distribution**

For simulating ion trajectories in the NAIS we need the neutral density distribution. This distribution dictates the starting positions of the ions and determines the ion-neutral scatter probability.

### **4.6.1. Choice of the model**

We intend to operate the NAIS with  $iKn^{-1} > 1$ . Since the mean free path of neutral atoms in their parent gas is of the same order of magnitude as that of the ions, we expect to work with a Knudsen number  $Kn$  of around 1. (do not confuse the Knudsen number  $Kn$  for neutral particles with the ionic Knudsen number  $iKn$ ). The situation around  $Kn=1$  is known as the transition regime. In this regime, inter-atomic collisions as well as wall effects can be relevant. Rademaker [33] compared three models: free molecular flow, variable hard-sphere and variable soft-sphere. The free molecular flow model does not consider any inter-atomic interactions while the other two models do. At  $Kn = 0.7$  he found no noteworthy difference in the final particle distribution for the different models. The simulated geometry was 100 nm spacing, 100 nm aperture diameter and 100 nm membrane thickness. In this configuration inter-atomic collisions are abundant, but did not manifest themselves in significant neutral particle density variation. Combined simulation and experimental work by Peatross [34] is in agreement with Rademaker's findings.

We assume for other geometries that the difference in neutral particle density, given that  $Kn$  is not much smaller than 0.7, is also well described by free molecular flow. In addition, we recognize that the performance of the NAIS is not very sensitive to the details of the neutral particle density. This means that even at lower Knudsen numbers, where we do start to expect some inaccuracies, free molecular flow modeling can still serve as a reasonable approximation for NAIS simulations.

### **4.6.2. Free molecular flow**

A major advantage of free molecular flow simulations is that the neutral particle density is scalable. So, we have to simulate every geometry only once. This is not possible for models that include particle-particle interactions. There are mainly two options for free molecular flow: Monte-Carlo particle tracking and the surface integral method. We need to know the density around the axis, which is a weak spot for a Monte-Carlo approach; not many particles contribute to the statistics close to the axis. The surface integral method does not suffer from such weakness. A commercial implementation of the method is offered by COMSOL multiphysics [35], which is used in this work.

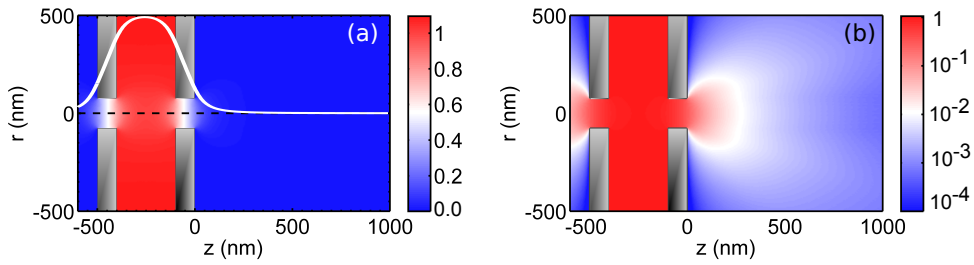


**Figure 4.10.** Normalized neutral particle density of NAIS chip geometry based on free molecular flow. a) Linear color scale. The white curve represents the axial density profile. b) A log color scale is used to reveal the distribution outside the chip better.

Figure 4.10 shows the result of a free molecular flow simulation of a particular chip. We see that the density decreases very rapidly from in between the membrane towards the vacuum region. Within the first micron, the density is decreased more than three orders of magnitude. Because of this rapid decrease we expect limited gas scattering outside the chip.

It is also interesting to note that the radial dependence is not very strong. This can be seen from the absence of curvature in the color gradient inside the aperture. When comparing the density profile in the  $z$ -direction on-axis and off-axis more closely, only minimal differences were observed indeed. Therefore, we only take the  $z$ -dependence into account in the ray trace simulations. On the right hand side of figure 4.10, for  $r$  larger than say 100 nm, we see radial dependence outside the chip. However, practically no ions come there and the density is very low anyway.

#### 4.6.3. Effective length

The length of the gas region is a crucial aspect of the NAIS. In first approximation this is equal to the membrane spacing. However, the aperture allows density outside the chip and a more appropriate measure of the gas length is the effective length:

$$l_{\text{eff}} = \frac{1}{n_{\text{max}}} \int n(z) dz \quad (4.37)$$

This essentially simplifies the axial particle density profile into a top hat distribution, with the top hat height equal to the maximum particle density of the true axial profile. That is, the particle density in the center of the chip. Note that when loosely talking about the pressure or particle density, the maximum in the center of the chip is meant. In chapter 5. a set of effective lengths accompanying particular geometries is given (table 5.2)

With this definition of the particle density, the total generated ion current can be calculated with

$$I = I_e \sigma + n_{\text{max}} l_{\text{eff}}. \quad (4.38)$$

For simulations, this identity is used to find the relation between the particle density scaling factor  $n_{\text{max}}$ , and the current  $I$ , for a particular chip geometry characterized by  $l_{\text{eff}}$ .

### 4.7. Monte-Carlo ray tracing

An accurate description of ion emission from the NAIS must include coulomb interaction. This is the topic of chapter 5 and here we only give an intermediate simulation result. The purpose of the simulations in this section is to explore the effects of gas scattering, but we keep in mind that accurate performance predictions are found in chapter 5.

$\Phi_I$	10	kV	$\Phi_e$	1.0	kV	spacing	300	nm
$E_1$	$3 \times 10^6$	V/m	$I_e$	100	nA	thickness	100	nm
$E_2$	$3 \times 10^6$	V/m	$d_e$	50	nm	aperture	150 $\varnothing$	nm
$T$	293	K	shape	Gaussian				
$N$	20 000							

Table 4.2. Simulation configuration.

4

We consider a quite typical configuration and the details are listed in table 4.2. We keep the fields in and outside equal and reasonably high as to minimize optical aberrations, as described in chapter 3.

#### 4.7.1. Trajectory visualization

In figure 4.11, a few particle trajectories are plotted. We can see how the trajectories of many particles in the  $iKn^{-1} = 25$  plot are fully dominated by scattering. Rather striking is that despite the scattering, still most particles are directed towards the aperture. Not in free flight, but in a drift-wise fashion.

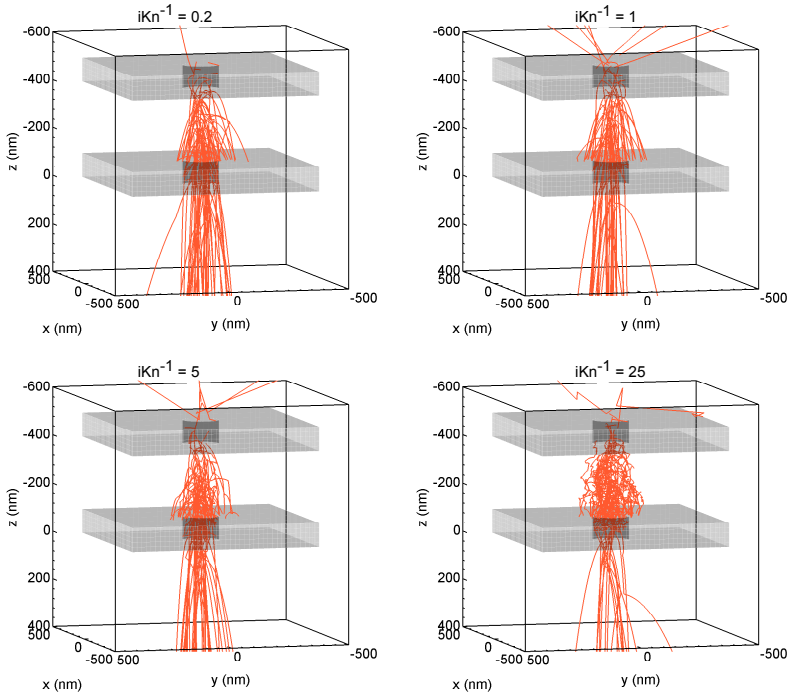


**Figure 4.11.** 100 simulated ion trajectories for a typical NAIS configuration. Four cases of increasing neutral particle density are shown, characterized by the inverse ionic Knudsen number. At  $iKn^{-1} = 0.2$  and also at  $iKn^{-1} = 1$ , gas scattering is limited, while at  $iKn^{-1} = 5$  and  $iKn^{-1} = 25$ , the effect becomes rather clear.

#### 4.7.2. Brightness and energy spread

More quantitative are the results shown in figure 4.12. The influence of gas scattering becomes clear when comparing the black-to-green brightness curves to the scatter-free gray dashed curves. For low  $iKn^{-1}$  there is no difference, but at higher values, the gas-scatter-including brightness curves are significantly reduced.

We can identify the responsible mechanisms by looking more quantitatively at the brightness reduction. For example, at  $n = 1.6 \times 10^{25} \text{ m}^{-3}$  ( $iKn^{-1} = 8.2$ ) the brightness at 50% of the beam current is 6.5 times lower than the (non-physical) scatter-free situation. The virtual source area has grown by a factor of 1.7 and the total emitted current is reduced by a factor 1.6. The remaining factor is 2.4 and we can conclude that a large influence on the brightness loss must be due to induced transverse energy. So, some of the scattered particles don't make it out due to scattering, but also quite some do exit the chip after experiencing one or more scatter events.

If we simply look at the obtained values for the brightness, we see that  $B > 1 \times 10^6 \text{ Am}^{-2} \text{ sr}^{-1} \text{ V}^{-1}$  in combination with several nA's of total current is not jeopardized by ion-neutral scattering.

The energy distributions depicted in 4.12b. show for low  $iKn^{-1}$  a bimodal distribution. This is also reported by Jun [2] and already discussed in section 3.4.5. For increasing particle density, at first only the right hand side of the distribution



is influenced. This part of the distribution originates from the back of the chip and travels longest through the gas, hence these are most prone to ion-neutral scattering. These particles become less likely to escape, but also transfer energy in collisions and end up elsewhere in the final distribution. Interestingly, this effectively lowers the energy spread of the final beam. If the pressure is further increased the intensity on the left hand side starts to increase. This relates to increased scattering and increased ion generation in front of the chip.

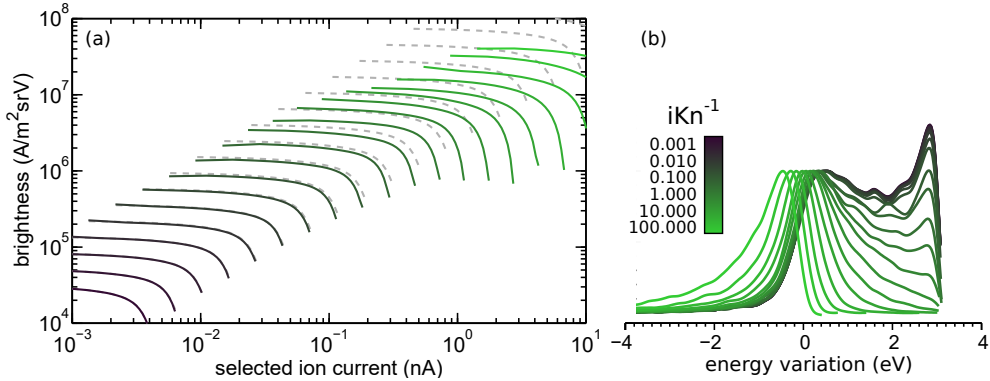


**Figure 4.12.** Monte Carlo ray trace result of a typical NAIS configuration using argon ions including electrostatic fields and ion-neutral scattering, but no coulomb interactions. a) The brightness as function of the post-acceleration selected beam current. The light gray dashed lines indicate the brightness assuming no gas scattering. b) Energy distribution functions of the final beam, shifted towards zero by subtracting the acceleration voltage. The distribution is a combination of initial positions in the potential landscape and the redistribution due to gas scattering. The distributions are arbitrarily scaled such that the shapes can be compared.

## 4.8. Conclusion

A crucial aspect of NAIS operation is the inevitable scattering of ions on neutral atoms. A validation study showed that a hard sphere collision model gives inaccurate results for two quantities used for model validation; the drift velocities and the transverse diffusion coefficient. A more advanced model gave excellent results and is used to model ion-neutral scattering in the NAIS. In this model a charge exchange event and an isotropic event are considered, with energy dependent cross sections.

The effective mean free path and the ionic Knudsen number are shown to be useful concepts for characterizing the NAIS. Reasonably simple fit functions allow easy use of these quantities. Evaluation of the unscattered ionization efficiency indicates that not much more than 1% of the electron beam current of unscattered ions can be generated in a typical NAIS configuration.

A Monte Carlo ray trace simulation of a nominal NAIS geometry showed promising performance. In a fairly moderate regime,  $iKn^{-1} = 1 - 10$ , we observe a brightness larger than  $1 \times 10^6$  A/m<sup>2</sup>srV, combined with sub 1 eV energy spread. We conclude that ion-neutral scattering is not a show-stopper for achieving competitive ion source performance.

An important result is the notion that the current and the brightness tend to keep increasing with increasing particle density, despite more ion-neutral scatter-

ing. Note that at the highest particle densities simulated, the assumption in the modeling, notably the molecular flow assumption, become endangered and the results become inaccurate. It is expected, however, that the observed trends are not affected by a somewhat different neutral particle density distribution.

A fortunate influence of gas scattering is a reduction of the energy spread. Ions originating from the back of the chip can be slowed down by transferring energy to neutral atoms. In addition, ions from the back have a chance of scattering towards the membrane, effectively acting as an energy filter.

We should note that the ray trace results in this chapter, although enlightening, are intermediate. Only the inclusion of coulomb interactions can yield measurable predictions. The next chapter is concerned with combining the work of this chapter with coulomb interaction calculations.

## References

1. V. Tondare. Towards a High Brightness, Monochromatic Electron Impact Gas Ion Source. Ph.D. thesis, Delft University of Technology. repository.tudelft.nl (2006).
2. D. Jun. Development of the nano-aperture ion source (NAIS). Ph.D. thesis, Delft University of Technology. repository.tudelft.nl (2014).
3. D. Rapp and W. E. Francis. "Charge Exchange between Gaseous Ions and Atoms". *J. Chem. Phys.* **37**, p. 2631 (1962).
4. K. Nanbu. "Probability Theory of Electron-Molecule, Ion-Molecule, Molecule-Molecule, and Coulomb Collisions for Particle Modeling of Materials Processing Plasmas and Gases". *IEEE Trans. Plasma Sci.* **28**, p. 3 (2000).
5. A. Phelps. "The application of scattering cross sections to ion flux models in discharge sheaths". *J. Appl. Phys.* **76**, p. 747 (1994).
6. S. H. Pullins and R. A. Dressler. "Guided-Ion Beam Measurements of Ar<sup>+</sup> + Ar Symmetric Charge-transfer Cross Sections at Ion Energies Ranging from 0.2 to 300 eV". *Z. Phys. Chem.* **214** (9), pp. 1279–1297 (2000).
7. A. V. Phelps. "Online collection cross sections". [jilawww.colorado.edu/~avp/collision\\_data](http://jilawww.colorado.edu/~avp/collision_data) (last revised 27-04-2002).
8. K. Nanbu and Y. Kitatani. "An ion-neutral species collision model for particle simulation of glow discharge". *Jpn. J. Appl. Phys.* **28**, p. 324 (1995).
9. K. Nanbu and G. Wakayama. "A Simple Model for Ar<sup>+</sup>-Ar, He<sup>+</sup>-He, Ne<sup>+</sup>-Ne and Kr<sup>+</sup>-Kr Collisions". *Jpn. J. Appl. Phys.* **38**, p. 6097 (1999).
10. P. Langevin. "A fundamental formula of kinetic theory". *Ann. Chim. Phys.* **5**, pp. 245–288 (1905).
11. L. Chanin and M. A. Biondi. "Temperature Dependence of Ion Mobilities in Helium, Neon, and Argon". *Phys. Rev.* **106**, p. 473 (1957).
12. J. Barata. "Integral and differential elastic collision cross-sections for low-energy Ar<sup>+</sup> ions with neutral Ar atoms". *Nucl. Instr. Meth. Phys. Res. A* **580**, pp. 14–7 (2007).
13. J. Jovanovic, S. Vrhovac, and Z. Petrovic. "Momentum transfer theory of ion transport under the influence of resonant charge transfer collisions: the case of argon and neon ions in parent gases". *Eur. Phys. J. D* **21**, p. 335–342 (2002).
14. S. Robertson and Z. Sternovsky. "Monte Carlo model of ion mobility and diffusion for low and high electric fields". *Phys. Rev.* **67**, pp. 046405–1 (2003).
15. Z. Ristivojevic and Z. L. Petrovic. "A Monte Carlo simulation of ion transport at finite temperatures". *Plasma Sources Sci. Technol.* **21**, p. 035001 (2012).
16. V. Vahedi and M. Surendra. "A Monte Carlo collision model for the particle-in-cell method applications to argon and oxygen discharges". *Comput. Phys. Commun.* **87**, pp. 179–198 (1995).
17. PulsarPhysics. "General Particle Tracer, version 3.10". [www.pulsar.nl/gpt](http://www.pulsar.nl/gpt) (2011).
18. SPOC. "Electron Optical Design, version 3.072". [www.lencova.com](http://www.lencova.com).
19. A. Roth. *Vacuum Technology* 2nd. ed. (Elsevier, New York, 1990).
20. H. Ellis, R. Y. Pai, E. W. MCDaniel, E. A. Mason, and L. A. Viehland. "Transport properties of gaseous ions over a wide energy range". *At. Data Nucl. Data Tables* **17**, pp. 177–210 (1976).
21. J. A. Hornbeck and J. P. Molnar. "Mass Spectrometric Studies of Molecular Ions in the Noble

- Gases". Phys. Rev. **84** (4), p. 621 (1951).
22. E. C. Beaty and P. L. Patterson. Phys. Rev. **137**, p. A346 (1965).
  23. T. Stefánsson and H. R. Skullerud. "Measurements of the ratio between the transverse diffusion coefficient and the mobility for argon ions in argon". J. Phys. B: At. Mol. Opt. Phys. **32**, p. 1057–1066 (1999).
  24. L. Viehland and E. Mason. "Transport properties of gaseous ions over a wide energy range, IV". At. Data Nucl. Data Tables **60** (1), p. 37 (1995).
  25. G. Sejkora, P. Girstmair, H. C. Bryant, and T. D. Mark. "Transverse diffusion of Ar<sup>+</sup> and Ar<sup>2+</sup> in Ar". Phys. Rev. A **29** (6), p. 3379 (1984).
  26. B. Schiestl, G. Sejkora, M. Lezius, P. S. M. Foltin, and T. Mark. Proc. 8th int. swarm seminar, Trondheim (1993).
  27. H. R. Skullerud and P. Larsen. "Mobility and diffusion of atomic helium and neon ions in their parent gases". J. Phys. B: At. Mol. Opt. Phys. **23**, p. 1017 (1990).
  28. T. Stefánsson, T. Berge, R. Lausund, and H. R. Skullerud. "Measurements of transport coefficients for lithium ions in argon and helium ions in helium with a drift-tube mass spectrometer". J. Phys. D: Appl. Phys. **21**, p. 1359 (1988).
  29. P. H. Larsen and M. T. Elford. "The mobilities of xenon ions in xenon and the derived charge transfer cross section for Xe<sup>+</sup>(2P<sub>3/2</sub>) ions in xenon". J. Phys. B: At. Mol. Opt. Phys. **19**, pp. 449–461 (1986).
  30. J. Barata. "Calculation of Drift Velocities and Diffusion Coefficients of Xe<sup>+</sup> Ions in Gaseous Xenon". IEEE Trans. Nucl. Sci. **52** (6), p. 2889 (2005).
  31. K. Tang and J. Toennies. "An improved simple model for the van der Waals potential based on universal damping functions for the dispersion coefficients". J. Chem. Phys. **80**, p. 3726 (1984).
  32. R. Rejoub, B. G. Lindsay, and R. F. Stebbings. "Determination of the absolute partial and total cross sections for electron-impact ionization of the rare gases". Phys. Rev. A **65**, p. 042713 (2002).
  33. G. Rademaker. Fabrication and analysis of a freestanding nanofluidic channel. Master's thesis, Delft University of Technology - Charged Particle Optics group (2014).
  34. J. Peatross and D. D. Meyerhofer. "Novel gas target for use in harmonic generation". Rev. Sci. Instrum. **64**, p. 3066 (1993).
  35. COMSOL. "COMSOL Multiphysics 4.4 - Molecular Flow Module". [www.comsol.com/molecular-flow-module](http://www.comsol.com/molecular-flow-module) (2013).

## List of symbols

$\sigma_{\text{iso}}$	isotropic cross section	m	$\lambda$	mean free path	m
$\sigma_{\text{cx}}$	charge exchange cross section	m	$\lambda_{\text{eff}}$	effective mean free path	m
$E_1$	inside-chip electric field	Vm <sup>-1</sup>	$\lambda_{\text{iso}}$	isotropic mean free path	m
$E_2$	outside-chip electric field	Vm <sup>-1</sup>	$\lambda_{\text{cx}}$	charge exchange mfp	m
$E$	electric field	Vm <sup>-1</sup>	$\rho(t)$	probability density	s <sup>-1</sup>
$f$	Maxwell-Boltzmann distribution	sm <sup>-1</sup>	$J_e$	electron current density	Am <sup>-2</sup>
$g$	neutral sample distribution	sm <sup>-1</sup>	$J_I$	ion current density	Am <sup>-2</sup>
$\sigma_I$	ionization cross section	m	$n$	particle density	m <sup>-3</sup>
$\epsilon$	ion energy	eV	$n_{\text{max}}$	max. particle density	m <sup>-3</sup>
$\mathbf{u}_i$	ion velocity	ms <sup>-1</sup>	$l_{\text{eff}}$	effective gas length	m
$\mathbf{u}_n$	neutral velocity	ms <sup>-1</sup>	$l$	gas length	m
$\hat{\mathbf{R}}$	random unit vector		iKn	ionic Knudsen number	
$\nu$	scattering frequency	s <sup>-1</sup>	$\eta_{\text{unscatt}}$	unscatt. ionization efficiency	%
$u_{\text{drift}}$	drift velocity	ms <sup>-1</sup>	$\eta_{\text{tot}}$	ionization efficiency	%
$t_{\text{sim}}$	total simulation time	s	$I$	ion beam current	A
$u_t$	thermal velocity	ms <sup>-1</sup>	$I_e$	electron beam current	A
$\mu$	ion mobility	mV <sup>-1</sup> s <sup>-1</sup>	$\Phi$	ion acceleration voltage	V
$D_t$	transverse diffusion coefficient	m <sup>2</sup> s <sup>-1</sup>	$\Phi_e$	electron landing voltage	V

# 5

## Simulating ion emission

*"The fact that we live at the bottom of a deep gravity well, on the surface of a gas covered planet going around a nuclear fireball 90 million miles away and think this to be normal is obviously some indication of how skewed our perspective tends to be."*

DOUGLAS ADAMS

## 5.1. Introduction

We apply electric and magnetic fields to tailor ion trajectories to our needs, however, the ions in the beam influence each other as well. Usually, in an undesired way. The so-called coulomb interactions have been an essential aspect of operation for many ions sources. Studies on the gallium LMIS showed that the source performance is limited by these interactions [1, 2]. For the ultra cold ion source, the coulomb interactions play a dominant role as well [3–5].

So far, coulomb interaction in the NAIS have been ignored. This was based on the fact that the NAIS operates with a relatively low current compared to for example the LMIS. In addition, the initial source size is larger. This may be true, however, the extraction field in a needle type source is much larger than found in a NAIS configuration. We have therefore investigated the influence of the stochastic coulomb interactions anyway. The aim is achieving a good source quality assessment and acquire guidance for optimization.

Besides free-space coulomb interactions, we consider the influence of surface induced charge. It is well known that a charged particle in proximity of a conductor induces charge on the surface of the conductor. This charge can influence the trajectory of the free space particle. One example is the deflection of low energy electrons in a pinhole [6]. In most cases though, this effect is very weak. For the emission region of the NAIS, the particles are traveling only at about 1 eV of kinetic energy, through an aperture of the order 100 nm. Neglecting the effect may not be appropriate.

A second unconventional aspect that is studied, is the influence of the electron beam on the ion beam. Due to the large mass difference, an electron scattering on an ion does not alter the ions trajectory very much. However, since we have a very high electron current (100nA typically), many electrons engage in scattering and a more elaborate analysis is required to determine the influence.

The regime where coulomb interactions become relevant is overlapping with the regime where ion-neutral scattering is present. Therefore, the model for ion-neutral scattering discussed in chapter 4 is included in the simulations presented here.

## 5.2. Ion-induced surface charge

A charged particle in the proximity of conducting surfaces will induce surface charge. A charged particle can not feel its own field, however, it does feel the effect of the induced surface charge. The electric field strength acting on a particle close to a conducting infinite plate in the x-y plane is simple to calculate using the method of images [7]. The result is

$$\mathbf{E}_q = -\kappa \frac{q}{(2h)^2} \hat{\mathbf{z}} \quad (5.1)$$

with  $h$  the distance between the charge and the plate and  $\kappa = 8.99 \times 10^9 \text{ Nm}^2 \text{ C}^{-2}$ . This solution is useful to get acquainted with the order of magnitude of the effect.

The electric field strength at 25 nm distance is 0.6 V/um, which is not negligible. At 5 nm it even reaches 14 V/um. The field strength can become equal or even exceed the typically applied electrostatic field, so the surface induced charge can certainly not be ignored a-priori.

The method of images is great for simple geometries, but is not a method that works in general. Interestingly, the method is so popular, that surface induced charge effects are often referred to as image charge.

### 5.2.1. Numerical approach

We will now consider a brute-force way to compute the self-field of a charged particle in any geometry. We assume a quasi static situation, which means in this context that the charge in the conductor reassembles instantaneously upon ion movement. We will ignore the influence of surface charge, induced by one ion, acting on another. This assumption is justified later.

If the ion is at position  $\mathbf{r}_q$ , the electrostatic potential in all space is described by the Poisson equation as

$$\epsilon_0 \nabla^2 \Phi(\mathbf{r}) = q \delta(\mathbf{r} - \mathbf{r}_q), \quad \Phi(\mathbf{r}_s) = 0 \quad (5.2)$$

The term  $q \delta(\mathbf{r} - \mathbf{r}_q)$  represents the ion as a point charge and  $\Phi(\mathbf{r}_s)$  is the potential on the electrode surfaces. Note that even in a rotationally symmetric electrode configuration a 3D solution is required, for the point charge breaks the symmetry.

The field  $\Phi(\mathbf{r}_s)$  is not directly useful. In fact, it is singular at the only position we would like to know it, that is, at  $\mathbf{r}_q$ . It is, however, not this field that affects the motion of the ion. The ion is only affected by the charge it has induced on the conducting surfaces. Locally, we can compute the surface charge density from  $\sigma(\mathbf{r}_s) = -\epsilon_0 (\hat{\mathbf{a}} \cdot \nabla \Phi(\mathbf{r}_s))$ . We can use this result to calculate the self-field by summing the contributions of all surface elements at position  $\mathbf{r}_s$  of surface area  $da$ , using Coulombs law. See figure 5.1a for a problem sketch. The vector from a particular surface charge element to the position of the ion is  $\mathbf{r}_{sq} = \mathbf{r}_q - \mathbf{r}_s$ , so we get

$$\mathbf{E}_q(\mathbf{r}_q) = \kappa \iint_S \frac{\mathbf{r}_q - \mathbf{r}_s}{|\mathbf{r}_q - \mathbf{r}_s|^3} \sigma(\mathbf{r}_s) da. \quad (5.3)$$

The field obtained in  $\mathbf{r}_q$  space can be used to describe the motion  $\mathbf{r}_q(t)$  of an ion in charge-free region of space confined by electrodes. The field is a little peculiar though, as we haven't acquired it as a solution of Maxwell's equations directly. In fact  $\nabla \cdot \mathbf{E}_q(\mathbf{r}_q) \neq 0$ , so it can't be a solution of Maxwell's equations in charge-free space (Laplace equation). We will therefore call it a virtual field, as this field never physically exists. To clarify the point, if an ion is at position  $\mathbf{r}_q$ , we can not use equation 5.3 to calculate the field for some other ion at location  $\mathbf{r}'_q$ . This would neglect the direct ion-to-ion coulomb interaction, which is a topic later on in this chapter. The field at some other location can be found from  $-\nabla \Phi(\mathbf{r}'_q)$ , but we do not use this. Here we only consider surface induced self-fields because these are far more relevant than surface induced effects on neighboring ions.

We can not a priori assume that this field can be written as a gradient, i.e.  $\mathbf{E}_q(\mathbf{r}_q) = -\nabla\Phi_q(\mathbf{r}_q)$ . However it is quite easy to show using Leibniz' rule that

$$\Phi_q(\mathbf{r}_q) = -\kappa \iint_S \frac{\sigma(\mathbf{r}_s)}{|\mathbf{r}_q - \mathbf{r}_s|} da. \quad (5.4)$$

The interpretation of this potential is the work required to escape from  $\mathbf{r}_q$  to infinity. We also conclude that  $\mathbf{E}_q$  is, as expected, a conservative vector field.

Interestingly, the result of equation 5.3 is a rotationally symmetric field, if the electrode configuration is rotationally symmetric, even though the solution to equation 5.2 is not rotationally symmetric. Numerically this means we need to perform a 3D calculation of equation 5.2, for only a 2D set of values for  $\mathbf{r}_q$ . This is still computationally heavy but manageable, while a 3D set for  $\mathbf{r}_q$  would be very unpleasant. We identify some more symmetry in our situation, which is shown in figure 5.1a.

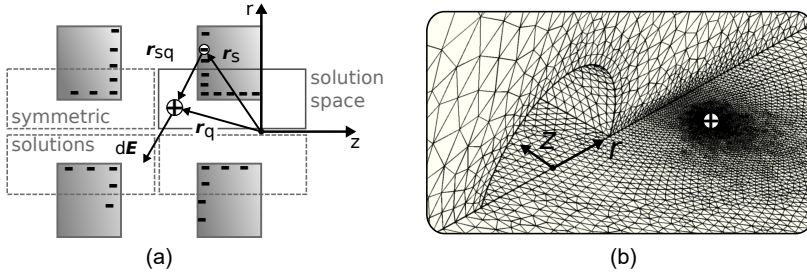


**Figure 5.1.** Finite element method (FEM) for surface induced self-field effects. a) NAIS electrode configuration cross section, showing the surface charge located at  $\mathbf{r}_s$  giving a contribution  $d\mathbf{E}$  to the free space charge at position  $\mathbf{r}_q$ . b) Cross sectional view of a 3D mesh for the FEM solution, showing the refinement at the location of the free charge.

For the numerical evaluation of  $\mathbf{E}_q(\mathbf{r}_q)$ , we have used COMSOL [8]. We perform a finite-element calculation of the 3D field for a set of 400 values of  $\mathbf{r}_q$ . The chip geometry considered has 100 nm membrane thickness, 100 nm aperture diameter and 200 nm membrane spacing. We found that it was absolutely crucial to heavily refine the mesh around the point charge. Such mesh refinement is shown in figure 5.1b. Because the free charge location is parametrized, we need to recalculate a new mesh for every solution. In total, such a field calculation took about one day on a decent desktop PC (CPU: Intel Xeon E5-1620). The resulting virtual electrostatic potential field is shown in figure 5.2.

We acknowledge that a boundary element method would be more natural to solve the surface induced self-field, as it directly gives the surface charge and doesn't suffer from the singularity at the charge location. We have used a finite element method (FEM) solver because it was more easily available to us and can do the job as well. We have tested the method by simulating a particle-plate configuration. We found excellent agreement between the numerical solution and the well-known analytical result for this situation. In the NAIS geometry, further mesh refinement did not yield noticeable change in the field hence we are confident the results are accurate.



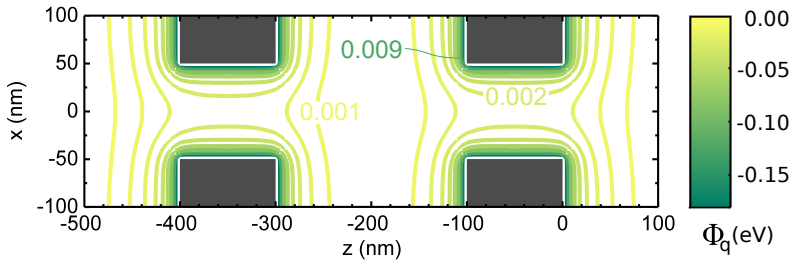


**Figure 5.2.** Electrostatic potential due to surface induced charge. The gradient of this field is the electrostatic self-field. Note that the field is virtual as it is not a solution to the Laplace equation, it is rather a look-up table for the self-induced field.

### 5.2.2. Analytical approximation: method of images

The FEM method described here is accurate, but not very convenient. It is tedious to set up and it takes a day to accurately compute the field of one particular geometry. It is therefore worthwhile to consider alternatives. In the center of the chip, the surface induced charge effects mostly cancel. We have found out that all relevant effects occurs in the exiting aperture and maybe the effect can be simplified by only considering the effect in a cylindrical geometry. Analytical approaches to the point-charge and cylinder system are available, [9, 10], but these are not at all simple.

We may try to find an image charge configuration to solve the situation of a point charge in a cylinder. It can be shown, unfortunately, that no such image charge equivalent situation exists. It seems unlikely that a multiple-charge image can be found either.

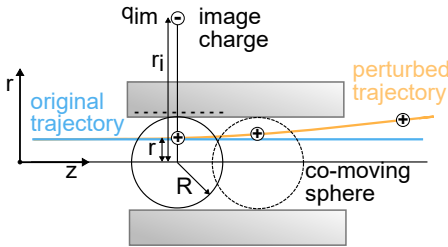


**Figure 5.3.** Approximate image charge configuration for the point charge in a cylinder. The image charge solution for a point charge and a sphere is moving along with the charge through the cylinder. This gives a good approximation because the forces in the  $z$ -direction are in both cases canceled out.

We can, however, boldly try to employ the well-known solution for a sphere and a point charge. A sphere that just fits inside a cylinder, positioned at the same  $z$ -coordinate as the charge will attain quite similar surface induced charge forces. See figure 5.3 for the visualization of this concept. Of course the sphere deviates from the cylinder, however the force in the  $z$ -direction cancels out in both cases so this a-symmetry is partially irrelevant.

If we place a virtual charge of magnitude  $q_{im}$  at  $r_{im}$  according to

$$q_{im} = -q \frac{R}{r_q}, \quad r_{im} = \frac{R^2}{r_q} \quad (5.5)$$



we obtain the image charge solution of a point charge inside a sphere [7]. The acquired self-field is then

$$\mathbf{E}(\mathbf{r}_q) = \kappa q \frac{R r_q}{(R^2 - r_q^2)^2} \hat{\mathbf{r}}. \quad (5.6)$$

We have acquired an extraordinary simple equation when compared to the full FEM solution method. It is of course not clear how good of an approximation this equation is. If  $r_q \rightarrow R$ , the cylinder and the sphere case both converge to the infinite plate case. On-axis, the field is zero in both cases. At least the limiting cases are equal.

In figure 5.4, a ray trace example comparing the full FEM calculation method and the simple analytical model given here is shown. In this example a uniform, 0.5 eV mono-energetic argon beam travels through a 100x100nm aperture. The correspondence can be considered quite good upon visual inspection in figure 5.4a; both the black and the blue rays behave similarly. The obvious notion for both models is that the beam is getting divergent and that the trajectories close to the aperture walls are drawn towards the wall. In figure 5.4b, we see more quantitatively that the analytical model predicts a slightly too weak final beam angle. Nevertheless, the range in the axial entrance distance from which the ions get attracted onto the inner aperture wall is remarkably close.

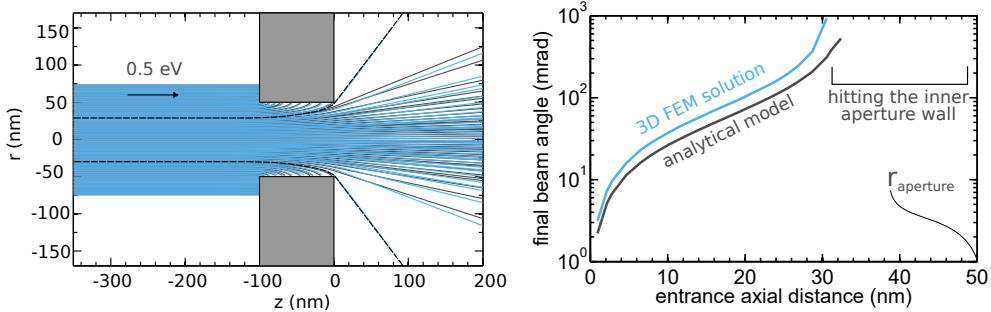


**Figure 5.4.** Test case for inspecting surface induced charge effects. A parallel beam with 0.5 eV kinetic energy fills a, perfectly conducting, aperture. A computational model and an analytical approximation are compared by using identical starting conditions for both ray traces. No other fields are applied. The dashed lines indicates that trajectories that are on the verge of escaping.

A more direct way of testing the suitability of the analytical model is simulating a full NAIS configuration and compare what we are after in the end: optical properties. Figure 5.5 shows the result of ray-tracing and we conclude that both models correspond very well to each other in terms of brightness. Also included is a simulation without any model for surface induced charge effects. Clearly, the effect is important for an accurate description of the ion emission. The brightness at low current is not very much affected, though.

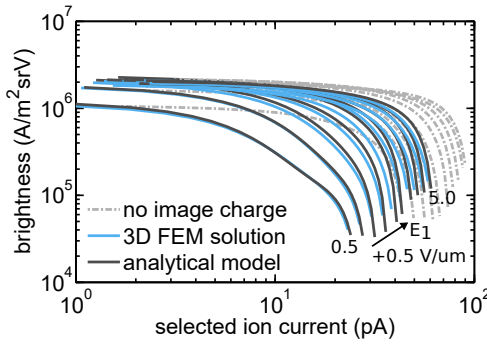


**Figure 5.5.** A comparison of two models for surface induced charge effects reveal good agreement between the models. This simulation corresponds to a spacing×thickness×aperture = 200×100×100 nm and inside and outside chip fields of  $E_1 = E_2 = 1$  kV/mm.

The work required to escape from a NAIS chip is described by equation 5.4. Figure 5.2 already shows that the effect of this should be rather limited. Only ions starting very close to the walls require more energy than a few tens of meV, but these are unlikely to escape the chip geometry anyway. We can inspect the chromatic effect of the image charge directly by looking at the fw50 energy spread of the ray trace simulation in figure 5.6. The energy spread contribution is negligible, except at the lowest bias voltage, where in this configuration it gave a 200 meV contribution. Again, we see no difference between the methods. Since the analytical model only considers the aperture, this energy spread contribution must all be due to particles generated in the aperture.

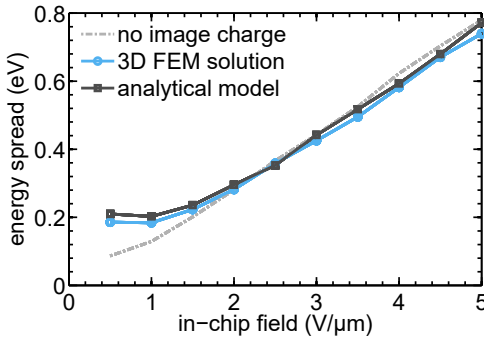


**Figure 5.6.** The comparison of the energy spread in the beam reveals that hardly any energy spread is introduced due to the surface induced charge, except for the very lowest in-chip fields. No noteworthy difference between the two models is observed. This simulation corresponds to a spacing-thickness-aperture combination of 200×100×100 nm and inside and outside chip fields of  $E_1 = E_2 = 1$  kV/mm.

Now we have gained confidence in the applicability of the analytical model we can investigate it a bit further. We expand equation 5.6 and get

$$\mathbf{E}(r_q) \approx \kappa \frac{q}{R^2} \left( \frac{r_q}{R} + \frac{2r_q^3}{R^3} + \frac{3r_q^5}{R^5} + O(r_q^7) \right) \hat{r} \quad (5.7)$$

We can see essentially a first order lens effect and higher order aberrations. Note that the higher order terms are not decreasing in magnitude very rapidly. At  $r_q = \frac{1}{2}\sqrt{2}R$ , the third order is already as large as the first order. The image charge effects influences the center of the beam only slightly, while strongly attracting the outer beam part close to the aperture walls.

We have learned that the surface induced charge can lead to significant displacement of the ion trajectories. It should therefore be included in further simulation

of the NAIS. The full calculation is a comprehensive process, but the analytical approximation gives good agreement for the brightness and the energy spread and can therefore be used in further study. Making the aperture a little bigger than 100 nm rapidly leads to less influence of the effect. A higher in-chip field and thinner membranes help to suppress the effect as well. Note that the particle mass does not influence the trajectory in an electrostatic field, so the effect is equal in magnitude for all ionic species.

### 5.3. Monte-Carlo ray tracing

One convenient way to calculate the particle-to-particle coulomb interactions is using the extended-two-particle approximation developed by Janssen [11, 12]. In situations where the beam envelope and beam voltage are not constant, an extension to the theory called the slice-method is required [13]. Unfortunately, the emission region of the NAIS does not fulfill the requirements for the extended-two-particle approximation to be valid. The angular current density needs to be uniform, which is not what we get out of a nano-aperture ion source. Furthermore, we can not take into account the details of the chip geometry such as volumetric emission or membrane blockage.

5

#### 5.3.1. Monte-Carlo coulomb interaction simulation

The most direct method of calculating coulomb interactions between particles in a beam, is summing over all the pair-wise coulomb forces:

$$\mathbf{F}_i = \kappa q_i \sum_{j=1}^N q_j \frac{\mathbf{r}_i - \mathbf{r}_j}{|\mathbf{r}_i - \mathbf{r}_j|^3}. \quad (5.8)$$

This can be used directly in a ray-tracing scheme. One big disadvantage is the inherent slowness of such a calculation; the number of calculations scales with the square of the number of particles involved. In addition, one needs quite some particles for decent statistics as the degrees of freedom of starting conditions is much larger than for non-interacting particles.

One method of reducing the calculation time is grouping particles such that only their net effect is used in the force calculation. This is called the Barnes–Hut algorithm (BH). We have used the commercial software GPT [14], which offers both the full pair-wise calculation and the BH simplification. In GPT, the grouped particles are approximated up to the fourth order multipole moment and a variable  $\theta$  indicates the crudeness of particle bunching for which 1 is very crude and 0 is equal to the full pair-wise calculation.

We have found that in NAIS simulations the BH approximation gives identical results as the full calculation even for  $\theta > 0.5$ . To be on the safe side we have used  $\theta = 0.25$ . The total emission current of the NAIS is relatively low, so the coulomb interaction is mostly caused by the nearest neighboring particle, hence the BH approximation is very natural.

The method of acquiring the optical properties of the beam after ray tracing is described in section 3.2.5. Gas scattering is included in ray tracing as well, and the details of the implemented model can be found in chapter 4. The total number of particles traced for a typical set of parameters is 20k, which gives enough statistics to also study a fraction of the beam.

It is important to keep the time step smaller than the average time between the generation of particles to avoid unphysical particle bunching. We typically set  $\Delta t < 0.3 \frac{e}{f}$ . Note that unphysical bunching is partially prevented automatically because of the volumetric emission. This time-step requirement is checked in addition to the time step requirements discussed in chapter 4 (equation 4.19).

### 5.3.2. Nominal geometry using argon

For understanding the main optical effects due to coulomb interactions we simulate a chip geometry with  $\text{spacing} \times \text{thickness} \times \text{aperture} = 300 \times 100 \times 150 \text{ nm}$ , using argon ions. This is considered a production feasible, ion optically decent, geometry. As described in chapter 3, we know that in order to avoid trouble with lens effects, we would like to have high and equal fields. We set  $E_1 = E_2 = 10 \text{ kV/mm}$ . The ebeam is assumed to be Gaussian shaped in the xy-plane with a 50 nm fw50 and 100 nA of current. The e-beam divergence and the influence of ionization on the e-beam current density is ignored. We interpret this simulation configuration as what is realistically achievable if the full system is well under control and up to spec.

$\Phi_1$	10	kV	$\Phi_e$	1.0	kV	spacing	300	nm
$E_1$	$1 \times 10^7$	V/m	$I_e$	100	nA	thickness	100	nm
$E_2$	$1 \times 10^7$	V/m	$d_e$	50	nm	aperture	150	nm
$T$	293	K	shape	Gaussian		species	argon	
$N$	20 000							

**Table 5.1.** Simulation settings for Monte-Carlo ray tracing as used throughout this chapter unless otherwise stated.

Ultimately we are interested in the most realistic simulation. This needs to include the electric fields, ion-neutral scattering, ion-ion interaction and surface induced coulomb interaction simultaneously. For better understanding, we compare such a complete model to a situation where no particle interaction are included and to one where only gas scattering is present. Figure 5.7 shows what a typical set of simulated trajectories looks like.

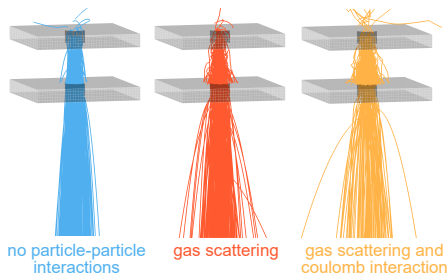


**Figure 5.7.** Trajectories of argon ions for three cases. No interactions yields only smooth trajectories and a narrow emitted beam. Including gas scattering broadens the beam and more particles are blocked. When including coulomb interactions, further broadening of the beam is observed.

Figure 5.8 shows the simulated practical brightness as formed by the inner 50% of the beam. Different emission currents are obtained by changing the particle density in the chip. A dry-run ignoring all particle-particle interactions shows the expected result, that is, the brightness scales linearly with the current indefinitely. In the low current regime, this dry run coincides with the particle interaction simulations and it is possible to increase the current and the brightness for free by increasing the particle density. The ion-neutral interaction included simulation shows a reduction of the brightness if the current of the beam is increased even further. It is very interesting to see that the ion-neutral interaction alone does not seem to form a true limit of the brightness as increasing the beam current keeps on giving a higher brightness. It is the coulomb interactions that pose the limit to the brightness ultimately. Note that both the ion-neutral and ion-ion interactions begin to become important more or less at the same current, which is truly a coincidence. We can reach  $1\text{e6 A/m}^2\text{srV}$  without being influenced very much by any particle interaction.

The effect of surface induced charge is best seen in the low current regime as particle-particle interactions are negligible here, while the surface induced charge effects do not depend on the particle density. The coulomb interaction included curve is not exactly converging towards the other curves. We observe a reduction of total emission current, however, without deteriorating the brightness. This means that the current was mostly scraped off from the outer part of the beam, which we can expect by looking at figure 5.4. It seems as if the surface induced charge effect is actually beneficial, as the brightness is higher in the lower current regime. This would be a misconception because ion-neutral scattering occurs at a lower current as well, so the peak brightness is not higher. This confusion would be removed by plotting the brightness versus  $i\text{Kn}^{-1}$ , but here we would like to have a direct beam property on the axis.

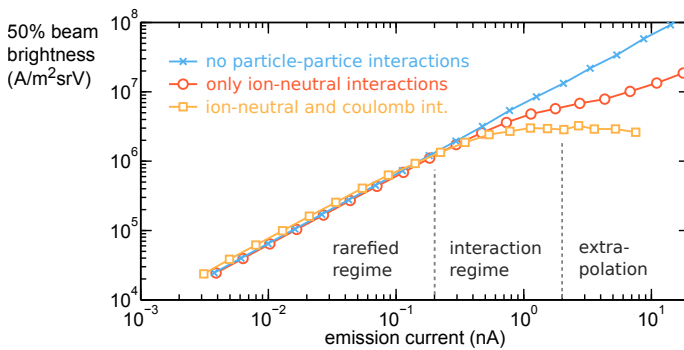


**Figure 5.8.** Monte-Carlo ray tracing result of 20k argon ions. The current in the beam is varied by using different particle densities in the chip. The 95% confidence interval for the statistical precision of the simulation is smaller than the marker sizes.

We should mention that currents above 2 nA in this simulation should be considered an extrapolation of the model. At such high currents, the approximation for a uniform e-beam in  $z$  becomes inaccurate and the effects of electron multiplication

and redirection during electron impact ionization should be taken into account for more accurate results. The background neutral particle density is also no longer well described by molecular flow. Furthermore, the required pressure for obtaining  $> 2$  nA emission current for this chip is in the several bar range. This pressure may pose a danger for the chips integrity and may also give a too high vacuum load.

Figure 5.9 shows three building blocks of the brightness: the virtual source size, the divergence angle and the beam current. The escape probability represents the fraction of current that can escape the chip and is plotted versus the total amount of generated current. In the lower current regime, the surface induced charge is responsible for lowering the virtual source size and increasing the divergence angle; essentially a lens effect. It furthermore lowers the escape probability, yielding a lower emission current. At higher currents, both ion-neutral and coulomb interaction effects result in virtual source size growth, added divergence and a lowering of the escape probability. Quite often, brightness loss can completely be attributed to trajectory displacement, but for the NAIS we find it is a combination of all three brightness constituting quantities.

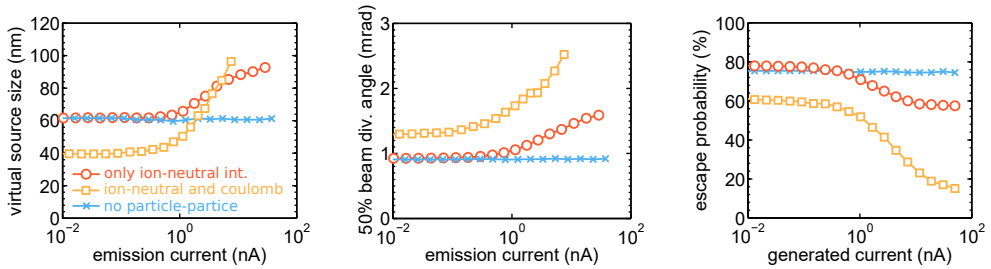


**Figure 5.9.** The virtual source size and the beam divergence angle characterize the shape of the beam. We can see the influence of gas scattering and coulomb interactions as we increase the emission current by increasing the particle density. The escape probability indicates what fraction of the generated current makes it out of the chip.

Figure 5.10 shows the brightness versus beam current as selected by an aperture after acceleration to high voltage. These curves give more detailed information than figure 5.8. We see that the saturation of the 50% beam brightness when increasing the particle density also holds for the axial practical brightness (or say, 5% beam brightness). We have transformed the particle density to the inverse ionic Knudsen number as discussed in chapter 4.

We may characterize the shape of the curves in figure Figure 5.10 by the ratio between the 50% brightness and the 5% beam brightness. In an idealized configuration, where no particles are blocked by the membrane and no particle-particle interactions exist, we found that the ratio between the 50% brightness and the 5% beam brightness is 0.7 (see equation 3.28). In this geometry, where we do include membrane blockage, the ratio in the low current regime is also about 0.7 and only weakly changes to 0.6 in the particle interaction dominated regime. We conclude that it is a quite general result that using only a fraction of the beam gives a slightly higher brightness than using 50%. Trying to use nearly 100% of the beam current gives a rapid drop of the average brightness.

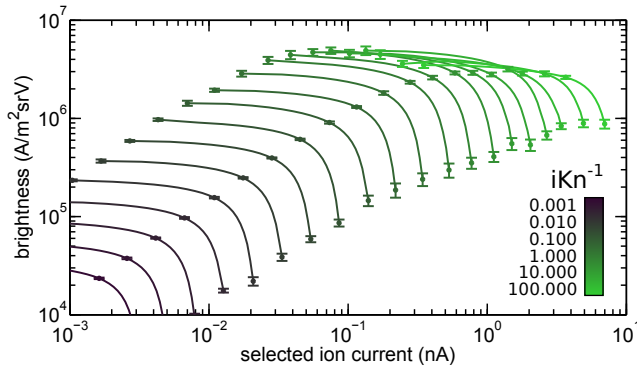


**Figure 5.10.** Brightness-current performance curves of a typical chip geometry for a wide range of particle densities as found by Monte-Carlo simulation. Ion-neutral scattering, ion-ion interaction and surface induced charge interaction are included. The error bars indicate the 95% confidence intervals of the statistical precision.

Besides brightness reduction, coulomb interactions may introduce energy spread via the Boersch effect. Figure 5.11 shows the distribution of the energy for a wide range of particle densities. Keep in mind that the curves are normalized for distribution shape comparison; the higher  $iKn^{-1}$  beams contain more current. At low  $iKn^{-1}$ , the energy distribution is formed by the ion initial positions, the potential landscape and the escape probability. The width of the distribution is loosely speaking equal to the bias voltage. At high voltage, we loose some ions from the back and we transfer some of the acquired energy through neutral particle collisions. Both effects lower the right hand side of the distribution. The amount of ions made in front of the chip becomes relatively more important and a larger left-hand-side tail is formed.

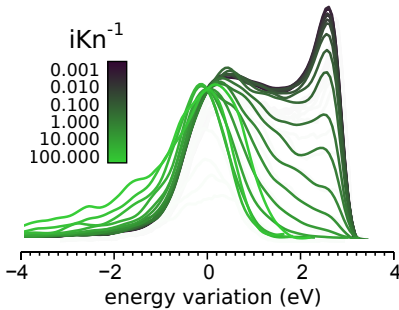


**Figure 5.11.** The energy intensity diagrams for various particle densities as indicated by the inverse ionic Knudsen number. The indicated energy is relative to the acceleration voltage. The distributions are arbitrarily normalized such that the shapes can be compared.

The described effects are perhaps more clearly captured in figure 5.12. At the lower currents, the non-interacting regime, no particle density dependence is present. This regime corresponds to the darkest curves in figure 5.11. For increasing  $iKn^{-1}$ , we see a decrease as fewer ions from the back maintain their energy up to the exit. This relates to the concept of a reduction in the mean free energy introduced in section 4.5.3. At the same time, when increasing the particle density, relatively more particles are generated in front of the chip and the contribution of the Boersch effects increases. The combination of the different effects lead to a minimum.



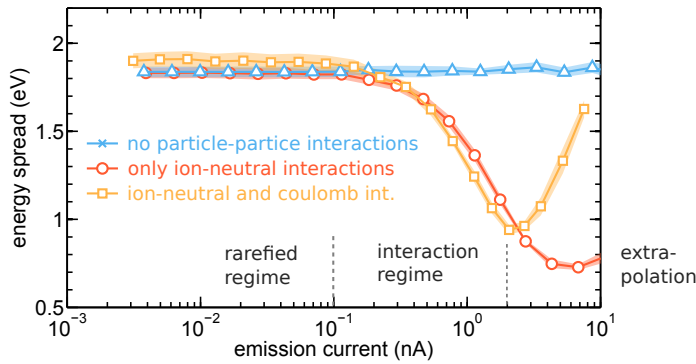


**Figure 5.12.** Monte-Carlo ray tracing result of 20k argon ions. The current in the beam is varied by using different particle densities in the chip. The shaded area indicates 95% confidence interval for the statistical precision of the simulation.

We have encountered a pleasant surprise; we seem to be able to decrease the energy spread by a factor of two by simply increasing the particle density. Increasing the particle density too much causes the Boersch effect to rapidly increase the energy spread.

### 5.3.3. Comparing chip geometries

We have studied a chip geometry that was considered nominal, but is it really the best choice? What happens if we can't produce these precise dimensions? In this section we explore the influence of geometrical variation of the chip.

The typical spot size of the electron beam in a NAIS optimized situation dictates typical aperture sizes of 100 to 500 nm. High fields give low coulomb interactions, low aberrations, and minimize gas scattering, so, preferably we maintain 10 kV/mm. In order to achieve a low energy spread and a high field strength, the spacing between the membranes should be kept small, typically smaller than 1  $\mu\text{m}$ . The fabrication challenges dictate the minimal membrane thickness, for which 100 nm is certainly feasible.

We have chosen a set of six geometries that are considered sensible configurations to explore in more detail. The dimensions are given in table 5.2. Chip S-2 is a fairly small chip and S-1 explores the potential benefits of very thin membranes. Chip M-1 is considered nominal and M-2 deviates by allowing more current to escape due to the bigger aperture. Chip L-1 and L-2 are exploring the boundaries of maximum chip size. In all simulations we set  $E_1 = E_2 = 10$  kV/mm.

chip	$l$ nm	$t$ nm	$d$ nm	$l_{\text{eff}}$ nm
S-1	100	20	100	155
S-2	100	100	100	226
M-1	300	100	150	428
M-2	300	100	300	498
L-1	1000	100	150	1111
L-2	1000	100	500	1409

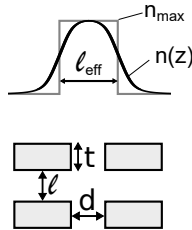


**Table 5.2.** Dimensions of the set of chips used for tray trace simulations. The first column is used as a reference to a particular geometry. The effective length is calculated according to equation 4.37 after the neutral particle density distributions have been calculated using the method described in section 4.6.



Simulating a larger set of permutations, or even a full geometrical optimization would be more complete. This does require much more computational time, which would become a serious issue. This also leads to more data, which is not necessarily making things clearer. The benefits are questionable anyhow, as we don't have full experimental control at this stage in the research and such detailed optimization can be considered premature.

Figure 5.13 shows the results of several ray tracing simulations of argon ions as a function of the inverse ionic Knudsen number. Because we are comparing different geometries, plotting as a function of particle density or emission current leads to problematic comparison, while at equal ionic Knudsen number, we are comparing the same amount of ion-neutral scattering. The beam properties are plotted together in one figure because the properties are linked and vary together. One can draw vertical lines and obtain a set of properties that is simultaneously achievable.

Note that when  $iKn^{-1} > 10$  we should be somewhat cautious in interpreting the results because the assumptions in the model become compromised. The issues are discussed in the previous section and the regime  $iKn^{-1} > 10$  may best be avoided unless one is interested in pushing and studying the limits of the NAIS.

The easiest thing to look at first is the total current. Directly obvious is the continuous increase of the current with  $iKn^{-1}$ . One may expect that gas scattering, possibly in combination with coulomb repulsion, leads to a saturation or even a decrease. It turns out that the increase of produced current outweighs the additional loss mechanisms. We do see the increase getting more shallow, particularly for chip L-1, which has a small aperture to spacing ratio. An emission current of 1 nA seems feasible for any chip. 10 nA seems reachable too if the chip has a large enough aperture, but we are reaching the extrapolation regime of the model.

We can inspect the differences in emission current more easily by looking at the escape probability. The obvious notion is that chips with larger apertures allow more ions to escape. Secondly, we see that the aspect ratio of aperture-to-spacing can best be large for current maximization. The NAIS trajectories are not scalable because the initial conditions do not scale along when scaling the geometry and potentials. Therefore, it is predominantly the absolute aperture size and not the aspect ratio which determines the escape probability. Over a three orders of magnitude variation in  $iKn^{-1}$ , the escape probability is only a factor of two lowered at most. The reduction of escape probability due to gas scattering is not nearly as dominant as one may suspect. The same was already visualized in figure 4.11.

Perhaps most important is the observation that  $B > 1 \times 10^6$  A/m<sup>2</sup>srV seems to be achievable with any chip. All brightness curves show comparable behavior with respect to one another. The small differences between the chips in the lower current regime is a combination of differences in surface induced coulomb interactions and differences in the shape of the electric field. A noteworthy difference between chips is higher current for larger apertures at the cost of some brightness loss.

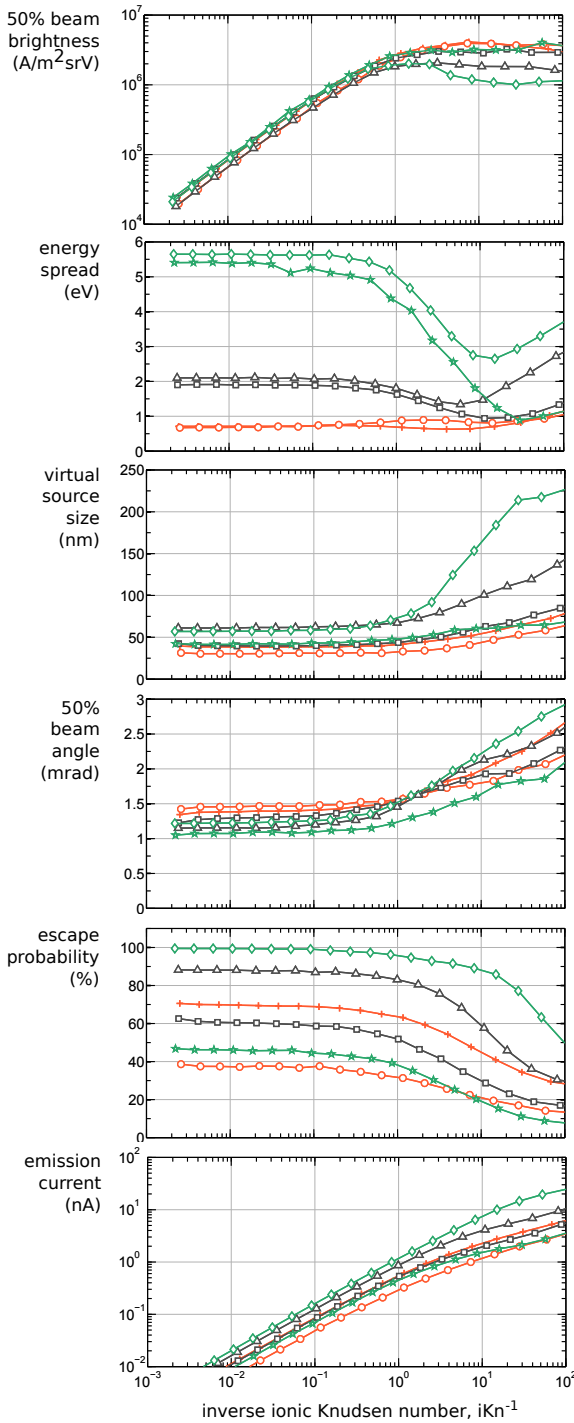


**Figure 5.13.** Results of Monte-Carlo ray tracing of 20kV argon ions for six different chips of characteristic dimensions. These simulation include the electric field in an outside the chip ( $E_1 = E_2 = 10$  kV/mm), ion-neutral gas scattering, surface induced charge effects, and ion-ion coulomb interactions. All curves share the ionic Knudsen number on the x-axis, which is discussed in detail in section 4.5.2; it represent roughly the number of ion-neutral scatter events for ions starting at the back of the chip. Varying the ionic Knudsen number is achieved by varying the neutral particle density. The brightness plotted is calculated by using 50% of the beam current as selected by an aperture down the column. The energy spread is measured as a fw50 of the 1D probability density function. The virtual source size is the 2D fw50 as formed by 50 % of the total emitted current. As a measure for the beam divergence we use the angle with respect to the optical axis such that the inner cone contains 50% of the total beam current. The ion escape probability is an average for all starting positions. Any particle hitting the membrane is assumed to be neutralized and removed from the simulation.

	l	- t	- d
S-1 :	100	- 20	- 100
S-2 :	100	- 100	- 100
M-1 :	300	- 100	- 150
M-2 :	300	- 100	- 300
L-1 :	1000	- 100	- 150
L-2 :	1000	- 100	- 500

A little peculiar is the dipping behavior of chip L-2 and weakly that of chip M-2. Interestingly, when running the simulation without coulomb interactions, this dip remains. The straightforward explanation is that the decreasing mechanisms outweigh the increase in generated current. However, from a phase space point of view, this is not satisfying. When  $iKn^{-1}$  is increased, the phase space density can only increase. This is best illustrated by an example: if the inverse ionic Knudsen number is doubled, the front half of the chip now effectively generates the same current as the full chip at half the  $iKn^{-1}$ , and the amount of scattering in this front half is also the same. The phase space density produced by this front half is thus the same as the original situation, but in addition, the particles from the back half increase the density too, although less due to more scattering. A higher phase space density means a higher brightness. So the question is, how can the brightness ever decrease with increasing  $iKn^{-1}$ .

Well, in fact, the differential brightness does increase. It is the practical brightness that is plotted here which decreases. The virtual source size grows due to scattering, and although the central phase space density does keep increasing, the overall average beam property, the practical brightness, does not. In normal beam lines we select the beam divergence angle, but use the full source size. However, we realize now it would be very convenient to do source area selection here as well, as by selecting the central part of the field, we select the high phase space density part and obtain a brighter beam.

Actually, we do have a real space capping aperture installed in a NAIS: the exit aperture itself. This explains why we don't see the dip in the smaller apertured configurations. It also explains why the dipping behavior is reversed when the large aperture starts to become limiting again. Note that the exit aperture is not only a real space limiting object, it also tends to cap off the larger angles. However, often we use only a small fraction of the central part of the beam. So, the exit aperture blocks current, but this isn't necessarily a bad thing; it mostly gets rid of unwanted current. It can be thought of as a phase space selecting window, with somewhat fuzzy boundaries. Due to this aperture capping, we never expect a virtual source size larger than the aperture size, except when trajectory displacement after the ions escaped the chip is important.

The energy spread shows a rather large difference between chips. The spread is mostly determined by the aperture spacing, as we keep the field constant. So, in general a larger energy spread is obtained for the larger spaced chips, although it can be reduced by working under reasonably high particle densities. The occurrence of a minimum was expected and discussed in the previous section. Note that the minimum does not occur for the smallest chips because the increased spread due to ions made in front of the chip is relatively more important.

Even though at high Knudsen numbers the simulation becomes a little unreliable, we are confident in the conclusion that brightness reaches a limit. Surely the inaccuracies lead to some shifting of the brightness curves but in whatever way the beam properties are formed, the coulomb interactions will limit the final beam. Looking at the specific shortcomings of the model, there is no reason to believe

that the inaccuracies will cause a different conclusion. This is supported by the fact that fairly different chip geometries over a wide  $\text{iKn}^{-1}$  range lead to a comparable brightness.

### 5.3.4. Helium, argon, and xenon compared

One of the main assets of the NAIS concept is the ability to use different gases. It is not obvious that other gases give the same performance as argon, since the ionization cross section and the ion-neutral interaction are different. In the introductory chapter we concluded that in the rarefied limit, the brightness is proportional to the ionization cross section. This means a 10 times higher brightness for xenon compared to helium. When including the molecular diameter to account for ion-neutral interactions, the difference was reduced to a factor 3.5.

When investigating the higher particle density regime in a more comprehensive way, we find that the difference in attainable brightness between helium, argon, and xenon is even less pronounced. Figure 5.14 shows the result of a Monte-Carlo ray trace simulation including ion-neutral scattering, ion-ion repulsion, and surface induced charge interaction. The geometry was spacing $\times$ thickness $\times$ aperture:  $300\times 100\times 150$  nm (chip M-1).

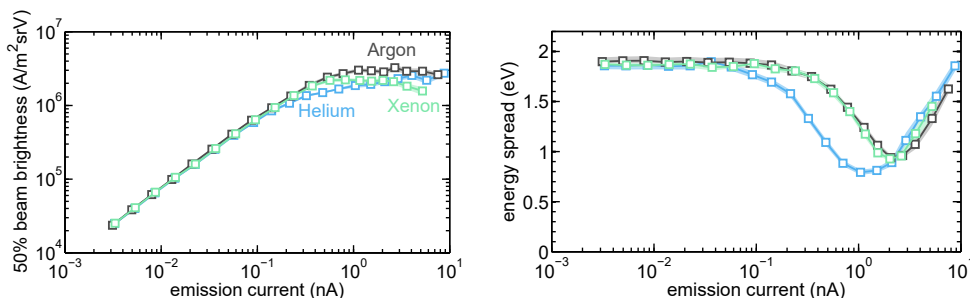


**Figure 5.14.** Monte-Carlo ray trace result for comparing the expected performance of helium, argon and xenon. The geometry used has spacing $\times$ thickness $\times$ aperture:  $300\times 100\times 150$  nm (chip M-1), and the fields  $E_1 = E_2 = 10$  kV/mm. The statistical error (95% confidence interval) is indicated by the shaded areas.

We find the maximum attainable brightness to be close to  $2.5 \times 10^6 \text{ A/m}^2 \text{srV}$  for all three species. It appears that the ion-neutral interaction and the coulomb interactions are balancing out the difference in ionization cross section. This precise balancing effect is not a general result, as different fields and a different geometry can cause larger discrepancies. Nevertheless, for most configurations we do not expect differences in brightness larger than a factor of two.

The energy spread does show different behavior for helium compared to argon and xenon. The dipping behavior of the energy spread occurs at a lower emission current. Since the ionization efficiency of helium is rather low, comparable gas scattering effects start becoming relevant at lower currents.

### 5.3.5. Increased electron beam current

So far we have assumed a 100 nA electron beam being focused in a 50 nm fw50 spot. This is based on a good electron column in combination with a Schottky electron gun. There may be tricks, however, to increase the current in the electron beam. We simulate one example to explore the benefits of engaging in the development of higher ebeam current. The same configuration as used for the simulations in 5.3.2 are used here, expect that the electron beam current is set to 300 nA in stead of 100 nA.

The maximum acquired 50% beam brightness found is  $B = 5.0 \pm 0.3 \times 10^6 \text{ A/m}^2 \text{ srV}$ , in combination with a total emission current of  $I = 1.6 \text{ nA}$ . The accompanying energy spread is  $\Delta\epsilon = 1.6 \text{ eV}$ . The brightness has increased by a factor of about 1.7 compared to a 100 nA ebeam. One may expect the proportional factor 3, but because coulomb interactions play such an important role, the advantage is not nearly as great as in a non-interacting configuration.

Interestingly, the brightness is no longer attaining at a plateau. For currents  $I > 1.6 \text{ nA}$  the brightness decreases with increasing current. For example, at  $I = 10.3 \text{ nA}$ , the brightness is  $B = 3.1 \pm 0.2 \times 10^6 \text{ A/m}^2 \text{ srV}$ . The energy spread slightly lowers to  $\Delta\epsilon = 1.1 \text{ eV}$  at such a high current.

### 5.3.6. Comparing operation conditions

In the previous sections we have assumed up-to-spec electrostatic fields and an up-to-spec electron beam probe size. These conditions are realistic and can be considered nominal. For comparison we consider some different configurations in this section. We investigate weak fields inside and outside the chip, a fairly large geometry (spacing×thickness×aperture: 1300×200×400 nm), and a large ebeam probe size.

From earlier simulations we know that a decent choice for the inverse ionic Knudsen number is in the range 1 to 10 (see figure 5.13). We fix the ionization efficiency to  $\eta_{\text{tot}} = 2.94\%$  yielding, for this particular chip geometry with effective length 1.593  $\mu\text{m}$ , an  $\text{iKn}^{-1}$  between 2.7 and 4.7. The required particle density maximum is  $2.36 \times 10^{24} \text{ m}^{-3}$ . The results of a set of Monte-Carlo ray trace simulations using these settings is shown in table 5.3. We take into account ebeam blockage by the top membrane, since a 200 nm ebeam fw50, and a 400 nm aperture diameter results in 6.3 % of ebeam current loss.

Table 5.3 lists the results of a large set of different configurations simulated. The table can serve as a reference and we discuss only the most important conclusions.

$d_e$ nm	$E_1$ V/ $\mu\text{m}$	$E_2$ V/ $\mu\text{m}$	iKn $^{-1}$	$I$ nA	$B_{50}$ A/m $^2$ srV	$\Delta\epsilon$ eV	$d_v$ nm
50	1	1	4.7	$0.41 \pm 0.01$	$2.1 \pm 0.2 \times 10^5$	$0.30 \pm 0.02$	$139 \pm 6$
	1	3	4.7	$0.52 \pm 0.01$	$5.4 \pm 0.3 \times 10^5$	$0.41 \pm 0.02$	$139 \pm 3$
	3	3	3.5	$1.06 \pm 0.02$	$5.6 \pm 0.4 \times 10^5$	$1.12 \pm 0.02$	$135 \pm 5$
	1	10	4.7	$0.72 \pm 0.01$	$7.1 \pm 0.5 \times 10^5$	$0.61 \pm 0.02$	$117 \pm 3$
	3	10	3.3	$1.26 \pm 0.02$	$1.0 \pm 0.1 \times 10^6$	$1.20 \pm 0.02$	$180 \pm 3$
	10	10	2.7	$2.17 \pm 0.02$	$1.6 \pm 0.0 \times 10^6$	$4.40 \pm 0.12$	$117 \pm 2$
	0	1	-	$0.22 \pm 0.01$	$2.1 \pm 0.2 \times 10^5$	$0.18 \pm 0.01$	$113 \pm 3$
	0	10	-	$0.40 \pm 0.02$	$6.0 \pm 0.8 \times 10^5$	$0.80 \pm 0.09$	$91 \pm 3$
	3	1	3.5	$0.93 \pm 0.02$	$9.4 \pm 0.7 \times 10^4$	$1.09 \pm 0.03$	$235 \pm 9$
	10	1	2.7	$1.94 \pm 0.01$	$2.8 \pm 0.1 \times 10^4$	$4.44 \pm 0.09$	$477 \pm 9$
200	1	1	4.7	$0.39 \pm 0.01$	$1.2 \pm 0.1 \times 10^5$	$0.36 \pm 0.02$	$188 \pm 8$
	1	3	4.7	$0.47 \pm 0.02$	$2.1 \pm 0.1 \times 10^5$	$0.45 \pm 0.02$	$204 \pm 4$
	3	3	3.5	$0.83 \pm 0.01$	$3.0 \pm 0.1 \times 10^5$	$1.28 \pm 0.04$	$183 \pm 5$
	1	10	4.7	$0.65 \pm 0.01$	$2.5 \pm 0.3 \times 10^5$	$0.59 \pm 0.03$	$131 \pm 6$
	3	10	3.5	$1.02 \pm 0.01$	$3.5 \pm 0.2 \times 10^5$	$1.26 \pm 0.06$	$189 \pm 3$
	10	10	2.7	$1.57 \pm 0.02$	$4.7 \pm 0.2 \times 10^5$	$4.76 \pm 0.14$	$187 \pm 3$
	0	1	-	$0.21 \pm 0.01$	$7.9 \pm 0.9 \times 10^4$	$0.21 \pm 0.01$	$191 \pm 6$
	0	10	-	$0.38 \pm 0.01$	$1.4 \pm 0.1 \times 10^5$	$0.82 \pm 0.08$	$123 \pm 4$
	3	1	3.5	$0.75 \pm 0.01$	$8.8 \pm 0.7 \times 10^4$	$1.25 \pm 0.04$	$255 \pm 7$
	10	1	2.7	$1.32 \pm 0.01$	$2.6 \pm 0.2 \times 10^4$	$4.94 \pm 0.16$	$470 \pm 13$

**Table 5.3.** Monte Carlo ray trace results for chip geometry spacing $\times$ thickness $\times$ aperture: 1300 $\times$ 200 $\times$ 400 nm. The comparison is made between a nominal 50 nm ebeam fw50 and a 200 nm fw50 and a variety of in and out of chip fields are considered. Throughout these simulations the total ionization efficiency is set to 2.94 %, which is achieved by setting  $n = 2.36 \times 10^{24} \text{ m}^{-3}$ . An electron beam current of 100 nA at 1 keV landing energy was used.

If the ebeam is nominal, but we use relatively weak fields of  $E_1 = E_2 = 1 \text{ V}\mu\text{m}^{-1}$ , we end up with a brightness of  $2 \times 10^5 \text{ A/m}^2 \text{ srV}$ , a tenfold decrease with respect to a  $10 \text{ V}\mu\text{m}^{-1}$  situation. We can gain a lot by increasing only  $E_2$  to  $3 \text{ V}\mu\text{m}^{-1}$ , but preferably to  $10 \text{ V}\mu\text{m}^{-1}$ . This indicates that brightness is mainly lost through trajectory displacement in the acceleration region. Other factors that reduce the brightness are the chip aberrations and in-chip coulomb aberrations are less important as increasing  $E_1$  from 1 to  $3 \text{ V}\mu\text{m}^{-1}$  as well hardly improves the brightness.

Rather surprisingly,  $E_1 = 0 \text{ V}\mu\text{m}^{-1}$  performs reasonably well. We note that the extraction current becomes rather low, such that coulomb interaction are less important. Furthermore,  $E_2$  can penetrate the chip and offer some ion acceleration.

We should clearly not use  $E_1 > E_2$ . This leads to large chip aberrations, and it extracts a large current, that under a weak acceleration field, leads to coulomb interactions. On top of that, the energy spread becomes large.

We now consider the situation of a 200 nm ebeam fw50. If the fields are  $E_1 = E_2 = 1 \text{ V}\mu\text{m}^{-1}$ , we drop a factor two in brightness compared to 50 nm ebeam. This is much less of a deterioration than purely based on the ebeam current density drop, which would give a factor 16. Because the brightness is influenced by gas scattering and coulomb interactions, the influence of the ebeam size is less pronounced. When using stronger fields we see the same trends as for the 50 nm ebeam, but with a somewhat lower brightness overall.

With this relatively large chip we can attain  $1 \times 10^6 \text{ A/m}^2 \text{ srV}$ , if we use  $E_2 \approx 10 \text{ V}\mu\text{m}^{-1}$ ,  $E_1 > 3 \text{ V}\mu\text{m}^{-1}$  and a 50 nm ebeam probe. Obtaining simultaneously a sub-1eV energy spread is rather tricky, and a smaller membrane spacing is needed to achieve this. Obtaining  $B > 1 \times 10^5 \text{ A/m}^2 \text{ srV}$  seems achievable for a wide range of operation conditions.

## 5.4. Ion-electron interactions

A rather special situation occurs for the NAIS, namely, we are dealing with a mixture of ions and electrons in the beam. At first glance one may ignore the influence of the electrons all together due to the large mass difference. Firstly, the velocity of the electrons is much higher than that of the ions, so the interaction time is very small. Secondly, the energy transfer can only be a fraction of the total energy due to momentum conservation. On the other hand, we should consider that every ion gets taken over by thousands of electrons during its acceleration and the collective effect may be of importance.

One way to investigate the effect is adding electrons to the Monte-Carlo simulation that was already established. It turns out that this is not so simple. The electrons are so fast in comparison with the ions, that we require extremely small time steps to properly discretize the interaction time. One ion encounters up to thirty thousand electrons and we need to simulate at least a few hundred ions to get sufficient statistics. Without any tricks to improve the current ray-tracing scheme, this isn't feasible. Therefore we have chosen to use an analytical approach similar to the extended two-particle approximation, although this specific problem is much simpler.

### 5.4.1. Introduction to the method

An appropriate model is Rutherford scattering: a charged particle scatters from a stationary target with an interaction potential governed by the coulomb force. It was developed for alpha particles scattering of a nucleus, but the formalism works equally well for particles of opposite sign. In this model, the target particle is infinitesimally small and any (non-elastic) effects due to the details of the electronic structure of the atom are ignored. We will assess this assumption later on. The rest of this section is concerned with the longer ranged coulomb interaction of electron-ion scattering. Note that this assumption is implicitly made in practically any calculation of the coulomb interactions in a charged particle beam.

Rutherford scattering describes a single scatter event, but we are interested in the collective effect of several consecutive events. We will need to use statistical methods to determine the collective effect. We consider the statistics of a single on-axis ion to be representative for the full beam, a concept that is borrowed from the extended two-particle approximation. The events can be assumed to be independent because we expect only small perturbations of the ion trajectory.

In the presented calculation we consider the simple case of an ion being accelerated in a uniform electric field  $E\hat{z}$ , starting at the origin. The method described here is not necessarily limited to only this simple case, but it is the most important case at present.

We define the positions at which a scatter event occurs by  $z_i$ , with  $i$  the index of the scatter event. When assuming uniform spacing between the scatter events and neglecting the ion velocity relative to the electron velocity, the time between two scatter events is  $\Delta t = e/I$ . Uniform acceleration yields  $z_i = \frac{1}{2} \frac{eE}{m} (\Delta t \cdot i)^2$ , with  $m$  the ion mass and  $E$  the electric field strength. The last scatter event occurs when the electrons are just repelled back, so  $z_N = \Phi_{e,0}/E$ , where  $N$  is the total number of scatter events, and  $e\Phi_{e,0}$  the initial electron energy. We can now write

$$z_i = \frac{e^3 E}{2mI_e^2} i^2, \quad N = \sqrt{\frac{2m\Phi_{e,0}}{eE^2} \frac{I_e}{e}}. \quad (5.9)$$

We may replace  $i$  by  $i - i_0$  where  $i_0$  is a value between 0 and 1 to account for the discretization error of the locations of the scatter events. We found that the value  $i_0$  does not influence the final result and was set to 0.5.

Some examples for the number of scatter events are instructive. Helium at 1 kV/mm acceleration voltage gives  $N = 5.7 \times 10^3$ , in contrast to  $N = 32.6 \times 10^3$  for xenon. The number scales inversely proportional to the field so at 10 kV/mm we reduce the numbers to  $0.6 \times 10^3$  and  $3.3 \times 10^3$  respectively.

#### 5.4.2. A single electron-ion scatter event

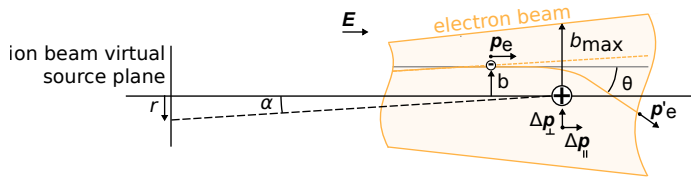


**Figure 5.15.** Electron-ion scattering. One particular electron trajectory is depicted; the shaded area indicates the range of possible electron trajectories.

We will now look at the effect of a single scatter event. Figure 5.15 accompanies the calculation presented hereafter. In the Rutherford model, the impact parameter  $b$  and the angle of the outgoing electron with respect to the  $z$ -axis  $\theta$  are related by

$$\tan \frac{\theta}{2} = \left( \frac{m + m_e}{m} \right)^3 \frac{\kappa e}{2\Phi_e b} \approx \frac{\kappa e}{2\Phi_e b} \quad (5.10)$$



If we assume an electron beam with uniform current density and radius  $b_{\max}$ , then the probability density function of the impact parameter is  $\rho(b) = 2b/b_{\max}^2$ . We can change variables  $b \rightarrow \theta$  using  $|\rho(b)db| = |f(\theta)d\theta|$ , with the relation given by equation 5.10 to obtain the probability density function for  $\theta$ :

$$f(\theta) = \left( \frac{\kappa e}{2\Phi_e b_{\max}} \left( \frac{m + m_e}{m} \right)^3 \right)^2 \frac{\cos \frac{\theta}{2}}{\sin^3 \frac{\theta}{2}} \approx \left( \frac{\kappa e}{2\Phi_e b_{\max}} \right)^2 \frac{\cos \frac{\theta}{2}}{\sin^3 \frac{\theta}{2}} \quad (5.11)$$

One essential aspect of the calculation is finding an appropriate expression for  $b_{\max}$ . We will use the ebeam diameter and assume all the electron trajectories are parallel to the z-axis. This is an approximation, as for example the trajectory furthest away from the axis makes angle  $\alpha_e$  with the optical axis. A more realistic maximum impact parameter might be  $b_{\max} = r_{\max} \cos \alpha_e$ . This correction, however, is best avoided, as it leads to unrealistically small impact parameters for highly curved electron trajectories, something we expect when the electron beam is close to being repelled. Omitting this correction for weakly curved trajectories is acceptable as it will be a very small correction. Furthermore, the error is most pronounced far away from the axis, for which the contribution to the ion's momentum change is least. We note that at the electron beam focus, the trajectories are rather chaotic and the parallel beam assumption seems unsound. However, the cosine of a typical maximum skew angle of 40 mrad is 0.9992, so again, the error made is only small.

A second aspect of is the curvature of the electron trajectories due to the decelerating field. Consideration of this effect would require the formalism for Rutherford scattering to be modified. We argue that only in the vicinity of the ion, curvature could be relevant for the interacting forces, but fortunately the curvature is of much larger length scale such that in the vicinity of the ion the electron trajectories are straight.

We furthermore ignore the trajectory displacement of the electrons. This assumption was checked by considering the average  $\theta$  deflection of a single scatter event and concluding that even at 10 to 100 scatter events, this is still much less than the typical beam divergence angle.

We do need to consider the evolution of  $b_{\max}$  along the beam line. The ebeam follows parabolic curves in the decelerating electric field. A derivation for the trajectory equation is very similar to what is shown in chapter 3 appendix A. The result is

$$b_{\max}(z) = \frac{1}{2} d_e + 2z\alpha_e \sqrt{\frac{\Phi_{e,0}}{Ez}} \left( \sqrt{\frac{\Phi_{e,0}}{Ez}} \pm \sqrt{\frac{\Phi_{e,0}}{Ez} - 1} \right) \quad (5.12)$$

with the  $\pm = -$  for the forward trajectory and  $\pm = +$  for the backward trajectory. The energies of the electrons and the ions are simply given by

$$\Phi_I(z) = \Phi_{I,0} + Ez, \quad \Phi_e(z) = \Phi_{e,0} - Ez. \quad (5.13)$$

It is not the outgoing angle of the electron but the properties of the ion that we are after, so we need to define the quantities of interest. If we ignore recoil, we can derive the momentum change of the ion caused by an electron using conservation of momentum. This gives  $\Delta p_{\parallel} = \sqrt{2me\Phi_e}(1 - \cos\theta)$  parallel to the optical axis. We can derive the energy acquired by the ion in the axial direction by considering the energy transfer associated with the parallel momentum transfer. The result is

$$\epsilon_i = e\Phi_e \frac{m_e}{m} \left( 1 - \cos\theta \sqrt{1 - \frac{m_e}{m} \left( 1 + \frac{m_e}{m} \right)^{-2} \sin^2 \frac{\theta}{2}} \right)^2 \approx e\Phi_e \frac{m_e}{m} (1 - \cos\theta)^2 \quad (5.14)$$

The more elaborate expression includes recoil, which is extremely small for the electron-ion combination.

We will also consider trajectory displacement, the most common way for coulomb interactions to cause loss of brightness. After a transverse momentum kick  $\Delta p_{\perp} = \sqrt{2me\Phi_e} \sin\theta$  in the transverse direction, the ion will acquire an angle  $\alpha$  with the optical axis described by  $\sqrt{2Me\Phi_i} \tan\alpha = \Delta p_{\perp}$ . In our uniform field acceleration situation, we know that the virtual source position is to first order located at  $-2z$  (see chapter 3), so the displacement in the virtual source plane is  $r_i = -2z \tan\alpha$ . Putting this together gives

$$r_i = 2z \sqrt{\frac{m_e}{m} \frac{\Phi_e}{\Phi_i} \left( 1 - \frac{m_e}{m} \left( 1 + \frac{m_e}{m} \right)^{-2} \sin^2 \frac{\theta}{2} \right)} \sin\theta \approx 2z \sqrt{\frac{m_e}{m} \frac{\Phi_e}{\Phi_i}} \sin\theta \quad (5.15)$$

#### 5.4.3. Combining multiple scatter events

Ultimately we are interested in the distribution of the random variable composed by the sum of many random variables. The total energy acquired by the ion due to electrons 1 to  $N$  is  $\epsilon = \epsilon_1 + \epsilon_2 + \dots + \epsilon_N$ . The contributions are not identically distributed because the electron and ion energy is varying along  $z$  and the electron beam diameter is not constant, which prevents us from directly using the classical central limit theorem (CLT). Fortunately, we have a set of probability density functions that are non-zero on only a finite domain, which implies Lyapunov's condition. The result is that we can still employ a version of the CLT. We define

$$\epsilon = \sum_{i=1}^N \epsilon_i, \quad \mu_{\epsilon} = \sum_{i=1}^N \mu_{\epsilon_i}, \quad \sigma_{\epsilon}^2 = \sum_{i=1}^N \sigma_{\epsilon_i}^2 \quad (5.16)$$

and based on the Lyapunov-CLT we state that  $\epsilon$  converges to a normal distribution with mean  $\mu_{\epsilon}$  and standard deviation  $\sigma_{\epsilon}$ .

We find  $\sigma_{\epsilon_i}$  from

$$\sigma_{\epsilon_i}^2 = \int f(\theta) (\epsilon_i(\theta) - \mu_{\epsilon_i})^2 d\theta \quad (5.17)$$

with  $f$  defined in equation 5.11. We prefer to find fw50 values and since we know the distribution is normal, we can use an appropriate constant to transform a standard

deviation to a fw50. The final results for the collective energy spread of many scatter event is

$$\Delta\epsilon_{50} = 1.349 \sqrt{\sum_{i=1}^N \int_{\theta_{\min}}^{\theta_{\max}} f(\theta; z_i) (\epsilon_i(\theta; z_i) - \mu_{\epsilon_i}(z_i))^2 d\theta}. \quad (5.18)$$

A fwhm would lead to a prefactor of 2.355, while 1 gives the standard deviation. Note that for clarity we have indicated the dependence on  $z_i$ , while this was omitted earlier.  $f(\theta; z_i)$  is the family of probability density functions that is parameterized by the z-coordinate  $z_i$ .  $\theta_{\min}$  is determined by the maximum impact parameter, i.e. the electron beam radius.  $\theta_{\max}$  is introduced to exclude scattering directly on the atom. This would require a more delicate approach and we want to exclude these effects.

We now develop the equation for the trajectory displacement. This is slightly more delicate than energy spread because we need to carefully deal with the 2-dimensional nature of the effect. We define the position of the ion in the virtual object plane as the vector  $\mathbf{R}_i = (x_i, y_i) = (r_i(\theta) \cos \phi, r_i(\theta) \sin \phi)$ . Note that due to rotational symmetry the  $\phi$  angle has a uniform distribution. We define a vector  $\mathbf{R} = \mathbf{R}_1 + \mathbf{R}_2 + \dots + \mathbf{R}_N$  describing the collective effect. Since this is a bi-variate distribution we need to use a covariance matrix rather than a variance. We get

$$\mathbf{R} = \sum_{i=1}^N \mathbf{R}_i, \quad C_R = \sum_{i=1}^N \begin{pmatrix} \langle x_i x_i \rangle & \langle x_i y_i \rangle \\ \langle x_i y_i \rangle & \langle y_i y_i \rangle \end{pmatrix} = \sum_{i=1}^N \begin{pmatrix} \sigma_{x_i}^2 & 0 \\ 0 & \sigma_{y_i}^2 \end{pmatrix} \quad (5.19)$$

Note that  $\mu_{\mathbf{R}} = 0$  and  $\langle x_i y_i \rangle = 0$  due to rotational symmetry.  $x_i$  and  $y_i$  are not, however, independent. The CLT holds also in more dimensions in the sense that the distribution of  $\mathbf{R}$  tends to the bi-variate normal distribution with covariance matrix  $C_R$ . By symmetry  $\sigma_{x_i}^2 = \sigma_{y_i}^2$  and we can find an expression for this quantity by using the probability density  $\rho(\theta, \phi) = (2\pi)^{-1} f(\theta)$  in combination with  $x_i = r_i(\theta) \cos \phi$ . We get

$$\sigma_{x_i}^2 = \frac{1}{2\pi} \iint f(\theta) r_i^2 \cos^2 \phi d\theta d\phi = \frac{1}{2} \int f(\theta) r_i^2 d\theta. \quad (5.20)$$

Since the final distribution of the collective effect is a bi-variate normal distribution, the 2D fw50 diameter is equal to the diagonal elements of  $C_R$  up to a numerical factor. The final expression is

$$d_{50} = 1.806 \sqrt{\sum_{i=1}^N \int_{\theta_{\min}}^{\theta_{\max}} f(\theta; z_i) r_i^2(\theta; z_i) d\theta} \quad (5.21)$$

The pre-factor is the same for a fwhm, while 0.769 gives the standard deviation.

#### 5.4.4. Numerical evaluation

Equation 5.18 and 5.21 are computed numerically for the case of 1 keV electrons, focused into a 50 nm fw50 diameter. Upon evaluating the  $\Delta\epsilon_{50}$  we found that the effect is essentially very small. In all cases we found  $\Delta\epsilon_{50} < 1$  meV. This is much smaller than even the initial thermal energy and plots are omitted because the influence is irrelevant.

The trajectory displacement was not so clearly insignificant. Figure 5.16 shows the numerical result for helium, argon and xenon on a typical range of field strengths. Notably, the effect can become comparable to the geometrical source size. We may however reduce the effect to well below 10 nm by using a 10 kV/mm acceleration field. This is in line with minimizing ion-ion type coulomb interactions.

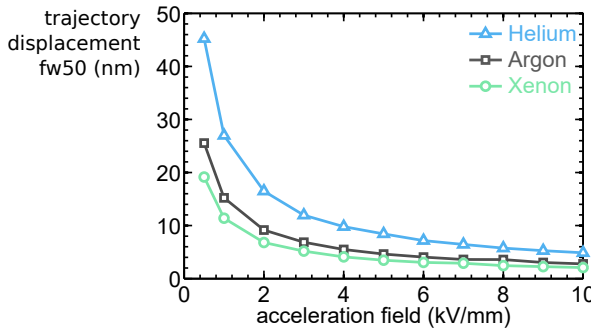


**Figure 5.16.** Trajectory displacement fw50 contribution to the virtual source as caused by many electrons scattering on the ions. The ebeam started with 100 nA of current and an initial energy of 1 keV focused down a 50 nm spot with half beam angle 40 mrad.

Figure 5.17 shows how the contribution of the trajectory displacement to the virtual source size is building up along the optical axis. In the first 100 nm after emission, no contribution can be made because the angular deviation is not transferred to a displacement, even though the ion energy is very low here. If we move further downstream, the effect becomes bigger and between 0.1 and 10  $\mu\text{m}$  most of the contribution is formed. Further down the optical axis the ion velocity and the ebeam diameter are increased, leading to a weakening of the contribution. In the very final stage there is a tiny bump, which happens when the electrons are just repelled and have a long interaction time.

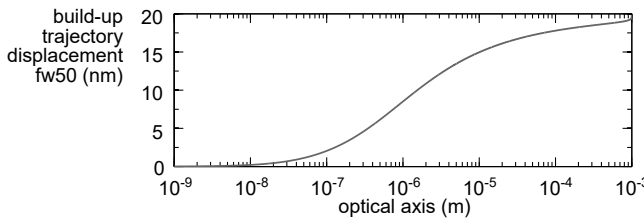


**Figure 5.17.** Accumulation of the trajectory displacement due to electrons scattering on argon ions, with  $E = 1 \text{ kV mm}^{-1}$ .

We found that lowering the initial ebeam energy increases the influence of the effect, even though this lowers the number of scatter events. This is attributed to the increased interaction time, which is reflected in equation 5.11.

We have experimented with values for  $\theta_{\text{max}}$ , corresponding to minimum impact parameters between 1 and 100 pm and found no significant difference to the trajec-

tory displacement calculation. The minimum impact parameter was fixed at 50 pm for further calculations. We conclude that the system is dominated by weak angle scattering and the assumption of no head-on collisions is substantiated. We can conclude that using the Rutherford model is thus acceptable. Mott cross sections or even more advanced models can describe electron-ion scattering in far more detail, but in our case such refinement won't be beneficial.

The trajectory displacement describes brightness loss by virtual source size growth, but neglects any added divergence in the beam. Usually this is a negligible contribution when compared to trajectory displacement. However, in an accelerating configuration, right in the beginning this may be important because the ion energy is very low. The possible influence was investigated by summing the transverse ion momentum. The resulting total momentum was much smaller than the thermal spread, hence this is of no concern.

We can state that the trajectory displacement to the ions caused by the electrons in the studied all-round NAIS configuration is not a dominating effect. In particular if the acceleration field is higher than 5 kV/mm the effect is smaller than 10 nm even for the most prone noble gas helium. Even though the effect is not dominating, the influence is only slightly smaller compared to a typical intrinsic virtual source size. We have learned that the effect can not in general be ignored a-priori and alternative configurations may suffer more problematically from the effect. The method described here can be used to study such situations. A decrease in electron energy, a smaller ebeam spot size, or an increase in ebeam current are all potential problematic changes. The contribution to the energy spread is negligible in all practical cases.

## 5.5. Conclusion

Simulations of ion emission were performed for realistic NAIS configurations including the electric fields, ion-neutral scattering, and coulomb interactions. Ultimately, the coulomb interactions pose a limit on the maximum attainable brightness. This limit can be extended by using strong electric fields of preferably 10 kV/mm. At such field strengths, a brightness between  $1 \times 10^6$  and  $5 \times 10^6$  A/m<sup>2</sup>srV seems achievable with an energy spread lower than 1 eV. For obtaining a sub-1 eV energy spread while maintaining the desired high electric fields it is required to use a membrane spacing of just a few hundred nanometer.

The ion-ion coulomb interactions were found to influence the beam in three ways: by trajectory displacement in the first microns after emission, by beam divergence growth inside the chip, and by increased membrane blockage.

When comparing chip geometries, some differences could be identified. The larger spaced chips have larger energy spreads when using the same electric fields. These larger energy spreads are reduced when using a relatively high particle density. Chips with larger apertures yield higher currents, but typically at the cost of some brightness loss.

The beam performance was quite insensitive to the noble gas species. The differences in ionization efficiency, ion-neutral scattering and coulomb interaction seems to balance each other out reasonably well, at least in the simulated configurations.

When the operation conditions are sub-optimal, it is still possible to obtain  $B \geq 1 \times 10^5 \text{ A/m}^2 \text{ srV}$  for a wide range of situations. However,  $B \geq 1 \times 10^6 \text{ A/m}^2 \text{ srV}$  and sub-1eV energy spread become mostly out of reach.

Surface induced charge forces were found to be important for NAIS emission, particularly for small aperture sizes of 100 nm or smaller and for weak in-chip fields. It seems best to use apertures of 150 nm or larger to avoid too much current to be lost by this effect. A lensing effect also became apparent, but this does not directly deteriorate the performance of the beam. The energy spread of the beam is hardly affected by the surface induced charge. A simple analytical approximation was found that gives decent accuracy and replaces a tedious field solving method.

The inevitable electron background passing through the ion beam gave rise to trajectory displacement of the ions. From the presented analytical calculations we can conclude that the effect is just small enough to be negligible, if the acceleration field is at least a few kV/mm. The contribution to the energy spread is negligible in all practical cases.

## References

1. C. W. Hagen, E. Fokkema, and P. Kruit. "Brightness measurements of a gallium liquid metal ion source". *J. Vac. Sci. Technol. B* **26** (6), p. 2091 (2008).
2. T. Radlicka and B. Lencova. "Coulomb interactions in Ga LMIS". *Ultramicroscopy* **108**, p. 445 (2008).
3. G. ten Haaf, S. Wouters, S. van der Geer, E. Vredenburg, and P. Mutsaers. "Performance predictions of a focused ion beam from a laser cooled and compressed atomic beam". *J. Appl. Phys.* **116**, p. 244301 (2014).
4. S. B. van der Geer, M. P. Reijnders, M. J. de Loos, E. J. D. Vredenburg, P. H. A. Mutsaers, and O. J. Luiten. "Simulated performance of an ultracold ion source". *J. Appl. Phys.* **102** (11), p. 094312 (2007).
5. A. V. Steele, B. Knuffman, and J. J. McClelland. "Inter-ion coulomb interactions in a magneto-optical trap ion source". *J. Appl. Phys.* **109**, p. 104308 (2011).
6. R. Birkhoff, J. Allen, V. Anderson, H. H. Jr., R. Becker, T. Ferrell, and D. Spears. "The ultimate electron lens- deflection of low-energy electrons by the image potential in a pinhole". *Optik* **55**, pp. 157–164 (1980).
7. D. J. Griffiths. *Introduction to Electrodynamics*, Third edition (Prentice-Hall Inc., 1999).
8. COMSOL. "COMSOL Multiphysics 4.4 - Electrostatics Module" (2013).
9. J. Hernandez and A. Assis. "Electric potential due to an infinite conducting cylinder with internal or external point charge". *J. Electrostat.* **63** (12), pp. 1115–1131 (2005).
10. C. J. Bouwkamp and N. G. De Bruijn. "The Electrostatic Field of a Point Charge Inside a Cylinder, in Connection with Wave Guide Theory". *J. Appl. Phys.* **18** (6), pp. 562–577 (1947).
11. G.H.Jansen. *Coulomb interactions in particle beams*. Ph.D. thesis, Delft University of technology (1988).
12. J. Orloff. *Handbook of Charged Particle Optics*, Second Edition (CRC Press, 2009). Chapter: Space Charge and Statistical Coulomb effects, authors: P. Kruit and G.H. Jansen.
13. X. Jiang. *Coulomb interactions in charged particle optical columns*. Ph.D. thesis, Delft University of technology (1996).
14. PulsarPhysics. "General Particle Tracer, version 3.10". [www.pulsar.nl/gpt](http://www.pulsar.nl/gpt) (2011).
15. T. Verduin, B. Cook, and P. Kruit. "Influence of gun design on Coulomb interactions in a field emission gun". *J. Vac. Sci. Technol. B* **29** (6) (2011).
16. B. Cook, T. Verduin, C. W. Hagen, and P. Kruit. "Brightness limitations of cold field emitters caused by Coulomb interactions". *J. Vac. Sci. Technol. B* **28** (6) (2010).

## Appendix A: the extended two-particle approximation and the slice method

Here we briefly summarize the necessary equations for computing coulomb interactions using the slice method. Although the method is not explicitly used in this chapter, it is used in the introduction chapter and in chapter 6.

The slice method can be an excellent tool; it is computationally quick, but also often insightful. For example, the slice method is used to investigate the coulomb interactions of electron emitters [15, 16]. The appropriate literature [11–13] can be a bit too much in depth for some readers. The intention here is to just give the equations such that the interested reader can start calculating in no-time.

The extended two-particle approximation, initially developed by Jansen [11], gives equations for the coulomb interaction effects for beam segments with uniform properties. The slice method applies this method to beams that don't have such uniformity. By slicing the beam up into segments that can be considered uniform locally, the total effect can be found by summing over the contributions of the slices [13] (see figure 5.18).

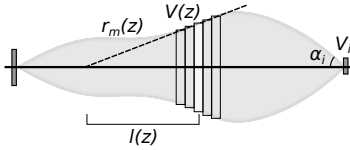


**Figure 5.18.** The slice method is based on an addition of contributions in thin beam segments for which the beam diameter and beam voltage can be considered constant.

The contribution due to stochastic coulomb interactions can be calculated from the slice-integral

$$r_{td} = \int M(z) l(z) \phi(z) dz. \quad (5.22)$$

$\phi(z)$  is the angular deflection per unit length. The multiplication with  $l$  transforms the angular deflection to lateral shift on the axis.  $M$  is the magnification of the virtual source position of that particular slice to the image or object position at which we want to calculate the contribution.

If the marginal ray trajectory  $r_m(z)$  is known, we can write

$$M(z) = \frac{r'_m(z)}{\alpha_i} \sqrt{\frac{V(z)}{V_i}}, \quad l(z) = \frac{r_m(z)}{r'_m(z)} \quad (5.23)$$

The value for the angular deflection in a slice depends on the regime and is given by

$$\phi(z) = 0.429 \frac{m^{3/2}}{\epsilon_0 q^{7/2}} \frac{I^3 r(z)}{V(z)^{5/2}} \quad \text{Pencil} \quad (5.24)$$

$$\phi(z) = 0.128 \frac{m^{1/3}}{\epsilon_0} \frac{I^{2/3}}{V(z)^{4/3} r(z)^{4/3}} \quad \text{Holtzmark} \quad (5.25)$$

$$\varphi(z) = \left( \frac{T_1 D_a^{18/7} D_r^6 I^{18/7} r(z)^{6/7} V(z)^{-15/7}}{T_4 + T_2^{1/7} D_r^6 D_a^2 I^2 r(z)^2 V(z)^{-1}} \right)^{7/6} \quad \text{Interpolation} \quad (5.26)$$

The constant in Jiang's interpolation formula are  $T_1 = 4.618 \times 10^{-2}$ ,  $T_2 = 2.041 \times 10^5$ ,  $T_4 = 6.250 \times 10^{-2}$ ,  $D_r = (2\epsilon_0 \pi / q)^{1/3}$ ,  $D_a = \sqrt{m} / (\pi 2^{7/2} \epsilon_0 q^{1/2})$ .

The contribution to the energy spread by the Boersch effect does not require any optical scaling and is given by

$$\Delta\epsilon = \int f_{\Delta\epsilon}(z) dz. \quad (5.27)$$

with the infinitesimal contribution in a slice given by

$$f_{\Delta\epsilon} = 0.642 * \frac{m}{\epsilon_0 q^2} \frac{I^2}{V(z)} \quad \text{Holtzmark} \quad (5.28)$$

$$f_{\Delta\epsilon} = 0.149 \frac{m^{1/3}}{\epsilon_0} \frac{I^{2/3}}{V(z)^{1/3} r(z)^{4/3}} \quad \text{Pencil} \quad (5.29)$$

$$f_{\Delta\epsilon} = \left( \frac{B_1 D_a^3 D_r^6 I^3 V(z)^{-3/2}}{1 + B_2^{1/4} D_r^6 D_a^2 I^2 r(z)^2 V(z)^{-1}} \right)^{2/3} \quad \text{Interpolation} \quad (5.30)$$

With  $B_1 = 7.861 \times 10^{-2}$  and  $B_2 = 6.828 \times 10^9$ .



## List of symbols

$E_q$	surface induced self-field	$C^{-1}$	$\Phi_e$	electrostatic energy electrons	eV
$\Phi_q(r_q)$	surface induced self-potential	V	$\Phi_{e,0}$	electr. landing energy electrons	eV
$\Phi(r)$	potential field	V	$\Phi_I$	electrostatic energy ions	eV
$r_q$	location of charge	m	$\Phi_{I,0}$	ion initial electrostatic energy	eV
$r_s$	location of surface element	m	$m_e$	electron mass	kg
$\hat{a}$	surface element unit vector		$m$	ion mass	kg
$\sigma(r_s)$	surface charge density	$Cm^{-2}$	$b$	impact parameter	m
$\kappa$	$1/4\pi\epsilon_0$	$Nm^2C^{-2}$	$b_{max}$	electron beam envelope	m
$\delta$	Dirac delta function		$\varphi$	angle around optical axis	rad
$e$	elementary charge	C	$\theta$	angle with optical axis	rad
$q$	ion charge	C	$f(\theta)$	probability density function	$rad^{-1}$
$R$	cylinder radius	m	$\epsilon$	additional ion energy	eV
$q_{im}$	image charge	C	$\mu_e$	expectation value ion energy	eV
$r_{im}$	image charge location	m	$\sigma_e$	standard dev. ion energy	eV
$\Phi$	ion acceleration voltage	V	$\mathbf{R}$	trajectory displacement	m
$E$	electric field	$Vm^{-1}$	$\sigma_x$	stand. dev. traj. displacement	m
$E_1$	inside-chip electric field	$Vm^{-1}$	$C_R$	covariance matrix traj. disp.	$m^2$
$E_2$	outside-chip electric field	$Vm^{-1}$	$\theta_{min}$	scatter angle cut-off	rad
iKn	ionic Knudsen number		$\theta_{max}$	scatter angle cut-off	rad
$N$	# simulated particles	#	$z_i$	position ith electron scatter	m
$N$	# electron-ion collisions	#	$\alpha$	ion scatter angle	rad
$I$	ion beam current	A	$\alpha_e$	electron divergence angle	rad
$I_e$	electron beam current	A	$\Delta p_{\perp}$	transverse ion mom. acquired	kgm/s
$d_v$	virtual source size	m	$\Delta p_{\parallel}$	parallel ion mom. acquired	kgm/s
$d_e$	electron probe size	m	$\Delta\epsilon_{50}$	fw50 electron-ion energy spread	eV
$I_e$	electron beam current	A	$d_{50}$	fw50 electron-ion traj. disp.	m

# 6

## Experimental source performance

*"Beliefs don't change facts. Facts, if you're reasonable, should change your beliefs."*

RICKY GERVAIS

## 6.1. Introduction

The simulations of ion emission from the NAIS discussed in chapter 5 promised an excellent brightness of  $B \geq 1 \times 10^6 \text{ A/m}^2\text{srV}$ . Even when the operation conditions are suboptimal we expect  $B \geq 1 \times 10^5 \text{ A/m}^2\text{srV}$ . This result is encouraging and motivates efforts for validating such performance.

The production of ion beams of several noble gas species have been demonstrated already [1], so the concept of generating ions in a NAIS configuration is not in question. The energy spread was also already investigated [2]. In this work we focus our attention on determining the brightness. A first brightness measurement for hydrogen in a NAIS configuration was performed by Liu et al. [3]. The conditions of operation were rather poor though, yielding brightnesses of  $B \leq 1 \times 10^3 \text{ A/m}^2\text{srV}$ . In addition, their method of measuring brightness did not include a probe or source size measurement, but was inferred from the aperture size. In some cases this can be correct, but the virtual source size can easily be smaller if the electron probe is smaller. On the other hand, gas scattering and coulomb interactions outside the chip can make the virtual source size larger. A reliable brightness measurement should include a probe size measurement.

## 6.2. Experimental method

When measuring brightness it is common to select a small fraction of the beam, say 100 pA or so. This selection is done by placing an aperture in the beam line such that the outer parts of the beam are blocked. The beam angle is then defined by this aperture and the angular current density can usually be considered uniform. In our setup we have no aperture available, as will be discussed later. Therefore, we are dealing with a non-uniform angular current density profile. This forces us to make a choice for what to use as a beam divergence angle. We use the angle  $\alpha_{50}$  which defines the beam cone containing 50% of the beam current.

The quantity we measure is the 50 % beam brightness, defined as

$$B_{50} = \frac{4I_{50}}{\pi^2 d_{50}^2 \alpha_{50}^2 \Phi}. \quad (6.1)$$

We use  $d_{50}$  for the fw50 of the focused spot.  $I_{50}$  is the current within that beam cone. This definition is consistent with what we have used in the simulations as a figure of merit. This is also the brightness an optical designer would need to use for probe calculations when 50% of the beam current is used to focus on the sample. We can interpret this definition as the practical brightness for beams with a non-uniform angular distribution. It is also consistent with equation 3.28 using  $\eta = 0.5$ .

In the experiment we need to measure the constituents of equation 6.1 simultaneously. The acceleration voltage  $\Phi$  is something we can simply control. The total current  $I_{100}$  is measured by letting the beam land on a conductor that is biased to +50 V with respect to the surroundings in order to prevent secondary electrons to escape. The current in the inner beam cone is simply  $I_{50} = \frac{1}{2} I_{100}$ . For determining the geometrical spot size  $d_{50}$  we need a to make an image of the source without

being deteriorated by aberrations, coulomb interactions, or other disturbances. We use an ion transmission imaging system such that we can make knife-edge scans and infer the spot size from those scans. We use a 25-75% rise distance, and convert it as  $\text{fw50} = 1.761 d_{25-75}$  (see table 3.1). By defocusing the beam and making knife-edge scans again, we can obtain information about the beam divergence angle  $\alpha_{50}$ . Figure 6.1 shows the concept of focused and defocused knife-edge scans.

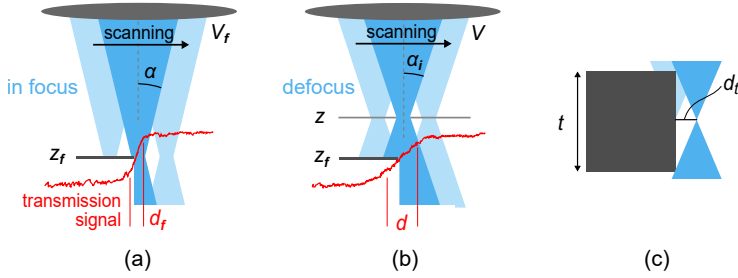


**Figure 6.1.** Knife-edge scanning the ion beam to determine the beam properties. a) The beam is focused on the knife-edge such that the source can be imaged. b) A defocused scan contains information about the divergence angle of the beam. c) A source of error in the acquired transmission signal is caused by the thickness of the knife-edge.

The general method of measuring a brightness is making a set of different defocus knife-edge scans and fitting the measured probe sizes to a defocus model. The probe size  $d$  as a function of the focus position  $z$  according to the proposed model is

$$d(z) = \left( d_{50}^s + \left| 2\alpha_{50}(z - z_f) \frac{M_a(z)}{M_a(z_f)} \right|^s \right)^{\frac{1}{s}}. \quad (6.2)$$

If the beam is focused on the knife-edge, the smallest probe size is acquired, denoted by  $d_{50}$ . The constant  $z_f$  is the  $z$ -position of the best focused image, i.e. the knife-edge location. In our setup it is not possible to control the working distance, so we can only defocus by changing the lens voltage. When doing this, we change the beam angle itself, which we have to correct by including the ratio of angular magnifications in the model. The free parameter  $s$  dictates how the defocusing and the geometrical spot size are added. Most correct would be a convolution of the distributions, but a power law is often a good approximation. We don't know what power is most appropriate, so we keep it as a free parameter.

For a single brightness data point, a set of probe sizes  $d_i$  is obtained and we record the accompanying lens voltages. We pre-calculate the focus position as a function of the lens voltage from a simulation. The pre-calculated data is used to transform the recorded lens voltages to focus positions. The same concept is used to find the angular magnifications as a function of the focus position  $z$ . The set of  $d_i$ 's with accompanying  $z$ -positions and  $M_a$ 's are the input for a least squares fit of equation 6.2. The outputs of the fitting procedure are  $\alpha$  and  $s$ , of which the former is the quantity we are after.

In conventional secondary electron detection schemes, rounded edges introduce a blur in the image, which is a known pitfall in probe size measurements [4]. However, we repel any secondary electrons and only transmitted ions are measured. Because the transition from full blockage to full transmission is fairly shape independent, our method is not directly limited by the shape of the knife-edge. Only ions that penetrate the material and come out again below or on the side can give an error in the measurement. The typical size associated with such a process is in the order of nanometers, which is much smaller than the typical probe size we intend to measure.

One error that can be introduced, is related to the thickness of the knife-edge, as illustrated in figure 6.2c. If we assume an infinitesimally small focus, we see that the beam can be partially blocked, even though the focus has moved beyond the knife edge. This is caused by the beam divergence hitting the side edge of the knife-edge. A rough estimate for the distance indicating 25% transmission to 75% transmission as caused by this effect is  $d_t = \frac{t}{4} \tan \alpha$ . The sample thickness needs to be sufficiently small to make this contribution insignificant.

In principle it is possible to calculate back the intensity distribution from a knife-edge scan if radial symmetry is assumed [5], although we have not used this option so far.

### 6.3. Experimental Setup

The purpose of the presented experimental setup is measuring source characteristics in the simplest possible way. Rather than designing a custom electron gun, we use a FEI Verios SEM to supply the electron beam. The optical setup resorts in the sample chamber of the SEM, so replacing the chip or adjusting the hardware only requires a sample chamber vent.

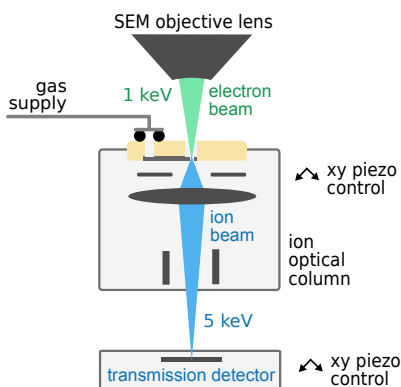


**Figure 6.2.** The general idea of the experimental setup is an ion optical column inside an SEM. Additionally we use a SECOM platform [6] for the xy control of the ion optical column and independently the ion transmission detector together with the knife-edge sample.

To further minimize design efforts, our device was retro-fitted to a so-called SECOM platform supplied by DELMIC [6]. This platform replaces a Verios SEM door and contains several piezo-electric precision stages. The optical column can be moved to make the nano-aperture coincide with the electron optical axis. The detector can be moved to position the knife-edge on the ion optical axis. Figure

6.2 indicates the general idea of the experimental setup and the rest of this section discusses the details of this system. Figure 6.3 gives an impression of the full system as installed in the laboratory.

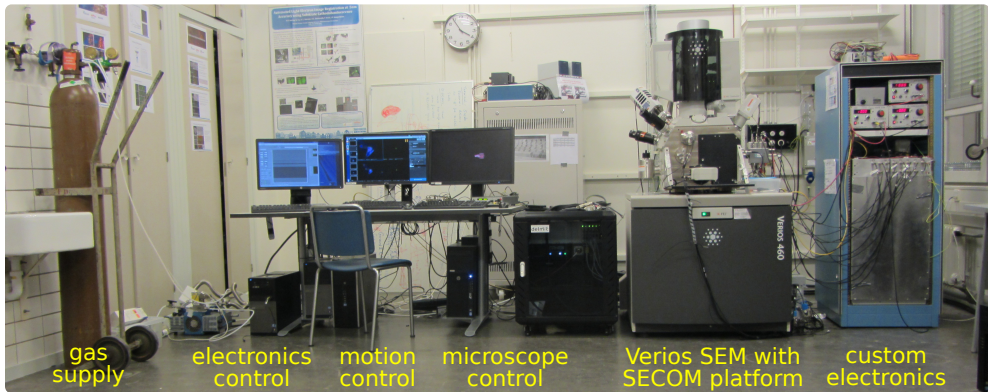


**Figure 6.3.** Impression of the laboratory.

### 6.3.1. Ion optics

Mounting the setup on a SECOM platform meant a serious constraint on the available space, resulting in a small ion optical system. The smallest number of elements in the column were used, which is in line with trying to make the simplest possible system. The optical design is shown in figure 6.4. We emphasize that the imaging system is not optimized for high resolution, but rather for making an easily measurable source image.

The system is source magnifying, yielding a couple of advantages. A rather large working distance becomes acceptable such that post-lens scanning is possible. This makes pivot-point scanning unnecessary and one octopole for scanning and stigmatism is sufficient. Furthermore, any absolute errors, such as mechanical vibrations, become less relevant.

The system does not comprise a beam limiting aperture half-way the column since we have no in-column electrical or mechanical beam adjustment. Getting the beam through the aperture would require tremendous mechanical accuracy of various parts, which is considered not feasible.

For a good measurement of the source properties we need to confirm that the aberrations are sufficiently low, as the probe size should be dominated by the source image. We also need to know the relation between the lens voltage and the image z-position in order to compute the beam divergence angle, as explained in the experimental method section. Clearly we need an ion optical simulation. Knowing the magnification for calculating the virtual source size is a plus, but not strictly necessary for calculating the brightness.

Electrostatic field solving and ray-tracing is performed using EOD [7]. An example beam envelope and the main optical properties are shown in figure 6.4. The simulation did exclude any effects that have to do with in-chip lens effects. These are considered intrinsic to the source and are the subject of chapter 3. We start the

beam with 100 eV of initial energy at position  $z = -30\mu\text{m}$  with respect to the chip position. This follows from the first order theory described in 3 with an acceleration field of  $3.3\text{ kV mm}^{-1}$

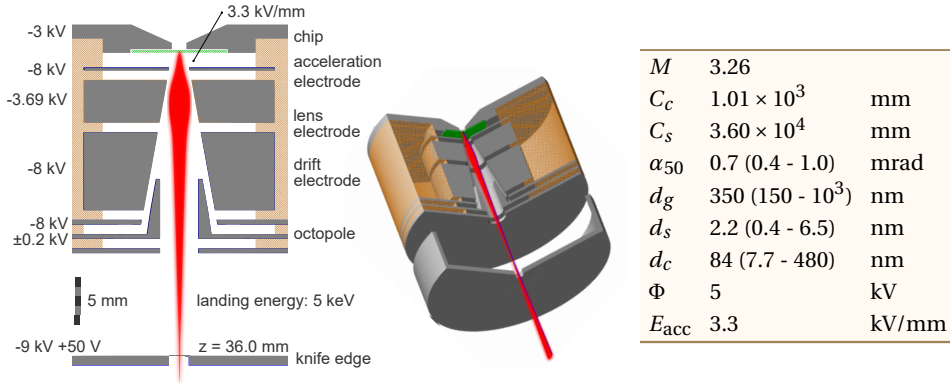


**Figure 6.4.** An ion optical simulation is performed using EOD [7]. We calculate optical properties for a nominal situation and indicate more extreme possible values between the brackets. Overall we assume a 1 eV energy spread, but for the worst case chromatic aberration 4 eV is used. This simulation does not include the details of the chip and the magnification refers to a virtual source that already includes any optical effects caused in and around the chip. The voltages indicated on the left all share a common -3kV addition because we decelerate the electron beam in front of the chip for better electron beam performance.

From the simulations described in chapter 5 we know that a typical normalized beam angle after uniform acceleration for the NAIS is  $0.15 \text{ mrad V}^{1/2}$ . For this setup, considering a 5 kV energy and a magnification of 3.26, the expected beam angle at the knife-edge is 0.7 mrad. This value may range between 0.4 to 1.0 mrad for alternative operation conditions. We use these values to estimate the aberration contributions. We expect a virtual source size between 50 and 300 nm.

The results in the table in figure 6.4 indicate that in most cases we expect the virtual source image to be the dominant probe contributor. Spherical aberration plays no role in the probe formation at all. This means that non-chromatic off-axis aberrations should be relatively small, as they are linked to the spherical aberration coefficient. The chromatic aberration can play a role in certain configurations.

An original design was less affected by chromatic aberration, but a fabrication error resulted in worse performance. If the electrode bore size of the acceleration electrode and the lens electrode are made smaller, we can improve upon this up to a factor 2 or so. This also slightly increases the magnification of the system up to 3.7. A design with smaller spaces between the electrodes could further decrease the aberrations, but this does increase the risk of arcing.

In order to quantify any misalignment of the chip, we can look at the amount of image shift  $\Delta r_i$  caused by a lens voltage change  $\Delta V_L$ , as a function of the chip misalignment  $r_{\text{chip}}$ . We found it can be described with better than 1% accuracy as  $\frac{\Delta r_i}{\Delta V_L} = 0.012 \cdot r_{\text{chip}}$  when using meters and volt.

The focusing lens electrode causes the beam to decelerate to about 700 eV of kinetic energy. This is relatively low for a charged particle beam and although originally not anticipated, coulomb interactions turn out to be relevant in some

situations. We have used the slice method (see chapter 5 appendix A) to estimate the effect for some typical cases; the result is shown in table 6.1. We find in general a negligible effect of the Boersch effect, but an important influence of the trajectory displacement.

Due to trajectory displacement, but also chromatic aberration, it is not possible to form an unperturbed source image in all cases. Only at low currents ( $< 300$  pA) this seems possible. At higher currents the measured brightness represents a lower limit.

$d_v$ nm	$B$ A/m <sup>2</sup> srV	$I$ nA	$d_{td}$ (He) nm	$d_{td}$ (Ar) nm	$\Delta\epsilon$ (He) eV	$\Delta\epsilon$ (Ar) eV
50	$1.0 \times 10^6$	0.2	0	11	0.002	0.020
50	$3.0 \times 10^6$	0.6	10	137	0.018	0.138
100	$1.0 \times 10^6$	1.0	37	301	0.045	0.295
100	$3.0 \times 10^5$	1.0	37	211	0.037	0.209
300	$1.0 \times 10^5$	5.0	302	907	0.296	0.888

**Table 6.1.** A set of hypothetical beam properties are used to estimate the influence of coulomb interaction in the decelerating lens using the slice method. The trajectory displacement  $d_{qq}$  is calculated at the virtual source plane so it can directly be compared to the virtual source size  $d_v$ .

### 6.3.2. Mechanical design

The mechanical design of the column is based on a PEEK insulating cylinder onto which electrodes are glued. The electrode on the top, the chip holder, is the only detachable part and allow chips to be replaced. Figure 6.5 shows this design in some detail. Electric discharge machining is used to make the inner bore after the separate electrodes were glued together. This ensures good alignment of the extractor, the lens electrode, and the drift space electrode. Special recesses were made at the electrode attachments to the PEEK for improved high voltage resilience, as can be seen in figure 6.5. Several high voltage test made clear that 5 kV (+ and -) can be applied confidently between all adjacent electrodes, excluding internally between the octopole electrodes.

We have started initially with a quadrupole, but discovered that full astigmatism correction is essential. The system was upgraded with an octopole, mounted to the bottom of the device. This explains the somewhat odd configuration of the octopole.

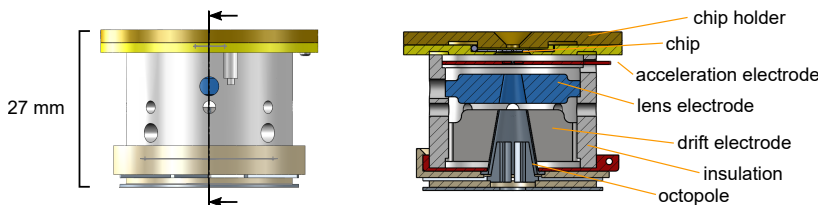


**Figure 6.5.** The small ion optical system fits inside a SEM chamber on a SECOM platform [6]. The electrodes are made from titanium and the insulating holder is PEEK. The central cone is made in one go using electric discharge machining after all the parts were glued in place. The octopole was added later. Three o-rings in the top lid fixate the chip. One of the o-rings is aligned with the gas channel entrance on the chip such that gas can be supplied.

One challenge is placing the chip in the center of the optical system. A conventional alignment method is using a rotating table in combination with micrometer



adjustment levers and a simple optical system to image the bores. This conflicts with our desire to quickly test several chips while the setup remains mounted in the SEM. Therefore, we have tried to use a method to auto-align the chips.

Sine the chips are fabricated using a KOH etch, the edges of the chip have a well defined angle of 54.74 degrees. The location of this edge is well defined with respect to the center of the free standing membrane up to lithographic precision. We employ this edge by letting it touch three silicon nitride precision spheres. These spheres are glued into the chip holder as can be seen in figure 6.6.

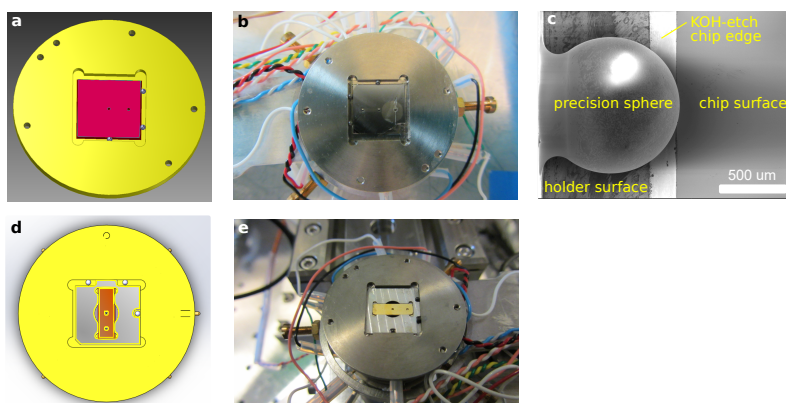


**Figure 6.6.** Alignment of chips with respect to the ion optical axis. a,b) The KOH edges of the chip touch the precision spheres in the chip holder. c) SEM images of the KOH edge sliding under and touching the precision sphere as intended. d,e) A different sized chip is fitted in the same structure by using an alignment adapter.

6

To test the chip placement reproducibility, we have repeatedly (15 times) put a dummy chip in and out the holder and measured the distance between the KOH-etch line and the edge of the chip holder (see figure 6.6c). The standard deviation of this measurement for the three spheres was 3.5, 3.8 and 4.9  $\mu\text{m}$  and the maximum observed variation was 10  $\mu\text{m}$ . In a separate test we measured the position of the precision spheres with respect to the optical axis and found only a 2  $\mu\text{m}$  error compared to the designed values. This is better than what could have been expected from mechanical fabrication tolerances. We conclude that if the chip KOH etch mask for the chips is designed in accordance with the current chip holder, we can expect alignment accuracy in the order of 5  $\mu\text{m}$ . Note that this assumes the aperture to be milled perfectly in the center of the free standing membrane.

### 6.3.3. Electron beam

The current and the spot size of the electron beam play a crucial role in the NAIS performance. We have made a rough assessment of the ebeam quality by inferring a spot size from a SEM image. This is not the most accurate method because the object being imaged can influence the inferred probe size [4]. The method is used for its simplicity and should give a reasonable indication.

The highest current mode of the FEI Verios SEM at 1 keV beam energy is 100 nA, but it actually delivered 121 nA. The ultra high resolution mode was used, which

refers to a magnetic immersion lens. We used a proprietary program owned by FEI to detect multiple edges in the images and use the peak of the histogram of rise distances as a figure of merit. An average is influenced more by false edge detects. Using table 3.1 we can calculate a fw50 from the 25%-75% rise distance output of the program.

When operating with -3 kV beam deceleration, the 25%-75% found is 175 nm, see figure 6.7a. The resulting ebeam performance is a 231 nm fw50 spot diameter with 121 nA of current. This is poorer than the 100 nA in 50 nm we have anticipated for high end operation. One known issue has to do with the introduction of our ion optical column. Because we decelerate near the sample, the shape of the chip holder (see figure 6.5) introduces aberrations. Without the lid a 158 nm fw50 spot diameter was obtained.

We conclude that the Verios SEM does not offer the specifications we believe a NAIS-optimized egun can deliver. Nevertheless, if we look at sub-optimal conditions simulation results in table 5.3, we can expect a brightness above  $1 \times 10^5 \text{ A/m}^2 \text{ srV}$  with this ebeam performance.

Two other configurations were examined as shown in figure 6.7b and 6.7c. A slightly higher landing energy of 3 keV, again using -3kV beam deceleration, yielded a 139 nm fw50 spot size. Using a significantly lower current of only 13 nA, at 1 keV landing energy yielded a 33 nm spot size.

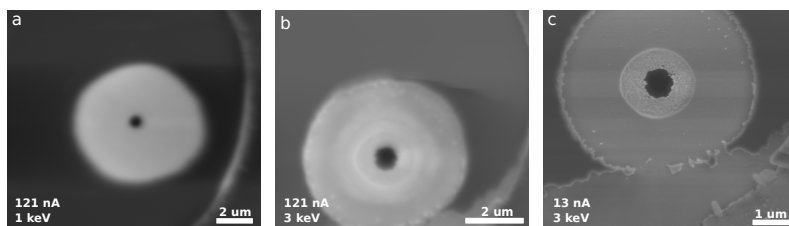


**Figure 6.7.** Verios SEM images of a nano aperture. a) Nominal operation conditions, estimated fw50 spot size 231 nm. b) Increased landing energy, estimated spot size: 139 nm. c) Decreased beam current, estimated spot size 33 nm. This aperture is the same as the one showed in figure b, but different from figure a.

#### 6.3.4. Ion detection

The most standard way of imaging with an ion beam is detecting the secondary electrons using an Everhart-Thornley detector (ETD). Since the knife-edge sample will be referenced to -8 kV and grounded elements are in the proximity, it is very difficult to guide the secondary electrons towards the detector entrance. Combined with the little space available, an ETD is not easy to incorporate in this system. In addition, as was already explained, a secondary electron image can be deceiving if not the sample, but the probe itself is of interest. So, instead of an ETD, we use an ion current transmission detector.

No ion transmission detector that fulfilled our constraints was available so we have designed one ourselves. A major challenge is that ions hitting a sensitive detector directly will induce damage. The concept we use is depicted in figure 6.8. Ions are repelled and steered away from the optical axis as a consequence of the

ex-centric recess. When the ions hit the metal surface with an energy of 5 keV, they will generate secondary electrons. The local potential is -8 kV, so the secondary electrons are accelerated towards ground potential, at which we have placed a solid state electron detector. Measuring these secondary electrons at ground potential is advantageous, as it is difficult to measure weak and fast signals on top of a high voltage. The solid state detector offers crucial signal amplification very early in the detector chain. The ion landing area is tilted to improve the acceptable incidence angle of the ion beam. If the incident ion beam makes an angle of more than 6 degrees with respect to the normal of the sample surface, the generated secondary electrons start to miss the detector surface.

The knife edge sample we use is a pattern of holes of  $45.7 \pm 0.2$   $\mu\text{m}$  in diameter. This diameter is much larger than the typical probe size we intend to measure such that we may approximate the curved edges as straight. The sample thickness is  $54.5 \pm 1$   $\mu\text{m}$ , thin enough to prevent any significant beam broadening. Following the analysis presented in section 6.2, we estimate the fw50 contribution due to the sample height to be about 13 nm for a 1 mrad beam angle.

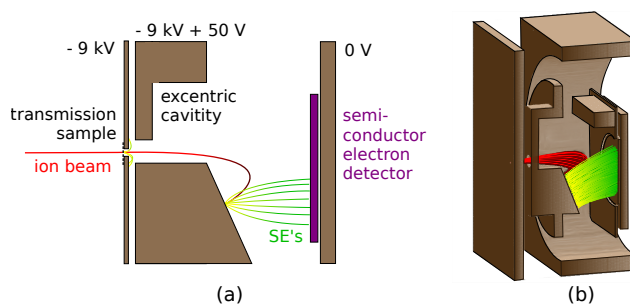


**Figure 6.8.** Ion transmission detector design. Ions enter the detector and are being decelerated and directed to the side due to an ex-centric cavity. Secondary electrons are generated at the ion impact location and accelerated towards the solid state electron detector plane. In the simulation shown in figure b, secondary electrons between 0 and 10 eV are emitted isotropically.

A commercial solid state electron detector by Opto Diode is used (AXUV63HS1). With a rise time of 2 ns it is fast enough for scanning purposes. The sensitivity for 8 keV electrons is  $0.23 \text{ A W}^{-1}$ , giving an amplification of about 1800. This means that a 1 nA ion beam, assuming an SE yield of 1, gives almost  $2 \mu\text{A}$  of current. This is fairly easy to measure even when scanning rapidly, say  $2 \mu\text{s}$  per pixel. The detector signal is amplified by a low noise trans-impedance current amplifier (FEMTO, DLPCA-200). At 400 kHz bandwidth we can amplify  $1 \times 10^6 \text{ V A}^{-1}$ , such that our 1 nA ion beam results in about 1 V at the data acquisition input.

Typically we scan at 50 Hz per line to avoid any 50 Hz disturbances. Using 800 pixels per line this means a dwell time of  $25 \mu\text{s}$ . At 360 pA of argon current we found a SNR of about 16 ( $\text{SNR} = \text{transmission detector current} / \text{RMS of the detector current noise}$ ). This is enough for pleasant experimentation and proper data analysis. As an absolute minimum, we may go down to a SNR of 2, corresponding to an ion current of 50 pA as the minimal required current in the present configuration at  $25 \mu\text{s}$  dwell time.

### 6.3.5. Electronics

For driving the experimental setup, custom electronics needed to be made. A detailed description of the system can be found in ref. [8]. We kept all voltages under 10 kV to keep the requirements for high voltage connectors and feedthroughs simple.

The biggest challenge was the high voltage referenced scan electrodes. Standard high voltage power supplies can not operate at scanning frequencies, so we need to stack fast, medium voltage range ( $\pm 200\text{V}$ ) amplifiers on top of a high voltage supply. A high voltage insulated box was built, housing all the electronics needed to generate a scan signal referenced to a high voltage.

We use a fiber cable as a means to communicate between the PC at ground potential and the electronics at high voltage. This fiber cable acts virtually as a USB connection. For making images it is essential to have synchronization scanning and detection, but the detector signal is measured at ground potential while the scan signal electronics resides at high voltage. We need to send a synchronization pulse between the detector DAQ and the scan signal DAQ. USB is not suitable for such time sensitive signals, so we use a high voltage insulating opto-coupler and let scanning and detection share the same sample clock.

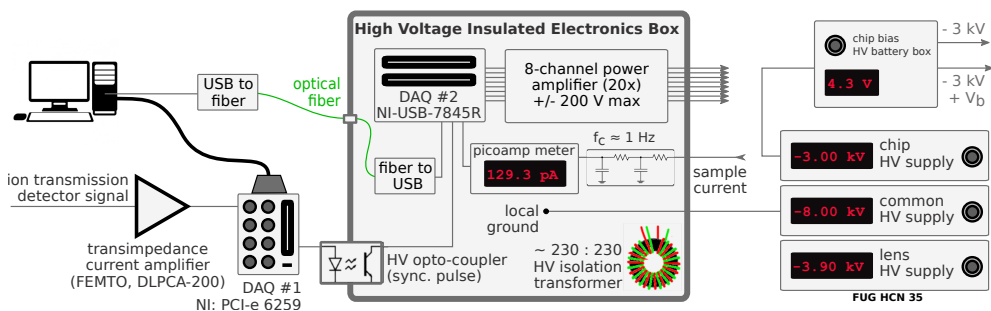


**Figure 6.9.** Overview of the most important components in the electronics that drive the ion optical column. Essential is the high voltage insulated box in which the scanning amplifiers and the accompanying driving electronics are housed. This box is required because the scan electrodes are referenced to a high voltage of -8 kV.

The deflection on the sample induced by a voltage applied to opposite octopole electrodes needs to be experimentally calibrated, but a rough estimate yielded  $5\mu\text{mV}^{-1}$ . The DAC (NI-USB-7845R) gives an output of  $\pm 10\text{V}$  and the amplifiers scale 20x giving  $\pm 200\text{V}$  as the maximum output. This yields about 2 mm field of view, which is sufficient to navigate across the sample. The DAC resolution is 16 bit, so the smallest output voltage step we can make is 6.1 mV, which relates to 31 nm as a minimal step size. This is 5 times smaller than the smallest expected spot size so we are not limited by the digital resolution. We may set the range to  $\pm 5\text{V}$  to obtain a 15 nm step size.

Since the chip will be referenced to a high voltage, we need to consider the problem of gaseous breakdown through the gas supply line. In a previous experimental setup we have addressed this problem by using a powder filled tube much like the

ideas found elsewhere [9, 10]. This concept was tested to maintain at least 30 kV, independent of the pressure.

We found that for lower voltages ( $<10$  kV), it is sufficient to use small PEEK hoses. We tested a 100 mm long hoses with 0.2 mm inner diameter in the pressure range 1-1000 mbar and concluded that 5 kV can easily be maintained, which is sufficient for our purpose. In fact, using these hoses, up to 14 kV without breakdown over a wide pressure range has been achieved. Note that for such high voltages care should be taken in placing the hoses sufficiently far away from grounded metal parts, as the electric field may be confined to a small part of the hose, which lowers the breakdown voltage. We believe that that small inner diameter of the hoses helps to interrupt avalanche breakdown effects.

The high voltage power supplies used were the FUG HCN-35. The typical ripple of these power supplies is specified as 0.6 V peak-to-peak [8]. We have used a second order RC filter with a cut-off frequency of 1 Hz to eliminate most ripple, since we keep the voltages static or quasi-static anyway. For the HV common, adjacent to the lens electrode, it was not possible to use such a filter due to complication with the electronics in the HV box. So, effectively we can expect a 0.6 V peak-to-peak voltage instability around the lens electrode. If the beam is on axis this is of no concern, but for an off-axis beam this may lead to off-axis chromatic aberration.

### 6.3.6. Gas chamber fabrication

The brightness measurements are performed using a set of chips produced externally by a semiconductor fabrication company. The fabrication methods and details of the structure are proprietary information so the chips can only be discussed briefly. The membranes are made of silicon nitride, encapsulated in metal. The metal coating ensures all surfaces facing the beam are conducting thereby preventing any charging, while the silicon nitride offers reliable membrane strength. The issue of poor flow conductance described in chapter 2 is adequately dealt with such that only the local radial pressure drop can be significant.

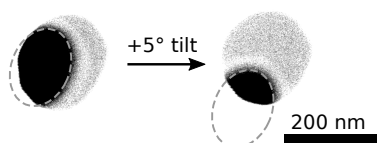


**Figure 6.10.** The membrane spacing can be estimated by comparing two SEM back-scatter images made with different stage tilt angle. The bottom aperture moves 105 nm relative to the top aperture upon a  $5^\circ$  stage tilt giving an estimate for the membrane spacing of 1200 nm. The images are heavily contrast-saturated such that bottom aperture becomes more clearly visible.

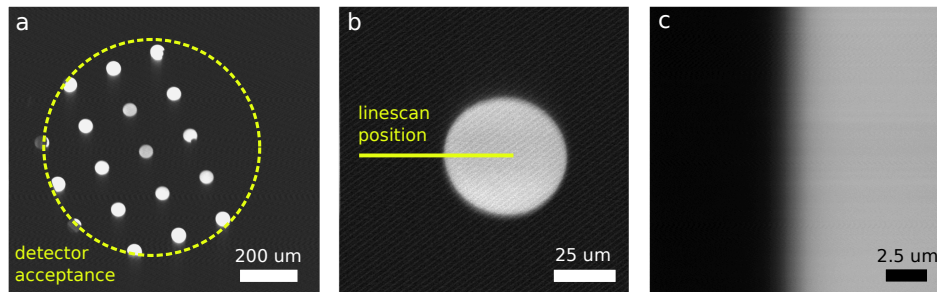
The general structure resembles the MEMS fabricated devices discussed in section 1.4.2. This means that two KOH etch openings are made through a wafer. One serves as a gas inlet, while the other allows the electrons to reach the free standing membranes. The ion side of the chip has a flat geometry such that the high acceleration field is not suppressed. The double aperture and the gas inlet are both made by FIB milling. The estimated membrane spacing is 1200 nm as measured by the method indicated in figure 6.10. We have used several of these chips, but we report on measurements using a chip with a 675 nm aperture diameter on the electron side and a 800 nm diameter aperture on the ion side.

In an attempt to quickly produce some additional chips, we have used the two-chip adhesive bonding technique, discussed in section 1.4. One simplification compared to the method by Jun et al. [2] was the use of silicon nitride membranes coated with metal, rather than the more challenging full metal membranes. This also offered the opportunity to investigate if the thin insulating surface at the inside of the chip is indeed problematic. The production results were rather dissatisfying as most chips suffered from heavy glue seepage between the two chips. Many did therefore not conduct any gas and others were far from the specified membrane spacing. This problem was also encountered by Jun et al. [2]. We should conclude that gluing chips is not an advisable way to proceed for the NAIS project. Not only does it deliver sub-optimal specs, the fabrication is not particularly quick and easy either. Nevertheless, we managed to produce some devices and we report on experiments with one particular chip, with a 10  $\mu\text{m}$  membrane spacing. Note that the brightness experiments are performed with the 1200 nm spaced, externally produced chips.

## 6.4. Brightness measurements

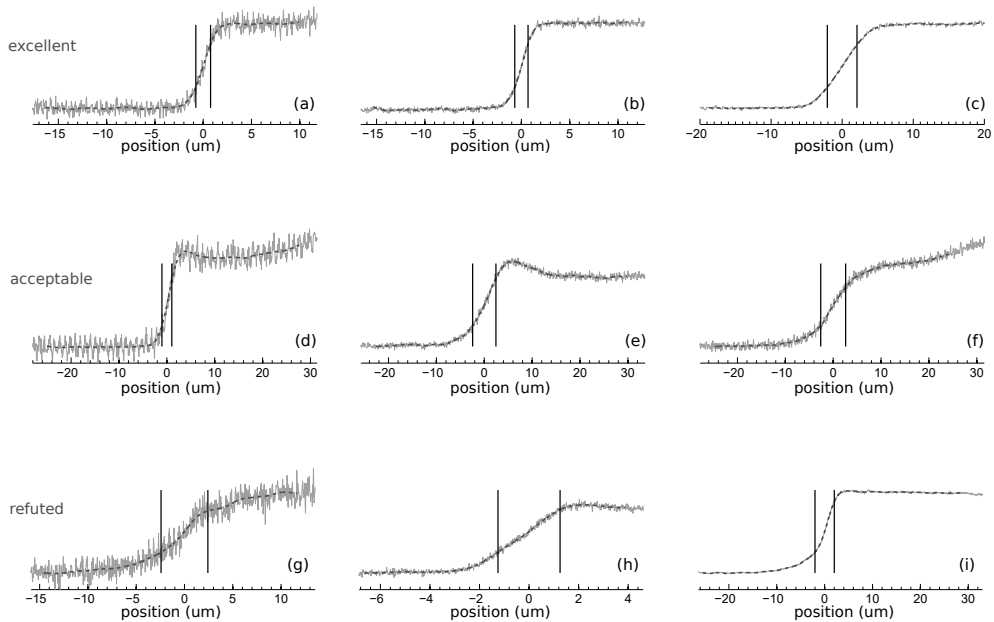
### 6.4.1. Line scan imaging and analysis

Figure 6.11 shows example ion transmission images intended for brightness measurements. Full 2D imaging is used for sample navigation and initial optimizing of the focus and the stigmator. Line scans are used for beam property analysis.



**Figure 6.11.** A typical knife-edge scan procedure using argon ions. a) An overview ion transmission image. b) Selecting a particular transmission aperture and determining the horizontal knife-edge scan location. d) Saving multiple equivalent knife-edge scans in one image by only scanning horizontally.

Hundreds of line scans are acquired and a selection is shown in figure 6.12. Often we acquire rather nice line scans such as the ones in figure 6.12a, 6.12b and 6.12c. The figures 6.12d-i show less ideal line scans. We attribute the differences to a combination of beam a-symmetry and detector response non-uniformity. Since the non-transmitting part of the line scan (LHS of the curves in figure 6.12) hardly suffered from such nuisances, we found it is more robust to use only the left hand-side of the steepest part in the line scan to determine the rise distance. Effectively we have defined the 25-75% rise distance as twice the 25-50% distance.



**Figure 6.12.** Examples of ion transmission knife-edge scan results. The selected line scans shown here represent the variety of results acquired in the experiments. All signal intensities are normalized. (a-c) Excellent quality line scans, with decreasing amount of relative noise. (d-f) Non-uniformity in the transmission signal makes these line scans more difficult to analyze, but these are still considered good enough to use for the calculation of beam properties. g) A fair amount of noise in combination with an a-symmetric and unstable signal makes this line scan unreliable. h) A kink in the rising part of the signal caused the steepest part of the edge to poorly represent the half-way point. i) A strong a-symmetry causes ambiguity in the rise distance as we are assuming rotational symmetry of the beam intensity. Most line scans look like a to f, but line scans such as g,h, or i are excluded for data analysis.

The large set of line scans for various operating conditions are fitted according to the model of equation 6.2. The data and the results are shown in figure 6.13. The quality of fitting the model varies between operating conditions. In particular, we find that measurements with a positive defocus ( $\Delta z \geq 0$ ) do not always match the model very well. We have found no satisfying explanation for that. The result of inaccurate fits is a large uncertainty in determining the beam divergence angle, which we quantify by a 95% confidence interval.



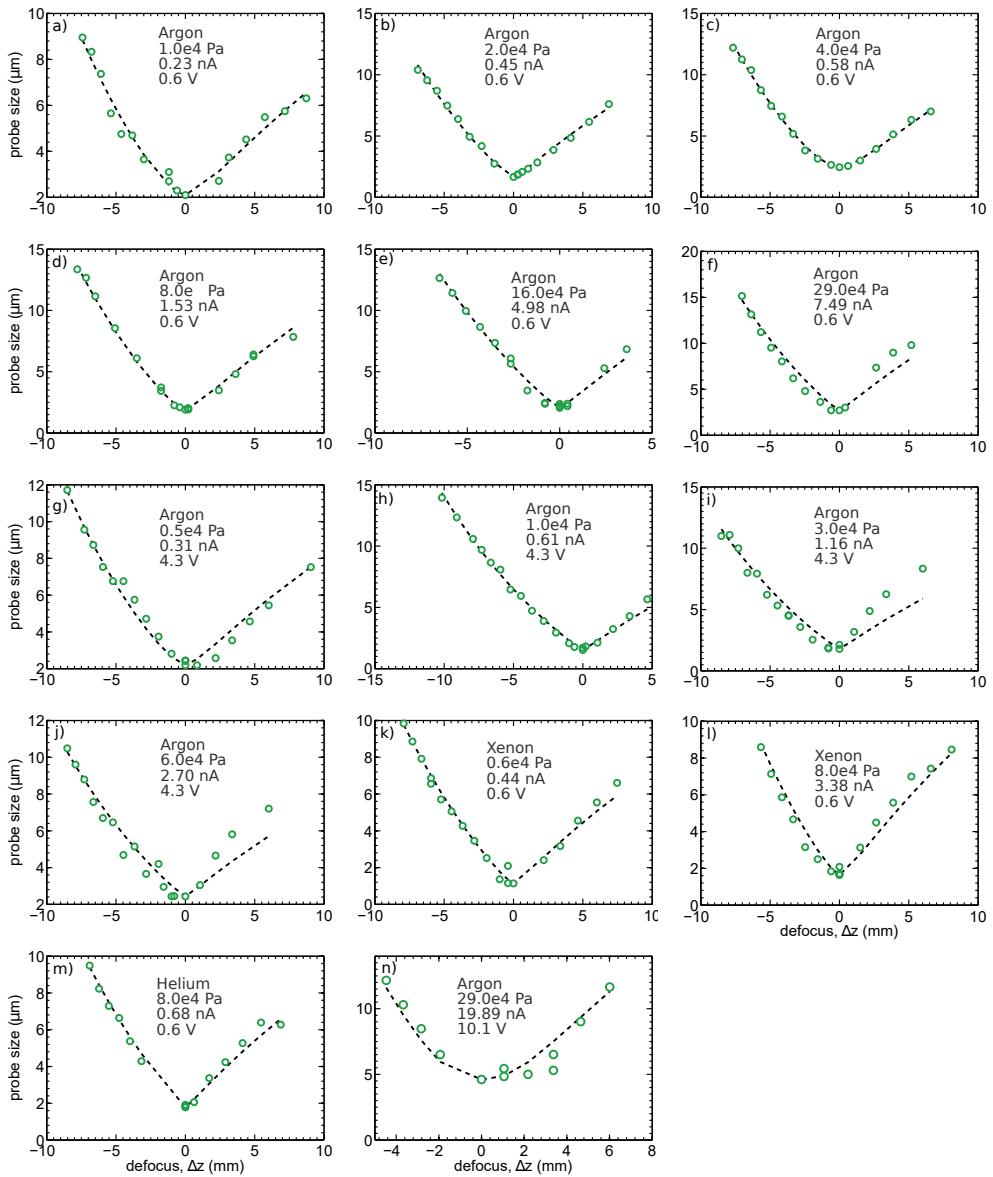


**Figure 6.13.** Defocus measurements for a range of operating conditions are plotted together with a fit of the model (equation 6.2). The probe sizes are acquired from analyzing line scan data and the defocus distance is calculated from the applied lens voltage via a simulated look-up table.

One of the challenges was aligning the chip to the ion optical axis without adjustment. To investigate the alignment accuracy, we varied the lens voltage and observed the amount the images shift. We tried different combination of chips and chip-adapters and found quite a spread in the observed image shift, in the range  $0.3\text{-}1.5\text{ }\mu\text{m V}^{-1}$ . Using the relation explained in section 6.3.1 we estimate that the range of alignment accuracies is  $30\text{-}125\text{ }\mu\text{m}$ . The best achieved alignment was  $0.34\text{ }\mu\text{m V}^{-1}$  yielding a chip misalignment of  $27\text{ }\mu\text{m}$ . This was the configuration used for the presented brightness measurements. The associated chromatic off-axis



aberration manifest itself as a 0.2-0.8  $\mu\text{m}$  peak-to-peak vibration in the image for the expected 0.6 V peak-to-peak voltage instability. This is smaller than the typical probe size we have measured.

The misalignment is certainly unwanted. The image shift is a nuisance during defocus experiments and off-axis (chromatic) aberrations are on the lure. Currently we do not believe it is a bottleneck though. There was no clear relationship between the misalignment and the smallest measurable probe size. Only for the worst misalignment did we see evidence for coma aberrations.

The alignment method was expected to give down to 5  $\mu\text{m}$  alignment accuracy, but this clearly wasn't achieved. We attribute this to the practical aspects of mounting and in an improved version the chip should be fixated before the top part is clamped on to the chip. The limited space and small parts involved make this no easy task.

#### 6.4.2. Brightness

The knife-edge scans and model fits are used to compute the brightness. The resulting measured brightnesses are shown in figure 6.14. The perhaps obvious, but most important observation, is the experimental demonstration of  $B \approx 1 \times 10^5 \text{ A/m}^2\text{srV}$ . A very promising result as well, is a brightness of  $3.5 \times 10^4 \text{ A/m}^2\text{srV}$  at 20 nA of emission current. This shows that also at the relatively large current regime, the NAIS is a viable concept. We emphasize that the latter seems only possible when using relatively large gas chamber dimensions with a large aperture.

6

During the experiments we have varied the inlet pressure to obtain different emission currents. We plot the brightness as a function of the emission current rather than the inlet pressure, such that the graph indicates the performance more clearly. This also enables comparison to simulations, shown in the same figure.

We see the experimental data following the trend of the simulation roughly. For low currents the brightness increases with increasing current, while later the brightness saturates. This corresponds to balancing the added current and the increased gas scattering and coulomb interactions.

The data and simulations are comparable in order of magnitude, but the measured data for argon is systematically less bright. The xenon and helium data match the simulation rather well, but considering the uncertainties and just using three data points this can only be considered coincidental. Note that the simulation only considers the acceleration region, while the measured data inevitably is affected by the entire optical system. One known consequence of that is the highest current data point (triangle) showing a quite low brightness. The coulomb interactions in the lens and the chromatic aberrations were expected to lower the brightness in this case.

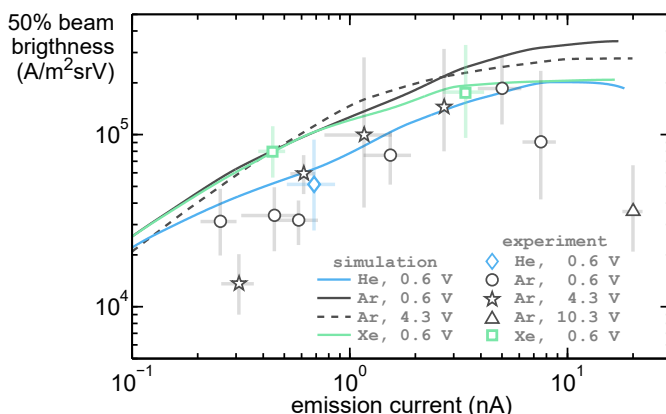


**Figure 6.14.** Measured brightness. For a particular gas species and membrane bias voltage we obtain different emission currents by varying the gas inlet pressure. The same chip was used for all the data in this graph, having a 1200 nm spacing, a 800 nm aperture side diameter, and 675 nm aperture on the electron side. The electron landing energy was 1 keV and the beam contained 121 nA of current. The error bars in the current represent minimum and maximum values measured. The error bars in the brightness are a combination of the 95% confidence interval of the model fitting and the error in the emission current. The simulated curves are based on the model discussed in chapter 4 and 5, using the dimensions and electron beam settings as acquired during the experiments. Only the acceleration region is included in the simulations. The indicated voltages refer to the applied membrane bias voltage.

We note that the measured current includes a rather large spread (10 to 50%). We found a lower current when the ion beam was focused on the detection plate, than when defocused. The detection plate was biased to +50 V so we believe almost no SE's can escape. Potential influences can be back-scattered ions, secondary ions, and local charging, however no satisfying complete and consistent explanation was found. The surface was molybdenum coating of several hundred nanometer on top of a silicon wafer surface. The same effect was observed on a stainless steel surface. The minimum and maximum measured values are introduced as error bars in figure 6.14. These minimum and maximum values are also added to the brightness uncertainty stemming from beam angle uncertainty. The uncertainty in the brightness is no longer strictly defined as a 95% confidence interval, but can be interpreted as a 95% or better chance of finding the real brightness within the error bars, under the assumption that no other errors are significant.

#### 6.4.3. Virtual source size and beam angle

We can inspect the virtual source size and the beam angle in figure 6.15 to understand the obtained brightness measurements better. The virtual beam angle is weakly increasing with inlet pressure, as expected from simulations. Also, the beam angle values are in the right ballpark when comparing to the simulations.

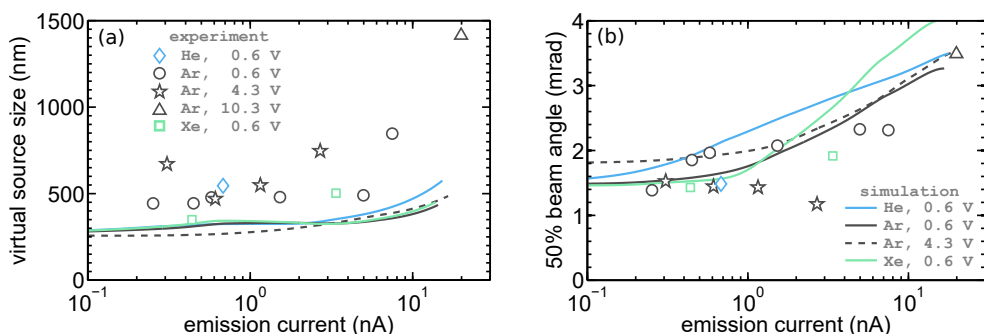


**Figure 6.15.** The source size and source angle in the virtual source plane are the constituents of the brightness measurements shown in figure 6.14. The virtual source is defined after acceleration up to 5 keV, but excludes the lens effect of the extractor electrode. The simulated curves are based on the model discussed in chapter 4 and 5, using the dimensions and electron beam settings as acquired during the experiments. Only the acceleration region is included in the simulations. The indicated voltages refers to the applied membrane bias voltage.

The virtual source size is more puzzling. At least in the lower current regime we expect the virtual source size to reflect the ebeam size, so a 200 to 300 nm fwhm. We see this in the simulations, but not in the measured data. The measured data is more or less a factor two larger than expected and shows unexpected variation between the data points.

It seemed that a resolution limit in our measurement system is the current bottleneck, rather than the source itself. We have tried to confirm this by generating a smaller virtual source size. When using an electron beam at an energy of 3 keV and 13.3 nA, the ebeam probe size was 33 nm. The measured virtual source size of the NAIS was 684 nm, which is comparable to the measurements with the bigger ebeam. In contrast, when deliberately enlarging the virtual source size, the measured virtual probe size does increase. Apparently the probe size measurements do not purely yield the virtual source size, but represent an upper bound. We have not been able to identify the cause of the error.

## 6.5. Emission current measurements

While the brightness measurements are the most important aspect of our experimental efforts, we report on a set of emission current measurements as well.

### 6.5.1. Pressure dependence

The measured total emission currents of different noble gases, as shown in figure 6.16, indicate an increasing current with increasing pressure. While this trend may seem obvious, this is not what was reported before. Jun performed similar measurements [2], but finds the curves attaining a maximum and decrease after a certain pressure. Such a reported decline does not follow from the simplified analysis presented in the introductory chapter, nor was it observed in any simulation. Experimentally we have never been able to reproduce the result and we are inclined to suspect some experimental error during the measurements performed by Jun.

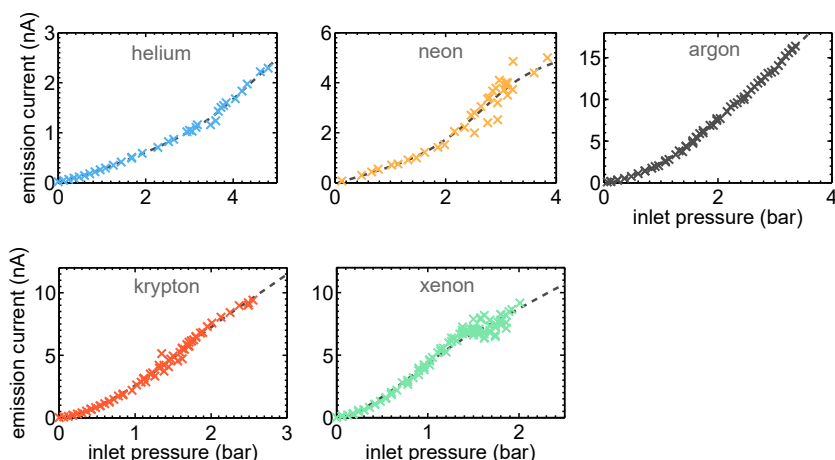


**Figure 6.16.** Total emission current measurements show a monotonic increase with pressure for all noble gases. The same chip as used for the reported brightness measurements was used, having an ion-side aperture of 800 nm. A bias voltage of 0.6 V was applied in combination with a 1 keV, 121 nA ebeam.

One peculiar detail is the concave start of all curves in figure 6.16, while for the low pressure regime a linear behavior is expected. We suspect it to be the result of outward bulging of the membranes, causing a longer effective ionization path for the electrons.

When recording a data set quickly upward in pressure, a factor of two difference in values could be obtained compared to ramping down and measuring again. When performing the measurements slowly, say one hour for one of these curves in figure 6.16, this inconsistency was absent. This may very well be related to the suspected bulging of the membranes. The deformation seems to take place on fairly slow time-scales of tens of seconds at least. In the case of neon and xenon and a little bit for krypton, some erratic behavior remained as seen in figure 6.16, which seems to have a different reason.

### 6.5.2. Current stability

Jun looked at stability and concluded that beam drift due to charging and depressurization can be a problem, but argues that in principle, very high current stability should be attainable [2]. In figure 6.17 we show a one-minute beam current measurements which demonstrates rather good stability indeed. Within this narrow time frame, the ebeam was stationary and the inlet pressure did not change more than 10 Pa.

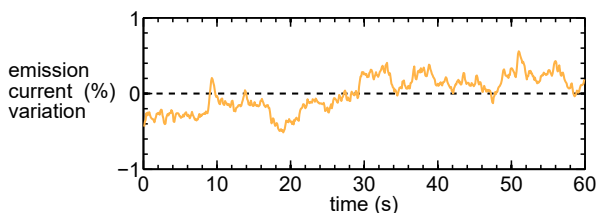


**Figure 6.17.** A one minute stability test of the ion beam current gave  $\sigma = 0.25\%$ . A 121 nA, 1 keV ebeam was used.  $P_{\text{inlet}} = 9.6 \times 10^4$  Pa,  $V_b = 0.0$  V,  $I_e = 13$  nA.

Hours of operation with the ebeam remaining inside the aperture is achieved on a regular basis, but over such long time scales the current fluctuates always at least a few percent. This is attributed to the small drift in the beam position in the order of 50 to 250 nm. For optimal stability it seems necessary to have an active compensation mechanism installed.

### Ionization efficiency

One of the assumptions in optimizing the NAIS is that the current generation scales with the ionization cross section. A simple ebeam energy variation experiment yielded confidence to this assumption. A chip with a relatively small aperture of 148 nm was used in combination with a 13 nA ebeam current, which we could focus into the aperture relatively easily. The pressure was set to  $P = 1.2 \times 10^4$  Pa and argon gas was used. The shape of the measured current is proportional to  $\sigma nL$ . A scaling factor (0.3) is inevitable because not all the current comes out and we do not know  $L$  and  $n$  very accurately. Below 500 eV it became difficult to focus the entire beam in the aperture.

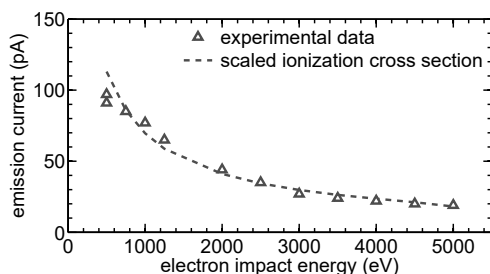


**Figure 6.18.** measured argon emission currents are compared to the ionization cross section energy dependence. The ebeam was maintained at 13 nA.  $P_{\text{inlet}} = 1.2 \times 10^4$  Pa and  $V_b = 0.0$  V.

### 6.5.3. Adhesively bonded chips

Some experimental efforts using glued chips are shared in this section. These chip are coated with metal, but have silicon nitride on the inner membrane surfaces. This means the ionization region is in line of sight with insulating layers, which potentially leads to charging effects of some kind.

Figure 6.19a shows a manifestation of what is believed to be charging indeed. After the chip was supplied with gas, suddenly the ebeam was unblanked and the emission current was measured. An immediate drop in current is observed, which continued until an equilibrium was attained at about 2/3 of the original current. To exclude ebeam drift or defocus as a cause, we have repositioned the ebeam during the measurement and checked if the ebeam focus was still adequate. These adjustment moments correspond to the absent data in the curves.

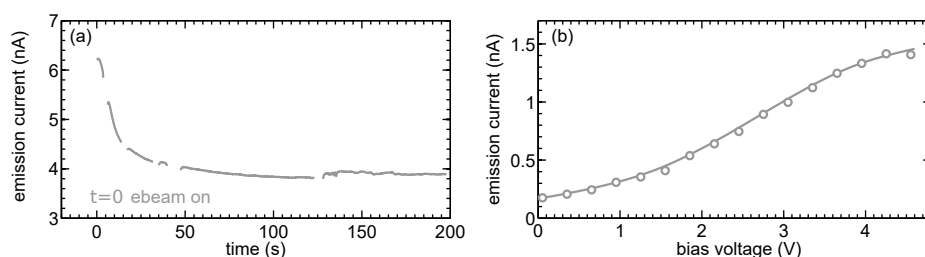


**Figure 6.19.** Current measured using adhesively bonded chips with an estimated spacing of  $10\mu\text{m}$  and aperture size of  $1\mu\text{m}$ , the pressure was fixed at  $P_{\text{inlet}} = 1 \times 10^5 \text{ Pa}$  and a  $1 \text{ keV}$ ,  $100 \text{ nA}$  ebeam was used. a) A rapid decrease in current when turning on the ebeam is observed until equilibrium is reached. Membrane charging is the most plausible explanation. The data-absent regions of the curve are moments when the ebeam was repositioned to the center of the aperture.  $V_b = 3.5 \text{ V}$ . b) Despite apparent charging of the membranes, the bias voltage did clearly affect the emission current in an expected fashion.

A cycle comparable to the one in figure 6.19a was reproduced multiple times using the same chip. A new cycle could be started after a night of no irradiation, or after performing a plasma-clean procedure. The latter yields free charges in the vacuum chamber, which apparently could neutralize the charging effects. Other cycles were no exact reproductions, indicating that perfect neutralization is probably not easily achievable. The electron beam energy for the curve in figure 6.19a was  $1 \text{ keV}$ , but we have experimented with irradiation of higher and lower energies. This should lead to different secondary electron yields, but similar charging behavior was observed for various energies. We have not observed a similar effect with fully metalized chips, which clearly points towards charging of the membranes being responsible for the behavior.

It may seem that the application of bias voltage is futile when the system is so heavily influenced by charging, but this was not the case. In figure 6.19b we can see an unambiguous response to the bias voltage. It is not clear how the charging is precisely acting. The fields inside the chip must be a complex manifestation of positive and negative residual charges on the top and bottom membrane, in combination with the applied field across the membrane.

A fairly strange observation was made when varying the inlet pressures. An abrupt increase in the current is acquired starting at about  $9 \times 10^4 \text{ Pa}$ . The effect was reproducible by increasing and decreasing the pressure. This resembles what is discussed in chapter 2 when looking at the gas flow rate, although a different chip was used. Both chips were based on silicon nitride without pillars, but are different in metal coating layer, adhesive, and some other details. While evidence for some bowing has been observed for pillar-based chips, such erratic behavior as seen here has never been seen with pillar-based chips.

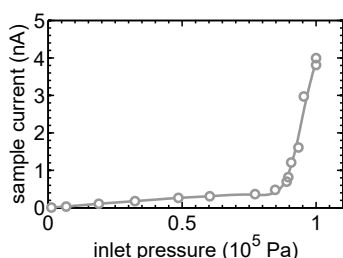


**Figure 6.20.** Current measured using adhesively bonded chips with an estimated spacing of  $10\mu\text{m}$  and aperture size of  $1\mu\text{m}$ . A 1 keV, 100 nA ebeam was used. A surprising response to the inlet pressure was attained at around  $9 \times 10^4$  Pa, where suddenly the measured emission current showed a steep increase.

## 6.6. Conclusion

### 6.6.1. Experimental results

As a project target we have aimed at a brightness of  $1 \times 10^6 \text{A/m}^2 \text{srV}$ . During the development of the experimental setup it became clear that the current setup is not capable of measuring such high brightness. We identify sub-optimal ebeam performance, too weak ion acceleration field, and too low ion lens voltage as known requirements for achieving  $B \geq 1 \times 10^6 \text{A/m}^2 \text{srV}$ . A brightness of  $B \approx 1 \times 10^5 \text{A/m}^2 \text{srV}$  did seem possible and was indeed measured. This can be considered a milestone in the project and such a brightness is already competitive.

The experimental results were in reasonable agreement with the simulation model, although the measured brightness was somewhat lower than predicted. From our experimental results we conclude that the brightness is limited mainly by a too large virtual source size. When a small ebeam probe size of 13 nm is used at 13 nA, no smaller probe size is measured either, clearly indicating a resolution limit in the measurement system. Investigating the cause of the resolution limit is the main task for obtaining better results in a follow-up experiment.

The emission current as a function of the pressure showed a monotonically increasing trend. This is what we expected from a simplified analysis and more advanced simulations, but disagrees with earlier experiments.

Some experiments with adhesively bonded chips with silicon nitride membranes demonstrated mostly problematic behavior. The emission current was time-dependent, indicating charging. The response to the inlet pressure was rather erratic, pointing towards mechanical problems. It is anyway difficult to produce small spaced glued chips and we conclude that such chips are inadequate for reliable nano-aperture ion source operation.

### 6.6.2. An improved experimental setup

While we do not fully understand all experimental results yet, we can suggest some concrete improvements to the setup. This will pave the way towards  $B \geq 1 \times 10^6 \text{A/m}^2 \text{srV}$  and helps to exclude certain brightness limitations, making experimental interpretation easier.

Replacing the decelerating lens with an accelerating lens improves on two fronts: it reduces the coulomb interactions and can offer lower aberrations. Driving the present design in acceleration mode would require 35 kV applied to the lens

electrode, which would lead to discharges. A different design is needed with more space between the electrodes and better anti-discharge measures.

A stronger accelerating field of 10 kV/mm right outside of the chip is also essential, and fairly easily achievable by placing the extraction electrode closer to the chip.

The inaccuracy in the current can most likely be reduced to a minimum if a Faraday cup is used. The difficulty in this setup, is that with the transmission detector, it will be hard to find. We advice a tiny Faraday cup right next to the transmission sample. By imaging the transmission sample beforehand using an SEM, it will be easy to aim the ion beam at the right position.

We know that the beam size without our device in the chamber gave a 158 nm probe size in stead of 231 nm. This means there is room for improvement by redesigning the top part of chip holder. Specifying tight tolerances for roundness and smoothness is crucial. The part also needs to be aligned with the ion optical column and thereby with the electron beam. A redesign that allows a smaller working distance from say 5 to 2 mm should yield an improvement as well. We furthermore note that the assessment of the egun performance was perhaps a bit too simple. Inferring a fw50 from one SEM image can be erroneous, but it is a key performance specification.

While precision measurements indicated that excellent alignment is feasible, we did not achieve it in practice. The main reason is too many degrees of freedom in the holder parts, making it difficult in practice to position them well. An improvement would have fewer freely moving parts. The chip itself should be fixated to the chip adapter, probably by glue.

## References

1. D. S. Jun, V. G. Kutchoukov, and P. Kruit. "Ion beams in SEM: An experiment towards a high brightness low energy spread electron impact gas ion source". *J. Vac. Sci. Technol. B* **29** (6), p. 06F603 (2011).
2. D. Jun, V. Kutchoukov, C. Heerkens, and P. Kruit. "Design and fabrication of a miniaturized gas ionization chamber for production of high quality ion beams". *Microelectron. Eng.* **97**, pp. 134–137 (2012).
3. N. Liu, X. Xu, R. Pang, P. Santhana Raman, A. Khursheed, and J. A. van Kan. "Brightness measurement of an electron impact gas ion source for proton beam writing applications". *Rev. Sci. Instrum.* **87** (2) (2016).
4. J. Orloff. "Measuring the beam size of a focused ion beam (FIB) system". *Proc. SPIE* **7729**, p. 77290C (2010).
5. R. M. O'Connell and R. A. Vogel. "Abel inversion of knife-edge data from radially symmetric pulsed laser beams". *Appl. Opt.* **26** (13), pp. 2528–2532 (1987).
6. DELMIC. "Secom platform for the FEI Verios - V1". [www.delmic.com/secom](http://www.delmic.com/secom) (2016).
7. SPOC. "Electron Optical Design, version 3.072". [www.lencova.com](http://www.lencova.com).
8. C. Schinkel. "Afstudeerscriptie: Hoogspanningsopstelling voor het nano-aperture ion source project". De Haagse Hogeschool (available: [hbo-kennisbank.nl](http://hbo-kennisbank.nl)) (2014).
9. G. C. King, M. Tronc, and R. C. Bradford. "A gas-supply line which permits a high voltage to be maintained across its ends". *J. Phys. E: Sci. Instrum.* **9** (12), p. 1049 (1976).
10. J. W. Pye. "A gas-phase high-voltage electrical isolator with controlled breakdown". *J. Phys. E: Sci. Instrum.* **11** (8), p. 825 (1978).



# *List of symbols*

$B_{50}$	50% beam brightness	$A/m^2srV$	$C_s$	spherical aberration coefficient	m
$I_{50}$	50% beam current	A	$C_c$	chromatic aberration coefficient	m
$d_{50}$	fw50 spot size	m	$d_s$	spherical aberr. contribution	m
$\alpha_{50}$	50% beam angle	rad	$d_c$	chromatic aberr. contribution	m
$s$	defocus model parameter		$d_g$	geometrical probe contribution	m
$M$	magnification		$d_{td}$	trajectory displacement contr.	m
$M_a$	angular magnification		$\Delta\epsilon$	fw50 energy spread	eV
$z$	coordinate along optical axis	m	$\Phi$	ion acceleration voltage	V
$z_f$	image plane location	m	$V_b$	bias voltage	V

# 7

## Other processes in the ionization volume

*"Whenever anyone says, 'theoretically', they really mean, 'not really'"*

DAVID PARNAS

*"We can only see a short distance ahead,  
but we can see plenty there that needs to be done."*

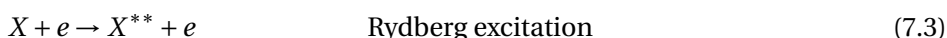
ALAN TURING

## 7.1. Introduction

Our goal for the NAIS is making single-charged positive ions, but inevitably, many more processes occur in the ionization region. So far, development of the NAIS has only been concerned with single-charged impact ionization. In this chapter we will identify possible other interactions and explore to what extent they affect the final beam composition. We use established theory to come to simple estimates for the final beam composition. No new experimental work is discussed. We focus our attention to argon gas, but the method should be easily extendible to other gases.

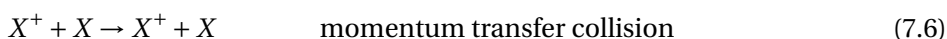
### 7.1.1. What else happens in the ionization region?

The electrons interact in various ways with the neutral gas. We may remove more than one electron and acquire multiply charged ions, scatter elastically and transfer momentum, or we may bring the atom into an excited state. The last possibility can be sub-divided into excitation to a radiative level, excitation to a metastable level, and excitation to a Rydberg state, which is a highly excited state close to ionization. The reaction equations of said processes are



We use  $X^+$  for ions,  $\tilde{X}$  for an energetic neutral,  $X^*$  for an excited atom (possibly metastable), and  $X^{**}$  for a Rydberg excitation.

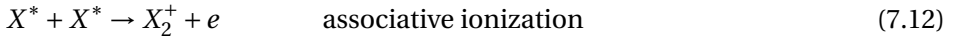
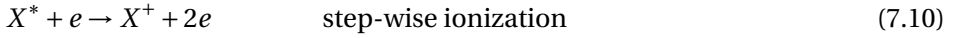
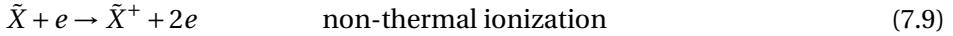
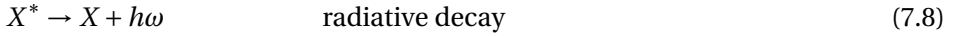
The reaction products may engage in a plurality of interactions [1, 2], but only those processes that could be relevant in our configuration are considered here. The ions may scatter on the neutrals on the way out of the interaction volume. Two elastic collisions that can be identified are



Such elastic collisions were already considered by using an atomic diameter in the introduction chapter. In chapter 4 this interaction is discussed in more detail.

The most obvious reaction of an excited state atom is relaxation to the ground state by photon emission. We also consider the formation of molecular noble gas ions, a compound which has been known since 1936 [3] (see also for example references [4, 5]). Two excited state atoms may form molecular ions via associative ionization and a second possibility is the encounter of a highly excited Rydberg atom and an unexcited atom, which is called Hornbeck-Molnar ionization. Molecular ion formation often needs to be considered in describing high density plasmas [1, 2]. Furthermore, we consider the ionization of a neutral atom with high momentum

due to an earlier elastic electron scatter event and we consider the ionization of an already excited atom. The reaction equations are:



### 7.1.2. Influence on the performance

A good question is: do any of these reactions matter for the NAIS performance? At the end of the day, all we care about is the final ion beam. An excited atom that emits a photon and comes back to the ground state does not jeopardize the final beam quality for example. For the other processes this is not so clear though.

Elastic collisions of electrons can be problematic if the energy transfer is larger than the thermal energy. If this happens with great abundance, the gas is no longer thermally distributed and we obtain a lower brightness. We first look at the possible energy transfer of an elastic collision event between an electron and an atom. The transferred energy from an electron to an atom at rest is  $\epsilon_a = \epsilon_e 4m/M(1 + m/M)^{-2} \sin^2\left(\frac{\theta}{2}\right)$ , with  $m/M$  the electron to atom mass and  $\epsilon_e$  the electron energy. For argon,  $m/M = 1.37\text{e-}5$ , which leads to a maximum at  $\theta = \pi$  of  $\epsilon_a = 55$  meV, for an electron beam energy of 1 keV. On average the energy transfer is lower because of the probability of scattering at different angles. We conclude that the acquired energy is in the order of the thermal energy, which is just enough to affect the brightness.

Higher charged and molecular ions may lead to problems as well. In a fully electrostatic system, all trajectories are independent of the mass and the charge (except for the sign of the charge). This means that  $\text{Ar}^+$ ,  $\text{Ar}^{2+}$ , and  $\text{Ar}_2^+$  are focused into the same spot. One problem is, however, that the user may not desire the heavier or the more energetic particles on the target. Secondly, the velocity differences can become a problem when scanning quickly. For example, if the scan electrodes are 100 mm above the sample and we consider a 10 keV argon beam, the difference in travel time for  $\text{Ar}^+$ ,  $\text{Ar}^{2+}$ , and  $\text{Ar}_2^+$  is in the 100 ns range. Since this is in the order of a possible pixel irradiation time, it can cause a lagging pixel blur. Another potential problem is magnetic field sensitivity. Magnetic deflection scales with  $\sqrt{q/m}$ , so if a magnetic field is present, we may end up with three different spots on the sample. Suppose an argon ion beam travels for 100 mm in a uniform 1  $\mu\text{T}$  field at 10 keV beam energy, the deflection of the three species is  $\text{Ar}^{2+}$ : 77 nm,  $\text{Ar}^+$ : 55 nm, and  $\text{Ar}_2^+$ : 38 nm. That is more than enough to be unpleasant. The earth magnetic field is about 50  $\mu\text{T}$ , so we would need excellent magnetic shielding or magnetic cancellation to prevent beam separation effects.

Due to the identified potential problems, a quantitative analysis of the produced species is required.

## 7.2. Calculation method

We will try to estimate the contributions of the various processes for argon gas. We begin by quantifying the relevant reactions by using total cross sections. The next step is considering the loss mechanisms of the reaction products.

### 7.2.1. Cross sections

Figure 7.1 shows the cross section of argon for excitation, elastic momentum transfer, and ionization. The rate at which excited atoms can be made is proportional to the cross section. So, we can see directly that the rate of excited species generation is only about 10% of the total ionization rate for 1 keV electrons. Since ionization yields secondary electrons, which have a lower energy, they could engage in more efficient excitation. However, it was explained earlier that we mostly intend to operate the NAIS under the condition that most electrons do not engage in any ionization at all. That means that only about 1 % of the primary current could become a slower electron. The cross section for excitation at lower energies, around the maximum, is about 10 times higher than at 1 keV, but since the secondary current is only about 1 % of the primary current, the net influence of the secondary induced excitation is at most 10 times lower than the primary excitations. The double to single ionization ratio at 1 keV is 0.0470 and the single to triple ratio is 0.0083. Since these are a direct processes there is not much we can do to tune this other than changing the electron beam impact energy.

We should be careful in considering what cross sections to use for what purpose. A total elastic cross section will give a huge overestimate of the momentum transfer because small angle scattering gives a big contribution to the inelastic cross section, while it hardly transfers momentum. The momentum cross section accounts for this, but often includes non-elastic contributions. This is useful if you want to know what happens to the electron, but we are interested in the atom. What we need is the elastic momentum transfer cross section. Surprisingly, it is not so easy to find this particular cross section up to 1 keV. We have used a set composed by Hayashi, which was made available online by Phelps [6]. This set was used and verified by Nanbu [7] and supposedly discussed by Kosaki and Hayashi [8] (in Japanese).

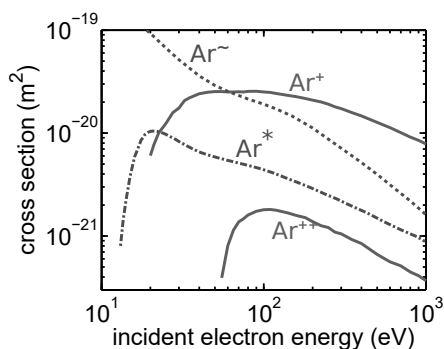


**Figure 7.1.** Electron beam impact single ionization ( $\text{Ar}^+$ ) [9], double ionization ( $\text{Ar}^{2+}$ ) [9], elastic momentum transfer ( $\text{Ar}^\sim$ ) [6] and total excitation cross sections ( $\text{Ar}^*$ ) [10] of electrons scattering on argon atoms.

Figure 7.1 shows the total cross section for excitation, however, for the Hornbeck-Molnar process [4, 11] we require the atoms to be in a highly excited state, i.e. a Rydberg state. The energy required to form a molecular argon ion from two ground state atoms is 14.71 eV [1] and the ionization potential of argon ions 15.76 eV [10]. In principle, any state with energy above 14.71 eV could participate in the Hornbeck-Molnar process and Bogeaerts argues that this is indeed the case [1]. We neglect the influence of kinetic (thermal) energy as it is relatively low at room temperature. The relevant excited states for the Hornbeck-Molnar are therefore all excited states above  $3d'[^3/2]_1$ , starting from the  $4d[^1/2]_1$  state. The cross sections for this level range are not directly available, but the individual level cross sections for the first 25 excited states are [10]. We subtract the sum of all states up to  $4d[^1/2]_1$  from the total to get the applicable cross section. See figure 7.2 for the result. We note that quite different cross sections for the total [12] and the individual levels [6] can be found elsewhere. Yanguas-Gil et al. [10] have considered a variety of sources and tested the cross sections for consistency with swarm parameter measurements and we use the set suggested by them.

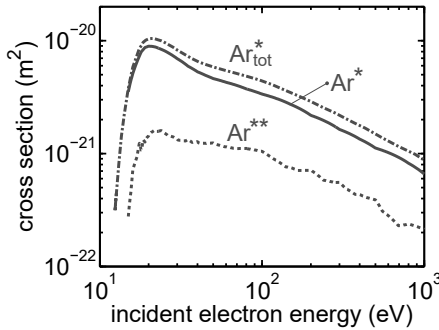


**Figure 7.2.** Total excitation cross sections of electron impact on argon gas and a summation of all individual level cross section below the  $4d[^1/2]_1$  state. Data taken from Yanguas-Gil [10]. The difference between these two cross sections represents the cross section for excitation to highly excited state that may participate in the Hornbeck-Molnar process.

### 7.2.2. Loss mechanisms

From the cross sections alone we can not estimate the rate of reaction products. The reaction constituents may diffuse away or relax to the ground state before engaging in a reaction. We therefore need to calculate the concentration of reaction constituents. We will simplify the chip by assuming all reactions happen inside a cylinder which we will call the interaction volume. The height is equal to the membrane spacing and the diameter equals the aperture size. Figure 7.3 illustrates this model. We assume that all charged species are extracted and become a part of the final beam. Excited species may engage in secondary reactions to form charged species, or may be lost due to diffusion or radiation. The rate equation for the total number of a particular constituent is

$$\dot{N}^x = \dot{N}_{\text{production}}^x - \dot{N}_{\text{reaction}}^x - \dot{N}_{\text{diffusion}}^x - \dot{N}_{\text{decay}}^x \quad (7.13)$$

$N^x$  is the total number of particles in the interaction volume of constituent  $x$ .

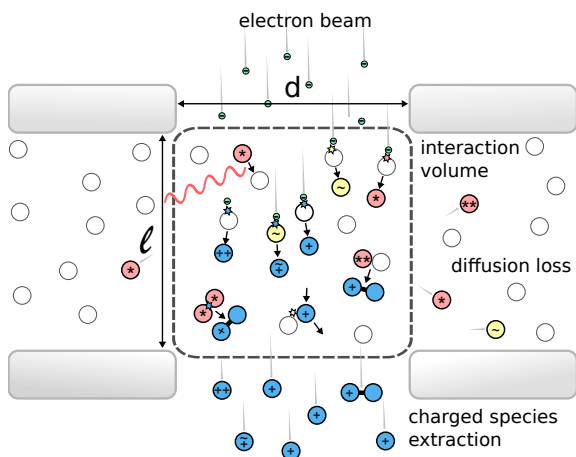


**Figure 7.3.** A sketch of the interaction volume showing the processes under consideration. We model the system as a cylinder of height  $l$  which is equal to the membrane spacing, and diameter  $d$  being equal to the aperture size. All means of ion formation are assumed to happen within this volume and all ionic species are assumed to escape the double membrane structure. Diffusion may occur in all directions

Since we will deal with particle numbers and time scales, it is good to get acquainted with some typical values for the NAIS first. The electron current is around 100 nA, so one electron every 1.6 ps, or about 600 billion electrons per second passing through the ionization volume. The typical flight time through a chip of, say 250 nm length, is 10 fs, so a snapshot of the ionization region will typically not contain any electrons. We operate at a typical ion current of 1 to 2 nA, which amounts to about one ion every 100 ps. We tune the extraction field such that the residential time is smaller than 100 ps, as we preferably have only one ion at a time in the interaction region to prevent ion-ion interaction. A field of 0.5 kV/mm across a few hundred nanometers of spacing leads to these time scales [13]. The number of molecules in the interaction volume is  $N = nAl$ . Since different chip sizes can be acceptable for the NAIS, the range of this value is rather broad, typically between  $1 \times 10^3$  and  $1 \times 10^5$ .

Diffusion is one mechanism for loosing excited state species before engaging in a reaction. For the RMS diffusion length in  $N_{\text{dim}}$  dimensions, it is well known that  $\langle x^2 \rangle - \langle x \rangle^2 = 2N_{\text{dim}}Dt$ . For the diffusion coefficient we can use  $D = \frac{1}{3}\lambda \langle v_t \rangle$ , with  $\langle v_t \rangle$  the mean thermal velocity of the particles. If after some time  $\tau$  the RMS distance due to diffusion is about equal to the typical size of the interaction volume  $s$ , we have lost a significant amount of atoms by diffusion. This can be interpreted as the diffusion time constant. So, we set  $\sqrt{\langle x^2 \rangle - \langle x \rangle^2} = s$  and get for the diffusion time constant

$$\tau_{\text{diff}} = \frac{3s^2}{2N_{\text{dim}}\lambda \langle v_t \rangle} \quad (7.14)$$

We can interpret this diffusion time as the average residential time of an excited atom in the interaction volume. A typical chip geometry may give for the interaction volume  $l = 250$  nm and  $d = 100$  nm. The particle density is such that  $\lambda = 125$  nm. If we consider 1 D diffusion along the cylinder ( $s = l$ ) and 2 D diffusion radially outward ( $s = d$ ), we obtain for  $\tau_{\text{diff}}$  in the length direction 2.15 ns and 172 ps in the

radial direction. We may inversely add them to obtain a single diffusion time of 159 ps for argon.

An estimate for the rate of atoms lost by diffusion is simply  $N^x(\tau_{\text{diff}})^{-1}$ . Note that we could of course solve Fick's law instead, which seems natural and more accurate. However this leads to some complications on how to model the geometry. Spherical symmetry is easily solved but isn't quite the right geometry for our cylindrically symmetric system. Solving in 1D and 2D separately lead to the problem that the membranes do not truly confine, but probably adsorb the excited states, so radially it can't be interpreted truly 2D. As solving Fick's law leads to comparable concessions, we simply use the diffusion time constant. Only a full 3D simulation, carefully taking the geometry into account would offer good accuracy, but for the purposes of simple estimation as presented here, this is avoided.

Relaxation to the ground state by photon emission is a second mechanism for loss of excited state atoms. For the lowest excited states of argon the lifetime is 2.2 ns [14], but higher levels have much longer lifetimes up to 300 ns [15, 16]. Note that two metastable levels of argon ( $4s[3/2]_2$ ,  $4s[3/2]_1$ ) have lifetimes of 55.9 s and 22.9 s [17]. We can conclude that this mechanism takes place on a time scale much larger than diffusion and optical relaxation only plays a minor role. This means we do not need to distinguish between metastable states and radiative states as essentially all states outlive diffusion. Only for relatively large chips at high pressures do we get diffusion times in the order of optical relaxation times, but only for the lowest excited levels.

### 7.3. Estimates of the beam composition

If we consider no reactions but only diffusion and radiation, we can estimate an upper bound for the number of excited state atoms. We use equation 7.13 in steady-state to get

$$\dot{N}^* = \dot{N}_e n \sigma_* l - \frac{N^*}{\tau_{\text{diff}}} - \frac{N^*}{\tau_{\text{rad}}} = 0 \quad \rightarrow \quad N^* = \frac{\dot{N}_e n \sigma_* l}{\tau_{\text{diff}}^{-1} + \tau_{\text{rad}}^{-1}} \quad (7.15)$$

For our estimate we take  $l = 250$  nm,  $d = 100$  nm and  $\lambda = 125$  nm, giving  $\tau_{\text{diff}} = 159$  ps. The ebeam is 1 keV and  $I_e = 100$  nA. For the radiative lifetime we use 20 ns, which is a little arbitrary, but this is also hardly of influence. We find for the number of excited state atoms in the interaction volume  $N^* = 0.39$ , and  $N^*/N = n^*/n \approx 1 \times 10^{-5}$ . This relative concentration of excited argon atoms to ground-state atoms is so low, that associative ionization is negligible. Mind that the rate of this process is proportional to  $N^{*2}$ . In other words, two excited atoms will never find each other before being diffused away. Step-wise ionization is also highly unlikely, as it is proportional to the relative concentration of excited to ground state atoms. The concentration of non-thermal atoms is  $\tilde{N} = 0.72$ ; very low as well, so non-thermal ionization gives a negligible contribution too. This particular example illustrates a more general result we have obtained from considering a variety of chip configurations. Namely, that step-wise ionization, non-thermal



ionization and associative ionization are negligible processes for any reasonable NAIS configuration (contributions are smaller than 0.001 % of the total current).

The Hornbeck-Molnar process cannot be disregarded on this basis. For the reaction rate we use  $k_{\text{HM}} = 2.0 \times 10^{-15} \text{ m}^3 \text{ s}^{-1}$ , as suggested by Bogaerts [1], without distinction in excited level. It is important to note though, that his reaction rate should be used with a concentration of excited states above 14.71 eV, and not with the total concentration of all the excited states. For comparison we can derive a cross section and a time scale from this reaction rate.  $\sigma_{\text{HM}} = k_{\text{HM}} / \langle v_t \rangle = 3.7 \times 10^{-18} \text{ m}^2$  and  $\tau_{\text{HM}} = (kn)^{-1} = 43 \text{ ps}$  if  $n = 1 \times 10^{25} \text{ m}^{-3}$ . The cross section is large, which may be attributed to the fact that Rydberg atoms have a large physical size. From the time scale we conclude that the reaction may very well compete with diffusion.

The rate at which the Hornbeck-Molnar process produces molecular argon ions is  $\dot{N}^{\text{Ar}_2^+} = k_{\text{HM}} n N^{**}$ . Substitution in equation 7.13 gives for the concentration of highly excited atoms

$$N^{**} = \frac{\dot{N}_e n \sigma_{**} l}{\tau_{\text{diff}}^{-1} + \tau_{\text{rad}}^{-1} + k_{\text{HM}} n}. \quad (7.16)$$

The radiative lifetime of the highly excited states needs to be taken, for which we use 200 ns. Effectively, radiation is negligible. The dissociation energy of molecular argon ions is 1.23 eV [18]. Since this energy is more than we typically have available in the interaction volume, thermally or by electric acceleration, we assume that all molecular ionic argon that is formed becomes a part of the final beam. The molecular argon current is given by

$$I[\text{Ar}_2^+] = \frac{I_e k_{\text{HM}} n^2 \sigma_{**} l}{\tau_{\text{diff}}^{-1} + \tau_{\text{rad}}^{-1} + k_{\text{HM}} n}. \quad (7.17)$$

7

We find that this current is in general not negligible and ionic molecular argon is expected to be formed.

The current from ions formed directly by impact ionization is given by

$$I[\text{Ar}^{i+}] = i \cdot I_e n \sigma_{i+} l. \quad (7.18)$$

On the way out, a double-charged ion may attain one electron from a neutral atom, resulting in two single-charged ions. The cross section for this process is  $\sigma = 0.11 \times 10^{-20} \text{ m}^2$  at a center of mass energy of 0.4 eV [19] (at 1 eV it lowers to  $0.051 \times 10^{-20} \text{ m}^2$ ). Since this cross section is smaller than the typical electron impact ionization cross section, we can directly conclude that this process is negligible because most electrons do not engage in ionization at all (see introduction chapter). This is a tricky argument so a numerical example is in place. The fraction of generated double-charged argon that engages in such a reaction is roughly  $n \sigma l$ , which gives for a typical configuration with, say  $n = 2.5 \times 10^{25} \text{ m}^{-3}$  and  $l = 200 \text{ nm}$ , a fraction of 0.6%. This was a worst case scenario estimate so quite confidently we can neglect redistribution of double-charged ions. We did not find a cross section

for triple ionized argon at such a low energy, but we expect the effect to be limited as well.

Table 7.1 summarizes the results for a few typical NAIS configurations. The relevant contributions to the final beam that have been identified are direct single, double and triple ionization, and Hornbeck-Molnar molecular ion formation. Other contributions are not listed as they are insignificant.

$l$ nm	$d$ nm	$\lambda$ nm	$n$ $\text{m}^{-3}$	$\tau_{\text{diff}}$ ps	$I[\text{Ar}^{1+}]$ nA (%)	$I[\text{Ar}^{2+}]$ nA (%)	$I[\text{Ar}^{3+}]$ nA (%)	$I[\text{Ar}_2^+]$ nA (%)
250	100	125	$1.8 \times 10^{25}$	159	3.5 (87.6)	0.33 (8.2)	0.087 (2.2)	0.082 (2.0)
250	100	250	$9.0 \times 10^{24}$	80	1.8 (88.1)	0.17 (8.3)	0.044 (2.2)	0.028 (1.4)
1000	200	500	$4.5 \times 10^{24}$	169	3.5 (88.1)	0.33 (8.3)	0.087 (2.2)	0.058 (1.4)
1000	500	100	$2.3 \times 10^{25}$	4776	17.6 (87.3)	1.66 (8.2)	0.437 (2.2)	0.478 (2.4)

**Table 7.1.** Calculation of different ionic species contributions for a few combinations of particle density and chip geometry. The main component of the current is in all cases singly charged argon. For this calculation the electron beam was 100 nA at 1 keV.

## 7.4. Conclusion

Besides electron impact ionization creating single charged atoms, double and triple charged impact ionization and the formation of molecular argon via the Hornbeck-Molnar process are identified as relevant processes in the NAIS. Other processes involving excited or energized atoms are negligible because these atoms diffuse away before engaging in a charge-producing interaction.

Calculations for a few typical situations indicate that most of the beam is comprised of singly charged argon, the species we are intending to make. Besides single charged argon, the beam current consist for about 8.2% out of double charged argon, 2.2% out of triple charged argon, and for roughly 2% out of molecular argon. There is no obvious way, if at all, to prevent the production of such species.

We should comment on the fact that we have simplified the geometry severely, notably by using a top-hat particle density distribution. One result of this is that the calculated currents at a particular particle density and gas region length are not very accurate. This should not change the relative contributions though. The simple method of describing diffusion will give an inaccuracy in the molecular argon contribution, and this number should therefore be considered only as a rough estimate. We have also neglected the blockage of ions due to the membranes. Hence, the calculated currents are generated currents. Again, the relative amounts should not be affected too much. Neglecting any process besides electron impact ionization and HM ionization is believed to be a sound assumption despite the simplifications made. The estimates of other contributions are so convincingly low, that an improvement in the accuracy can not lead to a different conclusion.

## References

1. A. Bogaerts and R. Gijbels. "Role of Ar<sup>2+</sup> and Ar<sup>+</sup> ions in a direct current argon glow discharge: A numerical description". *J. Appl. Phys.* **86** (8), pp. 4124–4133 (1999).
2. S. K. Lam, C.-E. Zheng, D. Lo, A. Dem'yanov, and A. P. Napartovich. "Kinetics of Ar<sup>2+</sup> in high-pressure pure argon". *J. Phys. D: Appl. Phys.* **33**, pp. 242–251 (2000).
3. O. Tüxen. "Massenspektrographische Untersuchungen negativer Ionen in Gasentladungen bei höheren Drucken". *Zeitschrift für Physik* **103** (7) (1936).
4. J. A. Hornbeck and J. P. Molnar. "Mass Spectrometric Studies of Molecular Ions in the Noble Gases". *Phys. Rev.* **84** (4), p. 621 (1951).
5. P. Becker and F. Lampe. "Mass-Spectrometric Study of the Bimolecular Formation of Diatomic Argon Ion". *J. Chem. Phys.* **42** (11), pp. 3857–3863 (1965).
6. A. V. Phelps. "Online collection cross sections". [jilawww.colorado.edu/~avp/collision\\_data](http://jilawww.colorado.edu/~avp/collision_data) (last revised 27-04-2002).
7. K. Nanbu and J. Kageyama. "Detailed structure of dc glow discharges - effects of pressure, applied voltage, and  $\gamma$ -coefficient". *Vacuum* **47** (6-8), pp. 1031–1033 (1996).
8. K. Kosaki and M. Hayashi. "Denkigakkai Zenkokutaiikai Yokoshu". Prepr. Natl. Meet. Inst. Electr. Eng. Jpn. (in Japanese) (1992).
9. R. Rejoub, B. G. Lindsay, and R. F. Stebbings. "Determination of the absolute partial and total cross sections for electron-impact ionization of the rare gases". *Phys. Rev. A* **65**, p. 042713 (2002).
10. A. Yanguas-Gil, J. Cotrino, and L. L. Alves. "An update of argon inelastic cross sections for plasma discharges". *J. Phys. D: Appl. Phys.* **38**, p. 1588 (2005).
11. A. Bultel and P. Vervisch. "The Hornbeck-Molnar process in argon". *J. Phys. B: At. Mol. Opt. Phys.* **35**, p. 111–124 (2002).
12. F. J. de Heer, R. H. J. Jansen, and W. van der Kaay. "Total cross sections for electron scattering by Ne, Ar, Kr and Xe". *J. Phys. B: Atom. Molec. Phys.* **12**, p. 979 (1979).
13. V. Tondare. Towards a High Brightness, Monochromatic Electron Impact Gas Ion Source. Ph.D. thesis, Delft University of Technology. repository.tudelft.nl (2006).
14. O. Sahin, I. Tapan, E. N. Ozmutlu, and R. Veenhof. "Penning transfer in argon-based gas mixtures". *J. Instrum.* **5** (05) (2010).
15. J. A. Aguilera, F. Blanco, J. Campos, and M. Ortiz. "Lifetimes of some 6p levels of neutral argon". *Phys. Rev. A* **45** (5), pp. 2753–2756 (1992).
16. M. B. Das and S. Karmakar. "Radiative Lifetimes of Some Excited States of Neutral Argon". *Phys. Scripta* **71** (3) (2005).
17. D. M. Filipovic, B. P. Marinkovic, V. Pejcev, and L. Vuskovic. "Electron-impact excitation of argon: II. The lowest resonance 4s[3/2] 1 and metastable 4s[3/2]2 and 4s'[A1/2]0 states". *J. Phys. B: At. Mol. Opt. Phys.* **33** (11) (2000).
18. B. M. Smirnov. *Theory of Gas Discharge Plasma* (Springer International Publishing, 2014).
19. K. Okuno. "Charge Transfer of Ar<sup>2+</sup> and Kr<sup>2+</sup> in Their Own Gases Studied by the Beam Guide Technique". *J. Phys. Soc. Jpn.* **55** (5), pp. 1504–1515 (1986).

## List of symbols

$\tilde{X}$	energetic atom		$\tau_{\text{diff}}$	diffusion time constant	s
$X^*$	excited atom		$\tau_{\text{rad}}$	radiative life time	s
$X^{**}$	highly excited atom		$\lambda$	mean free path	m
$X^+$	single-charged ion		$\dot{N}$	particle production/loss	$\text{s}^{-1}$
$X^{i+}$	multiple-charged ion		$N$	# of particles	#
$X_2^+$	diatomic ion		$N^*$	# of excited particles	#
$i$	ion charge number	#	$N^{**}$	# of highly excited part.	#
$D$	diffusion coefficient	$\text{m}^2 \text{s}^{-1}$	$n^*$	excited particle density	#
$I_e$	electron beam current	A	$\dot{N}_e$	electron rate	$\text{s}^{-1}$
$n$	neutral particle density	$\text{m}^{-3}$	$\sigma_{**}$	highly excited cross section	m
$l$	gas length	m	$\sigma_{\text{HM}}$	Hornbeck-Molnar cross section	m
$d$	aperture diameter	m	$k_{\text{HM}}$	Hornbeck-Molnar reaction rate	$\text{m}^3 \text{s}^{-1}$
$s$	typical length	m	$\tau_{\text{HM}}$	Hornbeck-Molnar time constant	s
$N_{\text{dim}}$	# diffusive dimensions	#	$I[\text{Ar}_2^+]$	diatomic argon current	A
$\langle v_t \rangle$	mean thermal velocity	$\text{m s}^{-1}$	$I[\text{Ar}^{i+}]$	argon ion current	A



# Acknowledgments

Pieter, thank you for developing me into the physicist I am today. A pragmatic and quantitative approach is something I have certainly learned from you. Thank you for giving me the freedom I desired and for listening sincerely when the project got difficult. I never never felt judged too much for my mistakes and you always kept looking forward with inspiring optimism.

I would like to thank FEI and FOM for their financial support. Greg, it was a pleasure to work with you. You have consistently shown trust in my capabilities and that is very much appreciated. Hiking through the lovely woods of Oregon and drinking some IPA's was just great fun. When I visited Portland, Sean, we worked together very pleasantly. I had fun working with you in the lab and when debating the silly-scan method. Aurelien, we already worked well together during my bachelor. Experimenting together in Delft more recently on the NAIS was very pleasant and useful as well. Thank you for introducing me to what has now become a passion: sport climbing. Piet, thank you for your interest in my work and reviewing some of my writing.

Kees, you ignited my passion for charged particles during my bachelor and I am very grateful for that. We always worked together pleasantly and you supported me whenever, however I needed it. Jacob, we got along very well, thank you for all the interesting discussions. Anjella, thank you for always helping out.

The NAIS project has been very technical in nature and wouldn't have been possible without the assistance of many skilled technicians. Jan, we got along very well from the day I entered the CPO group. Skillfully you have fabricated many instruments for me with unprecedented precision, always encouraging me to appreciate quality. Han, you were a great aid to the project in various electronic endeavors. Always willing to help me out very creatively when I panicked because my experiment wasn't running according to plan. Carel, you took on the challenge of producing NAIS chips. You never gave up and managed to solve a tremendous amount of tricky problems. Your involvement in the project is greatly appreciated. Ruud, as a skilled mechanical engineer you worked out some neat practical solutions in the early stages of the project, thank you. I also want to thank Paul, Ger and the late Cor.

When I found out that there was too much work in the project, I did some talent scouting and convinced you, Diederik, to join the NAIS team. You were mostly responsible for the mechanical design of the experimental setup but contributed to the project in many other ways as well. Great inventions we developed together such as the 'chip-sucker' and the 'turbo-hengel' can not be left unmentioned. Guido, you were given the near-impossible task to produce NAIS chips. You managed to

find very clever ways of solving numerous challenges involved. Next to that, you did important work on the neutral particle density distribution calculations. Thank you for having been so involved in the project. Christiaan, you delivered a great contribution to the project, that is, building the electronics for the experimental setup. I did not need to motivate you because you brought in enough enthusiasm by yourself. Thank you for your hard work.

Robert, I had the pleasure to be your office mate. We quickly found out we get along very well. Sometimes we had to be careful that we didn't talk all day about digital sound processing or the latest Tarantino movie. You are an excellent scientist and you have contributed quite directly to my project, notably in setting up COMSOL simulations for both neutral particle distribution calculations as well as the charge induced coulomb interactions.

Many people contributed in maintaining the pleasant atmosphere in the CPO group. Gerward, Thomas, Yan, Josey, Sangheetha, Marijke, and more recently Wilco, Aditi, Gaudhaman, Willem, Conny, Dusan, Martin and many students that come and go, thank you all. Ali, Vincenzo, Ben, Angela, Nalan, Christiaan, Daan, Chris, although you are no longer in the group for a while now, thank you. Martijn and Lenard, thanks for keeping my brain active via intellectual discussions and by giving it some rest when we were climbing together.

Katja, Stefan, Celmis, Berb, Dorus, Suus, Crystel, Eva, Vera, Jachym, Rick, Jasper, Jasper, Rein, Jesse, Luuk, Joost, and other friends, thanks for all the fun, craziness, and support. Thank you Mart for making an awesome cover illustration and thank you Mathieu and René for being my paranymphs, but all three more so for being such great friends.

Special thanks to my family, for all the good times, for accepting that I spend more time on equations than on replying to your messages, for supporting me no matter what.

Dear Mathia, you have supported me in this accomplishment in many ways. We faced some difficult challenges, but through it all we never let that take control. Although we have gone separate ways now, you were my soul mate for many years and I will always cherish the memories we made together.

# Curriculum Vitæ

*"Be less curious about people and more curious about ideas."*

MARIE CURIE

Leon van Kouwen, born in Nijmegen, June 10th, 1987.

Bachelor degree in Applied Physics, received in 2009, Delft University of Technology.  
Thesis subject: high resolution electron-beam-induced deposition in a scanning electron microscope.

Master degree in Applied Physics, received in 2011, Delft University of Technology.  
Thesis subject: design of a miniaturized scanning electron microscope.  
Internship: magnetic electron-spin rotator design, SPECS GmbH, Berlin

PhD Candidate at the Charged Particle Optics group Delft, started in 2012.  
Subject: the nano-aperture ion source (this dissertation).